Analysis of Reservoir Fracture Sealing in an Active Geothermal System, Kawerau Geothermal Field, New Zealand

---

A thesis submitted in fulfilment of the requirements for the Degree of

Master of Science (Geology)

At the Department of Geology, University of Otago, Dunedin New Zealand

---

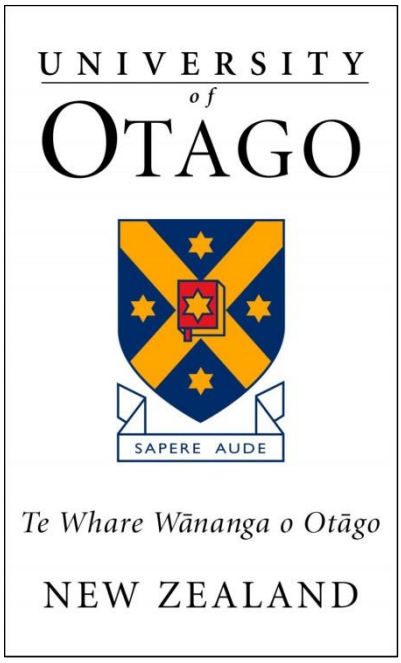

Aaron J. Lister

2016

Frontispiece

“Ahhh, but can you not also make bridges out of stone?”

Sir Vladimir

An explanation of the scientific method

Abstract

The microscopic crystallographic structures of geothermal minerals precipitated in fractures located within active geothermal reservoirs have the potential to record significant information concerning the kinematics of fracture formation and sealing over time. It is vitally important to understand these processes when developing reservoir models, especially when defining the influences of secondary permeability for high temperature geothermal systems.

This study highlights a multi-staged analysis of the mineral calcite that has been identified to control permeability in the reservoir of the Kawarau Geothermal Field, TVZ, New Zealand. Outlined is the methods of carrying out EBSD, EDX, Cathodoluminesce, ICPMS and a variety of other techniques to understand the process of fracture sealing using field samples. The initial study of the fracture identified two separate sealing mechanisms occurring between the different phases of calcite deposition. In addition the two phases of calcite deposition had different internal crystallographic structure and elemental composition. A 3-D analysis was then carried out by serial sectioning, this includes the process of 3-D EBSD by serial sectioning and builds on the initial findings. Finally the ICPMS analysis was unable to accurately date the bladed calcite, due to inadequate U-Th ratios. However, it did show that it is possible to carry high-precision geochemical analysis on geothermally precipitated bladed calcite. The Eu anomaly identified in the calcite highlights the complex history of geothermal fluids in the reservoir of Kawerau. These multiple aspects assist in providing a deeper understanding of how the geothermal system has changed over time.

By reconstructing calcite filled fractures using a range of alternative techniques in 2-D and 3-D, an advanced insight into the complex nature of vein crystal growth evolution and related chemical patterns can be extracted. These can then be used to constrain how veins control fracture permeability over time on a microscopic scale.

Table of Contents

List of Figures

Chapter 1

Chapter 2

Chapter 3

Chapter 4

List of Tables

Chapter 3

Chapter 4

Acknowledgements

Firstly I would like to express a huge thank you to my supervisors Professor Dave Prior and Dr. Dave McNamara for setting up the opportunity to undertake this project. Not only were you both an extensive source of knowledge and experience but you also provided many suggestions and reviews throughout this journey.

I would also like to acknowledge and thank the staff and students of the Geology Department at the University of Otago for their continued support and understanding throughout my brief time here. I would like to especially thank Marco Brenna, Andrew McNaughton, Mike Palin, Brent Pooley, and Luke Easterbrook for technical advice and help with sample preparation and analysis.

Acknowledgements must go GNS Sciences and the NGTA Trust for supplying core samples and information that assisted in the completion of this project.

Thanks must also go to my parents, Graeme and Eleanor for the guidance and support over my time spent at university. I would also like to thank Rachel for understanding why I could not come home some nights and bearing with the geology puns and trivia for the past few years, you always knew how to make me smile when things got tough.

With one final word I would like to thank everyone else who has been involved or has contributed in any way in the completion of this thesis.

Chapter 1

Introduction

1.1 General Overview

1.1.1 Geothermal Energy and Exploration

Since the first generation of electricity utilising the earth's heat, there has been a worldwide increase in the development of affordable and efficient renewable energy sources (Wohletz and Heiken, 1992; Holm et al., 2010). This has driven geothermal power generation and exploration in numerous countries where this is a viable resource, contributing to an estimated total global installed capacity of 18,500 MW in 2015 (Gupta and Roy, 2007; Holm et al., 2010; Jennejohn et al., 2012). With geothermal energy gaining in importance in New Zealand and around the world there has been continued research in developing existing geothermal systems and refining current exploration techniques (Grant and Bixley, 2011). To evaluate the production potential of an active geothermal field successfully it is essential to fully understand the extent and character of the prospective reservoir, this includes reservoir temperature, fluid types, geological history, and numerous other related characteristics that all contribute to the evolution of a field's permeability (Meunier, 2005; Leonard et al., 2010).

1.1.2 Fracture Sealing

One of the most recurring problems with understanding the functionality of geothermal fields, field development, and geothermal exploration is the process of fracture sealing. Fracture sealing is a naturally occurring process that affects the permeability of the entire field through mineralised scale build up. This issue is faced by many fields in geothermal regions around the world including; Iceland (Arnrrson, 1978; Meier, 2014), Japan (Saishu et al., 2015), the Americas (Sturchio and Binz, 1988; Davatzes and Hickman, 2010), The Philippines (Cope et al., 1985; Stimac et al., 2008), and here in New Zealand especially at fields like Ngawha, Broadlands, and Kawerau (Browne and Ellis, 1970; Henneberger and Browne, 1988; Simmons and Christenson, 1994; Dempsey et al., 2012; Wallis et al., 2012). There are a wide range of factors which affect the rate and type of sealing processes that occur, including rock chemistry, fluid chemistry, temperature, and pressure. The most common minerals that form fracture sealing precipitates include but are not limited to calcite ($CaCO_3$), Quartz (SiO_2), and to a minor extent zeolites, clay minerals, and sulphides such as pyrite (Noiriel et al., 2010).

1.1.3 The Taupo Volcanic Zone (TVZ)

The continental landmass that is New Zealand (Figure 1.1) straddles a complex subduction plate boundary that is dominated by transitional tectonic fault structures, continental margin, and back-arc volcanism (Cole 1979; Cole and Lewis, 1981; Rowland and Sibson, 2004).

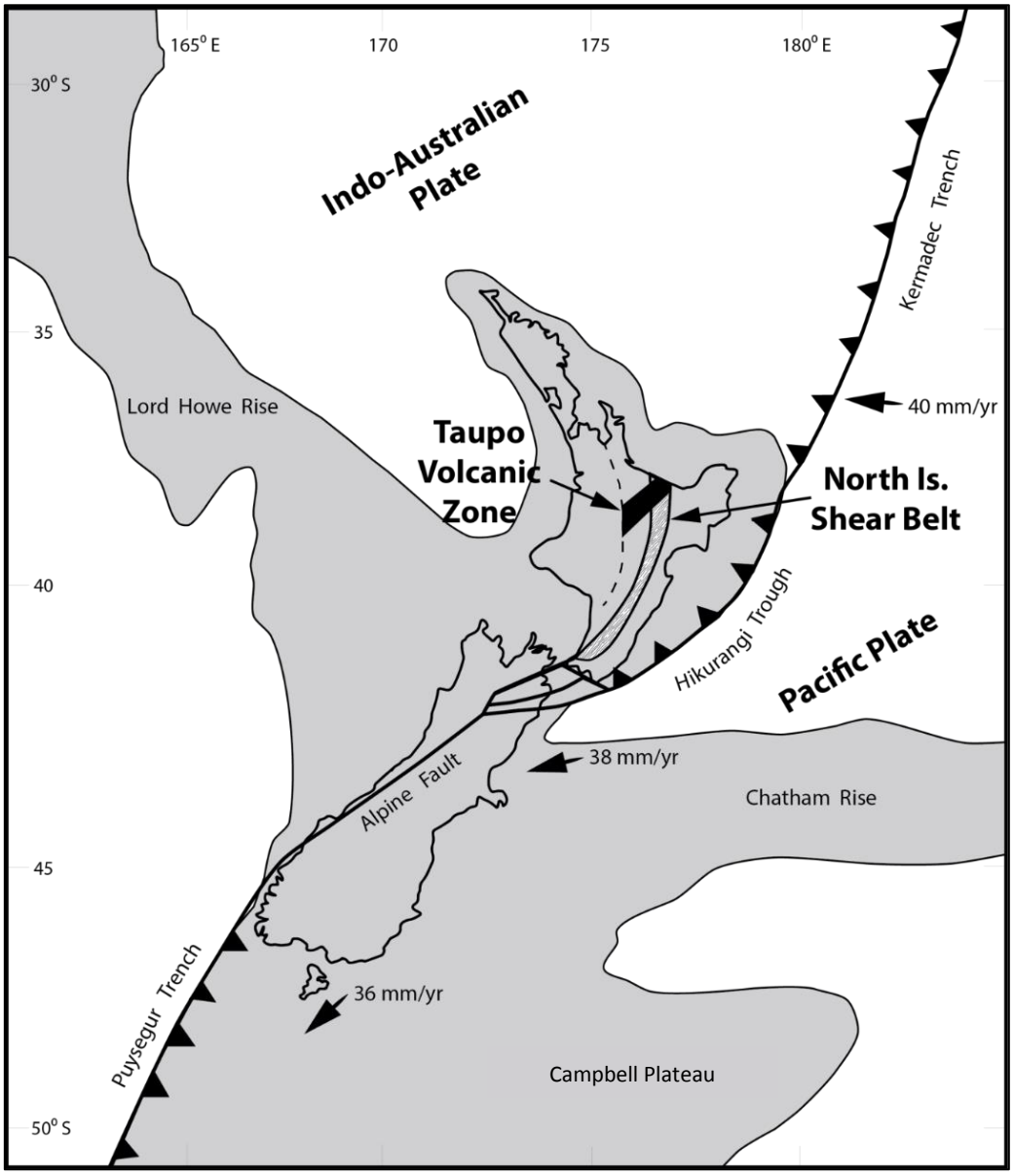

Figure 1.1 The location of New Zealand and the Taupo Volcanic Zone with respect to the Pacific and Indo-Australian plate boundary. Arrows indicate relative plate motion of the Pacific Plate in relation to the Indo-Australian Plate. From Cole (1990).

Within the centre of New Zealand's North Island is a localised zone of thinned crust (~15 km thick) known as The Taupo Volcanic Zone (TVZ) (Bibby et el., 1995; Alcaraz et al., 2011). This belt of rifting-induced faulting and thinned crust is associated with elevated volcanic

activity and is one of the highest crustal heat flux intensities in the world (Bibby et al., 1995). The TVZ is a composite volcano-tectonic, NNE trending depression that stretches from Ruapehu in the south to past White Island in the north (Cole et al., 1995). This 350 km long, segmented rift structure dominates the central region of the North Island of New Zealand and is responsible for the deposition of the majority of rock and sediments located in the central North Island (Cole et al., 1995; Wood et al., 2001). Due to the elevated heat anomaly and areas of high permeability which allow the circulation of fluids to transfer the heat from the source, the TVZ leads itself to be hydrothermally highly active (Bibby et al., 1995; Haughton et al., 1995; Spinks et al., 2005; Wilson and Rowland, 2015). Geothermal systems within the TVZ are thought to have been active for hundreds of thousands of years relating to long-lived heat up-flow zones which may have experienced multiple stages of evolution over their lifetime (Rowland and Sibson, 2004; Meunier, 2005; Leonard et al., 2010; Wilson and Rowland, 2015). The TVZ is described in greater detail in Chapter 2.

1.1.4 Hydrothermal Activity

Geothermal activity has long been recognised in the TVZ and is used for a range of primary industries (Cole and Lewis, 1981). The TVZ is a host to a number of high enthalpy geothermal systems (Bibby et al., 1995; Haughton et al., 1995; Spinks et al., 2005; Wilson and Rowland, 2015). There are 25 of these recognised geothermal systems within the TVZ (Figure 2.1); 17 of these systems have a potential geothermal resource >250°C and together generate a natural heat output of approximately 4200 MW (±500MW) (Bibby et al., 1995; Houghton et al., 1995; Weir, 2001; Spinks et al., 2005; Wilson and Rowland, 2015).

1.1.5 Study Location

The geothermal field that we have focussed on for this study is Kawerau, located in the north of the TVZ (Figure 2.1) which has a natural heat output of 100-150 MW_t (Bromley, 2002). This field has been the basis of many studies to characterise and develop an accurate geological model for geothermal activity, including: Basement geology (Studt, 1958; Browne, 1978a; Allis et al., 1993; Bignal and Milicich, 2012; Milicich 2013, Milicich et al., 2016), geothermal fluid flow and composition (Absar and Blattner, 1985; Christenson, 1987; Brathwaite et al., 2002; Wallis et al., 2012), subsurface structure (Grindley, 1986; Nairn and Beanland, 1989; Wood et al., 2001), and the evolution of the geothermal system (Browne, 1979; Nairn and Wiradiradja, 1980; Milicich et al,, 2013). Chapter 2 discusses this geothermal field in more depth, with Chapter 4 providing a review of the age and evolution of activity recognised at Kawerau.

1.2 Purpose and Scope of This Study

The purpose of this research is to develop a multi-dimensional understanding of fracture sealing within an active geothermal system by analysing mineralised fractures using a combination of new and existing methods. This process has been broken up into 3 sections which highlight the main stages of this study:

1) The first section aims at characterising examples of bladed calcite veins present in the Kawearu Geothermal Field using core from KA30 in the southern sealed area of the field. For this section electron backscatter diffraction (EBSD), energy dispersive x-ray (EDX), and cathodoluminescence (CL) are used to characterise the microstructures of the calcite present.

2) The second section aims at developing our understanding of these sealed fractures further by generating a 3-D model of a bladed calcite vein network to build on findings from Chapter 1.

3) Finally, in order to investigate the vein network and fracture sealing evolution through time, U-Series dating using laser ablation inductively coupled plasma mass spectrometry (LA-IC-PMS) was attempted. This step provides the isotopic and geochemical composition of the mineralisation while assessing the validity to develop this method further for dating geothermally precipitated calcite.

Each section is divided into individual chapters and laid out to systematically illustrate the scientific process for each phase of the multi-dimensional analysis. Chapter 2 is devoted to analysing the 2-D structure of the bladed calcite and introducing the concept of crystal growth, with Chapter 3 exploring the fracture network in 3-D space, and Chapter 4 examines the possibility of adding the 4^{th} dimension of time to the fracture sealing mineralisation in the basement reservoir. Due to time constraints available only a limited number of mineralised veins were investigated.

1.3 Contributors

- **A. J. Lister:** Responsible for the data collection and analysis for this study as well as primary author for Chapters 1, 3, 4, and 5. Carried out data collection and image analysis for Chapter 2 in addition to composing the methods and results for Chapter 2.

- **D. J. Prior:** Primary advisor at the University of Otago, assisted with SEM techniques, discussion of results, thesis reviews, and general guidance. Provided initial EBSD scans of the thin section.
- **D. D. McNamara:** Primary advisor at GNS Science. Primary author for the publication that is Chapter 2. Provided assistance with reviews, samples and discussion throughout the project.
- **M. Brenna:** Operated and instructed A. J. Lister on the SEM during the serial sectioning process.
- **J. M. Palin:** Operated and instructed A. J. Lister on the LA-ICP-MS, helped with geochemical data reduction, and provided reviews for Chapter 4.
- **A. McNaughton:** Carried out μCT imaging for all samples and assisted in the image analysis of the μCT data sets.

Chapter 2

Calcite Sealing in a Fractured Geothermal Reservoir: Insights From Combined EBSD and Chemistry Mapping

D.D. McNamara[1], A. J. Lister[2], & D. J. Prior[2]

[1] *GNS Science, Lower Hutt, New Zealand*

[2] *Department of Geology, University of Otago, Dunedin, New Zealand*

Abstract

Fractures play an important role as fluid flow pathways in geothermal resources hosted in indurated greywacke basement of the Taupo Volcanic Zone, New Zealand, including the Kawerau Geothermal Field. Over time, the permeability of such geothermal reservoirs can be degraded by fracture sealing as minerals deposit out of transported geothermal fluids. Calcite is one such fracture sealing mineral. This study, for the first time, utilises combined data from electron backscatter diffraction and chemical mapping to characterise calcite vein fill morphologies, and gain insight into the mechanisms of calcite fracture sealing in the Kawerau Geothermal Field. Two calcite sealing mechanisms are identified 1) asymmetrical syntaxial growth of calcite, inferred by the presence of single, twinned, calcite crystals spanning the entire fracture width, and 2) 3-D, interlocking growth of bladed vein calcite into free space as determined from chemical and crystallographic orientation mapping. This study also identifies other potential uses of combined EBSD and chemical mapping to understand geothermal field evolution including, potentially informing on levels of fluid supersaturation from the study of calcite lattice distortion, and providing information on a reservoir's history of stress, strain, and deformation through investigation of calcite crystal deformation and twinning patterns.

Journal of Volcanology and Geothermal Research 323 (2016) 38–52

Contents lists available at ScienceDirect

Journal of Volcanology and Geothermal Research

journal homepage: www.elsevier.com/locate/jvolgeores

Calcite sealing in a fractured geothermal reservoir: Insights from combined EBSD and chemistry mapping

David D. McNamara [a,*], Aaron Lister [b], Dave J. Prior [b]

[a] GNS Science, Lower Hutt, New Zealand
[b] Department of Geology, University of Otago, Dunedin, New Zealand

ARTICLE INFO

Article history:
Received 29 July 2015
Received in revised form 28 February 2016
Accepted 28 April 2016
Available online 10 May 2016

Keywords:
Calcite
Fracture sealing
Kawerau geothermal field
Reservoir
Permeability

ABSTRACT

Fractures play an important role as fluid flow pathways in geothermal resources hosted in indurated greywacke basement of the Taupo Volcanic Zone, New Zealand, including the Kawerau Geothermal Field. Over time, the permeability of such geothermal reservoirs can be degraded by fracture sealing as minerals deposit out of transported geothermal fluids. Calcite is one such fracture sealing mineral. This study, for the first time, utilises combined data from electron backscatter diffraction and chemical mapping to characterise calcite vein fill morphologies, and gain insight into the mechanisms of calcite fracture sealing in the Kawerau Geothermal Field. Two calcite sealing mechanisms are identified 1) asymmetrical syntaxial growth of calcite, inferred by the presence of single, twinned, calcite crystals spanning the entire fracture width, and 2) 3D, interlocking growth of bladed vein calcite into free space as determined from chemical and crystallographic orientation mapping. This study also identifies other potential uses of combined EBSD and chemical mapping to understand geothermal field evolution including, potentially informing on levels of fluid supersaturation from the study of calcite lattice distortion, and providing information on a reservoir's history of stress, strain, and deformation through investigation of calcite crystal deformation and twinning patterns.

1. Introduction

Development of natural and enhanced geothermal resources, hosted in crystalline, volcanic, plutonic or, metamorphic basement reservoirs, has increased over recent years (Wood et al., 2001; Asanuma et al., 2005; Sausse et al., 2006; Blackwell et al., 2007; Bertani, 2012). In these reservoir rocks, permeability is dominated by faults and fractures, with small contributions made by primary permeability (Brace, 1980; Davatzes and Hickman, 2010; Dezayes et al., 2010). As such, the study of how these structures are generated, their properties (e.g. orientation, spatial distribution, aperture, orientation with respect to the stress field), how they become filled with precipitated minerals, and their crack-seal cycle history is vital to understanding the evolution of geothermal systems and to their successful development. Progressive fracture sealing (i.e. vein formation) is known to create barriers and baffles to fluid flow in a geothermal reservoir, decreasing overall permeability and limiting the reservoir's effectiveness as a resource (Batzle and Simmons, 1976; Dobson et al., 2003; Genter et al., 2010). Study of this sealing process is vital to discerning the evolution and sustainability of fractured geothermal systems.

Fracture sealing creates veins which can be used to determine aspects of the geological history of the host rock. The mineralogy, geochemistry, microstructure, and fluid inclusion analysis of vein minerals provide information on pressure and temperature conditions of the reservoir rock, stress and strain that was occurring at or after the time they were precipitated, and on the composition and origin of related fluids. Vein formation (fracture sealing) is achieved by the precipitation of minerals from the circulating fluids, or from water–rock interactions, within geothermal systems, and can occur as a single precipitation event or as multiple crack-sealing events (Ramsay, 1980). Evidence for multiple sealing events comes from observation of multiple mineral phases, or sequential depositions of the same mineral phase in a vein. The classification of veins can be broken into i) syntaxial, ii) stretching, iii) antitaxial, and iv) pressure shadows/fringes (Fig. 1) (Bons et al., 2012). Syntaxial veins form where mineral growth occurs from one of or both fracture faces toward the centre, with crystals often becoming elongate in the growth direction. Syntaxial vein minerals often show lattice preferred orientations that strengthen with distance from the fracture wall as growth competition eliminates those crystals not oriented to the fast growth direction (Cox and Etheridge, 1983; Bons, 2001; Nüchter and Stöckhert, 2007; Okamoto and Sekine, 2011). Stretching veins grow in a similar way to syntaxial veins (Durney and Ramsay, 1973) but the crack surface cuts through previously precipitated vein crystals (localised stretching veins) or wall rock (delocalised stretching veins) as opposed to the mineral growth surface. Due to

* Corresponding author at: 1 Fairway Drive, GNS Science, Lower Hutt, 5040, New Zealand.
E-mail address: d.mcnamara@gns.cri.nz (D.D. McNamara).

http://dx.doi.org/10.1016/j.jvolgeores.2016.04.042
0377-0273/

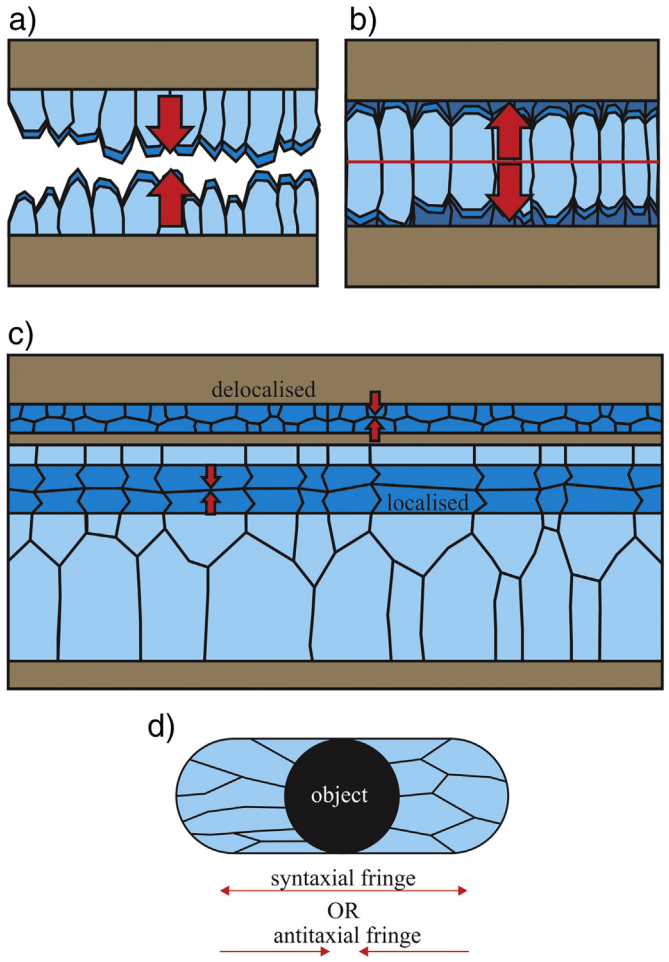

Fig. 1. Schematic models of various fracture sealing processes; a) syntaxial sealing, b) antitaxial sealing, c) stretching vein showing both delocalised vein growth (via fracture propagation through wall rock) and localised vein growth (fracture propagation across already deposited material), and d) vein formation from a pressure shadows/fringe occurring next to a rigid object.

their similarity a continuum exists between syntaxial and stretching veins. Localised stretching veins can seal a crack from both crack surfaces (bitaxial) or from one surface (unitaxial) (Hilgers et al., 2000). Antitaxial veins grow from a median suture in a fracture toward the fracture walls and usually contain fibrous crystals. They are defined by the presence of a median line/zone across which two-fold rotational symmetry is often observed in the fibre pattern. It is thought that antitaxial veins grow by crack-seal mechanisms, or that growth occurs on the closed interface between vein and wall rock. Antitaxial vein growth is also possible as a result of crystal growth, in a diffusional mass transfer (DMT) system, exerting outward force that pushes the wall rock apart (Wiltschko and Morse, 2001). Pressure shadows/fringes are a unique type of vein that forms in pressure shadows occurring next to a rigid object in a deforming material.

Determination of mineral sealing processes from microstructural and chemical data is made difficult due to the processes being highly sensitive to a wide range of factors; degree of fluid supersaturation, anisotropic growth kinetics (mineral growth), rates of local deformation, and rates of fluid transport (Hilgers et al., 2004). Calcite is a common mineral in many geological systems and geothermal reservoirs are no exception. Calcite is usually found in geothermal systems with temperatures of ~140–300 °C and where fluids have high concentrations of dissolved CO_2 (Simmons and Christenson, 1994; Browne, 1978) occurring both as a replacement of parent rock mineral phases, or as cement or vein fill. Hydrothermal calcite veins have been reported in geothermal systems in North America (Batzle and Simmons, 1976; Dobson et al., 2003), the granite, enhanced geothermal reservoir of Soultz-sous-Forêts (Hébert et al., 2011; Genter and Traineau, 1996), and in several geothermal fields located in the Taupo Volcanic Zone (TVZ), New Zealand (Krupp and Seward, 1987; Hedenquist, 1990; Wood et al., 2001). The precipitation of hydrothermal calcite is controlled dominantly by the movement of CO_2 in the reservoir as governed by boiling, dilution, and condensation, and to a lesser extent by pH, temperature, and the aqueous calcium ion activity (Fournier, 1985; Simmons and Christenson, 1994). As a result, calcite is a highly reactive mineral in a geothermal system such that varying temperature profiles along fluid flow pathways create zones where it can be dissolved and zones where it can be precipitated. Colder, circulating fluids often result in calcite dissolution, which, due to calcite's retrograde solubility (decreases with increasing temperature), is then precipitated back out elsewhere as the circulating fluid temperature increases (André et al., 2006). Platy calcite (also known as bladed calcite) is commonly found in veins and voids in geothermal reservoir rocks and is the result of precipitation from boiling fluids through the exsolution of CO_2. Observations of bladed calcite in geothermal wells are made by Tulloch (1982) who noted that the platy crystals grow outward from the walls in a direction perpendicular to the **c**-axis at a rate of ~0.1 mm/day.

The common occurrence of calcite as a fracture sealing mineral in geothermal fields makes it an ideal case study for examining hydrothermal fracture sealing. This work examines calcite-filled fractures from a sample of greywacke reservoir rock from the Kawerau Geothermal Field using, for the first time, combined chemical mapping techniques (cathodoluminescence (CL) and electron diffraction X-ray (EDX)), and electron backscatter diffraction (EBSD). Similar combinative studies attempting to infer the connection between microstructure and chemistry in veining are rare (Piazolo et al., 2005; Bons et al., 2012 and references therein) and many are more focused on detailed chemical and isotopic analyses (Barker et al., 2006, 2009). This paper aims to utilise these combined techniques to determine how hydrothermal calcite growth occurs in geothermal fractures and explore what the microstructure can tell us about the crack-seal evolution of the greywacke basement of the Kawerau Geothermal Field, and the implications this may have for reservoir permeability.

1.1. Geological setting

The Kawerau Geothermal Field is the most northern, active, high temperature (>300 °C), geothermal field in the TVZ (Fig. 2). The TVZ represents the active part of the Central Volcanic Region (CVR), an extensional intra-arc basin formed as a result of subduction of the Pacific Plate beneath the North Island of New Zealand (Wilson et al., 1995; Cole and Spinks, 2009; Begg and Mouslopoulou, 2010; Rowland and Simmons, 2012). The TVZ is segmented structurally, by offsets in its rift axis (Rowland and Sibson, 2001), and magmatically, such that the central TVZ is dominated by rhyolitic volcanism, while the north and south portions experience andesitic-dacitic volcanism (Rowland and Simmons, 2012; Wilson et al., 1995). Rifting commenced 1–2 Ma and continues to the present day with extension rates decreasing from ~15 mm/yr at the coast of the Bay of Plenty to ~3 mm/yr near the rift termination (south of Lake Taupo) (Villamor and Berryman, 2001; Wallace et al., 2004; Begg and Mouslopoulou, 2010; Chambefort et al., 2014). Extension in the TVZ is accommodated by the Taupo Rift, a series of dominantly NE–SW striking, normal faults with a vertical maximum principal stress (σ_1/S_v), a NW–SE extension/minimum horizontal stress direction (σ_3/S_{hmin}), and a NE–SW maximum horizontal stress direction (σ_2/S_{Hmax}) (Hurst et al., 2002; Nicol et al., 2006, Hurst et al., 2008, McLean and McNamara, 2011; Wallis et al., 2012; Townend et al., 2012; McNamara et al., 2015).

The Whakatane Graben, which subsides at rates >0.8 m/ky (Nairn and Beanland, 1989), is situated where the normal faulting of the TVZ intersects with the dominantly strike slip faults of the North Island

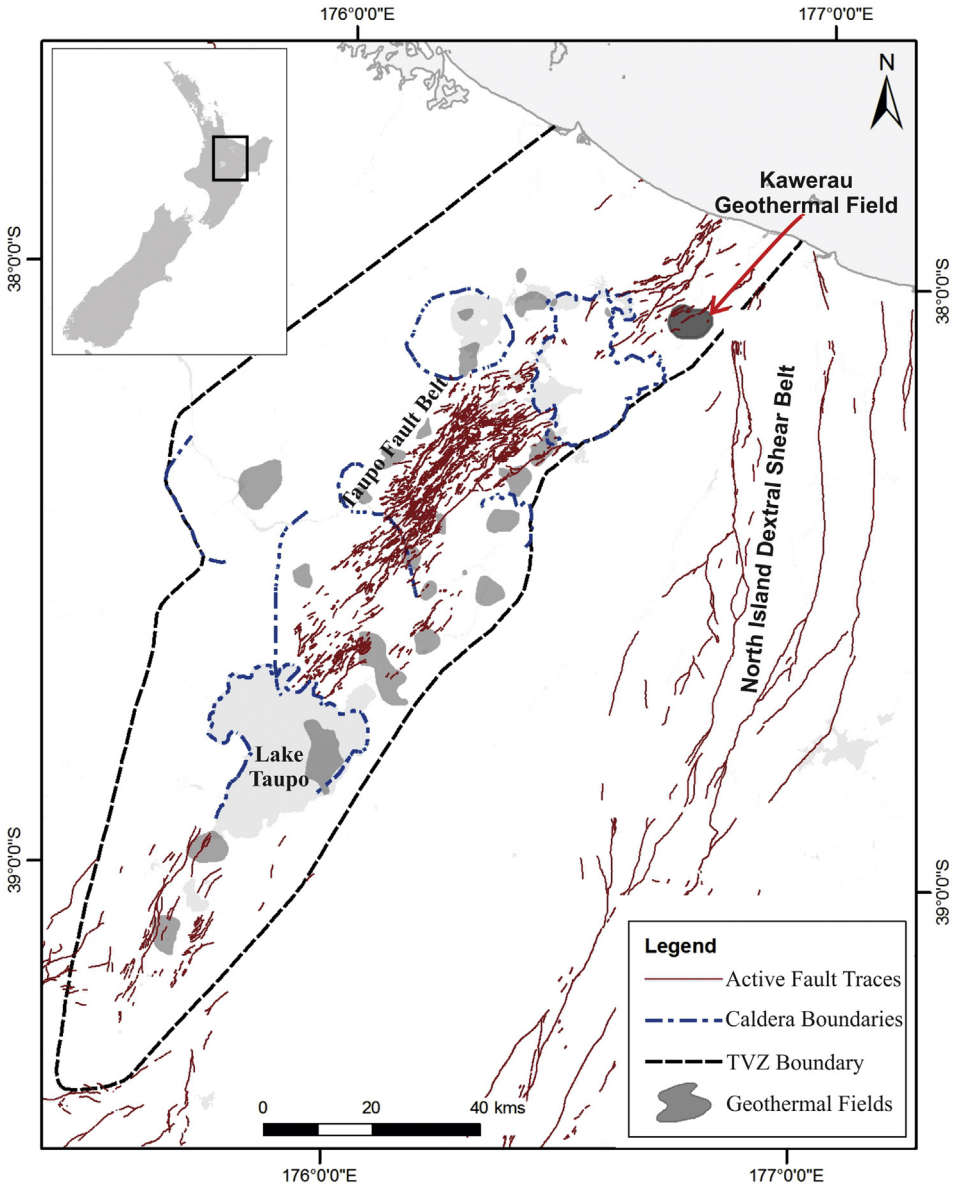

Fig. 2. Map of the Taupo Volcanic Zone showing the major structural features and the location of the Kawerau Geothermal Field. Inset provides geographical context within New Zealand.

Dextral Shear Belt (Begg and Mouslopoulou, 2010; Villamor et al., 2011; Seebeck et al., 2014). The Kawerau geothermal reservoir is located within the Whakatane Graben where rhyolite dominated volcanism of the central TVZ transitions into the andesite–dacite volcanism of the north TVZ segment (Wilson et al., 1995; Nairn, 2002). The geothermal resource is hosted in Mesozoic greywacke basement composed of medium-grained, andesite–dacite sourced sandstones with minor argillite and chert. The hosting basement terrane for the Kawerau geothermal resource has been debated to be either the Torlesse (Wood et al., 2001) or the Waipapa (Adams et al., 2009). It is thought that the transition between basement greywacke terranes in the TVZ occurs under or near the Kawerau Geothermal Field (Adams et al., 2009; Leonard et al., 2010; Milicich et al., 2013). The geothermal reservoir is overlain by ~1 km of Quaternary volcano-sedimentary deposits. Fluid flow within the greywacke basement of the Kawerau system is dominated and controlled by a series of faults and fractures as evident from NE–SW trending lineaments of hydrothermal features (Christenson, 1987), the spatial relation of structures imaged with borehole televiewers to zones of permeability (as measured by pressure, temperature, and fluid velocity logs) (Wallis et al., 2012), and the low permeability of the intact greywacke rock itself (Christenson, 1987; McNamara et al., 2014). Geothermal well performance indicates that while the north of the Kawerau Geothermal Field hosts permeability controlled by active structures, similar structures present in the south of the field, are likely inactive and sealed by hydrothermal mineral deposition, thus restricting permeability in this area (Christenson, 1997; Bignall and Milicich, 2012; Milicich et al., 2013).

1.2. Sample petrography

A sample of un-oriented, greywacke basement drill-core from well KA30 (comprising the interval 1098–1100 mRF), in the southern area of Kawerau Geothermal Field, was utilised for this work. A piece of the drill-core, displaying several intersecting veins, was thin-sectioned (Fig. 3). The greywacke is a clast supported, matrix poor, medium to coarse grained greywacke sandstone (0.25–1.5 mm) consisting of subangular–subrounded detrital quartz (10%), plagioclase and biotite/phlogopite (30%), and lithic fragments (50%). Lithic fragments include porphyritic lavas, rare plutonic fragments, and siltstone and sandstone fragments. The matrix is composed of indurated clay/silt. This greywacke is moderately altered with a hydrothermal assemblage of chlorite, leucoxene (a granular alteration product of titanium-rich

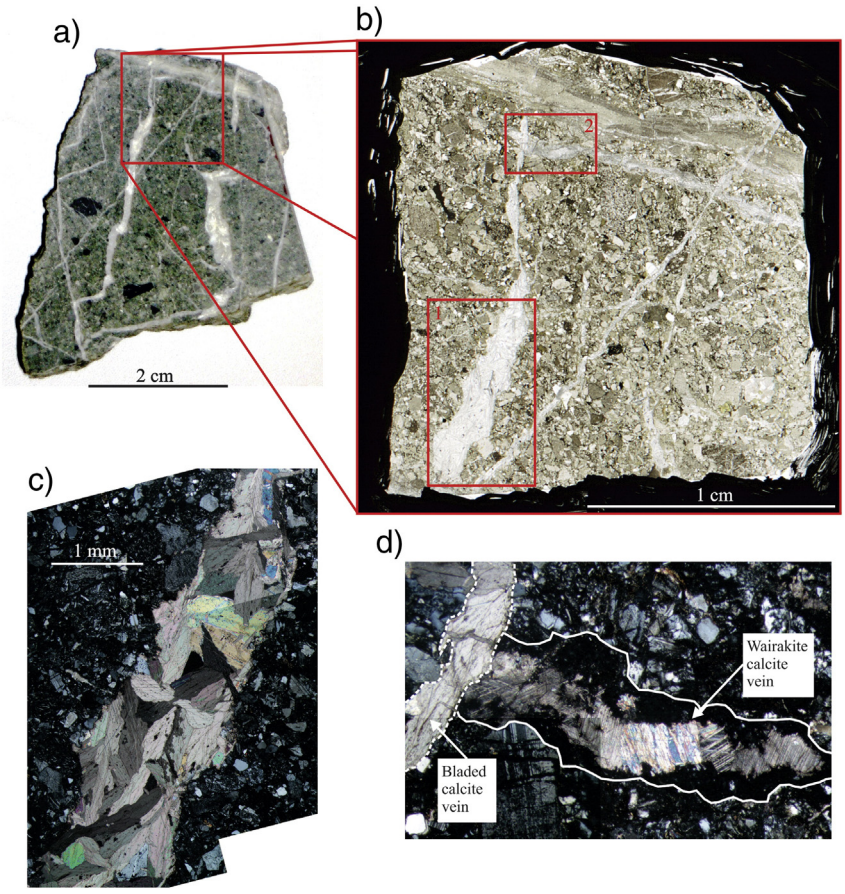

Fig. 3. a) Photograph of drill-core sample of greywacke reservoir rock from the Kawerau Geothermal Field used for study, b) Plane polarised, light microscopy image of the drill core sample. Red boxes outline individual areas selected for focused examination using CL, EDX, and EBSD, c) Cross polarised light microscopy image of the calcite vein from Area 1, d) Cross polarised light microscopy image of the calcite/wairakite vein from Area 2.

minerals), hydrothermal clays, and minor amounts of wairakite (zeolite; $Ca_8(Al_{16}Si_{32}O_{96})^*16H_2O$; Steiner, (1955)), epidote and disseminated pyrite.

The greywacke sample used in this study contains a complex set of cross cutting, mineralised fractures filled with calcite, wairakite, and small amounts of pyrite (Fig. 3). The youngest fracture set tends to be wider (~1–1.5 mm) than the older fractures they cross-cut and contain calcite as their only mineral fill. Calcite in these veins are either elongate (1–1.5 mm) in appearance (a texture known as bladed calcite), particularly in the wider veins, or have a blocky form. Smaller calcite crystal sizes, with irregular shape are observed nearer the fracture walls. Older fracture generations are filled with mixtures of calcite and wairakite noted to be in textural equilibrium (Christenson, 1987). Some of these vein textures show wairakite at fracture edges with a central calcite fill (Fig. 3). The fracture fill sequences documented here are similar to those described by Absar and Blattner (1985), though we note the lack of prehnite in our study sample.

Fracturing in the Kawerau Geothermal Field reservoir is thought to be hydraulic in origin. This is supported by observed vein mineral assemblages which follow models for mineralisation in hydraulic-fracturing (Phillips, 1972; Hedenquist and Henley, 1985) in rock with high tensile strength and low intrinsic permeability, both of which are true of the greywacke basement at Kawerau (McNamara et al., 2014). Additionally, veins are often noted to contain wall–rock fragments, providing evidence of the explosive nature of the fracturing events (Christenson, 1987). The greywacke wall rock proximal to all fractures in the studied sample shows damage (shattered quartz, feldspar, and lithic grains, and narrow, micro-fractured, damage zones around the main fracture structures) and supports interpretation of these fractures forming during an explosive, hydrofracturing process (Christenson, 1987). This effect is more pronounced around the older, wairakite/calcite filled fractures, than around the younger, bladed calcite filled fractures. The younger fracture generation examined in this study cross-cuts older fractures at a high angle and also cuts across larger quartz and lithic grains of the greywacke rock. Where shear markers can be identified either side of these younger fractures, small lateral offsets can be observed. The most obvious lateral offset noted is where a younger generation fracture offsets an older wairakite/calcite filled fracture by ~0.25 mm (Fig. 3c), indicating a shear component to the younger fracture.

Fluid inclusion homogenisation temperatures, freezing point depression data, and the presence of liquid and vapour rich fluid inclusions, indicate that Kawerau basement vein calcite deposited from boiling fluids (Christenson, 1987). The implication of a boiling parent fluid is that the confining pressure in the fracture was likely less than the hydrostatic pressure at depth. However the modal homogenisation temperatures noted by Christenson (1987) lie above the boiling point curve for water, indicating that fracture channels were also, at times, overpressured (above local hydrostatic). It is thought that this over pressurisation is a prerequisite for initiating the hydraulic fracturing in the Kawerau Geothermal Field in the first place. A combination of overpressured fluid in the fractures, and volcanic processes associated with Putauaki are thought to be responsible for the hydro-fracturing (Hedenquist and Henley, 1985; Phillips, 1972; Christenson, 1987). Hydrofracturing, which resulted in a sudden pressure drop, is responsible for the instantaneous flashing, and rapid supersaturation of calcite in the boiling fracture fluid, which resulted in rapid precipitation of calcite on the fracture walls, often with bladed crystal morphology (Christenson, 1987). Bladed calcite in veins at Kawerau Geothermal Field are thought to have undergone rapid growth due to observed

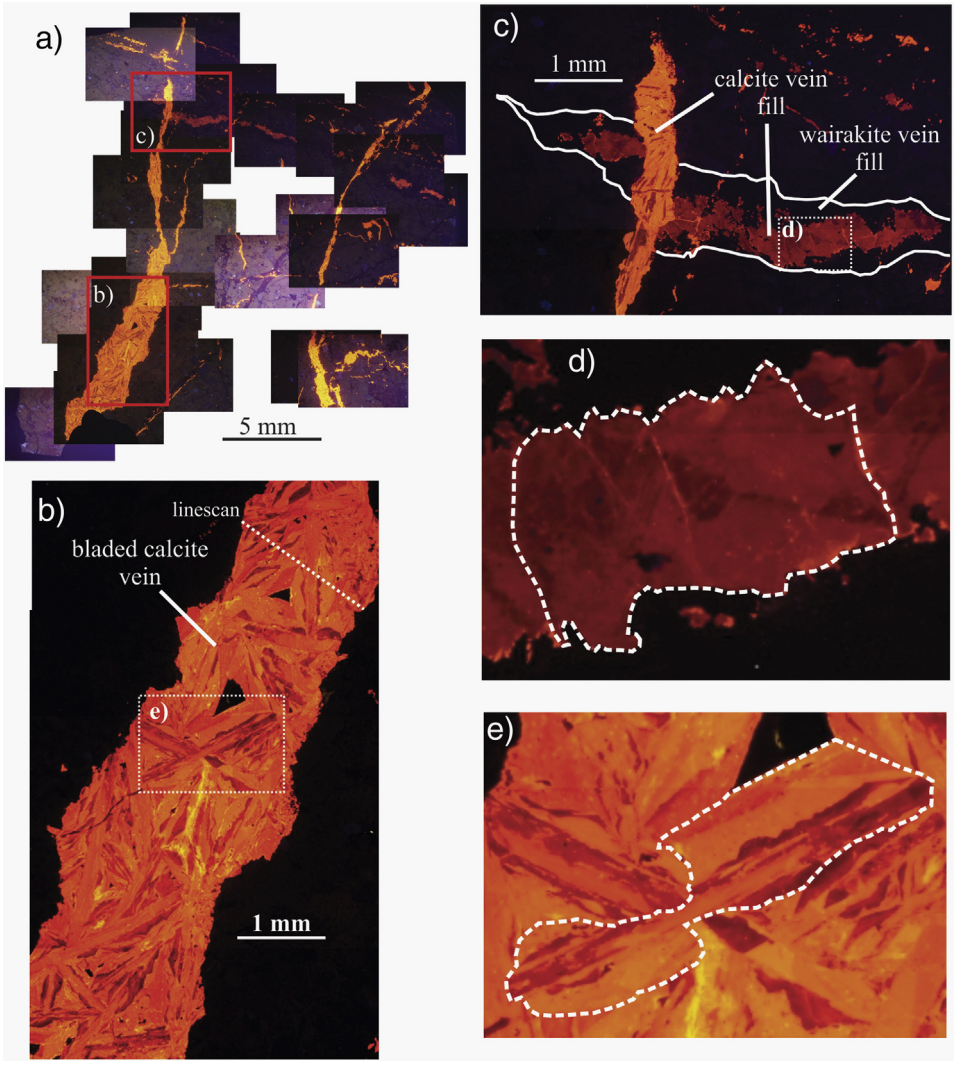

Fig. 4. Cathodoluminescence (CL) images of fractured greywacke reservoir rock from Kawerau Geothermal Field. a) CL image showing cross-cutting calcite and wairakite filled veins. Inset red boxes define areas of zoom in Fig. 4b and c, b) CL image of a bladed calcite filled vein from the youngest fracture generation. Inset dashed white box represents area of zoom in Fig. 4e, c) CL image of a calcite/wairakite filled vein cross-cut by a younger calcite filled vein (white lines mark older generation fracture edges), inset white dashed box represents area of zoom in Fig. 4d, d) CL image of a single calcite crystal from the older vein (outlined by white dashed line), e) CL image of a single bladed calcite crystal from the younger vein (outlines by a white dashed line).

pitted surfaces under SEM (Christenson, 1987), and observations of rapid growth of bladed calcite (~0.1 mm/day) in flowing wells at Kawerau (Tulloch, 1982).

Temperature conditions of calcite formation in veins at Kawerau Geothermal Field have been determined from fluid inclusion and stable isotope studies (Christenson, 1987; Absar, 1988). Temperatures for the deposition of the calcite from fluid inclusion measurements have not been made on the vein samples investigated in this paper but have been reported from bladed calcite veins in nearby wells at similar depths (Christenson, 1987). Fluid temperatures during bladed calcite precipitation are tentatively placed at ~270–305 °C. Isotope data (δO^{18}) from this calcite precipitation event indicates precipitation from meteroric fluids with a magmatic component (Absar, 1988). The formation depth of the youngest vein generation (bladed calcite) in the investigated sample can be assumed to be ~1100 m, assuming that the bladed calcite precipitation event likely represents, at its oldest, the initiation of the modern geothermal system in Kawerau (~16,000 yrs), and little erosion of cover material has occurred (Milicich et al., 2013). This postdates the deposition of nearly all the volcanosedimentary units that overlie the greywacke basement in this area (Milicich et al., 2014). Assuming a vein formation depth of 1100 m, fluid temperatures of ~270–305 °C, water density values of 1531–1846 kg/m^3, and the fact that bladed calcite precipitated from fluid under confining pressures lower than the hydrostatic pressure, an estimation of vein formation pressure is ~16–20 MPa. Attempting to determine the vein formation conditions for the older wairakite–calcite vein is more difficult. Wairakite, commonly found in hydrofractures in geothermal fields, is known to form when measured temperatures are in excess of 160 °C at Kawerau, and the later calcite in this vein, likely precipitated at temperatures similar to those of the younger vein (>~270 °C) (Christenson, 1987). Isotopic studies (δO^{18}) of wairakite–prehnite veins (Absar, 1988) suggest higher fluid temperatures of 280–300 °C and that this vein fill represents an earlier deposition event from meteoric fluids that predates the deposition of calcite. The timing of this older veining event remains equivocal and the depth of its formation, and thus pressure conditions, are undetermined.

2. Methodology

2.1. Sample preparation

A 30 μm thick thin section (Fig. 3b) was mechanically and chemically polished using diamond pastes down to 1 μm followed by colloidal silica. This process minimised negative effects of surface damage and

topography on EBSD mineral indexing (Prior et al., 1996). The edges of the prepared specimen were painted with carbon and the sample surface was carbon coated (~10 nm thick) to prevent charging in the SEM.

2.2. Electron backscatter diffraction (EBSD)

EBSD is a technique capable of rapid acquisition of large crystallographic orientation datasets of a rock's mineral phases (Prior et al., 1999). EBSD carried out in this work was performed using a Zeiss Sigma variable pressure field emission gun SEM fitted with an Oxford Instruments Nordlys F EBSD camera and an XMax 20 silicon drift EDX detector, located at the Otago Centre for Electron Microscopy (OCEM) at the University of Otago, Dunedin. To collect EBSD patterns, the thin section was tilted 70° to the incoming electron beam allowing for a diffraction pattern to be generated on a phosphor screen. EBSD was carried out using an acceleration voltage of 30 kV, beam current of ~90 nA, and a working distance of ~20 mm. Both EBSD and EDX data were collected using Oxford instruments AZTec software which undertook initial processing for both techniques. The mapped EBSD data was processed with HKL Channel5 software using methods comparable to Bestmann and Prior (2003).

2.3. Energy dispersive X-ray spectroscopy (EDX) and cathodoluminescence (CL)

EDX data were collected using Oxford Instruments AZTEC software with a XMAX20 silicon drift detector. Full spectrum EDX data were collected on a grid using an accelerating voltage of 15 to 20 kV and ~1–10 nA of beam current. Spectra (including map data) were processed using the TruMap and QCAL procedures within the AZTEC software. Map data presented here show counts within Kα energy windows corrected for peak overlaps and background counts.

CL images were taken using a Technosyn cold cathode stage mounted on an Olympus BX41 microscope with a trinoc head fitted with a digital camera. The CL apparatus was operated under vacuum (0.05–0.08 Torr / 17–20 V) at an accelerating voltage of 15–20 kV and a beam current of 550–600 μA.

3. Results

3.1. Cathodoluminescence (CL)

Fig. 4 shows CL images of the fractures in the sample: colours vary from fracture to fracture. The youngest generation of fracturing shows bright, yellow/orange coloured calcite (Fig. 4b) while the older fractures, cross-cut by the younger fractures, contain wairakite (dull, purple/blue CL colours) and calcite (dull, darker orange/red CL colours) (Fig. 4c). Individual calcite crystals in all fracture generations show variation of the orange/red CL colours, implying they are chemically zoned. Yellow cathodoluminesence in calcite is linked to higher Mn content, whereas red CL response is proportional to Fe content (Long and Agrell, 1965). Visa versa, the more red the CL colour the higher the Fe content and lower the Mn content.

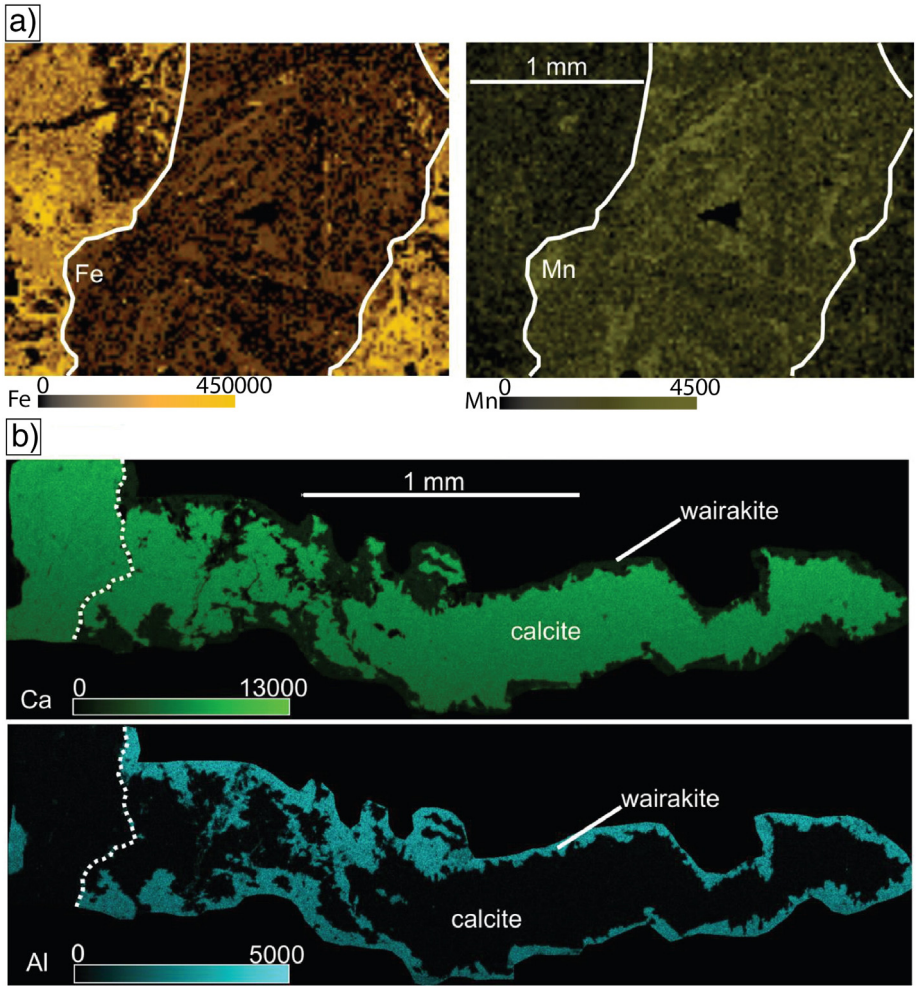

Fig. 5. a) Fe and Mn EDX count maps of bladed calcite crystals in the younger generation fracture (zone 1 in Fig. 3). White lines define the edge of the fracture. b) Ca and Al EDX count maps of a calcite and wairakite sealed older generation fracture (Zone 2 in Fig. 3). The dashed white line defines where the older generation fracture is cross-cut by the younger generation fracture.

Zonation in CL is more pronounced in calcite crystals sealing the younger generation of fractures (Fig. 4e). These calcite crystals show complicated zonation patterns. In some elongate calcite crystals, concentric zonation stretches along the crystal long axes in bands (Figs. 4e, 11). This concentric banding varies in width along the crystal axes; thinner along the long edges of the crystal and thicker at either end of the elongated crystals (Fig. 11). In some places along the crystal long axes a particular zonation band grows outward perpendicular to the long axes, creating a 'bulging' morphology (Fig. 4e). In elongate crystals that have such bulges, zonation appears as successive bands progressing outward from the core of the crystal and into the bulging area (Fig. 4e). Older fracture calcite crystals are zoned but have no discernible zonation pattern (Fig. 4d).

3.2. Energy dispersive X-ray spectroscopy (EDX)

EDX elemental count maps were generated for Area '1' (Fig. 4b, Fig. 5a), the generation of younger veins filled with bladed calcite (measurement point every 2 μm), and Area '2' (Fig. 4c, Fig. 5b), the older fracture generation containing wairakite and calcite (measurement point every 2 μm). EDX maps of Area 1 (Fig. 5a) show the same chemical zonation patterns observed in CL (Fig. 4b). EDX maps of Area 2 do not show the zonation patterns observed from CL (Fig. 4c). Ca and Al EDX count maps of Area 2 delineate the older wairakite vein fill from the younger calcite fill due to the differences in their chemical compositions (Fig. 5b).

An EDX linescan (in weight%) of a profile across zoned calcite crystals in the younger vein generation is shown in Fig. 6 next to corresponding CL and BSE images of the zonation. This plot shows that darker grey colours on the BSE image corresponds to purer calcite ($CaCO_3$), whereas lighter grey colours contain higher levels of Fe + Mn. Correlation of the linescan to the CL image shows more intricate chemical variation. Zones associated with purer $CaCO_3$ (seen on BSE image) appear as variable shades of dark red or orange CL colours. This implies additional chemical variation in these calcite crystals beyond Mn + Fe. Other major elements (O, C, Mg, Si, Al, Na) are ruled out as they display no variation after investigation by EDX. In places the Fe/Ca ratio is higher than the Mn/Ca ratio which is related to darker red CL coloured zones (~138–180 μm, 1029–1050 μm; Fig. 6).

3.3. Electron backscatter diffraction (EBSD)

EBSD maps of calcite crystals from both the youngest and an older generation of sealed fractures are shown in Figs. 7 and 9, respectively. EBSD grain maps of the younger fracture sealed by calcite mineralisation (Fig. 7) show predominantly large, elongate crystals of calcite (~0.5–2 mm long), and less frequent, large, blocky calcite forms (~0.5 mm long). Smaller-sized calcite crystals (~0.05–0.25 mm) are predominantly found near the fracture walls. Elongate calcite crystals are green and blue in the IPFZ map (Fig. 7b); the c-axes are at low angles to the thin section plane and perpendicular to crystal long axes (i.e. basal plane trace lies parallel to long axis). Calcite crystals with a blocky form have pink, orange, and red colours in the IPFZ map (Fig. 7b) corresponding to c-axes at high angles to the thin section plane. Most elongate calcite crystals show continuous distortion (low angle (<2°) misorientation) along their long axes while blocky calcite crystals show no measureable internal crystal distortion (Fig. 7c). Some calcite crystals (Fig. 7a, c) have 2°–5° sub-grain boundaries (displaying rotation around the m axes), and 5°–10° sub-grain boundaries (displaying rotation around the <02–21 > axis) (Fig. 7d). A small number of misorientation angle

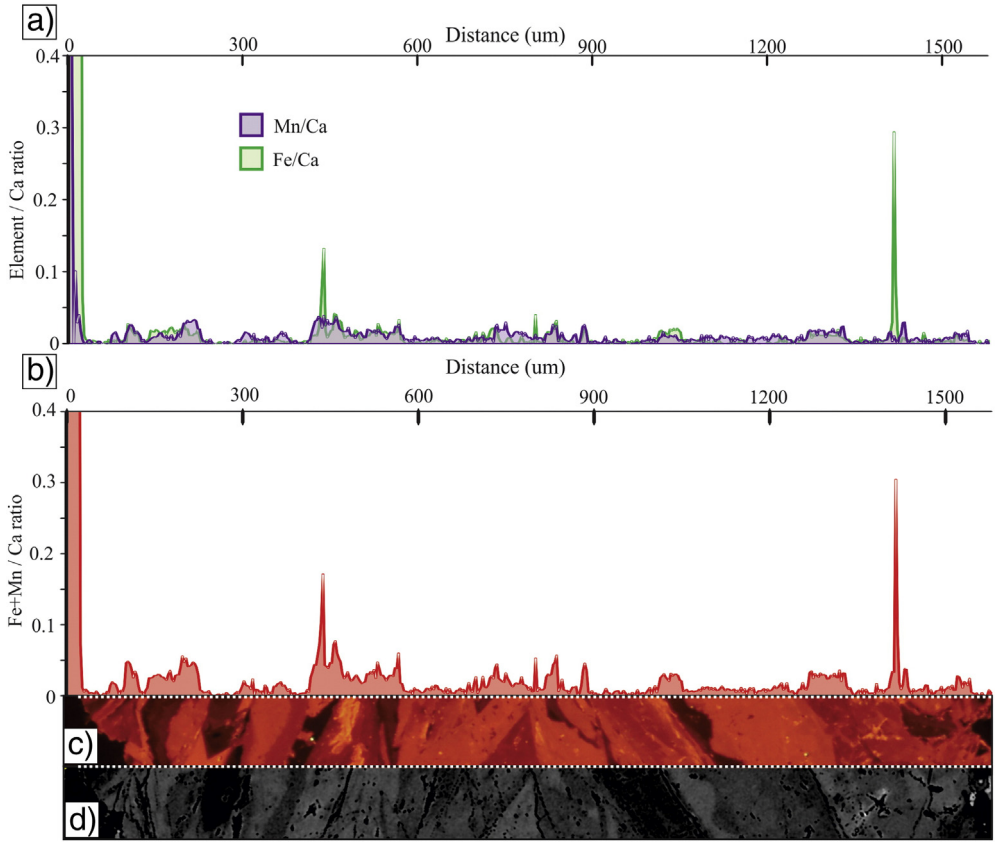

Fig. 6. EDX data from a linescan (dashed white line shown in Fig. 4b) across chemically zoned, bladed calcite crystals sealing the younger fracture generation. Fe, Ca, and Mn element wt% linescan data are plotted as Fe/Ca, Mn/Ca, and Fe + Mn/Ca ratios, such that when ratio = 0, calcite is pure $CaCO_3$ (with respect to Fe and Mn), and when the ratio > 0 there is higher Fe and Mn content in the calcite. a) Graph showing variation in Mn/Ca and Fe/Ca ratios, b) Graph showing variation in Fe + Mn/Ca ratio, c) CL microscopy image of calcite crystals in the younger fracture generation across which linescan data was collected and d) the same area under as a back scattered electron image.

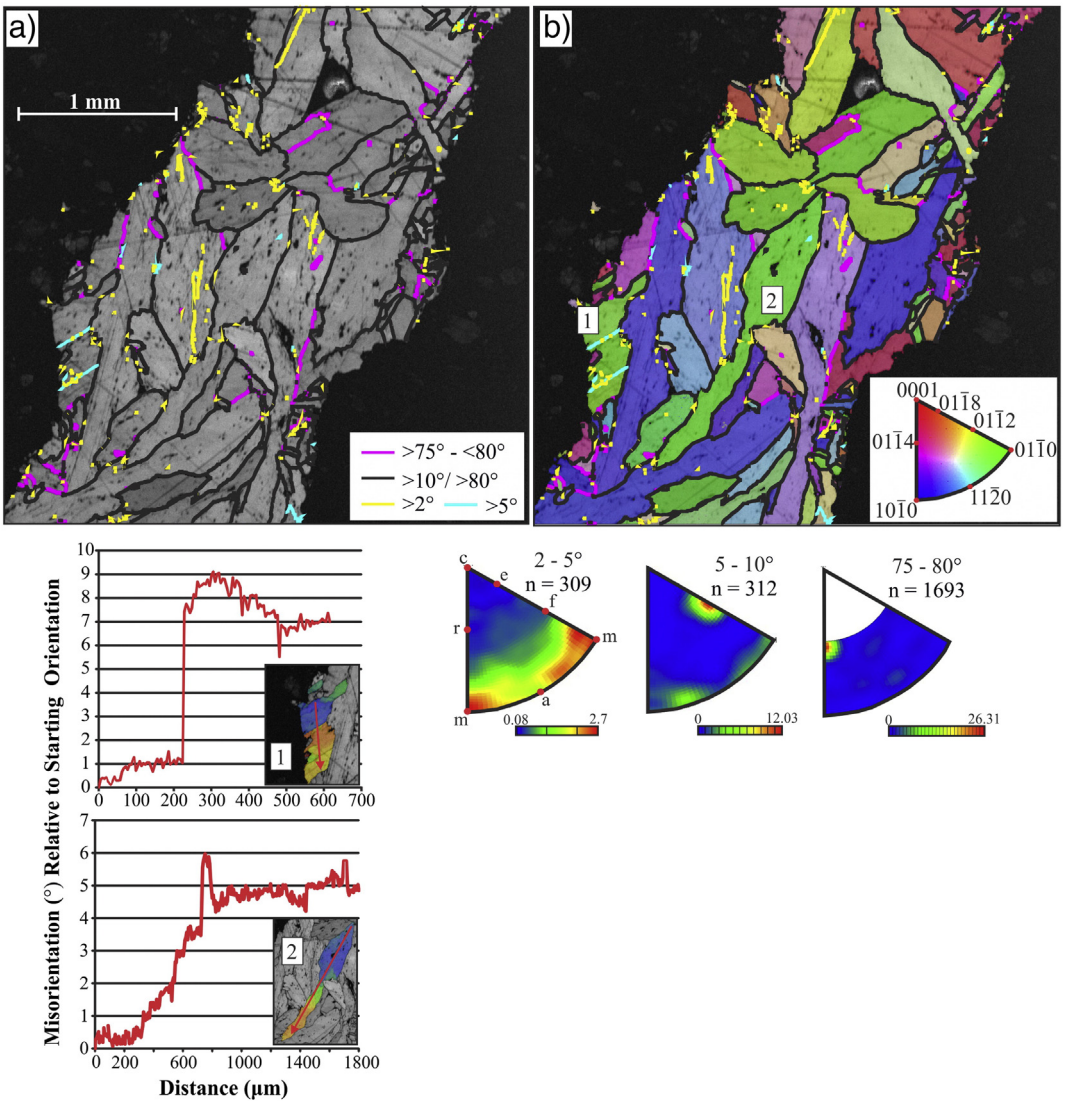

Fig. 7. EBSD data on calcite fracture fill from the youngest generation of fracturing. a) Band Contrast map with Grain Boundary overlay, b) Band Contrast map with an Inverse Pole Figure colour scale in the sample's Z direction and Grain Boundary overlay, c) Misorientation profiles of Grains 1 and 2 (labelled in 7b) following direction indicated by red arrows, insets are Band Contrast maps with Texture Component overlays for the crystals being profiled (crystal colour indicates amount of misorientaion from a given orientation on the crystal (blue = 0°, red = 10°), d) Contoured inverse pole figures for neighbouring calcite misorientations of 2°–5°, 5°–10°, and 75°–80°.

boundaries of 75°–80° are observed, with rotation axes indicative of calcite e-twins (20$\bar{2}$1, Fig. 7d). One point per grain calcite pole figures show calcite has a weak LPO in this fracture with the c-axes preferentially oriented perpendicular to the fracture wall (Fig. 8). Misorientation angle distribution analyses (Fig. 10a, b) shows little difference between random and neighbour pair misorientation angle distributions apart from a slightly higher frequency of low angle (<10°) and 75°–80° angle neighbour misorientations than the random frequency. (See Fig. 8.)

EBSD mapping of the older calcite vein (Fig. 9) shows calcite crystals of a single orientation have grown across the fracture. Calcite crystals commonly contain either one (smaller crystals ~0.13 mm) or two twin (larger crystals, ~0.63–0.75 mm) sets and one large grain (~0.88 mm) contains three sets of twins. All twin sets in these calcite crystals are e-twins. The host calcite crystals display continuous distortion (<2°). Other host calcite microstructures, such as common 2°–5° and rare 5°–10° sub-grain boundaries, are present and have dominant <a>rotation axes (<11–20>). Misorientation angle distribution analyses (Fig. 10c, d) shows a slightly higher frequency of low angle (<10°) neighbour misorientations than the random distribution, similar to the younger calcite vein.

4. Discussion

4.1. Insights into calcite growth in a geothermal fracture

The bladed calcite crystals in the younger vein investigated here do not appear to have grown following the typical symmetrical, vein-normal, growth directions expected in crack-seal fractures (Bons et al., 2012; Fig. 1). Rather the crystal morphology of this fracture implies calcite nucleated and grew outward in a number of directions with preferred crystallographic orientation, filling in available space, and eventually sealing the fracture with a 3D interlocking set of elongated crystals. The chemical zonation patterns observed in bladed calcite crystals, due to the variable inclusion of Fe and Mn into the calcite crystal structure as it precipitated, infer that they grew in a free fluid with changing composition (ten Have and Heijnen, 1985), and that they grew preferentially outward in two opposite directions (usually parallel to the fracture length) producing bladed morphologies. These observations, combined with information from EBSD texture component maps (Fig. 11), and the presence of a weak calcite vein LPO, show that these elongate calcite crystals grew outward from a central core along the

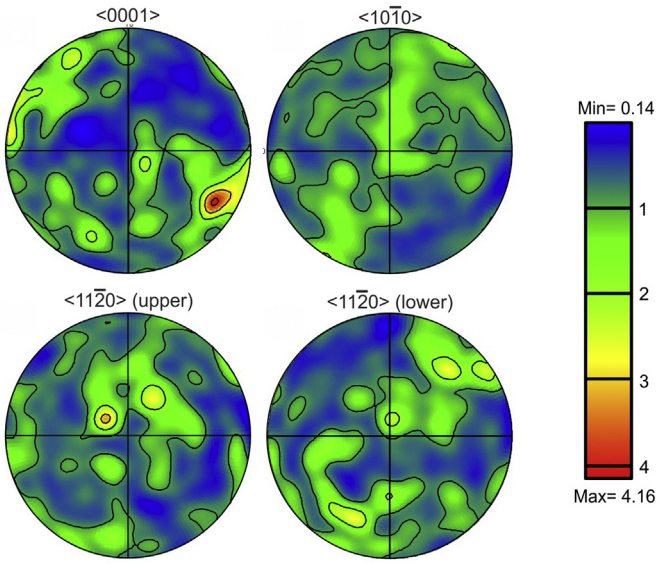

Fig. 8. Contoured pole figures of calcite crystal orientations in the younger generation fracture using one orientation measurement per calcite crystal (point per grain) for 1168 crystals. Pole figures are equal area projection, upper hemispheres and are contoured with a half width of 15° and a cluster size of 5° (Halfpenny, 2010).

crystallographic m axis, such that the c-axes are perpendicular to the fracture wall. This is similar to another observation made of bladed calcite crystal growth in a geothermal well pipe, where crystals grew perpendicular to their c-axis (Tulloch, 1982), and to records of elongate calcite vein growth in other studies (Bradshaw and Phillips, 1964; González-Casado and García-Cuevas, 1999; Friedman and Higgs, 1981).

Further evidence of a three-dimensional interlocking morphology for these calcite crystals are the 'cross-cutting' relationship that can be observed from EBSD maps (Figs. 7, 11). This and other aspects of the crystal texture in this vein, such as the chemical zonation patterns, suggest that calcite precipitated and grew long in their preferred direction (parallel to the plane of the vein) and began to experience space competition in those directions. In effect, calcite growth along the fast axes became locked as growing crystals intercepted each other. This left calcite with the option of growing outward parallel to their c-axes giving the bladed crystals their often observed 'bulge' morphology (Fig. 11). This continued, along with new calcite crystal nucleation (evidenced by small calcite crystals within the fracture), until nearly all the available fracture space was filled.

Potential models for the calcite morphology and microstructure observed in the younger vein investigated here include: growth of calcite crystals in 3D from numerous sites at the fracture wall, and calcite replacement of a pre-existing carbonate vein fill. The latter is unlikely given that bladed calcite is indicative of the near-instant, flash-sealing of hydro-fractures after they formed (Christenson, 1987). Progressive 3D growth from a number of sites provides a more probable method to generate the observed vein texture here. The walls of the investigated vein are irregular in shape as observed from hand-specimen and thin section (Fig. 3). This would have provided a number of variably oriented surfaces that allowed calcite crystals to nucleate, with some then growing rapidly along their m-axes outward and into the open fracture space, with their long-axes preferably aligned to a given surrounding stress field, while others form smaller calcite crystal clusters at the fracture wall as observed (Fig. 7). Fast growing elongate calcite crystals would experience space competition with each other, growing elongate around each other, providing the interlinked bladed texture observed.

Calcite morphologies in the older vein investigated do not have the bladed morphologies observed in the younger vein. They appear to have grown across the open width of the fracture as one single crystal, implying that crystal nucleation of calcite in this fracture was syntaxial, with initial growth on the wairakite crystals on one side of the vein wall, followed by asymmetrical growth (i.e. from one wall of the fracture only). Chemical zonation in these crystals does not appear to have a discernible pattern that can be related to growth. We argue here that the calcite in this vein does not represent wairakite replacement as the thin section and SEM observations clearly show textures expected from space infilling, and previous observations that the minerals in these veins are in textural equilibrium (Christenson, 1987, Absar and Blattner, 1985). However, further work to determine any potential control wairakite may have on the nucleation, crystal lattice orientation, and growth development of calcite, would benefit from further EBSD study. Initial attempts to do so in this investigation were hindered due to poor EBSD indexing of the wairakite phase.

Different calcite sealing mechanisms are present in the two different veins. Discerning the dominant cause for this variation is difficult given the large number of variables associated with calcite formation in the Kawerau Geothermal Field and the limitations of currently acquired data. Possible insight may come from cathodoluminesence observations. Rate of calcite crystallisation largely controls the morphology of precipitating calcite crystals (Folk, 1974). Fe and Mn incorporation into calcite can be affected by fluid composition (Wogelius et al., 1997), and also by calcite precipitation rates and temperature. Both the Fe and Mn content in calcite increases with decreasing precipitation rate, or increasing temperature, with the ratio of Mn/Fe increasing with decreasing precipitation rates (Dromgoole and Walter, 1990). The observed variation in cathodoluminesence between calcite in the older and younger vein may have resulted from different precipitation rates, which influenced the style of calcite growth and thus fracture sealing. We rule out the control of temperature on cathodoluminesence here as the younger and older vein calcite is thought to have precipitated from fluids of similar temperatures (Christenson, 1987). We note here that relationships between Fe and Mn incorporation into calcite and precipitation rates have not been tested at the geothermal fluid temperatures the calcite in this study precipitated from, and further research into that relationship is required.

Continuous lattice distortion across calcite crystals is observed in both fractures. This may indicate low levels of dislocation creep activity, enough to subtly deform the crystal lattice but not enough to create and migrate subgrain boundaries. However, simple grain growth can also generate the continuous lattice distortion observed here. Studies of the kinetics and mechanisms of carbonate/calcite growth show that for low levels of supersaturation in the precipitating fluid, {10–14} calcite face growth occurs at surface defects on the deposition surface, including screw dislocations, i.e. defect-originated growth, and at higher supersaturations growth progresses via a homogeneous surface nucleation process (Lefaucheux et al., 1973; Lefaucheux and Robert, 1977; Teng et al., 2000; Xu et al., 2014). A crystal growth explanation for the observed diffuse misorientation profiles in calcite crystals in the younger fracture is supported by its spatial correlation with calcite crystal growth directions (Fig. 11). Continuous distortion is only observed in elongate calcite crystals, with crystal misorientation increasing away from the crystal core (as determined from calcite CL maps). Thus as the calcite crystal grows, becoming elongate along its preferred growth axis (the m axis), it accumulates small lattice defects that subtly alter the crystal lattice orientation. This observation infers that the bladed calcite in this vein precipitated from boiling fluids with low levels of supersaturation with respect to calcite. This model of variable crystal growth direction bears similarities to textures noted in other vein crystal growth (Urai et al., 1991; Bons, 2001), and to mineral scale build up inside autoclaves (Timms et al., 2009).

4.2. Geothermal reservoir conditions from vein calcite deformation

Calcite crystals in both fractures contain low angle (2°–<10° misorientation) sub-grain boundaries. While these sub-grain boundaries are

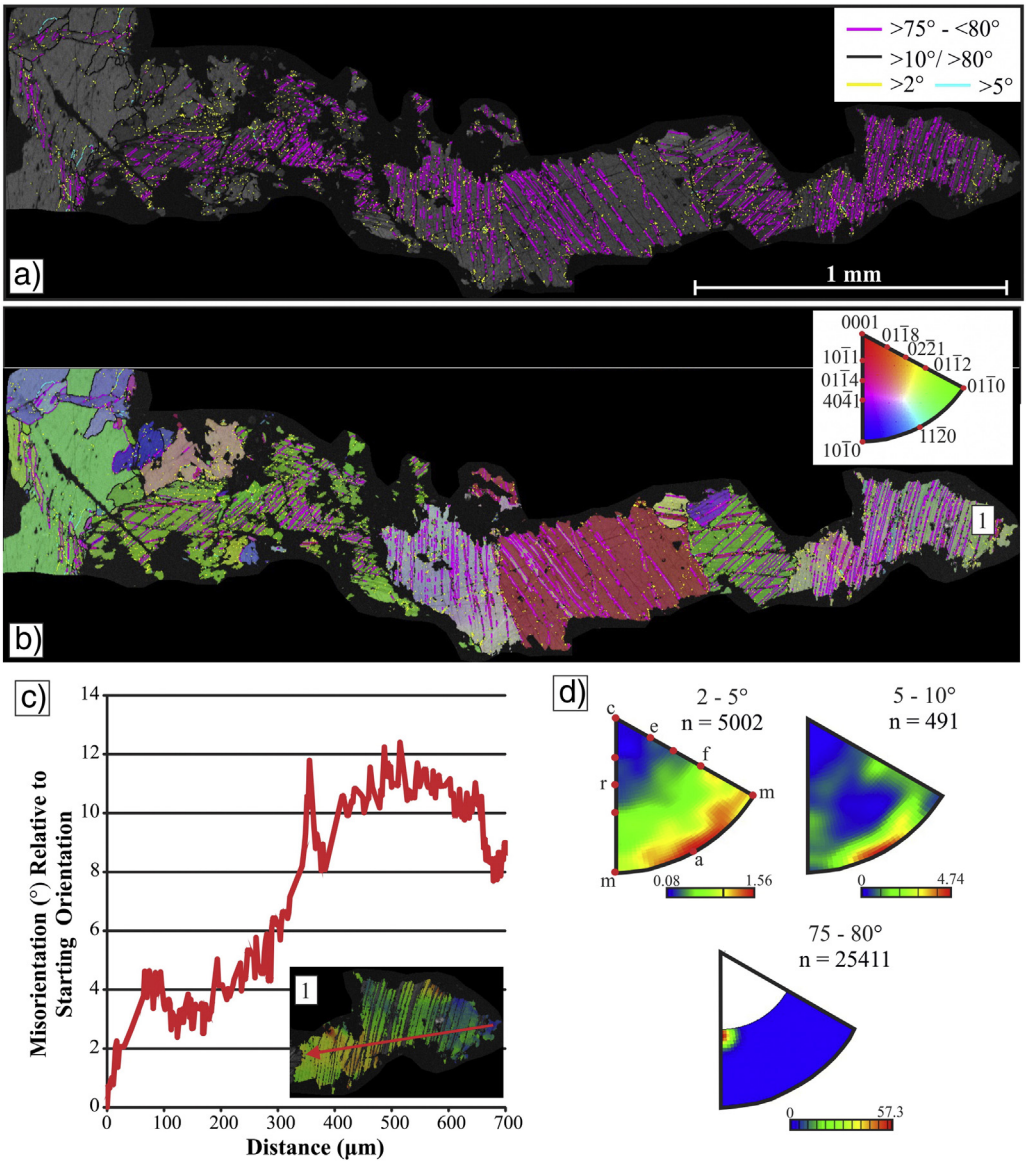

Fig. 9. EBSD data on calcite fracture fill from an older generation of fracturing. a) Band Contrast map with Grain Boundary overlay, b) band contrast map with Inverse Pole Figure (RGB colour scale) and Grain Boundary overlay, c) misorientation profile of Grain 1 (labelled in 8b) following direction indicated by red arrow, inset is Band Contrast map with Texture Component overlays for the crystal being profiled (colour indicates amount of misorientaion from a given orientation on the crystal; blue = 0°, red = 10°), d) contoured inverse pole figures for neighbouring calcite misorientations of 2°–5°, 5°–10°, and 75°–80°.

restricted to a few calcite crystals in the younger fracture, they are common in the calcite crystals of the older fracture. Subgrain development may be the result of deformation via dislocation creep in these calcite crystals, or, as discussed earlier, potentially a result of calcite growth incorporating surface defects. If we assume dislocation creep as the cause of subgrains in calcite we can conclude that crystals in the older fracture have undergone greater deformation than crystals in the younger fracture. Further to this, the misorientation axes of the subgrain boundaries found in the older and younger calcite crystals are different. The youngest fracture calcite has dominant *m* (for subgrain boundaries of 2–5° misorientation) and *sd* < 02–21 > (for subgrain boundaries of 5- < 10° misorientation) rotation axes. Rotation axes are dominantly *a* in calcite in the older fracture for all subgrain boundary categories. As such we can propose that that not only has calcite in each fracture generation undergone different amounts of dislocation creep, the slip systems by which it was operating also vary. The operation of various slip systems in calcite has been shown to be temperature dependent under particular strain rates and so documenting which ones are in operation in geothermal veins can potentially inform us of deformation and thermal history of a rock (De Bresser and Spiers, 1997). Application of this theory to calcite veins in geothermal reservoirs bear further study as it may prove a useful tool for estimating the thermal evolution of the resource.

Measuring the orientation of calcite c-axes allows determination of the 'tension' direction the rock was under (González-Casado and Garćia-Cuevas, 1999). The calcite sealing the youngest fracture generation shows a weak LPO, with calcite c-axes aligned perpendicular to the fracture wall (Fig. 13). As the sample investigated here does not have a geographical reference frame, we cannot infer the geographical extension direction associated with the formation of this fracture. We can, however, state that the extension direction during the time of calcite crystal growth in this fracture was perpendicular to the fracture length. An extension direction perpendicular to the fracture walls, in combination with the observed small, lateral offset of an older structure indicates this fracture was created through a combination of extension (mode I) and shear (mode II/III) kinematics.

Calcite crystals in both the older and younger fractures contain e-twins. Twinning density is higher in calcite crystals in the older fracture than the younger fracture. Mechanical twinning is a common

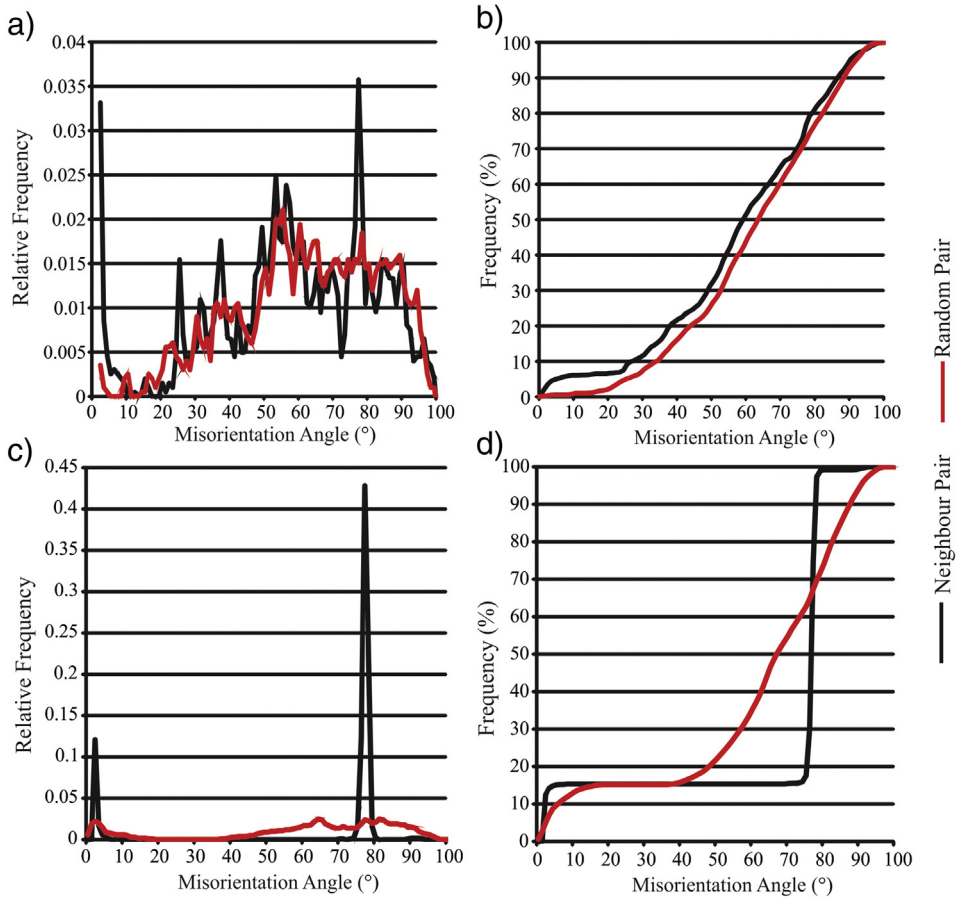

Fig. 10. Misorientation angle distribution analyses. Frequencies of misorientation angles for neighbour and random pair points for the younger calcite filled fracture showing a) relative frequency, and b) cumulative frequency. Frequencies of misorientation angles for neighbour and random pair points for the older calcite filled fracture showing c) relative frequency, and d) cumulative frequency.

microstructure in calcite and often operates as a deformation mechanism (Barber and Wenk, 1979; Burkhard, 1993; Larsson and Christy, 2008). The relationship between calcite twin structures, temperature, and stress and strain makes them useful for determining the magnitudes and orientations of the principal stress axes in tectonic environments (Jamison and Spang, 1976; Laurent et al., 1981; Groshong et al., 1984; Rowe and Rutter, 1990; Lacombe and Laurent, 1992; Ferrill et al., 2004; González-Casado et al., 2006; Chen et al., 2011). Certain twinning properties in calcite lend themselves to the determination of stress, for example, determination of strain associated with twinning can be done by measuring the average thickness of twins (the amount of simple shear deformation is proportional to the twin thickness) (Groshong, 1972; Groshong et al., 1984; Ferrill, 1991; Ferrill et al., 2004). Additionally, paleo-differential stress magnitudes can be determined from log twin density or the percentage of calcite crystals with one, two, or three twin sets (Rowe and Rutter, 1990).

The lack of twinning in the calcite crystals of the younger vein implies that the rock has experienced little strain since this sealing event. Thus, we suggest that the fracturing represented by the bladed calcite veins, at least for the basement rock in the vicinity of well KA30, marks the last significant brittle deformation event (hydrofracturing associated with volcanic activity of nearby Putauaki). However, the low number of grains captured in this dataset, and the lack of orthogonal sections to investigate, prevents a full strain and stress analysis using calcite twins. A preliminary calculation of the log twin density of calcite crystals in the older vein is presented here in order to highlight the potential of a further, more robust study of this kind in the future. These measurements of calcite twin density do not follow the prescribed methodology in Rowe and Rutter (1990), in that twin densities are not measured from this sample on orthogonal surfaces, rather they have been calculated based on one observed section. Using EBSD maps of the older calcite vein, we measured the number of twins/mm for each calcite crystal, defined by Rowe and Rutter (1990) as the rate of change of the number of lamellae of a given twin set with respect to grain diameter measured normal to the trace of the twin lamellae. This was done for the two twin sets observed, set 1 and set 2, with set 1 representing the oldest twinning in these crystals determined from cross-cutting relationships. Differential stress magnitudes are determined from these preliminary calcite log twin density data using the Rowe and Rutter (1990) equation determined from experimental and natural data [1990], assuming that the relationship derived from their study is applicable to all naturally deformed rocks, and that the density of nuclei for twin formation is constant around calcite crystal boundaries.

Based on the log twin densities from twin set 1, calcite crystals in the older vein have experienced high differential stresses at some stage after the calcite precipitated (~200–250 MPa ± 43 MPa) (Fig. 12). This differential stress magnitude recorded by calcite in the older vein represents a) the stress required to cause the greywacke rock to hydrofracture resulting in the formation of the younger bladed calcite vein, which may represent the last stage of brittle deformation of the basement rock in this area as discussed previously or b) possible deformation events that occurred after the calcite of the older vein has precipitated but before the hydrofracturing event that generated the younger calcite veins. Assuming that the calcite twinning in the older vein is recording the stress required to generate the younger hydrofracturing, differential stresses high enough to overcome the yield strength of the greywacke (which has UCS values ranging from

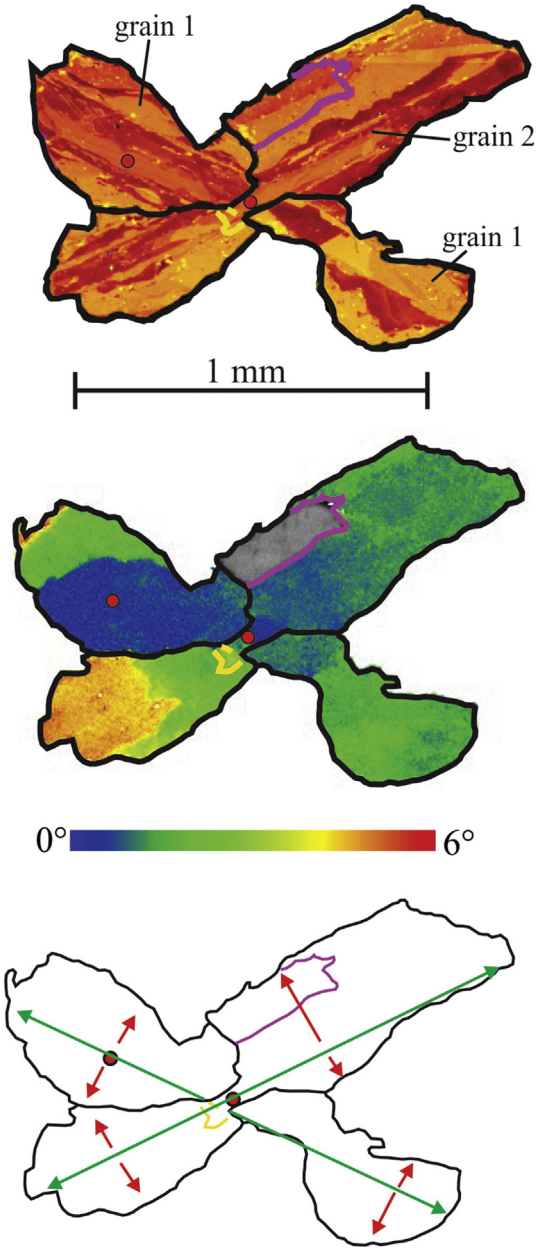

Fig. 11. a) CL images of two elongate, bladed calcite crystals from the younger fracture generation, b) EBSD texture component maps of the same two calcite crystals, c) schematic of the same crystals showing their fast growth direction (green arrows) and slower growth directions (red arrows). Red dots mark point where texture component map misorientations are scaled from, black lines = >10° misorientation boundaries (grain boundaries), purple lines = calcite twin boundaries, and yellow lines = sub-grain boundaries (2–5° misorientation).

164 to 310 MPa) would be required (Richards and Read, 2007; McNamara et al., 2014)). If the twinning in the older fracture calcite is a result of this event then the recorded differential stresses of ~205 MPa seem realistic but a more robust study of the calcite twinning should be carried out before drawing any final conclusions.

4.3. Fluid flow

Petrographic, microstructural and chemical mapping of vein fills in geothermal fractures can provide useful information on the evolution of structural permeability in the basement hosted reservoir at the Kawerau Geothermal Field. It is a general concept that progressive

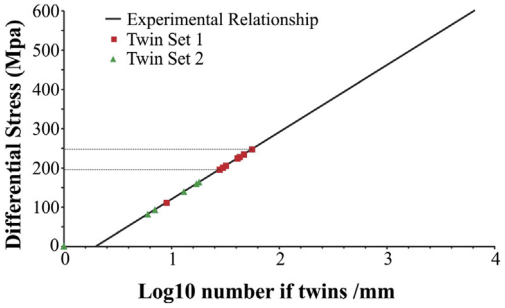

Fig. 12. Graph showing the determined relationship between differential stress and the log number of twins/mm in calcite crystals (from Rowe and Rutter, 1990) with two of the twin sets densities observed from calcite crystals in the older generation, wairakite/calcite sealed fracture.

mineralisation within a fracture decreases the porosity and permeability of that structure, but only if it ceases to propagate and open, and assuming that fracture opening is not concurrent with mineral precipitation, in which case the structure would potentially host little permeability at all. Given that the generation of the fractures studied here is associated with disruptive, energetic hydrofracturing, it is likely they were initially open to fluid flow. Fluid flow capability of the fractures was then progressively reduced by mineral precipitation, and gradual mechanical closing of these fractures due to post hydraulic fracturing decreased fluid pressure.

It is thought that as fracture sealing minerals grow from fracture walls there is a tendency for smaller fractures to be sealed off more efficiently and quickly than larger scale fractures. This would lead to wider fractures dominating the structural permeability of a rock (Marrett and Laubach, 1997). Fast rates of bladed calcite growth (~0.1 mm/day) (Tulloch, 1982), would suggest that even wide fractures are sealed quickly. As such, wide fractures may not represent the dominant permeable structures in a geothermal system as has been suggested by other studies (Sheridan et al., 2003; Davatzes and Hickman, 2009; McLean and McNamara, 2011; Wallis et al., 2012). Observations of the occurrence of wide aperture fractures existing outside permeable zones in geothermal wells have been noted in other studies, supporting this theory (McNamara et al., 2015; Massiot et al., 2015).

Finally, growth of bladed calcite, despite occurring at rapid rates, has the potential to act as a mechanism by which to preserve or prolong the permeable lifetime of the hydraulic fractures observed at Kawerau. Our microstructural and chemical investigation of bladed calcite crystals shows they can grow quickly from fracture walls to create a complex 3D interlocking structure. Rapid growth of this calcite crystal morphology may serve to prop open these wide fractures, acting against their tendency to close. By propping open the hydraulic fractures, longer

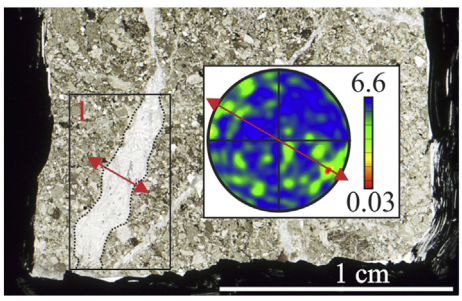

Fig. 13. Plane polarised light microscopy picture of the younger generation fracture sealed with bladed calcite. Inset is a contoured pole figure of the orientations of calcite crystal's c-axes (using one orientation point per crystal) within the dashed box (Area 1). Red arrows show the preferred orientation of the c-axes on the pole figure and the direction of extension on the photograph (determined from the c-axes preferred orientation).

time periods of fluid flow are supported until eventually calcite precipitation fills up all available space.

5. Conclusions

Observations of calcite crystal morphology, chemical zonation, and crystallographic patterns from two sealed geothermal fractures show different fracture sealing mechanisms in operation; asymmetrical syntaxial growth, and growth in free 3D space. Examination of a larger set of calcite fractures will be required to determine if a preferred calcite sealing mechanism exists in geothermal veins, and whether the sealing mechanisms is dependent on the how the calcite precipitates (e.g. whether boiling conditions are present at the time of calcite growth).

Combined EBSD/EDX/CL study of calcite sealed fractures in geothermal reservoirs shows promise as a useful tool in understanding its evolution:

- Lattice distortion associated with the continual growth of bladed calcite crystals may indicate defect-originated growth. This provides insight into the geothermal fluid conditions that precipitated these crystals as this type of calcite growth occurs from lower levels of supersaturation.
- The lack of significant twinning and micro-deformation (sign of deformation) in the bladed calcite of the youngest fracture generation implies that this fracture represents the most recent tectonic event, strong enough to create new fractures in the basement rock. The low occurrence of twinning also implies that since the time this fracture was sealed there has been little strain accumulation in the rock, or if there has been, none of it is accommodated by the calcite in this fracture.
- Observations of calcite twinning in older calcite filled fractures may potentially record differential stress magnitudes that this reservoir rock has been subjected to over time. A more in-depth study with appropriate orthogonal sections of these calcite filled fractures is required to obtain more accurate data.
- Determination of calcite lattice preferred orientations from sealed fractures can provide insight into the tension direction of the structure and possible variation in the orientation of tension over time.

Acknowledgements

Acknowledgements go to the Geothermal Resources of New Zealand research programme at GNS Science and the University of Otago for funding for this work, Ngati Tuwharetoa Geothermal Assets (NGTA) for supplying core samples from Kawerau Geothermal Field and for permission to release this data

The authors also acknowledge Dr Sarah Milicich for assistance with information surrounding the existing knowledge of the complex evolution of the greywacke basement at the Kawerau Geothermal Field.

References

Absar, A., Blattner, P., 1985. Successive Hydrothermal Events, as Indicated by Oxygen Isotope Composition and Petrography of Greywacke Basement Rocks, Kawerau Geothermal Field, New Zealand. Proceedings 7th New Zealand Geothermal Workshop.

Absar, A., 1988. Oxygen Isotope and Hydrothermal Alteration Studies at Kawerau and Ohaaki-Broadlands Geothermal Fields, New Zealand (Ph.D. Thesis) University of Auckland, New Zealand.

Adams, C.J., Mortimer, N., Campbell, H.J., Griffin, W.L., 2009. Age and isotropic characterisation of metasedimentary rocks from the Torlesse Supergroup and Waipapa group in the central North Island, New Zealand. N. Z. J. Geol. Geophys. 52, 149–170.

André, L., Rabemanana, V., Vuataz, F.–.D., 2006. Influence of water–rock interactions on fracture permeability of the deep reservoir at Soultz-sous-Forêts, France. Geothermics 35, 507–531.

Asanuma, H., Soma, N., Kaieda, H., Kumano, Y., Izumi, T., Tezuka, K., Niitsuma, H., Wyborn, D., 2005. Microseismic Monitoring of Hydraulic Stimulation at the Australian HDR Project in Cooper Basin. Proceedings World Geothermal Congress 2005.

Barber, D.J., Wenk, H.-R., 1979. Deformation twinning in calcite, dolomite, and other rhombohedral carbonates. Physics and Chemistry of Minerals 5, 141–165. http://dx.doi.org/10.1007/BF00307550.

Barker, S.L.L., Cox, S.F., Eggins, S.M., Gagan, M.K., 2006. Microchemical evidence for episodic growth of antitaxial veins during fracture-controlled fluid flow. Earth Planet. Sci. Lett. 250, 331–344. http://dx.doi.org/10.1016/j.epsl.2006.07.051.

Barker, S.L.L., Bennett, V.C., Cox, S.F., Norman, M.D., Gagan, M.K., 2009. Sm–Nd, Sr, C and O isotope systematics in hydrothermal calcite–fluorite veins: implications for fluid–rock reaction and geochronology. Chem. Geol. 268, 58–66. http://dx.doi.org/10.1016/j.chemgeo.2009.07.009.

Batzle, M.L., Simmons, G., 1976. Microfractures in rocks from two geothermal areas. Earth Planet. Sci. Lett. 30, 71–93.

Begg, J.G., Mouslopoulou, V., 2010. Analysis of late Holocene faulting within an active rift using lidar, Taupo rift, New Zealand. J. Volcanol. Geotherm. Res. 190, 152–167. http://dx.doi.org/10.1016/j.jvolgeores.2009.06.001.

Bertani, R., 2012. Geothermal power generation in the world 2005–2010 update report. Geothermics 41, 1–29. http://dx.doi.org/10.1016/j.geothermics.2011.10.001.

Bestmann, M., Prior, D.J., 2003. Intragranular dynamic recrystallization in naturally deformed calcite marble: diffusion accommodated grain boundary sliding as a result of subgrain rotation recrystallization. J. Struct. Geol. 25, 1597–1613.

Bignall, G., Milicich, S.D., 2012. Kawerau Geothermal Field: Geological Framework. GNS Science Consultancy Report 2012/118. Lower Hutt, New Zealand, Institute of Geological & Nuclear Sciences.

Blackwell, D.D., Negraru, P.T., Richards, M.C., 2007. Assessment of the enhanced geothermal system resource base of the United States. Nat. Resour. Res. 15, 283–308. http://dx.doi.org/10.1007/s11053-007-9028-7.

Bons, P.D., 2001. Development of crystal morphology during unitaxial growth in a progressively widening vein: I. The numerical model. J. Struct. Geol. 23, 865–872. http://dx.doi.org/10.1016/S0191-8141(00)00159-0.

Bons, P.D., Elburg, M.A., Gomez-Rivas, E., 2012. A review of the formation of tectonic veins and their microstructure. J. Struct. Geol. 43, 33–62.

Brace, W.F., 1980. Permeability of crystalline and argillaceous rocks. Int. J. Rock Mech. Min. Sci. Geomech. Abstr. 17, 241–251. http://dx.doi.org/10.1016/0148-9062(80)90807-4.

Bradshaw, R., Phillips, F.C., 1964. X-ray studies of natural fabrics. I. Growth-fabrics in hematite kidney ore and in fibrous calcite. Mineral. Mag. 36, 70–77.

Browne, P.R.L., 1978. Hydrothermal alteration in active geothermal fields. Annu. Rev. Earth Planet. Sci. 6, 229–250. http://dx.doi.org/10.1146/annurev.ea.06.050178.001305.

Burkhard, M., 1993. Calcite twins, their geometry, appearance and significance as stress–strain markers and indicators of tectonic regime: a review. J. Struct. Geol. 15, 351–368.

Chambefort, I., Lewis, B., Wilson, C.J.N., Rae, A.J., Coutts, C., Bignall, G., Ireland, T.R., 2014. Stratigraphy and structure of the Ngatamariki geothermal system from new zircon U–Pb geochronology: implications for Taupo volcanic zone evolution. J. Volcanol. Geotherm. Res. 274, 51–70. http://dx.doi.org/10.1016/j.jvolgeores.2014.01.015.

Chen, K., Kunz, M., Tamura, N., Wenk, H.-R., 2011. Deformation twinning and residual stress in calcite studied with synchrotron polychromatic X-ray microdiffraction. Phys. Chem. Miner. 38, 491–500.

Christenson, B.W., 1987. Fluid - Mineral Equilibria in the Kawerau Hydrothermal System, Taupo Volcanic Zone, New Zealand (Ph.D. Thesis) University of Auckland, New Zealand.

Christenson, B.W., 1997. Kawerau geothermal field: geochemical structure of the reservoir and its response to exploitation. Trans. Geotherm. Resour. Counc. 21, 17–24.

Cole, J.W., Spinks, K.D., 2009. Caldera volcanism and rift structure in the Taupo volcanic zone, New Zealand. Geol. Soc. Lond., Spec. Publ. 327, 9–29. http://dx.doi.org/10.1144/SP327.2.

Cox, S.F., Etheridge, M.A., 1983. Crack-seal fibre growth mechanisms and their significance in the development of oriented layer silicate microstructures. Tectonophysics 92, 147–170. http://dx.doi.org/10.1016/0040-1951(83)90088-4.

Davatzes, N.C., Hickman, S.H., 2010. Stress, Fracture, and Fluid-Flow Analysis Using Acoustic and Electrical Image Logs in Hot Fractured Granites of the Coso Geothermal Field, California, U.S.A. In: Pöppelreiter, M., García-Carballido, C., Kraaijveld, M. (Eds.), Dipmeter and Borehole Image Log Technology. AAPG Mem. 92, pp. 259–293. http://dx.doi.org/10.1306/13181288M923134.

Davatzes, N.C., Hickman, S.H., 2009. Fractures, Stress and Fluid Flow prior to Stimulation of well 27–15, Desert Peak, Nevada, EGS Project. Proceedings, 34th Workshop on Geothermal Reservoir Engineering.

De Bresser, J.H.P., Spiers, C.J., 1997. Strength characteristics of the *r*, *f*, and *c* slip systems in calcite. Tectonophysics 272, 1–23. http://dx.doi.org/10.1016/S0040-1951(96)00273-9.

Dezayes, C., Genter, A., Valley, B.T., 2010. Structure of the low permeable naturally fractured geothermal reservoir at Soultz. Compt. Rendus Geosci. 342, 517–530. http://dx.doi.org/10.1016/j.crte.2009.10.002.

Dobson, P.F., Kneafsey, T.J., Hulen, J., Simmons, A., 2003. Porosity, permeability, and fluid flow in the Yellowstone geothermal system, Wyoming. J. Volcanol. Geotherm. Res. 123, 313–324.

Dromgoole, E.L., Walter, L.M., 1990. Iron and manganese incorporation into calcite: effects of growth kinetics, temperature and solution chemistry. Chem. Geol. 81, 311–336.

Durney, D.W., Ramsay, J.G., 1973. Incremental Strains Measured by Syntectonic Crystal Growths. In: De Jong, K.A., Scholten, R. (Eds.), Gravity and Tectonics, pp. 67–96.

Ferrill, D.A., 1991. Calcite twin widths and intensities as metamorphic indicators in natural low-temperature deformation of limestone. J. Struct. Geol. 13, 667–675. http://dx.doi.org/10.1016/0191-8141(91)90029-I.

Ferrill, D.A., Morris, A.P., Evans, M.A., Burkhard, M., Groshong Jr., R.H., Onasch, C.M., 2004. Calcite twin morphology: a low-temperature deformation geothermometer. J. Struct. Geol. 26, 1521–1529. http://dx.doi.org/10.1016/j.jsg.2003.11.028.

Folk, R.L., 1974. The natural history of crystalline calcium carbonate: effect of magnesium content and salinity. J. Sediment. Petrol. 44, 40–53.

Fournier, R.O., 1985. Carbonate transport and deposition in the epithermal environment. Rev. Econ. Geol. 2, 63–71.

Friedman, M., Higgs, N.G., 1981. Calcite fabrics in experimental shear zones. In: Carter, N.L., Friedman, M., Logan, J.M., Stearns, D.W. (Eds.), Mechanical Behaviour of Crustal Rocks: the Handin Volume. American Geophysical Union, Washington, D. C. http://dx.doi.org/10.1029/GM024p0011.

Genter, A., Traineau, H., 1996. Analysis of macroscopic fractures in granite in the HDR geothermal well EPS-1, Soultz-sous-Forêts, France. J. Volcanol. Geotherm. Res. 72, 121–141.

Genter, A., Evans, K., Cuenot, N., Fritsch, D., Sanjuan, B., 2010. Contribution of the exploration of deep crystalline fractured reservoir of Soultz to the knowledge of enhanced geothermal systems (EGS). Compt. Rendus Geosci. 342, 502–516.

González-Casado, J.M., García-Cuevas, C., 1999. Calcite twins from microveins as indicators of deformation history. J. Struct. Geol. 21, 875–889. http://dx.doi.org/10.1016/S0191-8141(99)00081-4.

González-Casado, J.M., Gumiel, P., Giner-Robles, J.L., Campos, R., Moreno, A., 2006. Calcite e-twins as markers of recent tectonics: insights from Quaternary karstic deposits from SE Spain. Journal of Structural Geology 28, 1084–1092. Chicago.

Groshong, R.H., 1972. Strain calculated from twinning in calcite. Geol. Soc. Am. Bull. 83, 2025–2038. http://dx.doi.org/10.1130/0016-7606(1972)83[2025:SCFTIC]2.0.CO;2.

Groshong, R.H., Teufel, L.W., Gasteiger, C., 1984. Precision and accuracy of the calcite strain-gage technique. Geol. Soc. Am. Bull. 95, 357–363. http://dx.doi.org/10.1130/0016-7606(1984)95<357:PAAOTC>2.0.CO;2.

Halfpenny, A., 2010. Some important practical issues for the collection and manipulation of electron backscatter diffraction (EBSD) data from geological samples. J. Virtual Explor. 35. http://dx.doi.org/10.3809/jvirtex.2011.00272.

Hébert, R.L., Ledésert, B., Genter, A., Bartier, D., Dezayes, C., 2011. Mineral Precipitation in Geothermal Reservoir: the Study Case of Calcite in the Soultz-Sous-Forêts Enhanced Geothermal System. Proceedings, Thirty-Sixth Workshop on Geothermal Reservoir Engineering, SGP-TR-191.

Hedenquist, J.W., Henley, R.W., 1985. Effect of CO2 on freezing point depression measurements of fluid inclusions - evidence from active systems and implications for epithermal mineralization. Econ. Geol. 80, 1379–1406.

Hedenquist, J.W., 1990. The thermal and geochemical structure of the Broadlands–Ohaaki geothermal system, New Zealand. Geothermics 19, 151–185.

Hilgers, C., Koehn, D., Bons, P.D., Urai, J.L., 2000. Development of crystal morphology during unitaxial growth in a progressively widening vein: II. Numerical simulations of the evolution of antitaxial fibrous veins. J. Struct. Geol. 23, 873–885. http://dx.doi.org/10.1016/S0191-8141(00)00160-7.

Hilgers, C., Dilg-Gruschinski, K., Urai, J.L., 2004. Microstructural evolution of syntaxial veins formed by advective flow. Geology 32, 261–264.

Hurst, A.W., Bibby, H.M., Robinson, R.R., 2002. Earthquake focal mechanisms in the central Taupo Volcanic Zone and their relation to faulting and deformation. N. Z. J. Geol. Geophys. 45, 527–536. http://dx.doi.org/10.1080/00288306.2002.9514989.

Hurst, T., Bannister, S., Robinson, R., Scott, B., 2008. Characteristics of three recent earthquake sequences in the Taupo Volcanic Zone, New Zealand. Tectonophysics 452, 17–28. http://dx.doi.org/10.1016/j.tecto.2008.01.017.

Jamison, W.R., Spang, J.H., 1976. Use of calcite twin lamellae to infer differential stress. Geological Society of America Bulletin 87, 868–872.

Krupp, R.E., Seward, T.M., 1987. The Rotokawa geothermal system, New Zealand; an active epithermal gold-depositing environment. Econ. Geol. 82, 1109–1129. http://dx.doi.org/10.2113/gsecongeo.82.5.1109.

Lacombe, O., Laurent, P., 1992. Determination of principal stress magnitudes using calcite twins and rock mechanics data. Tectonophysics 202, 83–93. http://dx.doi.org/10.1016/0040-1951(92)90456-G.

Larsson, A.-K., Christy, A.G., 2008. On twinning and microstructures in calcite and dolomite. American Mineralogist 93, 103–113.

Laurent, P., Bernard, P., Vasseur, G., Etchecopar, A., 1981. Stress tensor determination from the study of e twins in calcite: a linear programming method. Tectonophysics 78, 651–660.

Lefaucheux, F., Robert, M.C., Authier, A., 1973. Étude des défauts créés lors de perturbations extérieures imposées au cours de la croissance hydrothermale de calcite. J. Cryst. Growth 19, 329–337. http://dx.doi.org/10.1016/0022-0248(73)90057-2.

Lefaucheux, F., Robert, M.C., 1977. Defects revealing two growth processes for a face case of hydrothermal synthetic calcite. J. Cryst. Growth 38, 29–37. http://dx.doi.org/10.1016/0022-0248(77)90369-4.

Leonard, G. S., J. G. Begg and C. J. N. Wilson (2010), Geology of the Rotorua area: scale 1: 250,000, Institute of Geological & Nuclear Sciences 1:250,000 geological map 5, Institute of Geological & Nuclear Sciences Limited, Lower Hutt, New Zealand.

Long, J.V.P., Agrell, S.O., 1965. The cathodoluminescence of minerals in thin section. Mineralogical Magazine 34, 318–326.

Marrett, R., Laubach, S.E., 1997. Diagenetic controls on fracture permeability and sealing. Int. J. Rock Mech. Min. Sci. 34.

Massiot, C., McNamara, D.D., Nicol, A., Townend, J., 2015. Fracture width and spacing distributions from borehole televiewer logs and core in the Rotokawa geothermal field, New Zealand. Proceedings World Geothermal Congress 2015.

McLean, K., McNamara, D.D., 2011. Fractures Interpreted from Acoustic Formation Imaging Technology: Correlation to Permeability. Proceedings, Thirty-Sixth Workshop on Geothermal Reservoir Engineering, SGP-TR-191.

McNamara, D.D., Faulkner, D., McCarney, E., 2014. Rock Properties of Greywacke Basement Hosting Geothermal Reservoirs, New Zealand: Preliminary Results. Proceedings, Thirty-Ninth Workshop on Geothermal Reservoir Engineering, SGP-TR-202.

McNamara, D.D., Massiot, C., Lewis, B., Wallis, I.C., 2015. Heterogeneity of structure and stress in the Rotokawa Geothermal Field, New Zealand. J. Geophys. Res. 120, 1243–1262. http://dx.doi.org/10.1002/2014JB011480.

Milicich, S.D., Wilson, C.J.N., Bignall, G., Pezaro, B., Bardsley, C., 2013. Reconstructing the geological and structural history of an active geothermal field: a case study from New Zealand. J. Volcanol. Geotherm. Res. 262, 7–24. http://dx.doi.org/10.1016/j.jvolgeores.2013.06.004.

Milicich, S.D., Bardsley, C., Bignal, G., Wilson, C.J.N., 2014. 3-D interpretive modelling applied to the geology of the Kawerau geothermal system, Taupo volcanic zone, New Zealand. Geothermics 51, 344–350.

Nairn, I.A., Beanland, S., 1989. Geological setting of the 1987 Edgecumbe earthquake, New Zealand. N. Z. J. Geol. Geophys. 32, 1–13.

Nairn, I. A. (2002), Geology of the Okataina Volcanic Centre: scale 1:50,000, Institute of Geological & Nuclear Sciences geological map 25, Institute of Geological & Nuclear Sciences Limited, Lower Hutt, New Zealand.

Nicol, A., Walsh, J., Berryman, K., Villamor, P., 2006. Interdependence of fault displacement rates and paleoearthquakes in an active rift. Geology 34, 865. http://dx.doi.org/10.1130/G22335.1.

Nüchter, J.-.A., Stöckhert, B., 2007. Vein quartz microfabrics indicating progressive evolution of fractures into cavities during postseismic creep in the middle crust. J. Struct. Geol. 29, 1445–1462.

Okamoto, A., Sekine, K., 2011. Texture of syntaxial quartz veins synthesized by hydrothermal experiments. J. Struct. Geol. 33, 1764–1775.

Phillips, W.J., 1972. Hydraulic fracturing and mineralization. J. Geol. Soc. Lond. 128, 337–359.

Piazolo, S., Prior, D.J., Holness, M.D., 2005. The use of combined cathodoluminescence and EBSD analysis: a case study investigating grain boundary migration mechanisms in quartz. J. Microsc. 217, 152–161. http://dx.doi.org/10.1111/j.1365-2818.2005.01423.x.

Prior, D.J., Trimby, P.W., Weber, U.D., 1996. Orientation contrast imaging of microstructures in rocks using forescatter detectors in the scanning electron microscope. Mineral. Mag. 60, 859–869.

Prior, D.J., Boyle, A.P., Brenker, F., Cheadle, M.C., Day, A., Lopez, G., Peruzzo, L., Potts, G.J., Reddy, S., Spiess, R., Timms, N.E., 1999. The application of electron backscatter diffraction and orientation contrast imaging in the SEM to textural problems in rocks. Am. Mineral. 84, 1741–1759.

Ramsay, J.G., 1980. The crack-seal mechanism of rock deformation. Nature 284, 135–139. http://dx.doi.org/10.1038/284135a0.

Richards, L., Read, S.A.L., 2007. New Zealand Greywacke Characteristics and Influences on Rock Mass Behaviour. 11th Congress of the International Society for Rock Mechanics.

Rowe, K.J., Rutter, E.H., 1990. Palaeostress estimation using calcite twinning: experimental calibration and application to nature. J. Struct. Geol. 12, 1–17.

Rowland, J.V., Simmons, S.F., 2012. Hydrologic, magmatic, and tectonic controls on hydrothermal flow, Taupo volcanic zone, New Zealand: implications for the formation of epithermal vein deposits. Econ. Geol. 107, 427–457. http://dx.doi.org/10.2113/econgeo.107.3.427.

Rowland, J.V., Sibson, R.H., 2001. Extensional fault kinetics within the Taupo Volcanic Zone. New Zealand: Soft-linked segmentation of a continental rift system, New Zealand Journal of Geology and Geophysics 44, 271–283. http://dx.doi.org/10.1080/00288306.2001.9514938.

Sausse, J., Fourar, M., Genter, A., 2006. Permeability and alteration within the Soultz granite inferred from geophysical and flow log analysis. Geothermics 35, 544–560. http://dx.doi.org/10.1016/j.geothermics.2006.07.003.

Seebeck, H., Nicol, A., Villamor, P., Ristau, J., Pettinga, J., 2014. Structure and kinematics of the Taupo Rift, New Zealand. Tectonics 33. http://dx.doi.org/10.1002/2014TC003569.

Sheridan, J., Kovac, K., Rose, P.E., Barton, C., McCulloch, J., Berard, B., Moore, J.M., Petty, S., Spielman, P., 2003. In Situ Stress, Fracture and Fluid Flow Analysis — East Flank of the Coso Geothermal Field. Proceedings, Twenty-Eighth Workshop on Geothermal Reservoir Engineering, SGP-TR-173.

Simmons, S.F., Christenson, B.W., 1994. Origins of calcite in a boiling geothermal system. Am. J. Sci. 294, 361–400.

Steiner, A., 1955. Wairakite, the calcium analogue of analcime, a new zeolite mineral. Mineral. Mag. 30, 691–698.

ten Have, T., Heijnen, W., 1985. Cathodoluminescence activation and zonation in carbonate rocks: an experimental approach. Geol. Mijnb. 64, 297–310.

Teng, H.H., Dove, P.M., De Yoreo, J.J., 2000. Kinetics of calcite growth: surface processes and relationships to macroscopic rate laws. Geochim. Cosmochim. Acta 64, 2255–2266. http://dx.doi.org/10.1016/S0016-7037(00)00341-0.

Timms, N.E., Li, J., Reddy, S.M., 2009. Quantitative microstructural characterization of natrojarosite scale formed during high-pressure acid leaching of lateritic nickel ore. Am. Mineral. 94, 1111–1119. http://dx.doi.org/10.2138/am.2009.3104.

Townend, J., Sherburn, S., Arnold, R., Boese, C., Woods, L., 2012. Three-dimensional variations in present-day tectonic stress along the Australia–Pacific plate boundary in New Zealand. Earth Planet. Sci. Lett. 353-354, 47–59. http://dx.doi.org/10.1016/j.epsl.2012.08.003.

Tulloch, A.J., 1982. Mineralogical Observations on Carbonate Scaling in Geothermal Wells at Kawerau and Broadlands. Proceedings 4th New Zealand Geothermal Workshop.

Urai, J.L., Williams, P.F., van Roermund, H.L.M., 1991. Kinematics of crystal growth in syntectonic fibrous veins. J. Struct. Geol. 13, 823–836. http://dx.doi.org/10.1016/0191-8141(91)90007-6.

Villamor, P., Berryman, K.R., 2001. A late Quaternary extension rate in the Taupo Volcanic Zone, New Zealand, derived from fault slip data. N. Z. J. Geol. Geophys. 44, 243–269. http://dx.doi.org/10.1080/00288306.2001.9514937.

Villamor, P., Berryman, K.R., Nairn, I.A., Wilson, K., Litchfield, N., Ries, W., 2011. Associations between volcanic eruptions from Okataina volcanic centre and surface rupture of nearby active faults, Taupo rift, New Zealand: insights into the nature of volcano-tectonic interactions,. Geol. Soc. Am. Bull. 123, 1383–1405.

Wallace, L.M., Beavan, J., McCaffrey, R., Darby, D., 2004. Subduction zone coupling and tectonic block rotations in the North Island, New Zealand. J. Geophys. Res. 109, 1978–2012. http://dx.doi.org/10.1029/2004JB003241.

Wallis, I.C., McNamara, D.D., Rowland, J., Massiot, C., 2012. The nature of fracture permeability in the basement greywacke at Kawerau geothermal field, New Zealand. Proceedings, thirty-Seventh Workshop on Geothermal Reservoir Engineering, SGP-TR-194.

Wilson, C.J.N., Houghton, B.F., McWilliams, M.O., Lanphere, M.A., Weaver, S.D., Briggs, R.M., 1995. Volcanic and structural evolution of the Taupo volcanic zone, New Zealand: a review. J. Volcanol. Geotherm. Res. 68, 1–28. http://dx.doi.org/10.1016/0377-0273(95)00006-G.

Wiltschko, D.V., Morse, J.W., 2001. Crystallization pressure versus "crack seal" as the mechanism for banded veins. Geology 29, 79–82. http://dx.doi.org/10.1130/0091-7613(2001)029<0079:CPVCSA>2.0.CO;2.

Wogelius, R.A., Fraser, D.G., Wall, G.R., Grime, G.W., 1997. Trace element and isotopic zonation in vein calcite from the Mendip Hills, UK, with spatial-process correlation analysis. Geochim. Cosmochim. Acta 61, 2037–2051.

Wood, C.P., Brathwaite, R.L., Rosenberg, M.D., 2001. Basement structure, lithology and permeability at Kawerau and Ohaaki geothermal fields, New Zealand. Geothermics 30, 461–481. http://dx.doi.org/10.1016/S0375-6505(01)00003-7.

Xu, M., Kovarik, L., Arey, B.W., Felmy, A.R., Rosso, K.M., Kerisit, S., 2014. Kinetics and mechanisms of cadmium carbonate heteroepitaxial growth at the calcite (10-14) surface. Geochim. Cosmochim. Acta 134, 221–233. http://dx.doi.org/10.1016/j.gca.2013.11.036.

Chapter 3

3-D Electron Backscatter Diffraction (EBSD) Reconstruction of Calcite Sealing in an Active Geothermal Reservoir: A Nº 8 Wired Approach

A. J. Lister[1], D. D. Prior[1], D. D. McNamara[2] & M. Brenna[1]

[1] *Department of Geology, University of Otago, Dunedin, New Zealand*

[2] *GNS Science, Lower Hutt, New Zealand*

Abstract

This chapter describes the generation of a 3-D visualisation of a fracture sealed with calcite mineralisation by electron backscatter diffraction (EBSD) serial sectioning, including details on sample preparation. Furthermore, this chapter also describes the methods taken during the material characterisation and image segmentation, as well as the results of the final 3-D microstructural reconstruction. The 3-D structure of bladed calcite sealing the examined fracture and associated fractures provide an insight into the understanding of calcite sealing mechanisms and the permeability of greywacke basement reservoir rock.

Observations of the crystallographic growth morphologies and interactions of the calcite are similar to those seen in the 2-D analysis. The bladed calcite crystals appear to grow in an interconnecting relationship within free space in addition to growing from fracture walls. Several blocky calcite crystals in the main fracture grew in a preferential direction across the fracture. Both of these phases of calcite can be seen to merge with each other along the fracture throughout the 3-D analysis.

This study illustrates the need for a well thought out serial sectioning process and the requirement for precise sectioning distances between each slice. To overcome inconsistencies in slice separation an automated system is recommended. Immense care must also be taken in sample preparation if this method is to be used for future 3-D EBSD characterisation. This method for analysing the crystallographic growth mechanisms for geothermally precipitated calcite in fractured reservoir rocks is an innovative technique that provides an insight into crystal growth using information from the z-axis which is not conventionally observed in 2-D analysis.

3.1 Introduction

Polycrystalline materials such as ceramics, metals and minerals that make up most of the inorganic world around us comprise of an array of microscopic crystals of different sizes and orientations. The description and orientation of these crystals plays an important role in the understanding of the material's physical characteristics. As outlined previously, electron backscatter (EBSD), energy dispersive x-ray (EDX), and cathodoluminescence (CL) are great analytical techniques to quantify the microstructure, microchemistry, and crystallographic orientations of a range of materials and thus provide an insight into their physical properties, and in the case of vein filling minerals, their sealing and growth mechanisms (Machel and Burton, 1991; Reeder, 1991; Wilkinson et al., 2009; Melcher et al., 2010; Uchic, 2011).

Both EBSD and EDX are surface sensitive, material analysis techniques that can characterise grain size, orientation, and chemical composition of a 2-D surface (Melcher et al., 2010). What is missing from these techniques is information in the z-direction which can be provided by using such methods as μCT, tomography, and serial sectioning (Uchic, 2011). These techniques provide information on a material's 3-D structure, volume, and grain interaction, which allows a deeper understanding of the crack-seal processes that occur in fractures.

In the many fields of research that utilise EBSD for crystallographic information, especially geology, it is common for an in-depth study to be carried out stereographically using 2-D investigative methods (Zaefferer et al., 2008). The results of a 2-D EBSD and EDX investigation into calcite sealed fractures from a geothermal reservoir are discussed in-depth in the previous Chapter. This work provided an insight into the composition of the mineralised fractures and the sealing mechanisms in operation in this region of the field. However, this study is limited in that it only provides information on the fracture sealing calcite as it appears on the 2-D surface of the thin section.

This chapter presents a review of the processes and techniques we used for developing a 3-D model of the bladed calcite fracture using EBSD, EDX, CL, and μCT techniques. The purpose of using a combined approach was to provide a comprehensive understanding of the internal microstructures of the mineralised fracture.

Through 3-D EBSD serial sectioning we aim to:

1. Provide a 3-D visualisation of hydrothermal calcite in the mineralised fracture using serial sectioning methods.
2. Assess the relationship between the various stages of calcite mineralisation previously identified as well as the sealing mechanisms related to the calcite phase of fracture sealing.

3.1.1 Brief Overview of 3-D Electron Backscatter Diffraction (EBSD) and Serial Sectioning

Using crystallographic orientation to analyse the 3-D structure of a polycrystalline material is by no means a new technique. Early techniques such as the universal stage provided a manual way to determine a materials internal structure (Dodge, 1923; Uchic, 2011). Despite only providing limited information in the z-direction (a few microns deep) it was still a unique method available to acquire 3-D crystallographic information of a material. This method is however time consuming, due to the manual operation involved in data acquisition, and is restricted to translucent materials (Dodge, 1923).

With the development and advances in SEM technology, EBSD techniques, and dedicated software, the acquisition of crystallographic data for a range of materials (translucent and opaque) became possible and more time efficient (Mariani et al., 2008; Wilkinson et al., 2009). The 3-D characterisation of crystallographic microstructures can be carried out by two means, either by serial section or by some form of transmissive radiation (Zaefferer et al., 2008; Uchic, 2011). The advances in EBSD acquisition allowed for multiple data sets to be generated by serial sectioning which in turn could be manipulated to produce a representative 3-D model of a material's crystal structure (Alkemper and Voorhees, 2001; Liu et al., 2008). The process of serial sectioning takes a series of slices in the z-direction of the sample surface at uniform steps with an EBSD scan preformed at each step (Figure 3.1). These EBSD scans can then be compiled to form a stack of scans spatially related to each other, which in turn is used to generate a 3-D model (Figure 3.1). This model can provide a complete understanding of the internal structures of a material, such as grain volume, crystal boundary conditions, and grain boundary interactions (Liu et al., 2008). There are several methods that have been developed for serial sectioning, each being specific to the material being analysed and the equipment that is available (Alkemper and Voorhees, 2001; Jorgensen et al., 2009; Uchic, 2011).

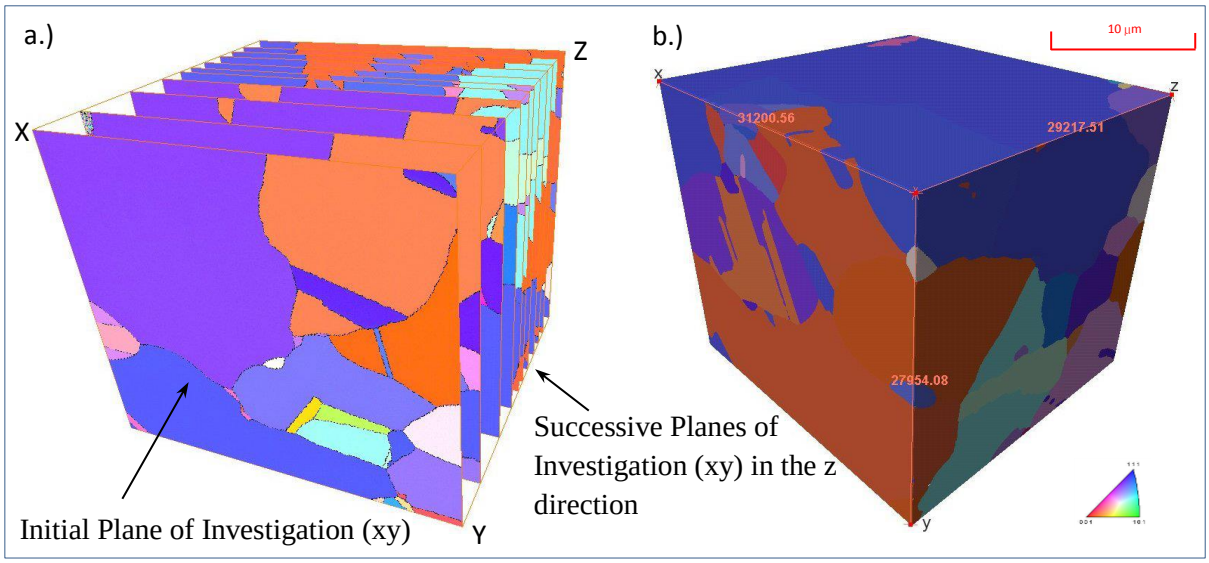

Figure 3.1 An illustration of an image stack built from 2-D orientation maps (a.) and a final 3-D volume (31.2 µm x 29.2 µm x 27.9 µm) with reference triangle using a Euler colour scheme (b.) from a previous study using a Ni sample (Adapted from Baris, 2014).

Serial sectioning is a destructive process during which a slice of the sample is cut away in the z-direction of the initial EBSD mapped surface, with an EBSD scan being performed on the newly exposed surface (Uchic, 2011). The modern convention for 3-D EBSD by serial sectioning is to use an automated sectioning process or a dual beam SEM-FIB (Focused Ion Beam) in conjunction with an EBSD camera. This method provides successive sections for EBSD mapping with precise uniform separation, a z-direction resolution of up to 100 nm and a magnification resolution of 50 nm (Spanos et al., 2008). The later technique uses the addition of an ion gun, generally in the form of a focused Ga^+ sourced beam, to acquire EBSD data as well as sputter, mill, and cut the sample to size (Liu et al., 2008; Uchic, 2011). Using SEM-FIB produces well defined, clear, nano-scale images. This process is very time consuming to produce this high resolution nano-scale information.

For this study a FIB or other automated section apparatus was not used to section the sample due to the lack of access to this piece of equipment, the limiting factor of sample size, and the time required to carry out 3-D EBSD sectioning on a large fracture.

3.2 Methods

3.2.1 Sample Selection and Preparation

Due to the size of the sample area and the intended volume to be studied we developed a new serial-sectioning process. We adapted and modified the methods outlined by both Kral (2000; 2004) and Uchic (2011) to suit the material we were using and the tools available to us. This included the optimised use of SEM time and sample preparation methods. A sample of fragmented drill-core of greywacke rock was selected which contained a near vertical, straight, and continuous vein of bladed calcite (Figure 3.2). These features were used to optimise data acquisition time within the SEM and for correlating the dimensional analysis between the various stages of this study.

The greywacke fragment that was selected was approximately 8 mm x 20 mm x 15mm and contained a dominant 1 mm wide, near vertical fracture that was sealed with bladed calcite, wairakite, and calcite mineralisation. There was also a series of adjacent narrow fractures sealed with both calcite and wairakite. Sample preparation methods were tested and optimised using common samples of analogous greywacke sourced from surface outcrops. The results of these initial testing methods and parameters are presented in Appendix 1. During this initial analysis parameters for scanning in the SEM was optimised for carrying out EBSD.

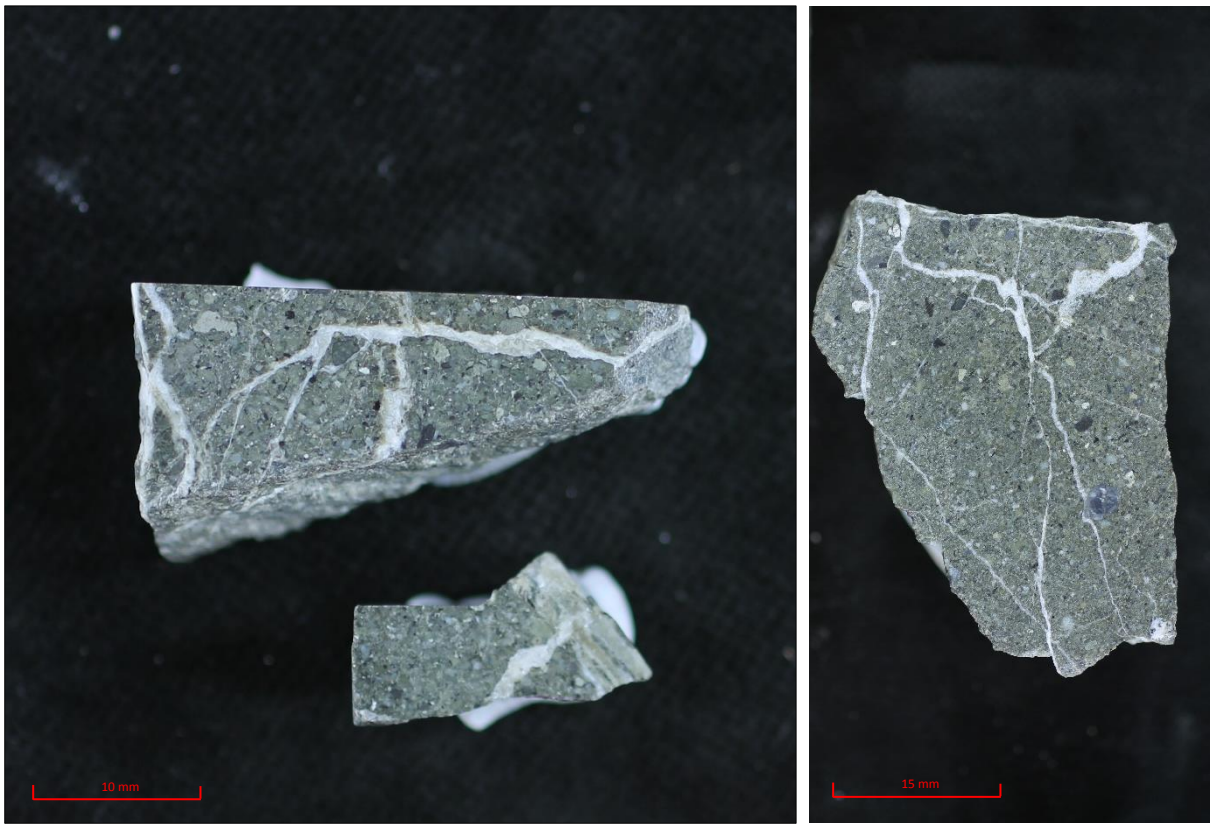

Figure 3.2 Photographs of selected fragments of the greywacke core from 1213 mRF, well KA30.

As previously mentioned the selected piece of greywacke drill-core underwent a series of tests and examinations prior to sectioning. First the sample was scanned with the Skyscan 1172 µCT Scanner located at the Otago Centre for Electron Microscopy (OCEM). This procedure provided information on the 3-D morphology of the fracture in the greywacke core which was used as guidance for a targeted serial sectioning of the sealed fracture.

Prior to SEM analysis the core sample was specially prepared for the process of repeated sectioning and scanning. To successfully maintain its integrity as one piece during the serial sectioning process, the sample was encased in a solid briquette of powered KonductoMet, a phenolic mounting carbonite (See Appendix 2 for the mounting process). A briquette made of carbonite was used instead of no plug or one made of epoxy resin had several advantages (See Appendix 1):

1. The conductivity of the carbonite briquette prevented charging inside the SEM.
2. Once treated in the mounting press the powered carbonite has a similar hardness to the rock sample and prevented differential polishing across the plug-rock interface of the sectioned surface unlike an epoxy resin plug.

3. The plug provided a rigid base allowing the rock sample to remain in exactly the same position and orientation for every subsequent sectioning and scan.

Following the carbonite mounting process the sample plug was scanned a second time in the µCT-scanner, at a lower resolution. This scan was undertaken to assess the condition of the sample and orientation of the fracture within the plug after the mounting process. The damage caused to the sample due to crushing suffered during the mounting process is discussed in the µCT results sections later.

Sectioning of the plug was carried out by placing it in a briquette holder for grinding with a weight and a micrometre to monitor the amount removed for each slice (Figure 3.3). The grinding was preformed using 2100 grit silicon carbide sandpaper until the desired amount of sample was removed. The grinding process was followed by both mechanical and chemical polishing using 3µm diamond paste and then 1µm diamond paste with a final polish of colloidal silica to prepare the sample for EBSD. The sample was re-measured and visually inspected prior to scanning in the SEM to assess if the surface was adequate for EBSD mapping. Additional stages of colloidal silica polishing were carried out when improvement of the finished surface was required. A scanned image of each prepared surface can be found in Appendix 3.

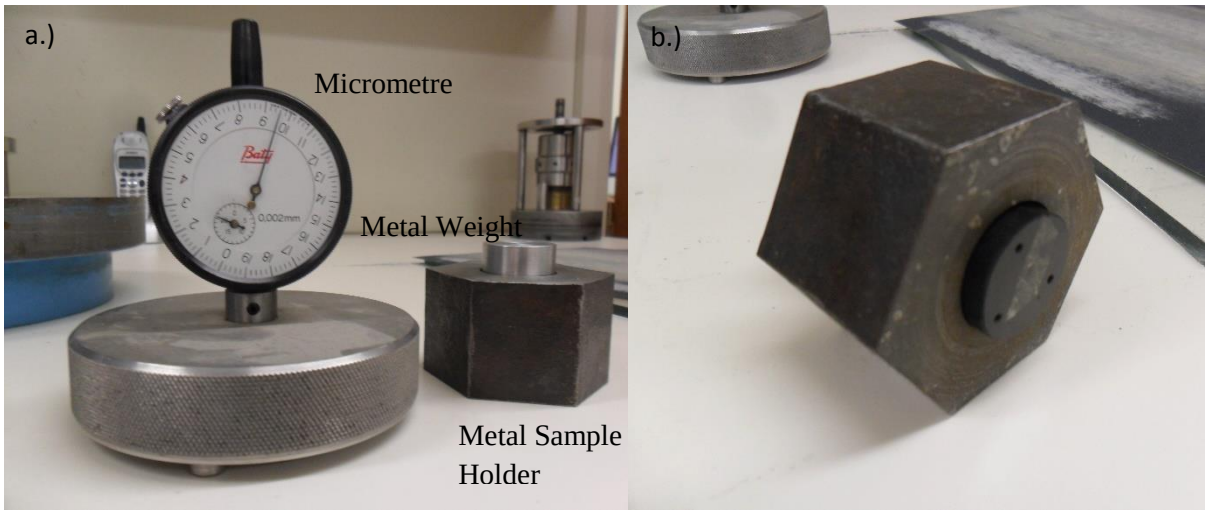

Figure 3.3 a.) The micrometre and the metal sample holder with weight used for grinding down the briquette. b.) Shows the bottom of the metal grinding holder with the briquette in place.

The aim was to achieve surface slices that were 100 µm apart though the separation ranged between 140µm and 700 µm. Several of the final slices were spaced at 10 µm apart to assess if we could achieve this separation with the process we were using (See Appendix 4).

To maintain constant positioning within the SEM holder and to aid in data analysis the finished carbonite plug included a series of marker schemes as can be seen in Figure 3.4. To achieve this, the plug was squared off by machining a flat surface to two edges for a flush fit within the SEM holder. In addition three 2 mm diameter Fiducial marker holes were drilled perpendicular to the sample surface to assist in orientating the scanned images in the same x-y orientation during data analysis and image segmentation (scan separation and alignment).

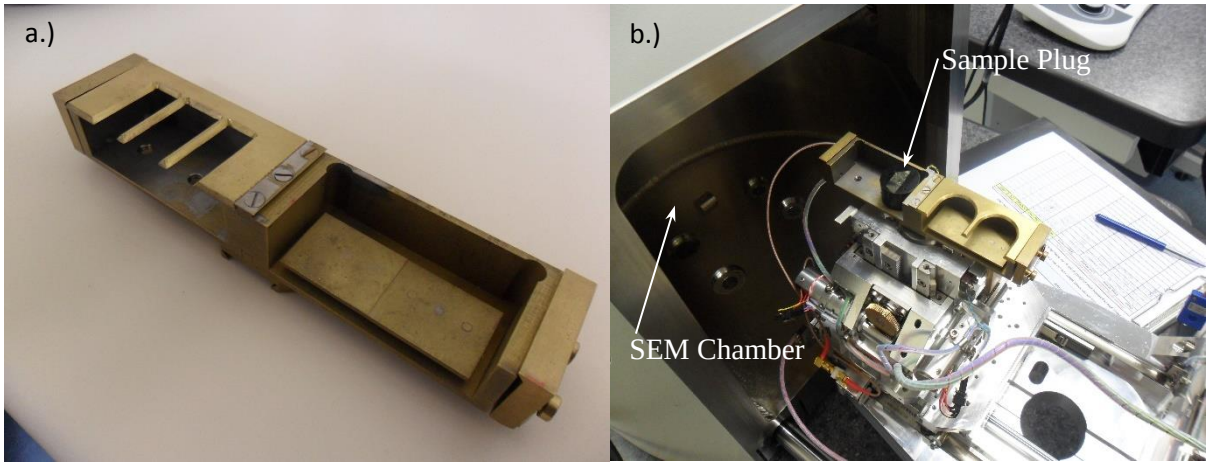

Figure 3.4 a.) The brass sample holder for the SEM. b.) The sample briquette and holder in the SEM, here you can see the marker schemes we used in practice.

Prior to each EBSD scan the freshly polished sample surface was treated with a sputter coating of vaporised carbon to minimise charging of the surface within the SEM. The process of sputter coating is outlined in Appendix 2.

3.2.2 Electron Backscatter Diffraction (EBSD), Energy Dispersive X-Ray (EDX) & Cathodoluminescence (CL) Techniques and Scanning

The procedures involved in this step of the study, including EBSD data collection, are similar to those outlined in Chapter 2. It must be noted here that some of the SEM parameters used were modified for serial sectioning. For each EBSD map a step size of 10 μm was used for each of the 7 sectioned slices of the sample. As suggested by Uchic (2011) each sliced surface had an accompanying backscatter image to provide additional data on such characteristics as chemical and elemental distribution and selected surfaces have supplementary EDX data (slices 3, 4, 5, 6, and 7) and CL images (slice 5 and 6).

3.2.3 3-D Electron Backscatter Diffraction (EBSD) Modelling and Image Analysis

EBSD maps and additional elemental data, collected as a series of images, were used to generate a 3-D representation of the crystallographic orientation of the calcite crystals in the fracture. The 3-D visualisation techniques used in this study are discussed below and utilise a combination of various image analysis software packages.

3.2.3.1 Data Analysis and Image Segmentation Workflow

The following details the process tree with which the initial EBSD and elemental point data was processed for each imaged slice and then translated into a working 3-D representation of the sealed fracture:

- The EBSD and EDX data were initially collected and analysed using Oxford Instruments AZTec software. This step included generating HKL Channel5 files from the initial AZtec files. In addition the EDX data maps were inspected using AZtec to develop line-scans and digital element maps to be overlaid on the backscatter image similar to Chapter 2.
- The HKL Channel5 files were then transferred into HKL Tango, An EBSD post-processing software program. Noise reduction was carried out on the EBSD data sets to improve the quality of the final mapped images by removing non-indexed or mis-indexed pixels. Orientation maps were collected using Inverse Pole Figure (IPF) colours for the 3 orientations (x, y, and z) along with grain boundary maps.
- All EBSD maps were then processed through ArcGIS using geo-referencing to remove any distortion associated by electron optics (Figure 3.5). The precise alignment of the sliced surfaces is a key stage of image analysis as it determines the quality of the final 3-D reconstructed volume. Therefore ArcGIS was also used to apply an x-y-z co-ordinate system to each slice image.
- CL and EDX images were overlaid onto the manipulated EBSD orientation maps to generate a stack of images to upload into the 3-D modelling software.
- A combination of ARANZ Geo Leapfrog, ImageJ, and Paraview were used to generate a 3-D visualisation of the calcite crystals in the fracture network.
- The process of generating the image stack and a 3-D volume involved several steps in Leapfrog. Firstly each slice (x-y-z referenced image) was imported as a surface to work

on. Then the fracture wall was outlined using polylines and structural discs for each surface. The polylines were then turned into structural lines to form the fracture walls. To aid in this step the resolution and structural discs were re-orientated to adjust the fracture appearance. Once the best representation of the fracture walls was achieved they were transformed into a block model with sub blocks for various recognised phases of fracture sealing.

- We then carried out final processing of the recorded images, visualisation of the EBSD surfaces, and 3-D structure. This was done by dividing the main fracture into zones for ease of discussion (Figure 3.6).

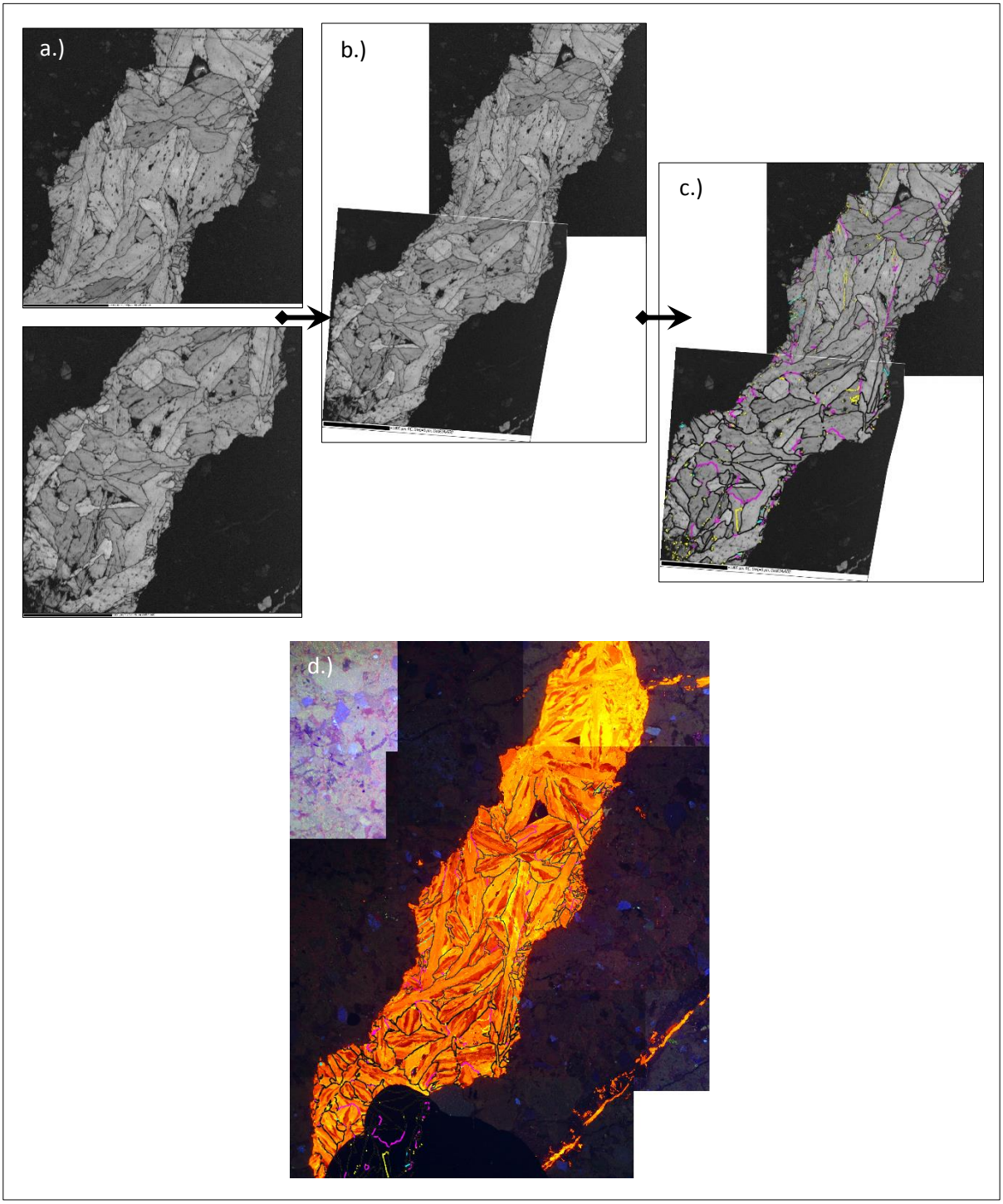

Figure 3.5 The process of EBSD image adjustment to correct for image distortion due to electron optics within the SEM using images from the thin section in Chapter 2 as an example. Initial SEM images show distortion along the bottom of the image (a.), this was then stitched together in ArcGIS to accommodate this distortion (b.) an EBSD grain boundary map was then overlaid and again corrected for distortion using ArcGIS (c.), the final corrected EBSD grain boundary map overlaid on the CL image (d.).

3.3 Results

To aid in discussing the results for the serial sectioning stage of this investigation the x-y plane of the sample was broken down into distinct regions which displayed varying structural and chemical characteristics (Figure 3.6).

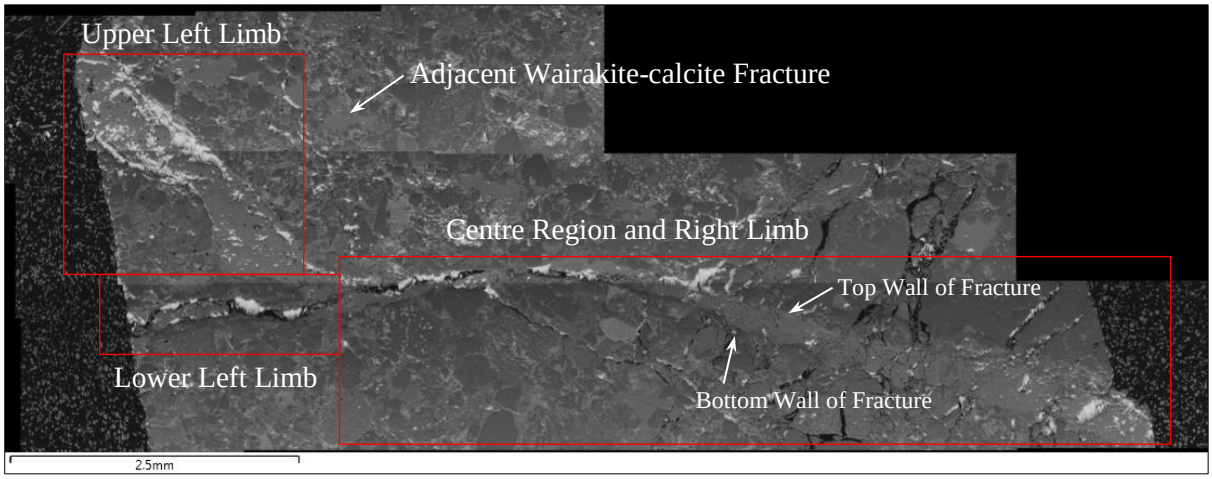

Figure 3.6 The various areas of the facture referred to in the text.

3.3.1 µCT 3-D Results

The rock sample was scanned within the µCT-Scanner several times throughout the initial stages of sample preparation for serial sectioning. The first scan of the sample provided the internal structure of the fracture network present within the sample which displayed as changes in greyscale due to variations in sample density. The sample comprised two sealed fractures which intersected each other. The main fracture is near vertical with a second fracture that intersects it perpendicular at depth. Small splays from the main, central fracture in the sample were also imaged. Figure 3.7 shows the main fracture in a variety of orientations using high resolution µCT-Scan images.

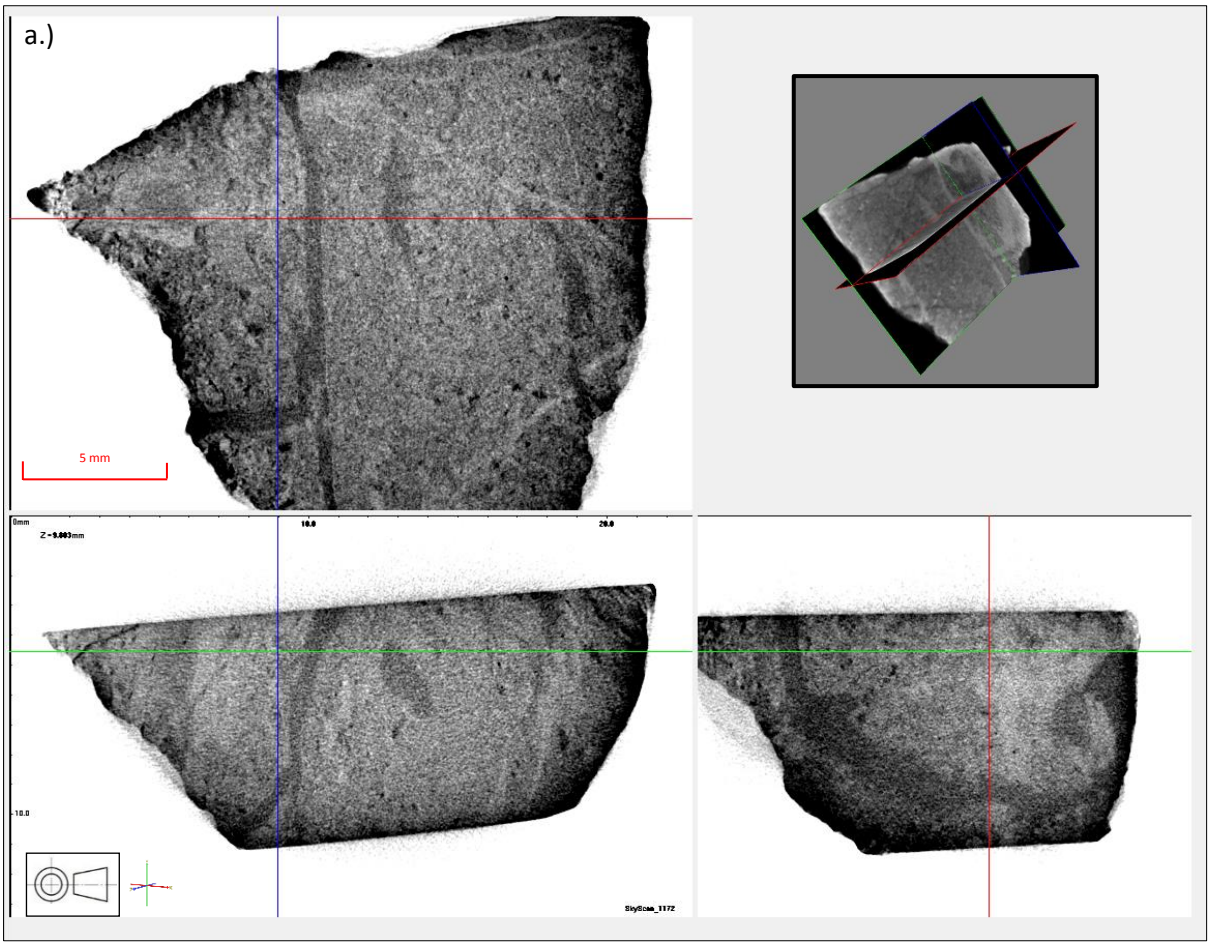

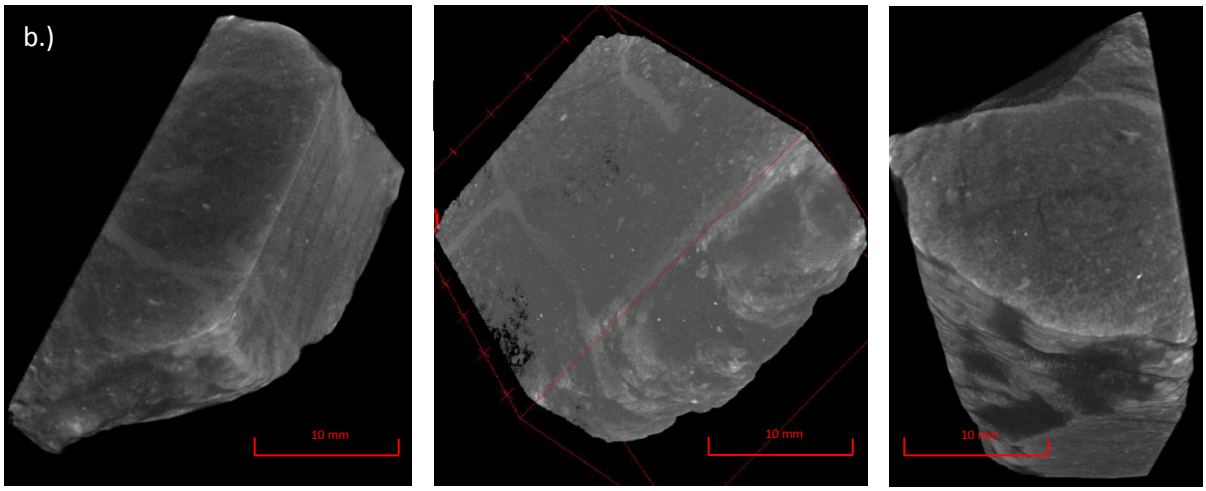

Figure 3.7 a.) Inverse colour orthographic projection of the µCT scan of the core sample, the calcite fracture appeared lighter in the scans, insert is the sample viewed in 3-D using the x-y-z plans. b.) Various orientations of the solid 3-D model showing the structure of the fracture.

A second µCT-Scan was carried out after the fragment had been encased in the carbonite plug. Even though the second scan of the plug was run at a lower resolution the vein and rock were still distinguishable from each other and the carbonite material. The scan revealed several zones of crushed material and large cracks within the sample that formed due to the mounting process.

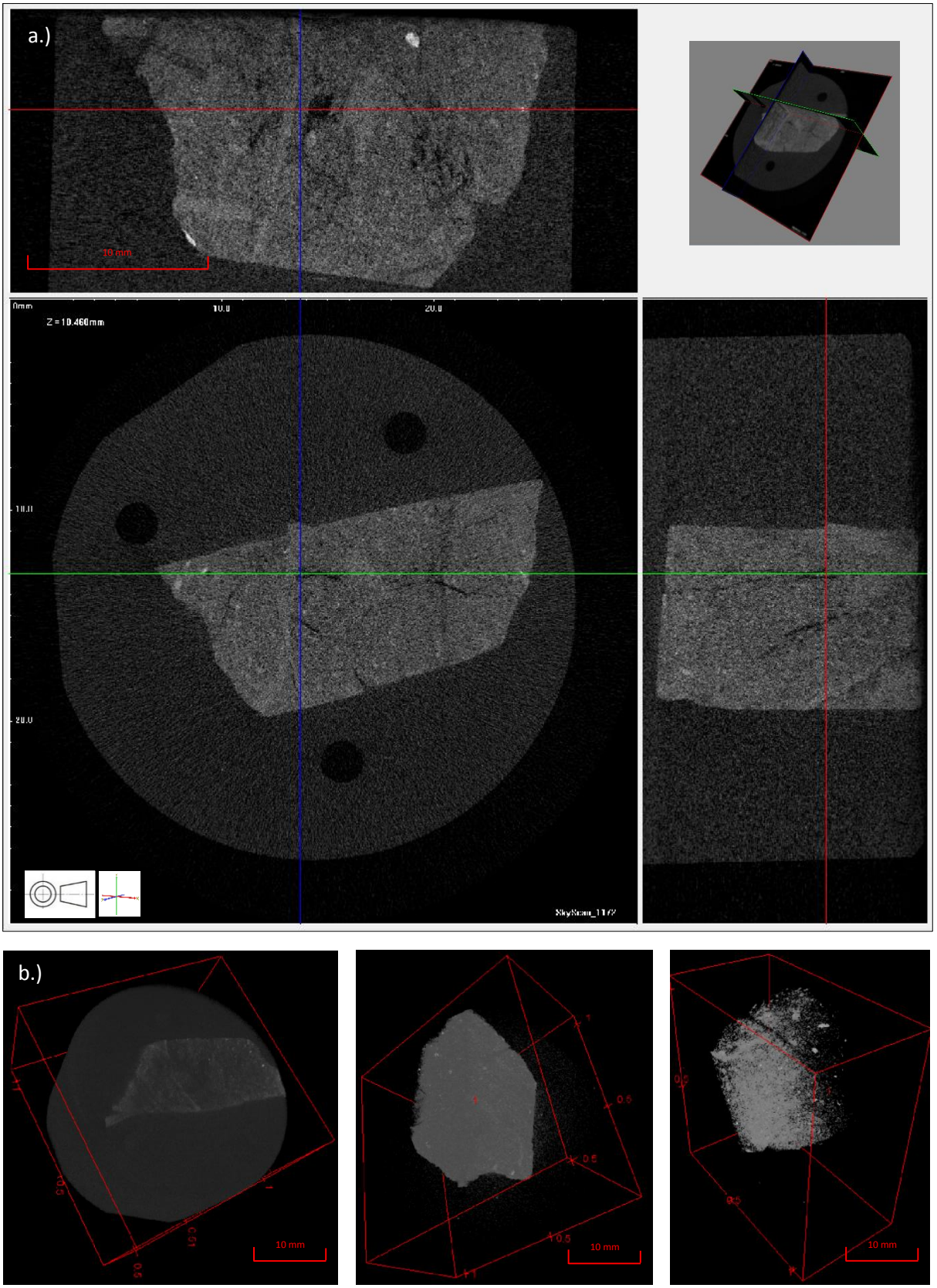

Figure 3.8 a.) Original colour orthographic projection of the µCT (lower resolution) scan for the briquette, the calcite fracture appeared lighter in the scans, insert is the sample viewed in 3-D along the plans. In this scan the damage cracks can be clearly seen. b.) Various orientations of the solid 3-D model showing the structure of the fracture and the position of the sample in the briquette (colour threshold has been reduced left to right).

The crushed zones were localised in areas throughout the sample especially near the base and to one end of the sample. The central section of the fracture was increasingly damaged with depth which resulted in poor EBSD indexing as can be seen in the final few slices.

The damage caused during the preparation procedure resulted in issues with the polishing process, which in turn resulted in decreased quality of the surface available for imaging due to grain plucking and the creation of surface topography (clearly visible in backscatter images). This surface damage reduced the quality of the EBSD phase indexing for areas of the sealed fracture where individual grains could not be distinguished on the polished surface, especially along the centre portion of the fracture (Figure 3.9).

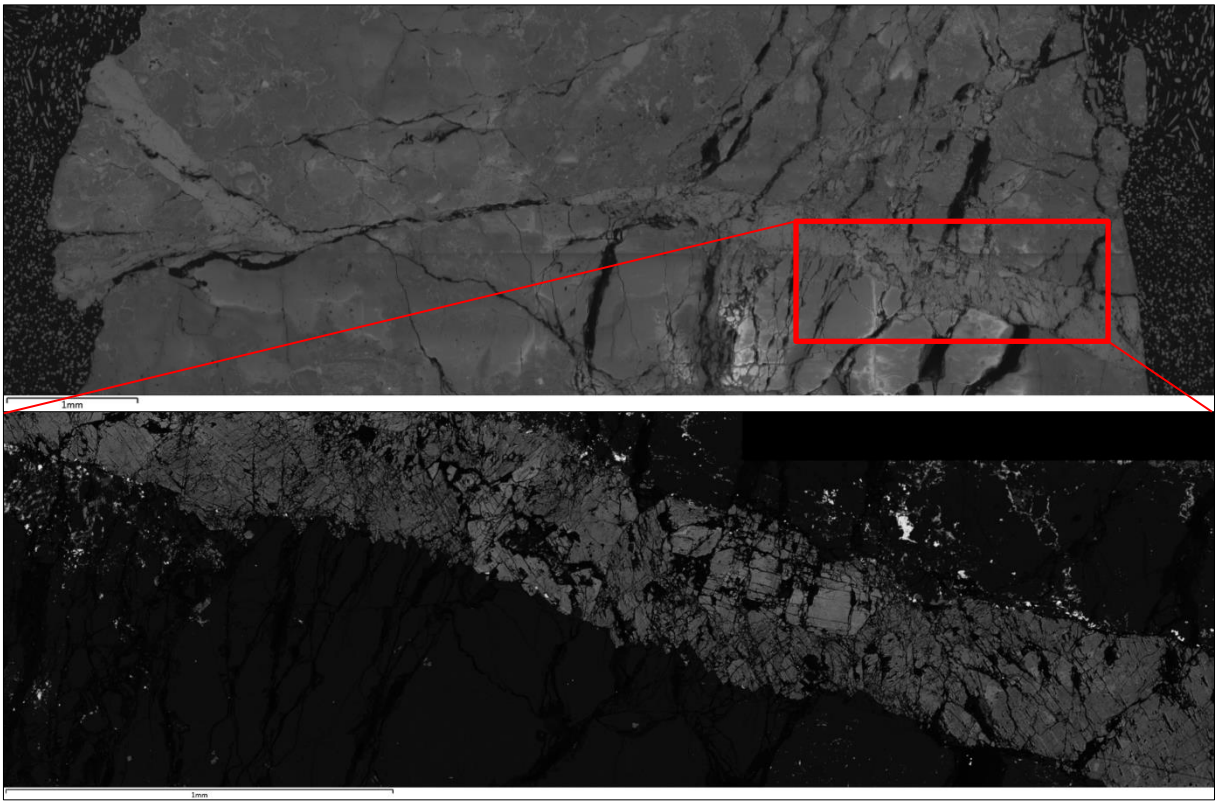

Figure 3.9 Electron images displaying examples of damage seen in slice 2. This shows both crushed zones, pitting and major cracks bisecting the fracture along with distorted and fragmented grains. This reduced the ability to index the calcite grains during EBSD. Further examples of damage can be seen in Appendices 3, 5, 6, and 7.

3.3.2 Elemental Energy Dispersive X-Ray (EDX) Point Maps and Cathodoluminescence (CL) Imagery

The combination of CL and EDX mapping provides an understanding of the variation in mineralisation composition as it changes in the z-direction of the briquette. As explained in Chapter 2 the CL and EDX images provide an insight into the elemental distribution within the

bladed calcite in addition to any other stages of sealing mineralisation present. The supplementary EDX elemental point maps and CL images for the particular sliced surfaces are located in Appendix 5 and 6 respectively.

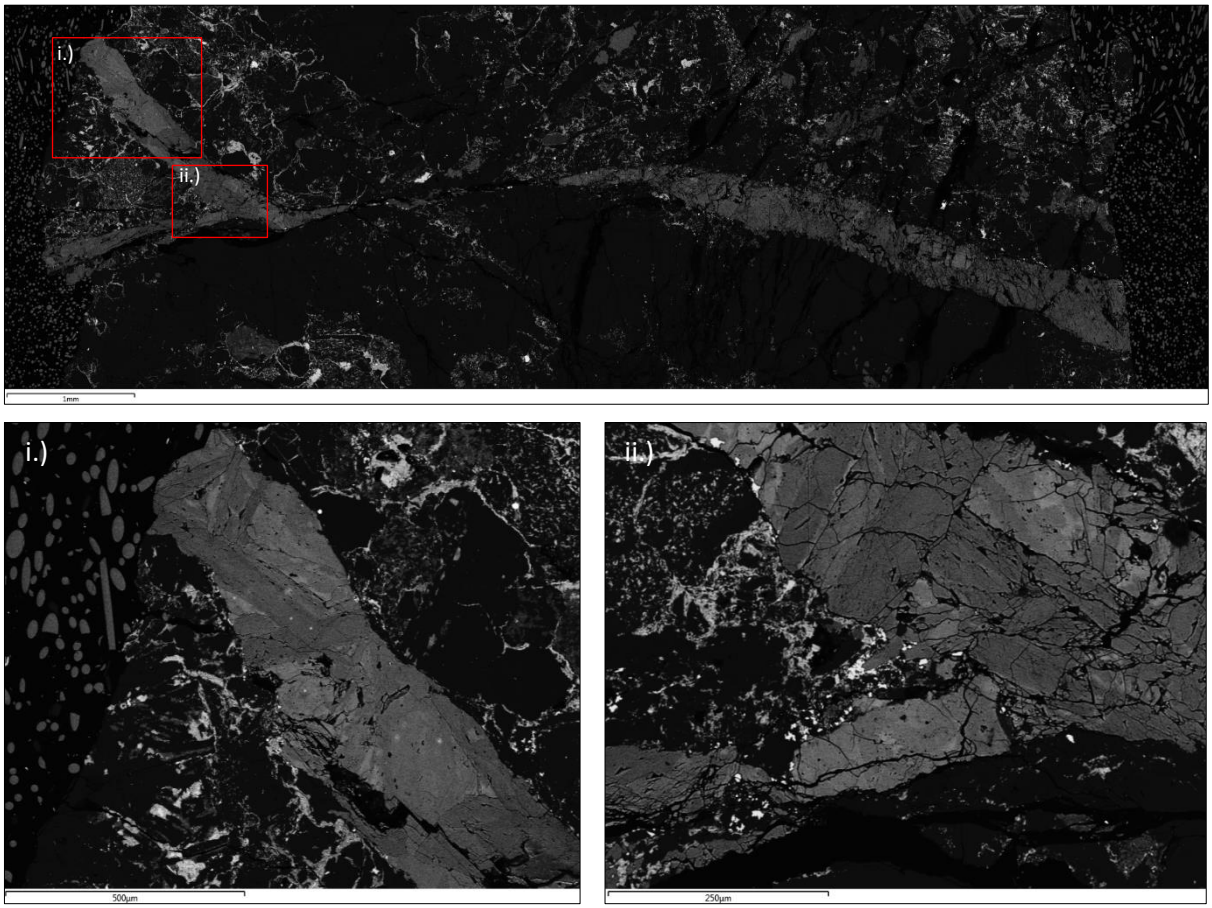

Figure 3.10 SEM Back scatter images (slice 2) displaying the elemental zoning observed in the bladed calcite. Light grey represents higher concentrations of Mn in the calcite and darker grey regions indicate higher Fe contents.

The concentric chemical patterns in the calcite crystals were only weakly imaged in the SEM back scatter images, especially the Mn signal (Figure 3.10). Both phases of calcite sealing mineralisation previously observed in this region of the geothermal field (in Chapter 2) were able to be identified using both the CL imagery and EDX maps. The extents of wairakite and calcite mineralisation was identified by overlaying the Si, Al, and O EDX point maps with Ca due to the difference in chemical composition of wairakite and calcite. The calcite associated with the wairakite in the adjacent fracture appeared to occur as void filling and replacement growth within the wairakite mineralisation (Figure 3.11).

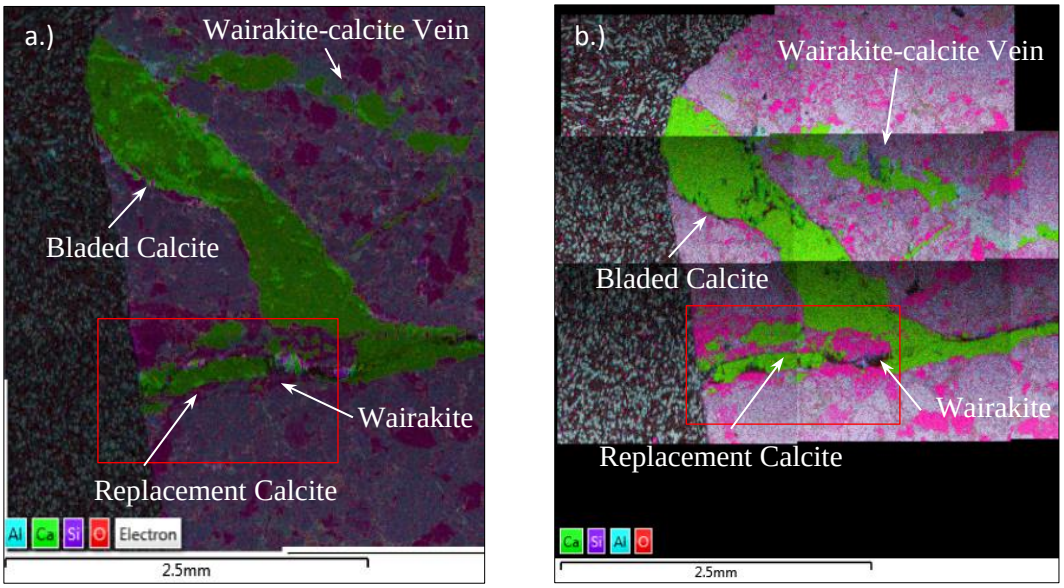

Figure 3.11 EDX layered elemental count maps of slice 6 (a.) and slice 7 (b.) which show the interaction between the two phases of calcite. Insert shows area of possible reactivation or void filling of the younger phase of mineralisation.

In the CL images, different phases of calcite precipitation are clearly distinguishable as seen in the previous Chapter. Figure 3.12 shows calcite in the younger fracture generations having brighter (more yellow in colour) CL colours, while the calcite in the older fracture generation has duller CL colours (more red in colour). CL images also indicate that certain areas (lower left limb) of the main horizontal fracture have wairakite sealing with possible reactivation or void filling by the younger bladed calcite (Figure 3.12). Chemical zonation for Fe and Mn in calcite crystals are visible in CL and appeared more pronounced in the younger generation of calcite sealing then the older generation.

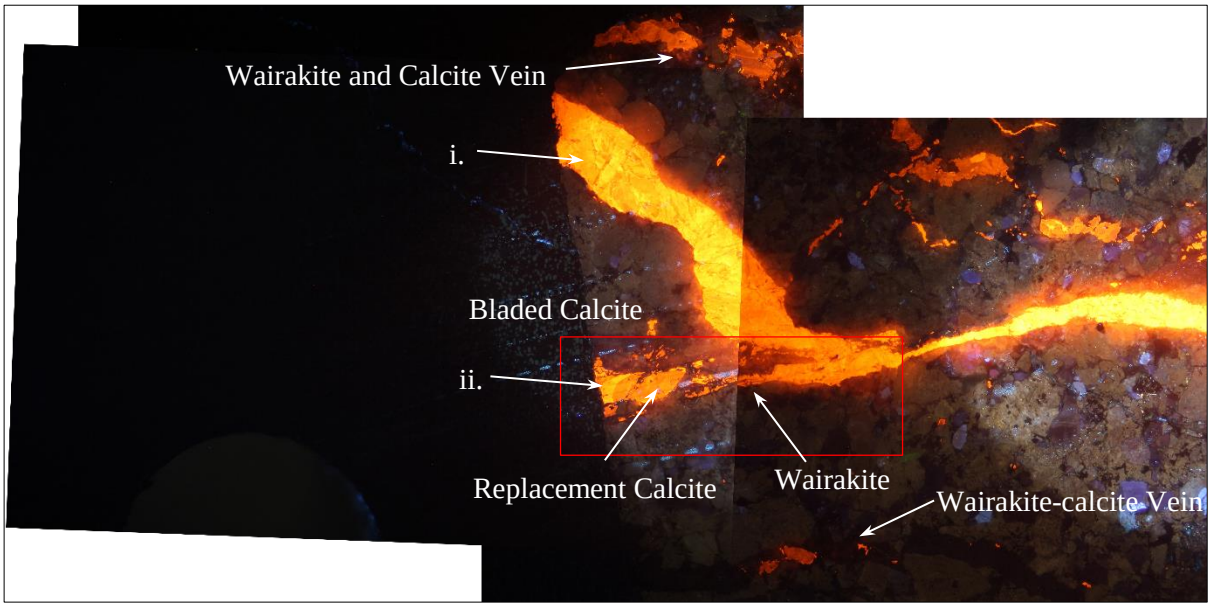

Figure 3.12 CL image of the left limb of the fracture (slice 5), the 2 phases of calcite can be clearly seen in the brightness contrast of both fractures. Insert shows the possible reactivation or void filling can be seen in the lower left of the limb. The wairakite-calcite in the top adjacent fracture contains calcite with a replacement texture. In addition several grains appear to have darker (higher Fe content) cores i and ii.

3.3.3 2-D Surface Preparation and Electron Backscatter Diffraction (EBSD) Results

Table 3.1 contains a description of each sectioned surface that was investigated using EBSD, including surface appearance, damage, measurement parameters of the slice, and information on the polishing process.

Table 3.1 Slice data and surface description.

Slice Nº.	Approximate Slice Separation Measurement (µm)	Surface Damage	Additional Information
1	0	None visible	Partial right limb showing only.
2	170	Present	Whole vein imaged
3	100	Present	
4	>100	Major cracks	
5	750	Major cracks and plucking	Required epoxy to set cracks and to be re-polished.
6	230	Major cracks	Surface required a better polish.
7	14	Mid-region crushed	Poor indexing across the sample with no indexed grains in mid region.
8	70	Major cracks plus mid region crushed	Prepared but not scanned.

The 2-D EBSD maps reflect what was observed in the 2-D EBSD results discussed in Chapter 2. For comparison a full set of EBSD maps for all sectioned surfaces are located in Appendix 7. Bladed calcite in the main fracture is comprised of large, elongate crystals that appear to have grown in an interlocking fashion both within free space and from the fracture walls (Figure 3.12). Calcite precipitation in the adjacent fracture occurred either as replacement growth of the wairakite or grew from fracture walls after the wairakite sealed fracture was reactivated (Figure 3.12). Figure 3.13 shows calcite crystals of slice 1 which appear to have grown across the fracture in a preferred direction (bottom to top). The calcite grains in slice 1 and a sub-set of grains in the right limb of the main fracture (slices 2, 3, 4, and 5) also show multiple e-twins. The calcite within the centre of the adjacent wairakite sealed fracture also exhibits e-twins.

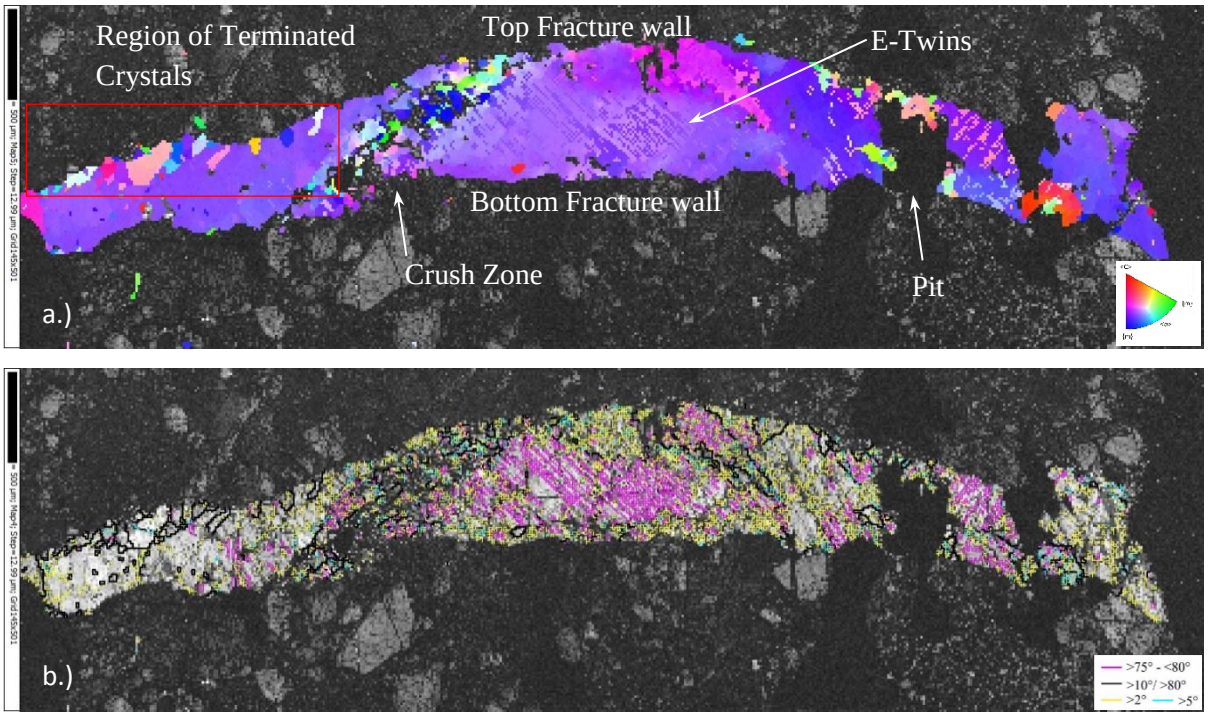

Figure 3.13 EBSD, IPF colour (a.), and grain boundary (b.) from the initial surface shows several major calcite crystals preferentially orientated (purple), insert area shows terminated crystal growth for grains orientated differently. Shown also is the crystal damage which indicates the difficulties correlating orientations across the grains. Colour represented by IPF in the z-direction.

Calcite crystal damage increased with each sectioning in the z-direction especially along the central section of the fracture. This resulted in poor EBSD indexing of the calcite on each sequential image slice.

3.3.4 The 3-D Electron Backscatter Diffraction (EBSD) Model

Figure 3.14 shows the EBSD maps of each of the 2-D sample slices as an image stack that the 3-D volume can be generated from. The final reconstructed model of the sealed fracture contains EBSD scans of each of the 7 slices, which provides data in the z-direction for approximately 1.5 mm. From this a reconstructed volume of approximately 15 mm^3 of the fractured sample is produced. The 3-D representations of the fractured sample were made using Leapfrog, a geological 3-D mapping software. This software was useful as the x-y-z referenced images could be imported as 2-D surfaces and separated by the distance between each section. For visualisation purposes the separation distance in the z-axis has been exaggerated by an arbitrary factor to display all steps between surfaces for both the image stack and the 3-D volume.

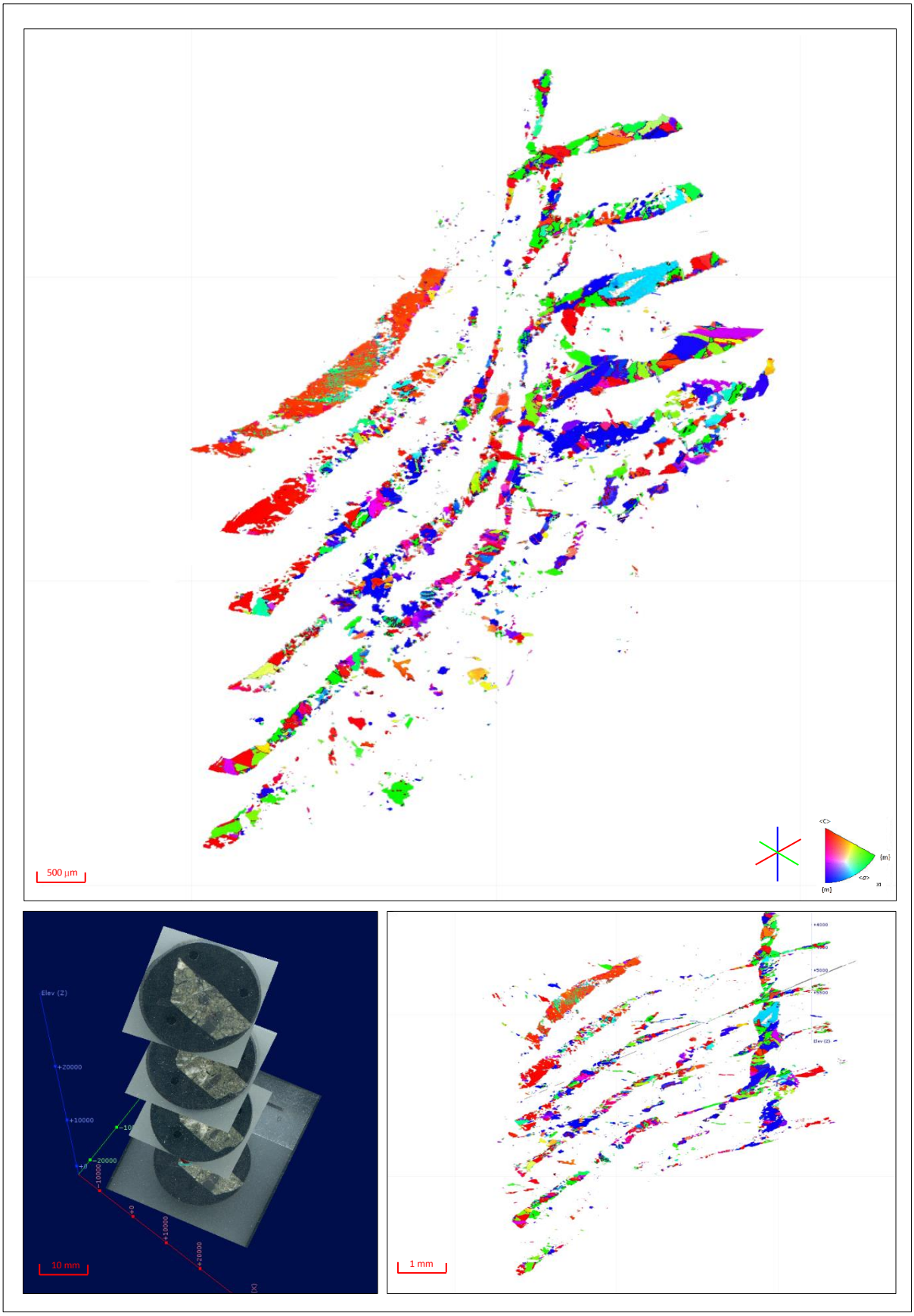

Figure 3.14 The resulting image stack of the EBSD slices using IPF x colours and surface scans loaded into the x-y-z reference frame by Leapfrog. Note that the vertical scale has been exaggerated to separate the slices.

The final 3-D representation of the entire fracture is shown in Figure 3.15. This model shows the 3-D structure of the fractures in conjunction with the 2-D EBSD surfaces. Mineralisation of the fracture can be divided into 3 separate types of fracture sealing phases depending on the morphology of the minerals. The main fracture (the blue and red plane in Figure 3.15) is comprised of both bladed calcite and blocky twinned calcite crystals. The bladed calcite is dominant to the left-hand side of the fracture in Figure 3.15 whereas the right hand side of the fracture is dominated by blocky calcite crystals. There was no clear boundary between these two zones of calcite morphologies along the centre of the fracture due to the poor indexing and damage in the sample.

The second type of sealing mineralisation is the lower limb of the left side of the sample (Figure 3.11 and 3.15). The mineralogical texture visible in this fracture limb suggests initial sealing by wairakite, followed by further calcite sealing. The calcite decreases with depth in the z-direction within this limb of the fracture.

The oldest recognised stage of fracture sealing (the yellow plane in Figure 3.15) comprises both wairakite and calcite deposition with blocky calcite occurring along the centre of the fracture with wairakite mineralisation on the fracture walls. This likely represents two phases of deposition, initial wairakite, followed by re-opening of the fracture and then calcite precipitation.

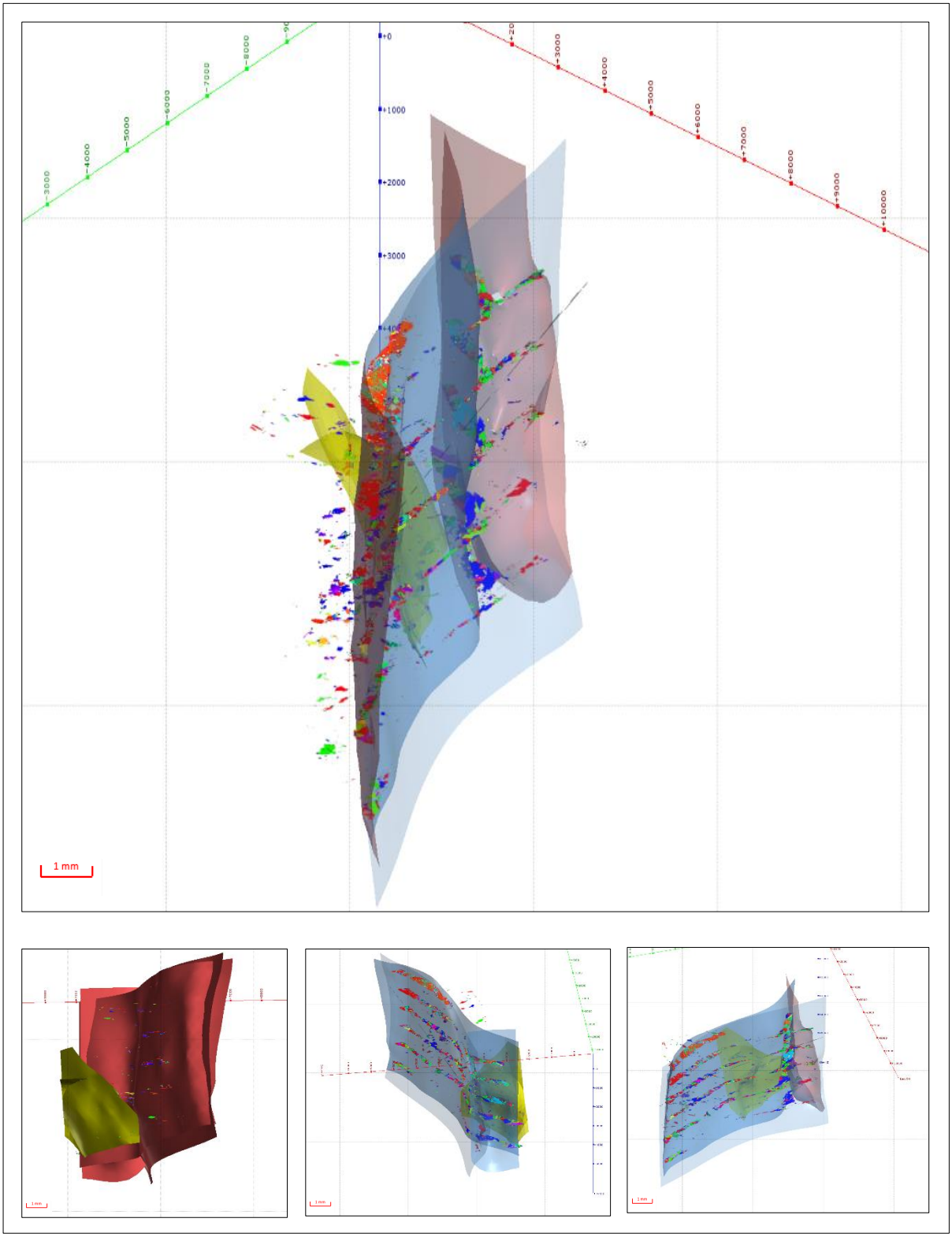

Figure 3.15 3-D volume of the fractures re-created from the image stack. The younger calcite fracture is represented by blue and red sided surfaces and the wairakite-calcite fracture is represented by the intersecting yellow volume. The EBSD surfaces are represented in IPF x-direction. Note the arbitrary vertical exaggeration in the z-axis to separate the sectioned slices.

3.4 Discussion

3.4.1 The 3-D Model

The final 3-D representation is a combination of 2-D EBSD surfaces and solid volumes that represent the separate phases of mineralisation. By adding an extra dimension to the 2-D analysis of the calcite mineralisation several of the conclusions can be explored further with the additional information. The same crystal morphologies, sealing mechanisms and interactions identified in the thin section can be seen in the 3-D model.

The bladed calcite has a distinctive appearance, growing in a 3-D interlocking pattern with preferential crystal growth perpendicular to the calcite c-axis. Once the bladed crystals began to inhibit each other's growth in this direction further growth occurred parallel to the calcite c-axes, creating bulging crystal textures. Evidence of interlocking crystal growth in 3-D space can be seen in the bladed calcite. Slice 2 to 6 (See Appendix 7 for Figures) show the best occurrence of this phenomenon with grains able to be seen between surfaces. This interlocking growth feature could possibility be limited in the sectioned slices because the separation distances may be greater than the interlocking relationship.

Similar calcite crystal morphologies to the older calcite sealing phase identified in the 2-D EBSD analysis of Chapter 2 can be found in two regions of the 3-D fracture. The first example can be seen on slice 1 where the EBSD map shows up to 3 large crystals that all have a similar crystallographic orientation (Figure 3.13). These grains exhibit multiple e-twins and a continuous lattice distortion as discussed in Chapter 2. It can also be seen that the preferred crystal growth direction has inhibited the growth of multiple grains along the top of the fracture (Figure 3.13). This may indicate that as the fracture was sealed certain orientations of crystal growth were favoured over other calcite orientations that precipitated on the top fracture wall. These large grains are less apparent as you move along the z-direction, possibly allowing space for crystals that precipitated on the top of the fracture to grow (Figure 3.13). Due to preparation damage it is hard to correlate the microstructures observed on slice 1 through to deeper slices where it appears that there may be no preference to growth direction from either side of the fracture.

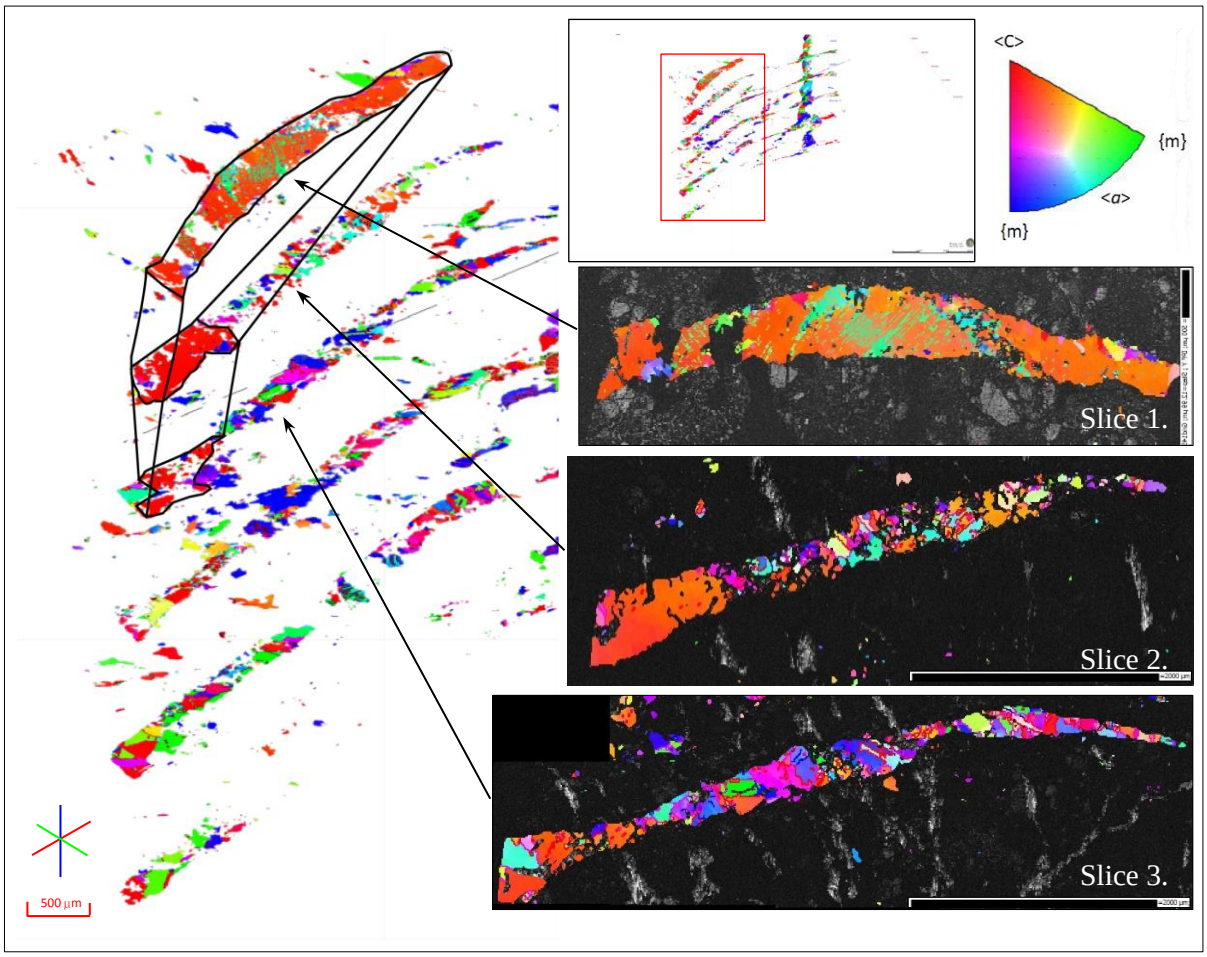

Figure 3.16 EBSD maps showing the transition from a dominate crystal orientation in slice 1 to a more randomly orientated crystal network with depth, all maps are IPF x. Note the arbitrary vertical exaggeration in the z-axis to separate the sectioned slices.

A second example of similar calcite crystal morphologies to the older calcite sealing phase of sealing identified in Chapter 2 can be seen in the adjacent wairakite and calcite sealed fracture that appears in the top left of the EBSD scan from slice 4 down. The calcite in this fracture has a replacement-reactivation texture and can be found substituting for the wairakite and filling voids. This is unlike the right limb of the fracture where wairakite is absent.

These two examples show there is a preferential syntaxial sealing mechanism occurring in the phases of calcite fracture sealing observed in this sample. This preferential form of crystal growth may be related to fluid composition and fracture size within the reservoir. This can be seen in 3-D with the occurrence of smaller fractures being preferentially sealed off to fluids by calcite mineralisation consisting of smaller grains and larger sections having elongated, interlocking crystals.

3.4.2 Serial Sectioning Method: Difficulties with Preparation, Scanning and Data Processing.

Throughout this stage of the study there were several issues encountered with the process of sample preparation and the method of creating the 3-D representation. The sample preparation for repeated serial sectioning was difficult initially due to the size of the sample of core fragment. Most studies that attempt to characterise EBSD by 3-D analysis focus on a much smaller area (microns to nano-meters) (Liu et al., 2008; Mariani et al., 2008; Uchic, 2011). These previous studies were also carried out on simple materials (e.g. single phase metals), using carefully controlled slice distances, and are able to take advantage of the dedicated 3-D software such as Amira, Paraview, and ImageJ. Multiphase materials such as rock forming minerals require a dedicated process to be developed for scanning and 3-D modelling (Dingley and Randle, 1992). In addition carrying out 3-D EBSD in a dual beam SEM-FIB maintains equal x-y-z steps (i.e. step size = slice separation) (Uchic, 2011; Ratter 2012).

To overcome these implications a new approach needed to be developed for serial sectioning in order to investigate materials the size of the bladed calcite crystals (~0.5-2mm long) in our sample which also accounted for the complicated crystal structure of the various rock minerals. To capture the large range of grain sizes in the sample with each slice, an EBSD scanning step size of 10 μm was used with a slice separation measurement of approximately 100 μm. Since the step size and the surface separation were different by an order of magnitude it was difficult to transfer pixels into a 3-D volume element or voxel for 3-D analysis. In addition the method used for grinding and polishing resulted in a variation in slice distances which ranged from 750 μm to 14 μm.

Using the μCT-Scanner to determine the orientation of the internal structure for the fracture was crucial for developing a successful serial sectioning regime. The pre-scanning image analysis allowed targeted serial sectioning to be carried out with little variation of the fracture orientation. This outcome reduced SEM scan time which was a limiting factor for the EBSD scanning resolution that could be achieved.

The manual process of serial sectioning also created undesirable damage which was compounded with the preparing of each sequential surface for EBSD mapping. The process of mounting the sample in a powered carbonite briquette had the biggest impact on the surface EBSD results. Even though the briquette retained the sample in one piece the subsequent

damage to the calcite crystals in the fracture lead to issues with surface polishing and EBSD indexing. The ability to index calcite crystals for EBSD decreased with each step in the z-direction with the final slices having very poor calcite indexing across the entire fracture. The μCT-Scan was successful in identifying the extent of calcite crystal damage present prior to each serial sectioning stage.

Due to the destructive nature of serial sectioning sample surface damage occurred as each section was removed. This process not only removes the previously scanned area it also induced damage on the new surface before EBSD mapping, a phenomenon also reported in other studies attempting this process (Uchic, 2011; Ratter, 2012; Baris, 2014). Surface damage was repeatedly experienced during the polishing of the new surfaces with plucking of grains a common occurrence. This surface damage was undoubtedly intensified due to the fact that the sample had experienced internal damage during the mounting which was only added to with each sectioning phase.

It must also be noted that the reliability of the spread of size grains identified is restricted due to the disparity between sectioning step size and the smallest grain size able to be measured (Uchic, 2011). This means that crystal grains that are less than the separation distance may be overlooked if they occur between the sliced surfaces or if minimal intersection occurs (Uchic, 2011; Baris, 2014). Other 3-D serial sectioning studies that use this technique still document a minimal reconstructed volume (Baris, 2014).

The size of the EBSD scans of the mineralised fracture generated a contrast intensity across the SEM operational window. This was due to the distance variation between the detector and the sample resulting in a scatter of excited ions resulting in a drop in signal intensity as the sample traversed down the automated area.

The time investment in preparing and analysing each individual slice for 3-D EBSD reconstruction is high. This is primarily due to manual surface preparation and the processing time of data for each additional sectioned surface. Conversely due to scanning optimisation undertaken early on in the project, sample selection, and alignment, the data acquisition was relatively efficient for a project of this size and nature. Although the procedure of EBSD scanning was made more time efficient, only a limited number of surface slices were completed within the timeframe available.

3.5 Conclusion

In this chapter we have presented the technique of microstructural characterisation for a large calcite sealed fracture in 3-D space using serial sectioning. Using EBSD and selected elemental maps of progressive slices of a calcite sealed fracture we are able to gain an insight into the 3-D crystallography of bladed calcite as well as the potential mechanisms of fracture sealing that occurred. Our findings are summarised below:

- The 3-D EBSD and chemical evaluation of the sealing phases present within this fracture sample are consistent with that observed in Chapter 2 and in previous studies at Kawerau. The interaction between the generations of fracture sealing events is varied across the fracture which builds from the initial conclusion. The various stages of mineralisation present are characterised by preferred modes of crystal growth as identified in Chapter 2. The older phase of calcite fracture sealing, which shows mainly blocky crystal forms grew syntaxiatlly across the fracture with a preferred direction in areas of the fracture, whereas, younger bladed calcite grew in an 3-D interlocking manner in free-space.
- The generation of a specific serial sectioning process that we have developed in this study demonstrates the need for a well thought out step by step process which is essential for 3-D EBSD. This includes sample selection and SEM scanning optimisation. As this study shows immense care must be taken in sample and surface preparation including slice separation distance, which needs to be well constrained for 3-D reconstruction. If the sample is to be encased in a briquette caution must be taken during the mounting process as not to induce internal damage. In addition developing an image stack that can be imported into a dedicated 3-D modelling software is necessary to successfully create grain volumes.
- Using a reconstructed 3-D EBSD model to better evaluating fracture sealing mechanisms for geothermally precipitated calcite can be a useful tool. However, there is a payoff with information gained through destroying the sample by serial sectioning and the time required for preparation and image analysis.
- Time requirements of such an analysis on this scale with the manual processing time that was required throughout leads to the recommendation of the use and development of an automated serial sectioning and computational process which is a balance of signal resolution and required time. In other words a smaller section may provide a

higher image resolution for grain growth orientation and boundary interaction but may overlook critical interactions between various stages of mineralisation on a grander scale as seen in this brief investigation.

Chapter 4

Evolution of Fracture Sealing Processes, Kawerau Geothermal Field, Taupo Volcanic Zone (TVZ), NZ: U-Series Dating of Calcite Filled Fractures

A. J. Lister[1], J. M Palin[1], D. J. Prior[1] & D. D. McNamara[2]

[1] *The Department of Geology, University of Otago, Dunedin, New Zealand*

[2] *GNS Science, Lower Hutt, New Zealand*

Abstract

A key element in the optimal utilisation of any active geothermal system is an accurate understanding of their geological and structural evolution over time. Field development and heat extraction is dependent on the understanding of fluid flow and migration, of which fracture sealing is an important control. Therefore, it is essential to be able to accurately predict not only the spatial extent of sealing but also the temporal changes overtime.

The Kawerau Geothermal is one of the longest-lived active geothermal systems in the Taupo Volcanic Zone (TVZ) and has undergone extensive exploration and development as an energy source. We present here an attempt to better constrain the age of geothermal activity at Kawerau using Uranium-series (U-Series) disequilibrium analysis to date mineralised carbonate fractures identified within the reservoir.

The main outcome of this study is that in-situ Laser Ablation Inductively Coupled Plasma Mass Spectrometry (LA-ICP-MS) has the potential to date carbonate veins where an adequate level of Th and U is measured. Additional processes may be required to provide accurate ages for calcite sealing events with insufficient U or elevated Th levels. Both a positive and a negative Eu anomaly were also identified for the range of calcite grains that were analysed. This indicates that the fluids that the bladed calcite precipitated from had undergone a complex flow history within the reservoir. Even though we were unable to successfully date the bladed calcite we have proposed a chronological link of the various phases of sealing mineralisation observed with previous studies.

4.1 Introduction

The Kawerau Geothermal Field is the northern-most active, high temperature (>300°C) geothermal field of the Taupo Volcanic Zone (TVZ) and is one of the longest-lived active geothermal systems associated with the modern TVZ (Milicich et al., 2013; Wilson et al., 2015). Therefore it is an ideal field to attempt to refine the geological timeline for geothermal activity using uranium-series (U-Series) disequilibrium analysis by Laser Ablation Inductively Coupled Plasma Mass Spectrometry (LA-ICP-MS) on fracture sealing mineralisation. By constraining the timing of geothermal activity, a better understanding can be developed of the relationships of the multiple fracture sealing events and the migration of heated fluids from the heat source evident at Kawerau.

The Kawerau geothermal field has been the basis for several attempts to outline the age of geothermal activity present in the region, however, these are based on stratigraphic relationships of formations and only present minimum ages of activity (Browne, 1979; Absar and Blattner, 1985; Christenson, 1987; Milicich et al., 2013). In addition, several studies have been carried out to better characterise the geochemical and isotopic signature of the rock and fluids at Kawerau (Absar and Blattner, 1985; Christenson, 1987). Kawerau is a field that has experienced several recognised periods of large scale carbonate sealing within the reservoir which has caused a zone of low permeability in the south of the field (Milicich and Bignal 2012). Wells in the south of the field close to the identified heat source have recorded extensive mineralisation, minimal permeability, and some of the highest measured temperatures within the TVZ (e.g. KA34 with measured temperatures up to 350°C) (Milicich and Bignal 2012). This lack of production permeability in the south has led to production wells targeting heated fluids in more permeable zones in the central region or relying on intersecting permeable faults and fractures (Wallis et al., 2012).

Various methods have been previously employed to date active geothermal systems in the TVZ and around the world. A brief summary of current dating techniques that have been employed for fields in the TVZ are located in Table 4.1. Each method is able to date a certain feature or aspect of the geothermal system and can be used in combination with other techniques to provide an age to a field. This table is by no means complete and only provides a brief insight into the diverse range of techniques that have been employed to date geothermal activity within the TVZ. There has been some work undertaken to attempt to date fracture sealing within other geothermal fields of the TVZ with varied levels of success (Grimes et al., 1998; Bignall et al.,

2010; Milicich et al., 2013; Wilson et al., 2015). Additionally, a number of fracture sealing events have been successfully dated around the world including Turkey (Unal-Imer et al., 2014) and in America (Sturchio and Binz, 1988).

Table 4.1 A summary of several methods currently employed for dating geothermal activity in the TVZ (Modified from Grimes et al., 1998 and Wilson et al., 2015).

Method	**Method of Dating**	**Requirements and Limitations**	**Fields Where This Has Been Used**	**References**
Zircon (U-Series)	U-Pb	Requires the occurrence of zircon crystals	Kawerau (NZ), Ngatamariki (NZ), Mangakino (NZ), Wairakei (NZ)	Eastwood et al., 2013; Milicich et al. 2013; Wilson et al., 2015; Chambefort et al 2014
Zircons and amphiboles (Ar accumulation)	$^{40}Ar/^{39}Ar$ or K-Ar	Requires the occurrence of zircon/amphibole crystals	Ngatamariki (NZ)	Arehart et al., 2002
Carbonate (U-Series)	U-Th	Accurate and well defined U-Th ratios required	Tauhara (NZ)	Grimes et al., 1998
Hydrothermal eruptions	Identified altered eruption breccia and ^{14}C dating	Requires the presence of organics and/or Eruption lithics.	Kawerau (NZ), Waiotapu (NZ),	Browne, 1979; Nain and Wiradiradja, 1980; Hedenquist and Henley, 1985; Christenson, 1987, 1997
Mineralisation and alteration rates	Calculated extents of these processes	Alteration rates need to be known.	Tauhara (NZ), Kawerau (NZ)	Kakimoto,1983; Absar, 1988
Subsidence rates			Wairakei (NZ)	Grindley, 1965
Geological sequences	Law of superposition (often linked to $^{40}Ar/^{39}Ar$, K-Ar and U-Pb ages for dateable formations)	Datable and recognisable marker layers (lava flows and pyroclastic layers etc.)	Kawerau (NZ)	Absar and Blatten, 1985; Wilson et al., 2015

NB: This table is by no means complete and only provides a brief insight into the diverse range of techniques that have been employed to date geothermal activity within the TVZ and around the world.

This study presents the LA-ICP-MS analysis of several mineralised veins located within the reservoir, focusing on the final bladed calcite phase and its relationship with previous stages of fracture sealing. The LA-ICP-MS analysis that is used for The U-Series analysis also generates a range of major and trace element geochemical analyses that will also be discussed here. This study will attempt to date the bladed calcite as well as build on previous works to develop a greater understanding of the chronology of geothermal activity at Kawerau. In this section we aim to address the following 3 questions:

1. Is it possible using in-situ laser ablation and U-Series dating to provide an age for the bladed calcite mineralisation?
2. What is the geochemical and isotopic distribution spatially within the bladed calcite and if possible, the other phases of carbonate mineralisation?
3. Can we refine the age model of hydrothermal activity at Kawerau by chronologically ordering the mineralisation episodes of identified sealing events, with ages where possible?

4.1.1 Age of Geothermal Activity at Kawerau

Browne (1979) has previously determined that the minimum age of activity at The Kawerau Geothermal Field is 200,000 ± 30,000 years using ^{14}C dating of hydrothermally altered eruption fragments found in the Matahina Ignimbrite. Further analysis of the Matahina Ignimbrite by Bailey and Carr (1994) redefined the age of this formation to be 322,000 ± 7,000 years old. Christenson (1987) postulates the age of geothermal activity at Kawerau could extend to be at least 400,000 years, using stratigraphic and petrographic observations from the eastern side of the field. At least two other episodes of recent hydrothermal eruptions have been identified with eruption deposits located near the surface along the south eastern margin of the field (Christenson, 1987, 1997; Milicich and Bignall, 2012). These deposits have been dated at 14,500 and 9,000 ya and include hydrofractured clasts with evidence of repeated multiple fracturing and sealing episodes (Nairn and Wiradiradja, 1980). In addition, Milicich et al. (2013) has carried out extensive U-Pb dating of zircons from altered volcanic units identified at depth, these new ages and stratigraphic interpretations are summarised and presented in Figure 4.1.

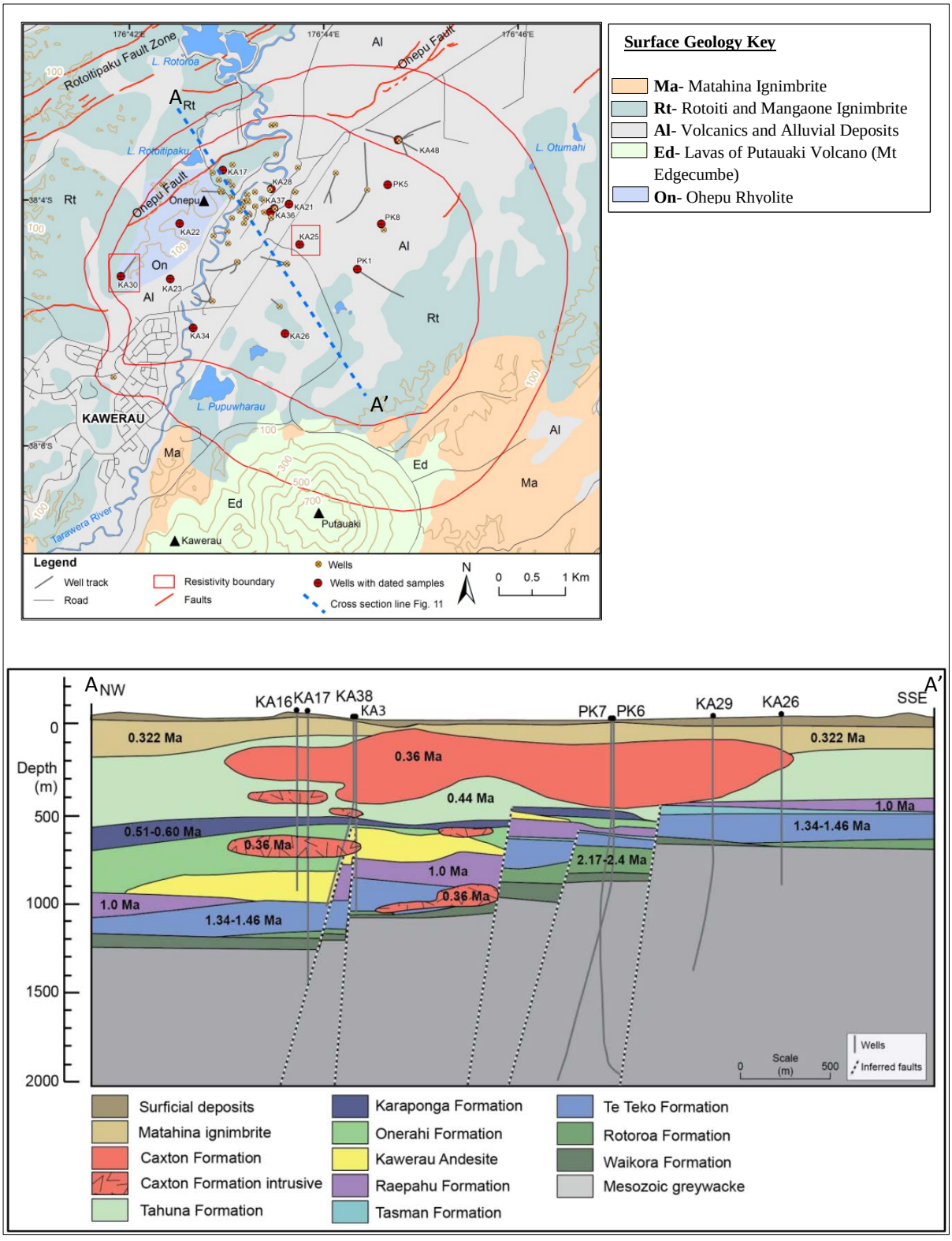

Figure 4.1 Cross section A-A' across the Kawerau Geothermal Field with the ages of the major formations identified with the new stratigraphic interpretation, ages are from Milicich et al. (2013) and Leonard et al. (2010). Insert displays the locations of wellbores, active faults, and simplified surface geology at Kawerau, highlighted are the wells KA25 which has been previously dated by Browne (1978) and KA30 which is the main focus of this study. (Image modified from Milicich et al., 2013 and Wilson et al., 2015).

Several previous studies (Nairn and Wiradadja, 1980; Absar and Blattner, 1985: Absar 1986; Christenson, 1987, 1997) have attributed periods of alteration mineralisation with influxes of geothermal fluids and gasses related to impulses of volcanic and plutonic activity within the region (Figure 4.1). All of these studies aid in establishing the tectono-magmatic evolution of the field while providing limited information on ages of hydrothermal activity (Milicich et al., 2013; Wilson 2015).

4.1.2 U-Series Dating Principals

U-Series dating is a powerful tool for dating the time of formation of a variety of geological materials (Ludwig and Titterington, 1994). This method has the potential to accurately date young events up to a limit of 500,000 years (Turner et al., 2001; Eggins et al., 2005). Both silicate and carbonate materials younger than 35 ka have been dated with varying degrees of accuracy using this method (Schwarcz and Latham, 1989; Turner et. al, 2000; Geyh, 2001). The ability of calcite to incorporate U relies on a complex combination of pH and the concentrations of both CO_2 and U present (Moyes et al., 2000). Under certain conditions U is weakly absorbed as a monolayer within the crystal structure, while in other environments it can precipitate on the calcite surface or as coupled substitution (Moyes et al., 2000). The method of U-Series for dating a mineral is based on the generation of radiogenic Th from the decay of U with the measured Th relating to the age of the material (Geyh, 2001).

Two assumptions underpin accurate U-Series disequilibrium dating (Geyth. 2001):

1.) The material is free of initial Th immediately after formation.
2.) The material in question can be classified as a closed system since formation.

There are two key considerations when applying this method to dating fracture sealing mineralisation that impinge on these assumptions.

Firstly many naturally formed carbonate minerals especially geothermal precipitated calcite entrain minute amounts of detrital material, generally in the form of silicic inclusions (Schwarcz and Latham, 1989). This differs from the ideal U-Series system as many studies have shown that detrital material can contribute varying levels of U and Th during the ablation process (Schwarcz and Latham, 1989; Geyh, 2001). This additional U and Th can range from negligible to excessive amounts depending on the nature of the material's crystallisation (Geyh, 2001).

Secondly the boiling environment that precipitates calcite in the bladed form in open fracture space due to the loss of carbon dioxide can occur very rapidly (Tulloch, 1982; Simmons and Christenson, 1994). In addition, the diffusivity of both Th and U in carbonates is very slow due to their elemental size. Therefore, the bladed carbonate in this case can be thought of as a closed system that records the geochemical signature at the time of precipitation.

If significant Th is present in the material that is being analysed, an adjustment for the U-Th relationship must be incorporated into the dating process (Ludwig and Titterington, 1994). There have been numerous studies to quantify the effectiveness of this method to date carbonates with extensive levels of Th from silicate inclusions or "dirty calcite" (Schwarcz and Latham, 1989; Ludwig and Titterington, 1994).

Grimes et al., (1998) was the first to use the U-Th disequilibrium method to date hydrothermal activity for a geothermal system in the TVZ. This study utilised calcite veins in drill core from the Tauhara Geothermal Field to date the mineralisation activity to 99,000 ± 44,000 years old, much younger than the accepted age of the field of 200,000 years (Kakimoto, 1983; Grimes et al., 1998). The isotope measurements of the vein calcite were carried out by mass spectrometer on hand picked separates that had undergone an acid leaching process refined by Bischoff and Fitzpatrick (1991) (Grimes et al., 1998). Grimes et al. (1998) highlights the difficulties of using individual samples due to the contamination of detrital silicate material which can be minimised by using the leachate isochron method of Schwarcz and Latham (1989). This study also recommends varying the acid leach process used for the firing and weak acid leaching method to reduce the Th and U carryover.

The ICP-MS is ideal for the collection of U-Series isotope ratios in low-concentrations (<0.1 ppm) with close to 100% collection and ionisation of both Th and U by the plasma beam (Turner et al., 2001). Furthermore, using in-situ laser ablation has several advantages over conventional methods including rapid measurement and the ease of sample preparation removing the need for time consuming leachate and dissolution methods (Eggins et al., 2005). In-situ laser ablation also has the ability to provide continuous, high spatial resolution elemental and isotopic profiles along samples ideal for bladed calcite that display chemical zoning (Eggins et al., 2005). Provided the U-Th ratios are acceptable ICP-MS is a good method for dating geothermal carbonates in-situ while providing spatially accurate bulk geochemical analysis. This technique has the potential to greatly improve the understanding of the evolution

of geothermal activity for a field including; changes in fluid migration, major alteration events, periods of fracturing, and mineralised sealing episodes (Ku, 1976; Grimes et al., 1998).

4.2 Methodology

4.2.1 Sample Selection and Preparation

The basement greywacke was sampled from fragments of core from KA30 at a depth of 1213 mRF, as in the rest of this study. Samples of core that contained a variety of fracture sizes and vein interactions were selected. These fractures have previously been identified to be commonly filled with both calcite and wairakite, a Ca rich zeolite, which represent several stages of mineral deposition and fracture sealing within the greywacke hosted reservoir.

For this study we carried out two series of LA-ICP-MS analysis with the following samples:

1. The same thin section from the 2-D investigation (Chapter 2) underwent multiple in-situ track and spot analysis.
2. An in-situ laser ablation analysis was carried out on cut and polished surfaces of several rock core fragments.

The rock fragments for the second in-situ analyses were cut perpendicular to the main fractures of bladed calcite. This exposed a flat surface which was further polished using standard polishing techniques to provide a level surface free of relief for optimal analysis during laser ablation (Figure 4.2).

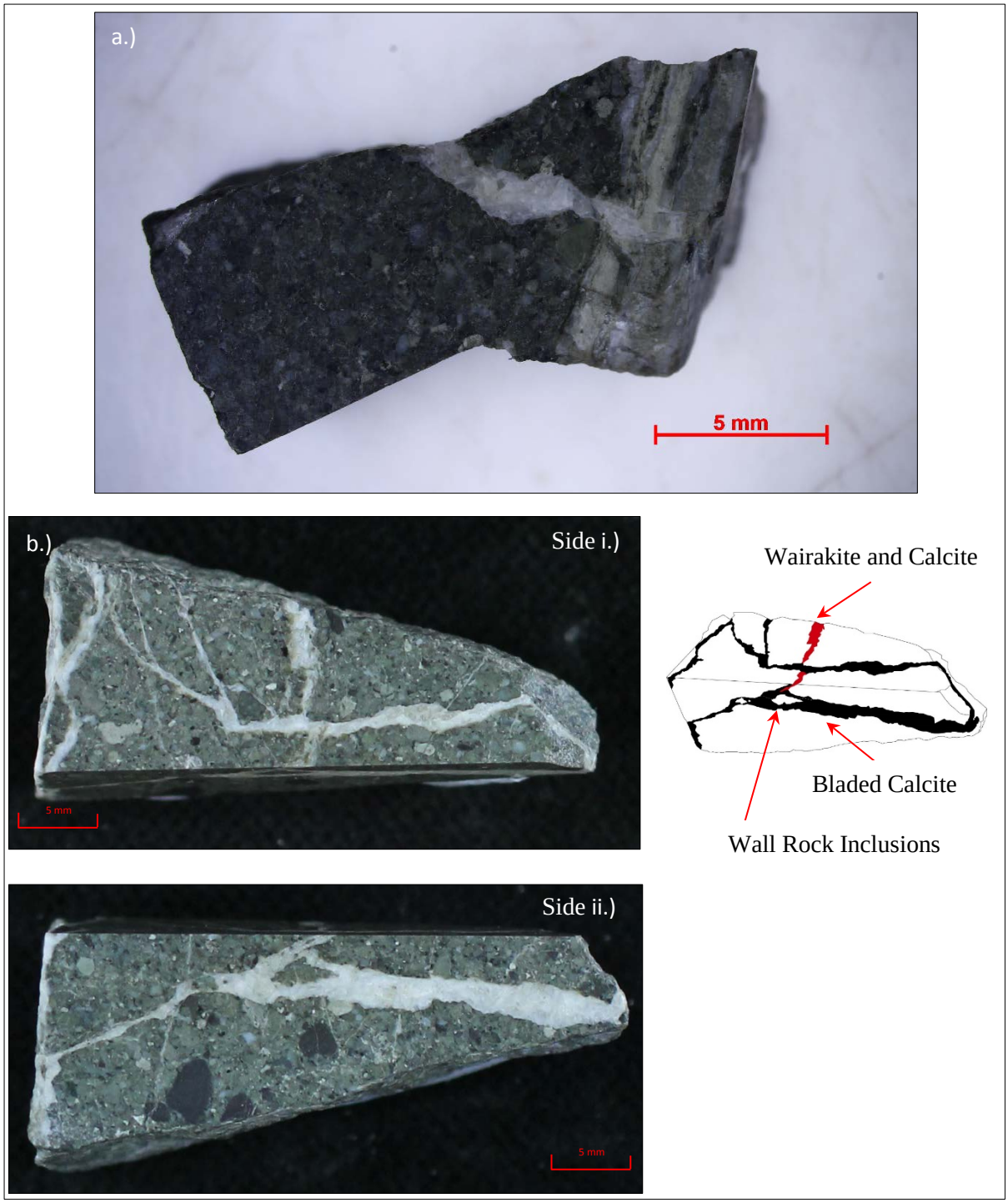

Figure 4.2 Photographs of the drill core sample fragments of greywacke reservoir rock from the Kawerau Geothermal Field used for the in-situ laser ablation geochemical analysis, a.) is sample A and b.) is sample B with sides i and ii shown.

4.2.2 Laser Ablation Inductively Coupled Plasma Mass Spectrometry (LA-ICP-MS)

The LA-ICP-MS isotopic and geochemical analysis was undertaken using the Resonetics RESOlution M-50-LR excimer (193 nm) laser ablation system at the Otago Community Trust Centre for Trace Element Analysis, located at the University of Otago, Dunedin, New Zealand.

Two series of in-situ analyses were carried out for this stage of the analysis to provide a comprehensive geochemical analysis of the bladed calcite crystals in the sealed fractures. The initial analysis was carried out using a thin sectioned sample from Chapter 2 to assess the suitability of this method for dating purposes. A series of tracks and spot analyses were evaluated. These were labelled TS-KA30-2, TS-KA30-3, TS-KA30-4 etc. to distinguish the thin section analysis from the core fragments, subsequently labelled KA30 A and KA30 B. The TS-KA30 analysis was dispersed evenly along the main bladed calcite fracture in a variety of crystal types (rims vs. cores and Fe enriched vs. Mn enriched zones). Figure 4.3 displays the location of laser spots and tracks with the respective laser variables and initial comments located in Appendix 8. Each location was pre-ablated to remove contaminates incorporated in handling and thin section preparation. It can also be noted the laser beam and pre-ablation variables were repeatedly adjusted to find a balance between gaining sufficient results and to prevent the laser hitting the underlying glass slide and epoxy.

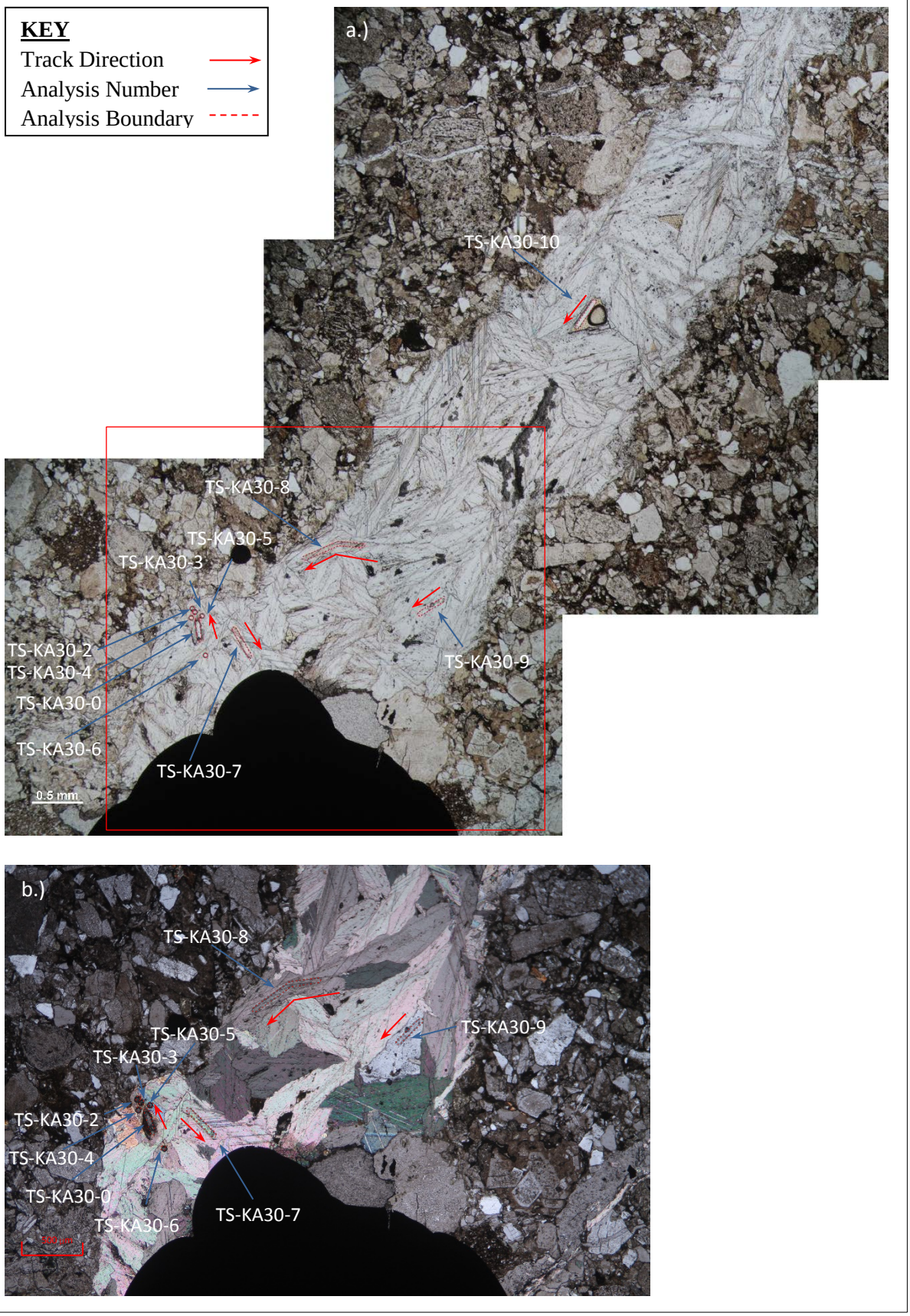

Figure 4.3 Location of laser ablation spot and track analyses carried out on the thin section including track direction. a.) is in plan polarised light (4x) with b.) the corresponding cross-polarised light image of the lower section of the fracture (insert).

The second isotopic analysis was carried out on several similar bladed calcite veins located in rock core fragments from the same depth. This in-situ testing was carried out to remove any possible interfering signals produced by thin section preparation and possible signatures from ablating the under laying glass slide. For each of the two veins (KA30 A and KA30 B) 3 locations with 3 (a, b, and c) tracks each were completed, the first track being the pre-ablation blast with 2 sequential tracks deeper into the sample (Figure 4.4). Consequently, a total of 18 tracks including pre-ablation tracks were carried out and analysed on the rock core fragments. Figure 4.5 and 4.6 display the locations of each analysis. The laser and track parameters for the in-situ testing were carried out utilising a laser spot size of Ø 75 µm and a frequency of 10 Hz that tracked at a speed of 10 μm^{-1} for 40 s to produce a track length of 400 µm, this remained constant for the total 18 tracks. Further information on laser parameters for both rock fragments can be found in Appendix 9.

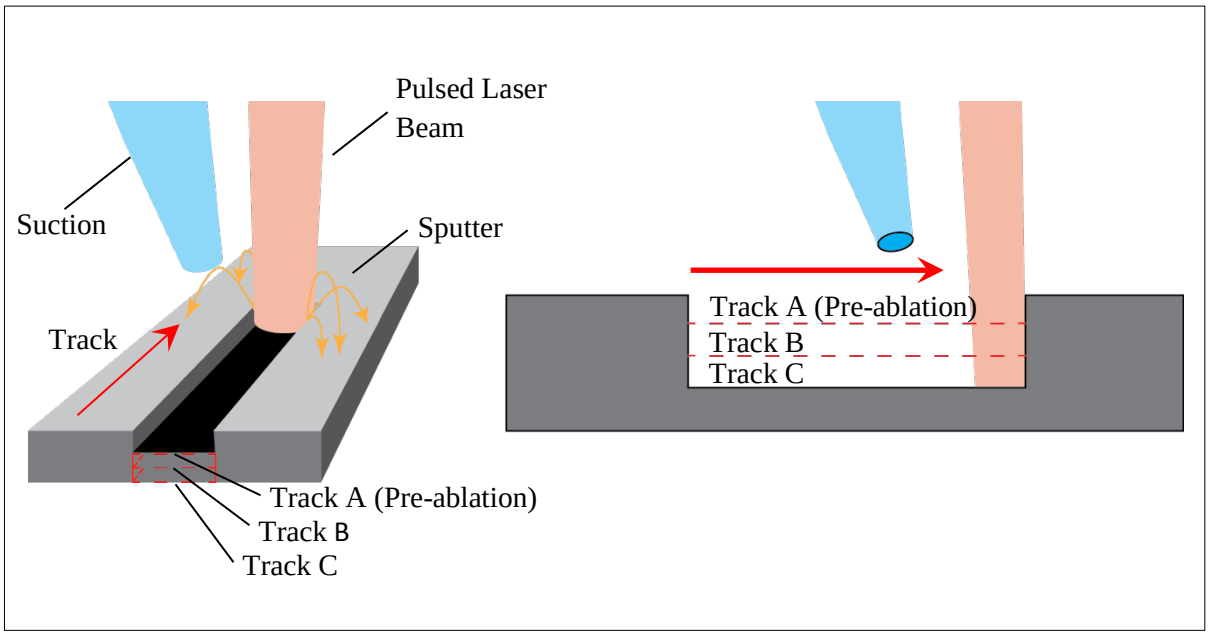

Figure 4.4 The process of laser ablation carried out for the core fragments KA30 A and KA30 B, indicating the layered tracks A, B, and C.

For both samples, Pearce 610J, a material of standardised composition was used as references to eliminate signal drift incurred during data acquisition and to correct for erroneous background elemental signatures. Standard signatures were collected 3 times during laser ablation, once initially before the sample, second between each of the core fragments and finally at the conclusion of the ablation process. The raw data collected was processed using an offline Excel spread sheet devoted to geochemical analysis by LA-ICP-MS.

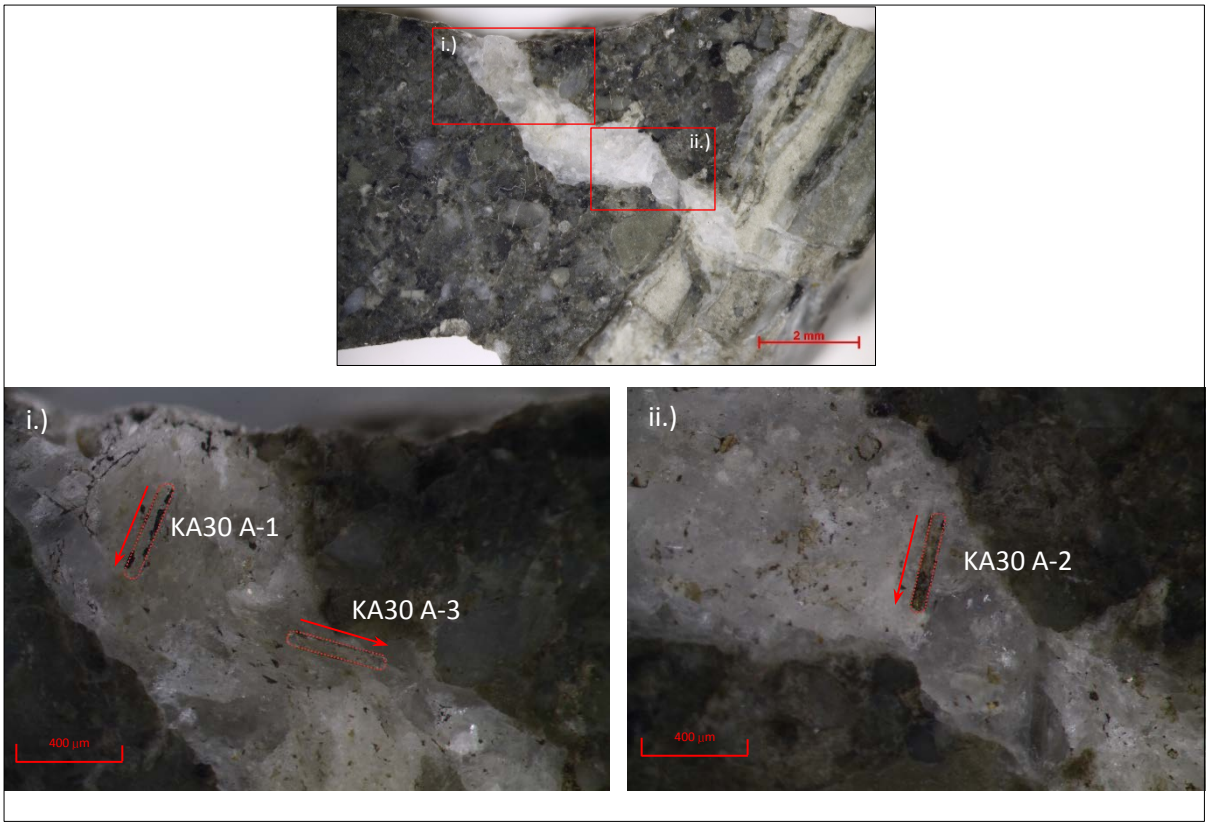

Figure 4.5 Laser ablation track direction and location for rock fragment KA30 A.

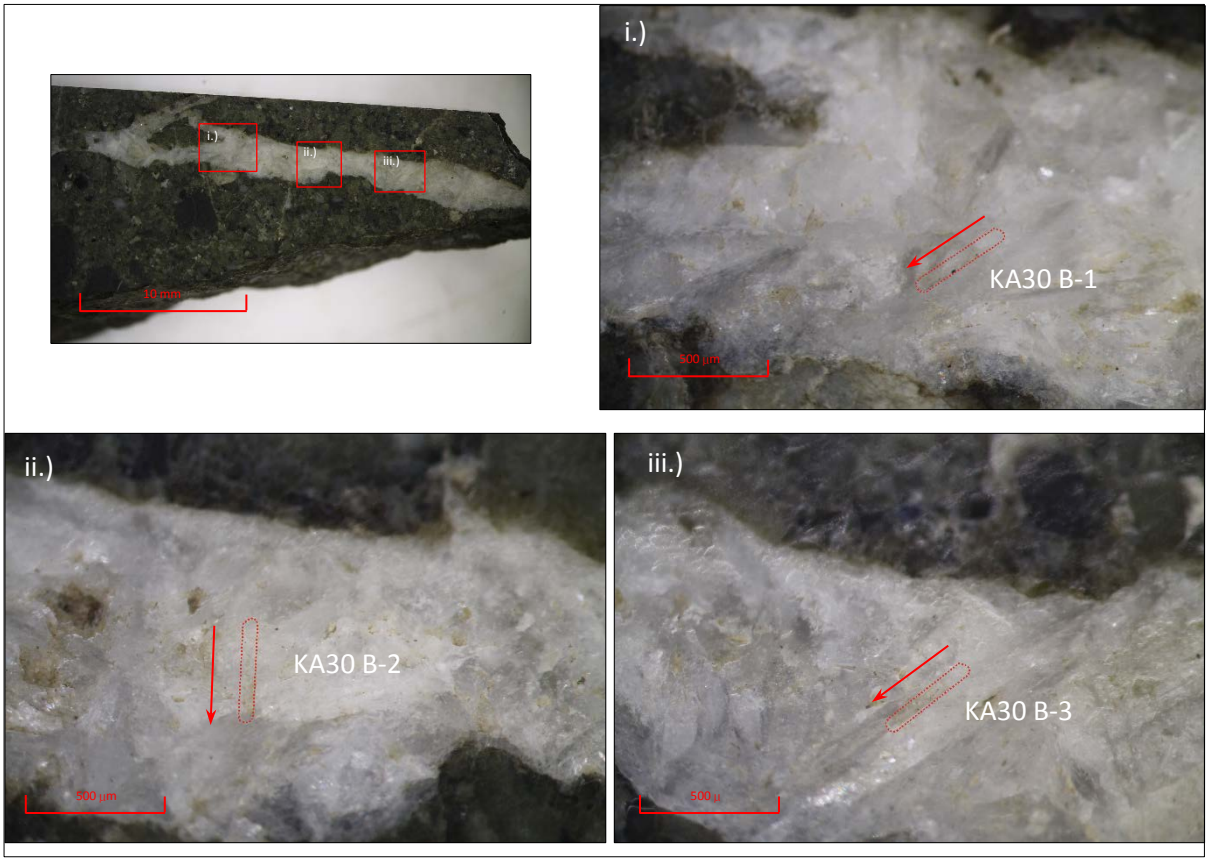

Figure 4.6 Laser ablation track direction and location for rock fragment KA30 B on side ii.)

4.2.3 μCT, Electron Backscatter Diffraction (EBSD), Energy Dispersive X-Ray Spectroscopy (EDX) and Cathodoluminescence (CL) Techniques

Supplementary to the LA-ICP-MS several additional techniques were used both pre and post laser ablation to assist in the reconstruction of the calcite crystal structure evolution in the sealed fracture. This included a combination of selected techniques including, Cathodoluminescence (CL), μCT, Energy Dispersive X-Ray Spectroscopy (EDX), and Electron Backscatter Diffraction (EBSD). Further information on these techniques can be found in Chapter 2 and 3. The flow chart of Figure 4.7 outlines which techniques were carried out during what stage of this phase of the study for the thin section and Figure 4.8 for rock fragments KA30 A and KA30 B. μCT scans were taken at high resolution to assess the internal structure of the fracture network of both drill core fragments.

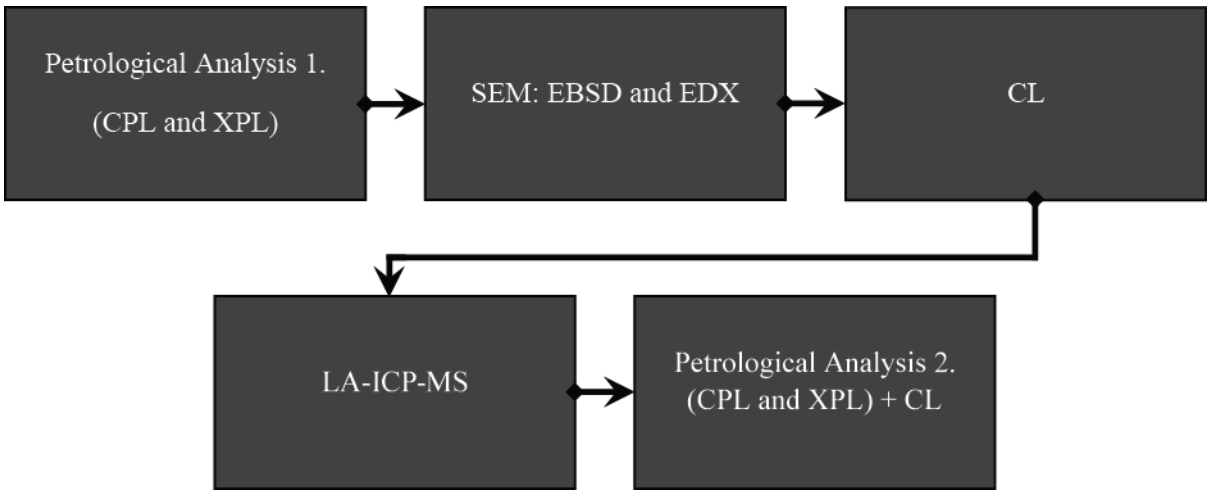

Figure 4.7 Flow diagram indicating the various stages of the analysis carried out as part of the LA-ICP-MS geochemical investigation of the thin section, TS-KA30, including steps undertaken in Chapter 2.

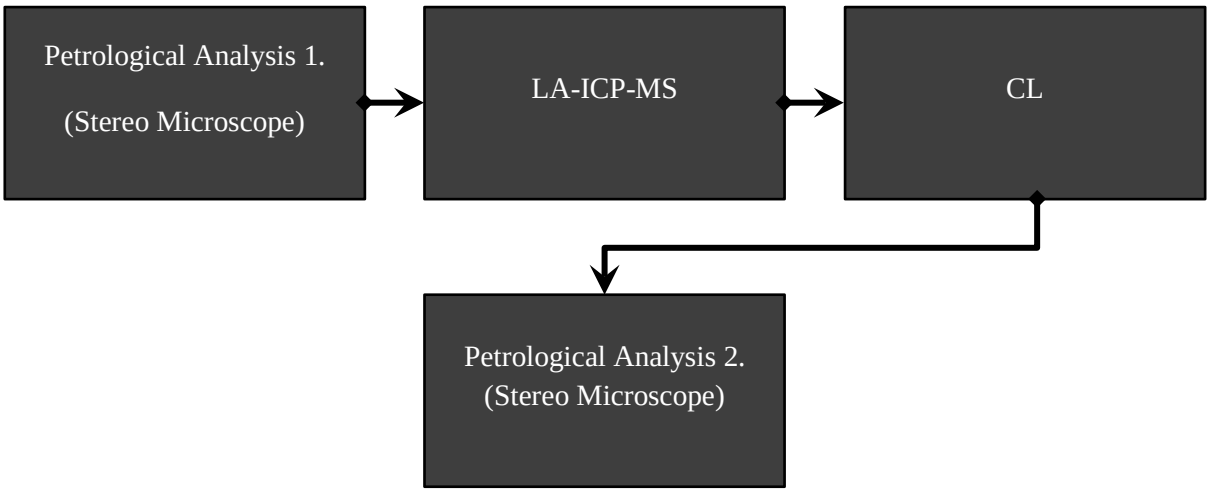

Figure 4.8 Flow diagram indicating the various stages of the analysis carried out as part of the LA-ICP-MS geochemical investigation of both core fragments, KA30 A and KA 30 B.

4.3 Results

4.3.1 Initial Thin Section and Rock Fragment Analysis

4.3.1.1 Thin section

The initial petrographic results of the thin section are located in Chapter 2 with more relevant details relating to the chronological ordering of sealing activity provided below. Early investigations carried out on the thin section indicate two distinct carbonate type sealing minerals. These have been recognised to represent different stages of fracture sealing within the reservoir. The initial stage of fracture sealing is the wairakite-calcite mineralisation. This phase of sealing represents early wairakite mineralisation with late stage calcite deposition in void space or as wairakite replacement in the centre of the fracture. This fracture is cut perpendicular by a later stage of bladed calcite.

4.3.1.1 Rock Core Fragments

The rock fragments were observed using a stereo microscope which indicates that there is an intricate relationship between the various phases of mineralised fractures in both samples.

Rock fragment A contains a bladed carbonate vein that intersects a series of parallel lath like structures of various opacity and colour that divide slithers of wall rock. The clearer minerals are calcite with the duller mineralisation showing various stages of wairakite and rare quartz grains. The bladed vein contains crystals 0.1-1.0 mm in size and again crosscuts the duller blockier calcite with various stages of wairakite mineralisation (Figure 4.5).

The second rock fragment (Sample B) was cut and polished to display two perpendicular faces of the fracture network (Figure 4.6). There is a larger sealed fracture (5 mm wide) which is filled with bladed calcite with crystals 0.1-3.0 mm long. The bladed calcite fracture cuts a dull white vein that contained various stages of calcite and wairakite mineralisation. The phases of mineralisation are more easily identified in CL. On the face (i) the fractures appear perpendicular to one another while on face (ii) they appear to intersect at approximately 45° (Figure 4.9). The fracture that contains bladed calcite crystals terminates adjacent to the fracture intersection (face ii) (Figure 4.9a and 4.9b). The bladed calcite mineralisation has sealed the horizontally orientated fracture for the remaining length of the sample for side ii. Wairakite is not present in the bladed calcite fracture. There are several smaller veins that criss-cross the sample at various angles and appear to be a part of both phases of mineralisation.

Some of the fractures appear to have stained fracture walls in which staining persists to approximately 0.1 mm into the wall rock.

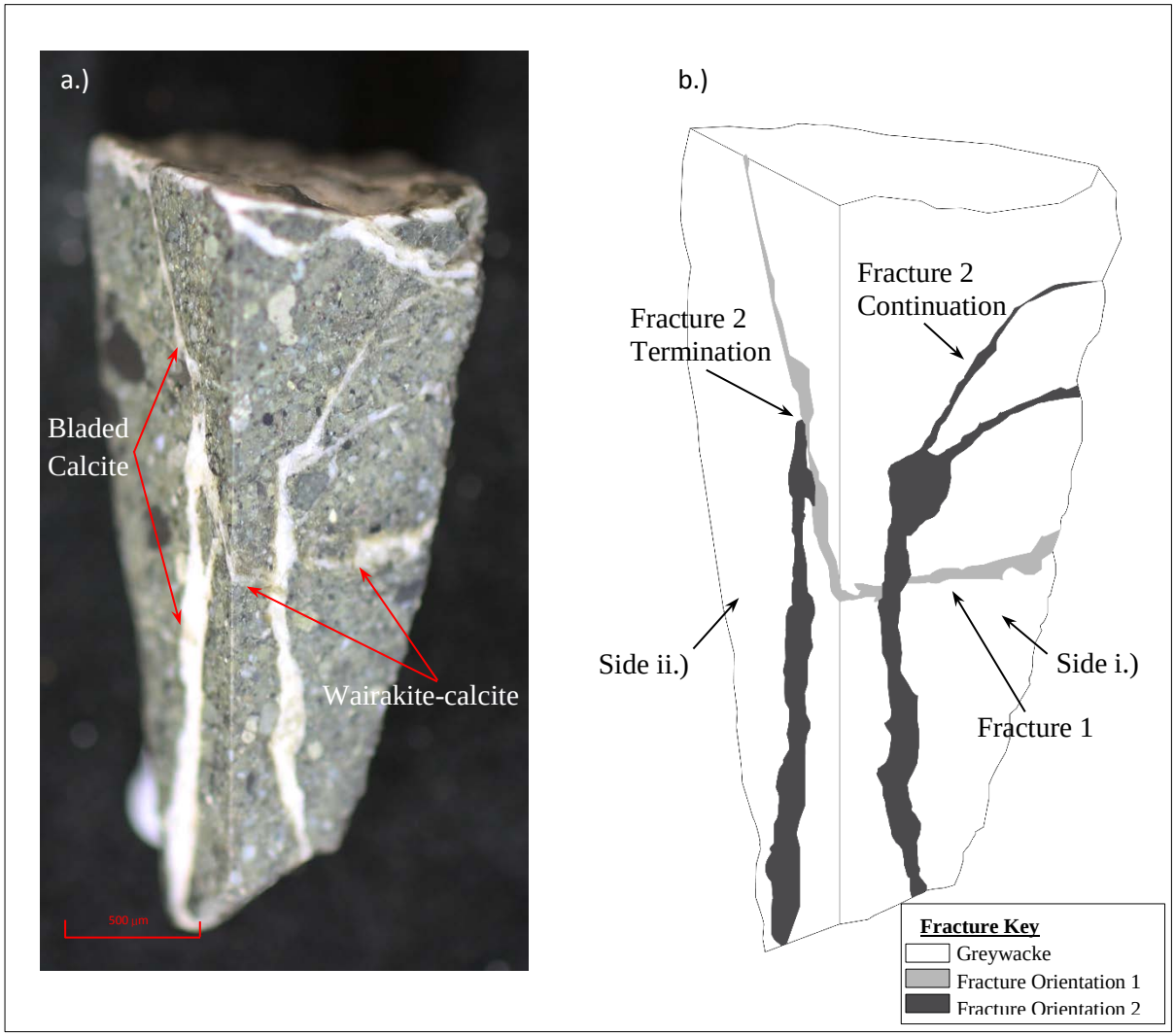

Figure 4.9 Fracture orientations observed in KA30 B. a.) Identifies the mineralisation phase for each section of each of the fractures and b.) displays the separate fractures in a graphic representation highlighting the intricate relationships between both orientated fractures.

4.3.2 Electron Backscatter Diffraction (EBSD) and Energy Dispersive X-Ray Spectroscopy (EDX)

The EBSD and the EDX results are explained in depth in Chapter 2 for the thin section. The grain boundaries for the bladed calcite were used to verify the extent of each calcite crystal that was analysed. The Inverse Pole Figure (IPF) z-direction diagram of Figure 4.10 displays the crystal orientation of the grains that underwent laser ablation in relation to the U-Th levels.

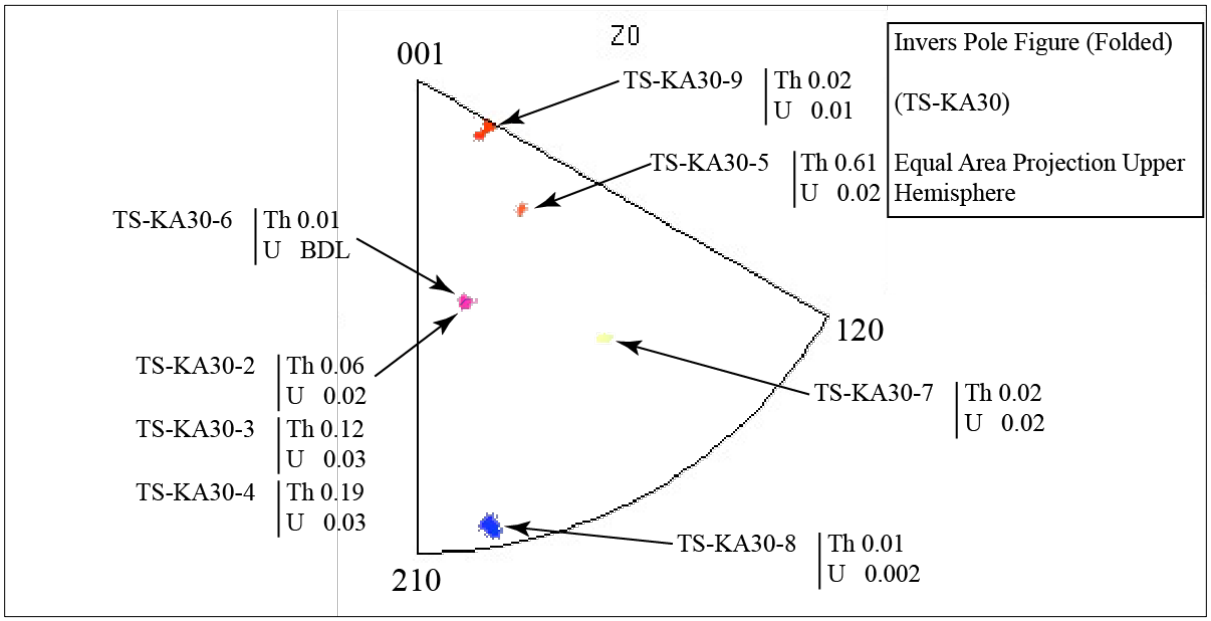

Figure 4.10 Inverse pole figure in the z-direction showing the relationship between the crystal orientation and the recorded U and Th levels.

4.3.3 Cathodoluminescence (CL)

CL image analysis of the calcite veins indicate an obvious difference between the phases of mineralised calcite veins as shown by variations in the colour related to the reflected wavelength emissions (Machel et. al, 1991; Machel and Burton, 1991). This variability is related to the composition of the calcite, especially the Fe and Mn levels as explained in Chapter 2. An in depth analysis of the CL image results for thin section is also outlined in Chapter 2. Additional CL images were collected and analysed following the ICP-MS of the thin section. These images focussed on areas where laser ablation had been carried out to correlate the geochemical analysis with the CL images and the elemental zoning within the bladed calcite (Figure 4.11).

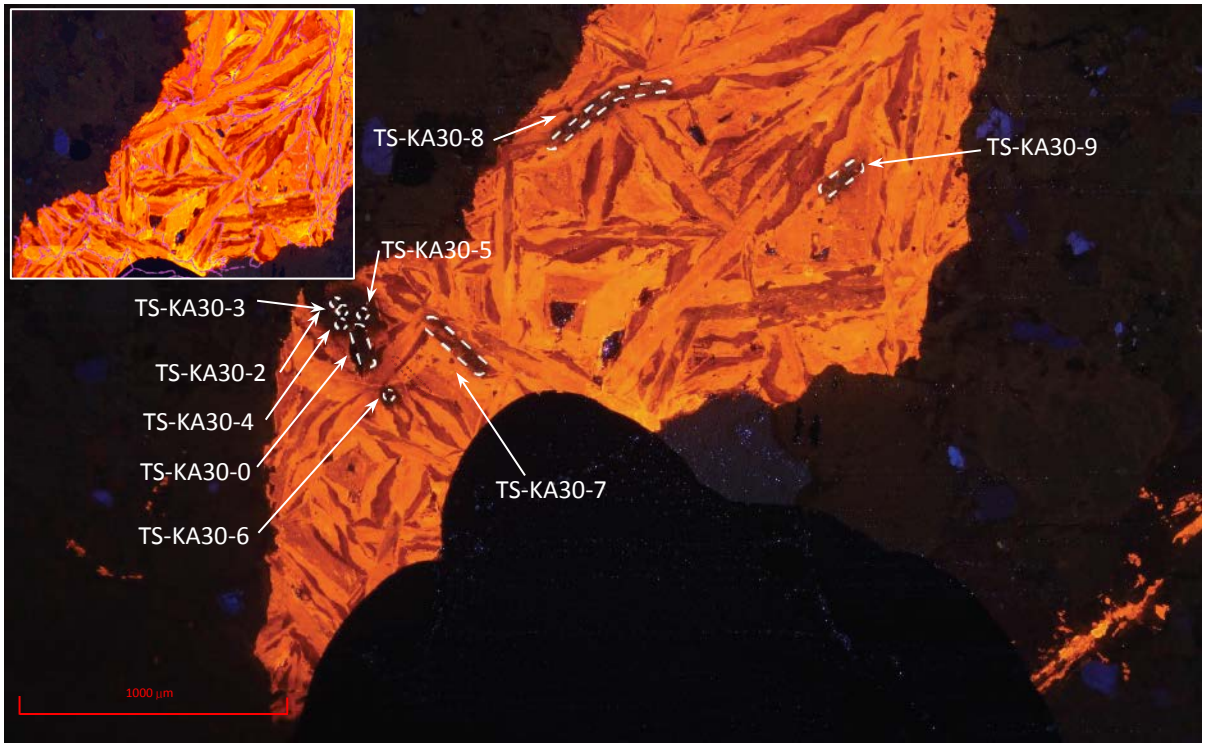

Figure 4.11 CL image of the lower section of the fracture for TS-KA30 showing the spot and track locations of the laser ablation analysis and the Fe (red orange) and Mn (yellow orange) enriched zones of the bladed calcite. Insert shows the calcite grain boundaries overlaid on the initial CL image taken before laser ablation.

The sealed fractures from both the drill-core samples show similar relationships to that observed from the thin section, with cross cutting calcite veins displaying variation in CL colour related to the alteration phase and mineralisation type.

The polished face (Figure 4.12) that was imaged for core fragment KA30 A has a bright orange bladed vein which cross-cuts a series of alternating dull-red calcite and wairakite (dull bluish-purple in CL) sealed fracture. There is evidence of brighter (more yellow) calcite disseminated within the series of wairakite-calcite sealed fracture (Figure 4.12). Also seen in the bladed sealed fracture is the internal Fe and Mn elemental zoning, observed in the thin section CL analysis (Figure 4.11), though this zoning appears not as distinct.

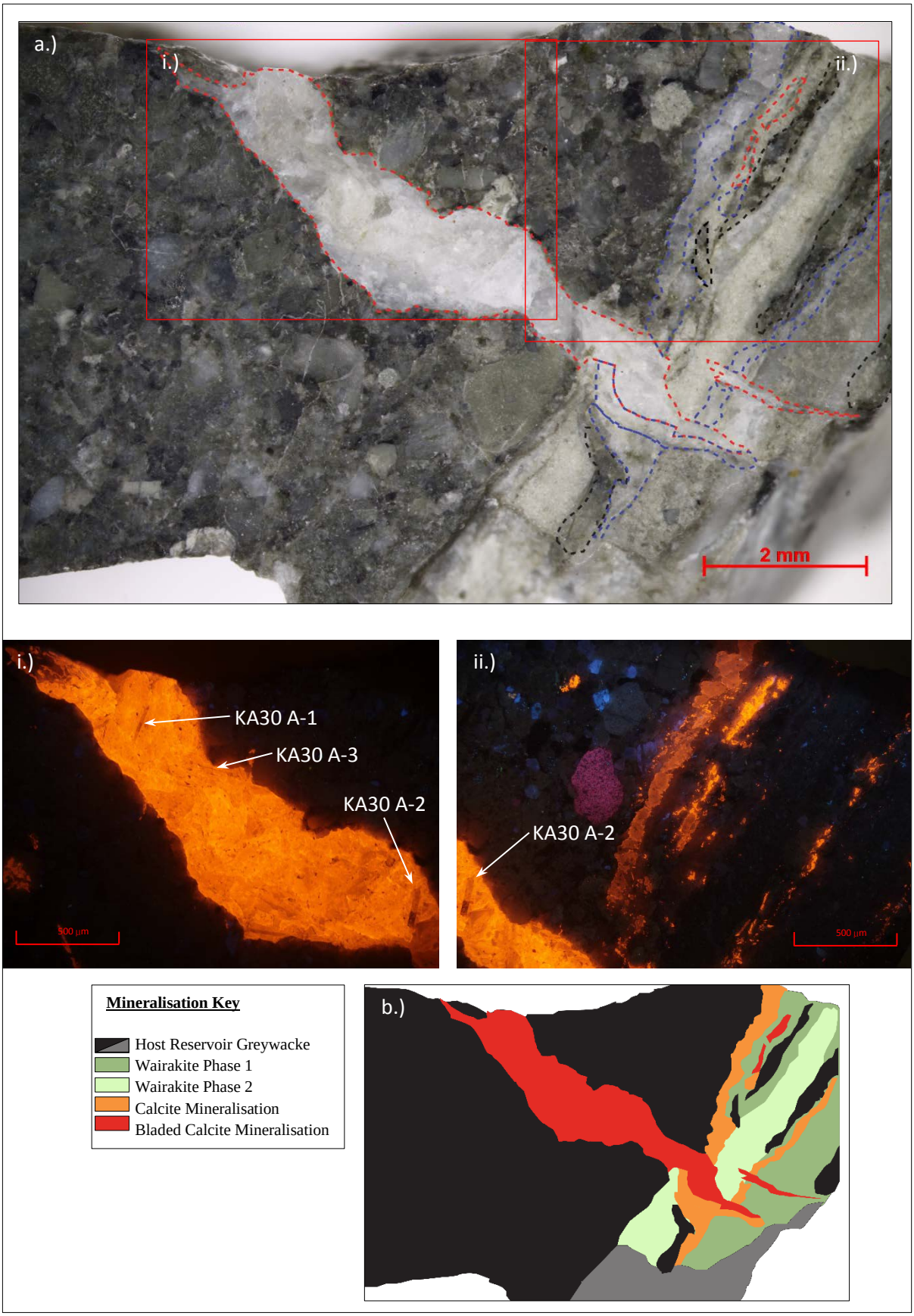

Figure 4.12 The various stages of sealing mineralisation observed in KA30 A. a.) Displays the observed phases of sealing minerals, bladed calcite (red), early calcite (blue), and wall rock inclusions (black). i.) and ii.) Shows the CL images of the insert areas displaying the CL colour shifts between the bladed calcite (bright orange) and early wairakite-calcite mineralisation (blue and dull orange). b.) Is a graphic representation of mineralisation and fracture orientation of the insert area.

Figure 4.13 shows the CL analysis of KA30 B which was carried out on the polished face ii. As explained above there are two stages of mineralisation orientated oblique to each other. The distinct contrast in calcite colour in CL between the two orientations of fractures is not as clear as viewed in the thin section TS-KA30 and core fragment KA30 A (Figure 4.14). Both stages of calcite mineralisation are not distinctly different visually in terms of their red and yellow colouring. The most obvious difference between the two orientations of fractures is the crystal structure and the occurrence of wairakite. An earlier stage of calcite mineralisation in the near vertical fracture shows several bladed calcite crystals but is associated with wairakite mineral precipitation, especially along the fracture wall (Figure 4.14). Within the horizontal fracture a subsequent stage of calcite mineralisation is made distinctive by bladed calcite forms. The bladed calcite crystals have distinct concentric elemental zoning along the crystal's long axes. Red (Fe richer) zones are predominantly found at crystal cores and show more euhedral shapes than the yellow (Mn richer) rims (Figure 4.13). In some areas the Fe-Mn zonation patterns can be difficult to determine due to their resolution and size within the bladed calcite crystals.

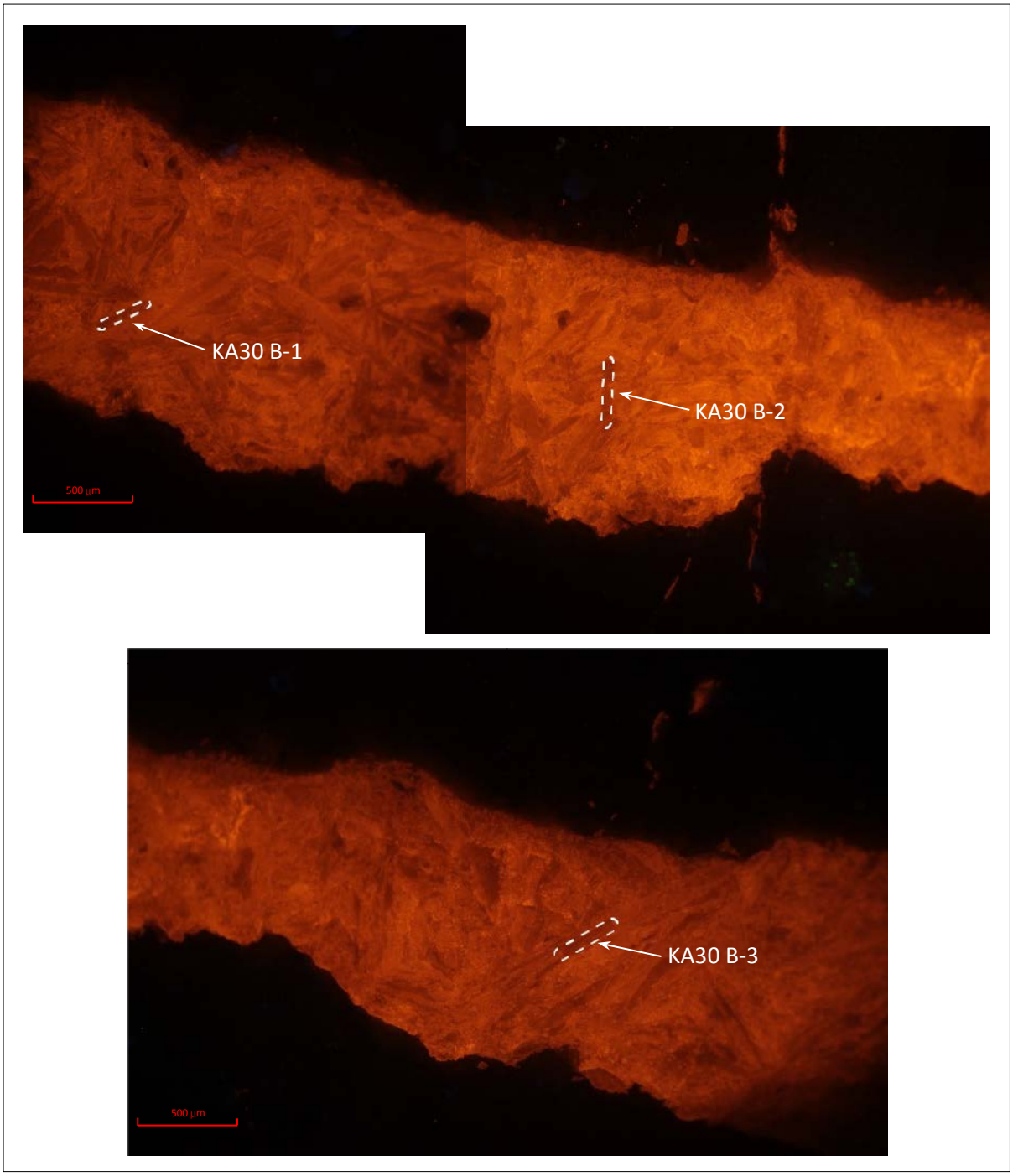

Figure 4.13 CL images of Rock Fragment B side i.) showing the 3 laser spots and the bladed calcite with Fe and Mn elemental zones.

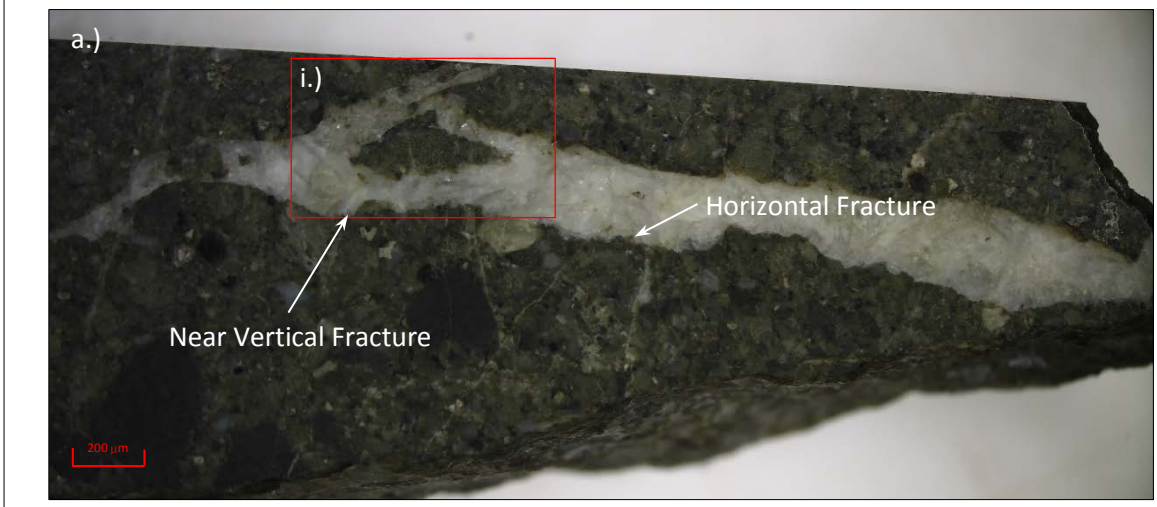

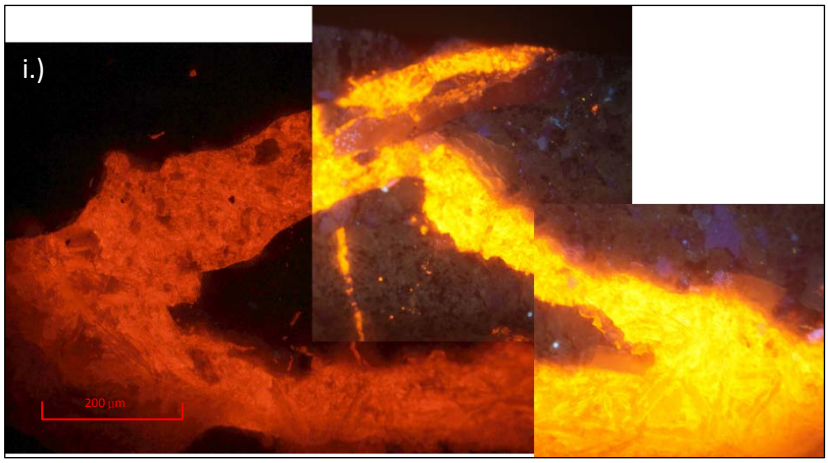

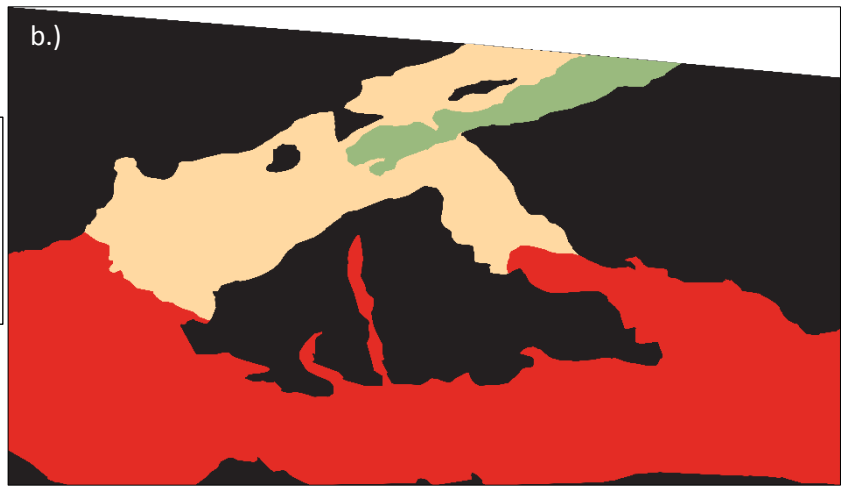

Mineralisation Key

- Host Reservoir Greywacke
- Wairakite Mineralisation
- Calcite Mineralisation
- Bladed Calcite Mineralisation

Figure 4.14 The various stages of sealing mineralisation observed in KA30 B (side i). a.) Displays the complicated interactions between the various phases of deposition. I.) Is the CL image of the corresponding area. b.) is a graphic representation of mineralisation and fracture orientation of the insert area. NB.) The variations of brightness across the CL image were due exposure time of image accusation.

4.3.4 Laser Ablation Inductively Coupled Plasma Mass Spectrometry (LA-ICP-MS) Isotope and Geochemical Analysis

The ICP-MS results are discussed in this section with an Excel spreadsheet containing the full results of the geochemical analysis including all elements and processed concentrations in Appendix 10.

4.3.4.1 Identifying Appropriate Laser Parameters for the Thin Section (TS-KA30)

This section is about finding appropriate laser parameters for the thin section to provide optimal results. Below is the results for each location and the outcome for the laser parameters:

Site 1 directly ablated the glass slide, followed by ablation at site 2 in order to determine a proxy for the thickness of carbonate on the slide (approximately 30 µm). Sites 3-4 varied in laser strength to determine how this affected how quickly the laser ablated the carbonate and reached the glass underneath. Site 5 was located in "dirty carbonate" to determine variation within a crystal. Site 6 was positioned in the same crystal as 1-4 to see if it was connected in 3-D space (Figure 4.11). Sites 7-9 were all tracks in various crystals to trial track speed, ablation rate, and spot size. Sites 10, 11 and 12 were all located in epoxy and glass to produce a data set for the epoxy and glass to compare to the rest of the data in order to identify possible contamination.

4.3.4.2 Th-U levels

The corrected U-Th results, including measured ratios, are shown in Table 4.2 for the analysis of thin section TS-KA30 and Table 4.3 for both rock fragments (KA30 A and KA30 B). CL elemental zones are identified by colour from Figure 4.11 for the thin section (TS-KA30) and Figure 4.12 and 4.13 for the core fragments (KA30 A and KA30 B).

Table 4.2 Th and U concentrations with activity ratios in the bladed calcite from the thin section (Source: Data Table, Appendix 10).

Sample Name & Nº	Track or Spot	Th Concentrations (ppm)	U Concentrations (ppm)	Th/U Ratio	Elemental Zones (Both SEM/CL Image Colours)
TS-KA30-2	Spot	0.06 ± 0.02	0.02 ± 0.01	3	Fe enriched dark grey/red orange region
TS-KA30-3	Spot	0.12 ± 0.02	0.01 ± 0.007	12	Fe enriched dark grey/red orange region edge
TS-KA30-4	Spot	0.19 ± 0.04	0.03 ± 0.01	6.3	Fe enriched dark grey/red orange region
TS-KA30-5	Spot	0.61 ± 0.07	0.02 ± 0.01	31	Mn enriched light grey/ yellow orange region
TS-KA30-6	Spot	0.01 ± 0.007	Bdl	-	Across a range of zones
TS-KA30-7	Track	0.02 ± 0.007	0.02 ± 0.01	1	Across a range of zones
TS-KA30-8	Track	0.01 ± 0.005	0.003 ± 0.002	3.3	Fe enriched dark grey/red orange region
TS-KA30-9	Track	0.02 ± 0.007	0.01 ± 0.005	2	Mn enriched light grey/ yellow orange region
TS-KA30-12	Spot	1.87 ± 0.1	1.34 ± 0.1	1.4	Glass
TS-KA30-02G	Spot	1.70 ± 0.2	1.16 ± 0.1	1.5	Glass
1 TS-KA30-0	Track	1.19 ± 0.1	1.40 ± 0.2	0.85	Glass

(Bdl)= Below detection limit

The U concentrations of the bladed calcite range from 0.003-0.3 ppm and the Th concentrations range from 0.01-0.61 ppm. This shows the variation in Th and U levels throughout the mineralised fracture since the analyses were done in a variety of Fe and Mn zones within the calcite. There is no clear connection between core and rim or dark grey/red orange (Fe enriched) and light grey/yellow orange (Mn enriched) regions in respect to the Th and U levels (Figure 4.11). The first 4 analyses where taken in the same crystal and show the variations towards the crystal base. Spot 5 has a high recorded Th level compared with other measured levels, this spot was in a crystal which has a complicated zoning pattern and adjacent to the first 4. The final 3 tracks all show the recorded levels for 3 separate crystals spaced across the fracture. Track 7 was carried out across a complex chemical zonation pattern compared to track 8 and 9 which were both carried out within a single chemical zone (Figure 4.11).

The 3 tracks that contained signatures from the glass slide can clearly be seen to have elevated levels of both U and Th and were able to be grouped together at the end of the results Table. These analyses are shown to display the difference between glass slide and calcite crystal. The results for epoxy and multiple glass slide spots are not presented within this table.

Table 4.3 Th and U concentrations and activity ratios in fragment A and B for the bladed calcite mineralisation (Source Data Table, Appendix 10).

Sample Name & Nº	Th Concentrations (ppm)	U Concentrations (ppm)	Th/U Ratio	Comments and Observations (From CL Images)
KA30 A-1a	0.08 ± 0.005	0.0013 ± 0.0005	62	• Within one crystal. • Track along the edge rim. • Towards crystal apex. • Near the centre of the fracture.
KA30 A-1b	0.09 ± 0.005	0.0013 ± 0.0006	69	
KA30 A-1c	0.08 ± 0.005	0.0024 ± 0.0006	33	
KA30 A-2a	0.22 ± 0.02	0.05 ± 0.004	4.4	• Multiple crystals. • Near the centre of the fracture. • KA30 A-2d, Extra Track (mislabelled in raw data)
KA30 A-2b	0.25 ± 0.01	0.05 ± 0.003	5	
KA30 A-2c	0.30 ± 0.05	0.05 ± 0.006	6	
KA30 A-2d	0.25 ± 0.01	0.05 ± 0.005	5	
KA30 A-3a	0.25 ± 0.01	0.04 ± 0.004	6.3	• Within one crystal. • Track along the edge rim. • Towards crystal apex. • Near the edge of the fracture.
KA30 A-3b	0.13 ± 0.02	0.02 ± 0.004	6.5	
KA30 A-3c	0.12 ± 0.02	0.02 ± 0.003	6	
KA30 B-1a	0.10 ± 0.005	0.03 ± 0.002	3.3	• Within one crystal. • Track along the edge rim. • Towards crystal base. • Near the centre of the fracture.
KA30 B-1b	0.09 ± 0.006	0.02 ± 0.002	4.5	
KA30 B-1c	0.09 ± 0.005	0.02 ± 0.002	4.5	
KA30 B-2a	0.04 ± 0.004	0.02 ± 0.002	2	• Across multiple crystals and elemental zones. • Across the centre of the fracture.
KA30 B-2b	0.02 ± 0.003	0.02 ± 0.002	1	
KA30 B-2c	0.03 ± 0.003	0.04 ± 0.007	0.75	
KA30 B-3a	0.18 ± 0.01	0.02 ± 0.002	9	• Within one crystal. • Track diagonal across the crystal • Towards the apex of the crystal • Near the centre of the fracture.
KA30 B-3b	0.24 ± 0.03	0.02 ± 0.002	12	
KA30 B-3c	0.20 ± 0.02	0.02 ± 0.002	10	

For both rock fragments the U concentrations of the bladed calcite range from 0.013-0.05 ppm and the Th concentrations range from 0.08-0.30 ppm. There are distinct variations between localities in both the U and Th levels with each location ranging between ±1-±8 ppm for each of the 3 tracks (a, b, and c), with the exception of the KA30 A-3 with a range of ±13 ppm for all 3 tracks. There is a wider range in recorded U when compared to Th across all locations. There is however, no obvious trends between U and Th levels and location of tracks in relation to the fracture wall or crystal boundary for both fragment A and B. Due to the laser diameter

being larger than the recognised Fe-Mn zonation patterns it was difficult to distinguish different the U and Th signatures of the individual carbonate chemical zones.

The graph in Figure 4.15 represents the Th/U ratios and shows the distribution for all 3 samples. This graph also indicates that the recorded ratios are not adequate for U-Series dating, and that these samples cannot be used for dating without further analysis.

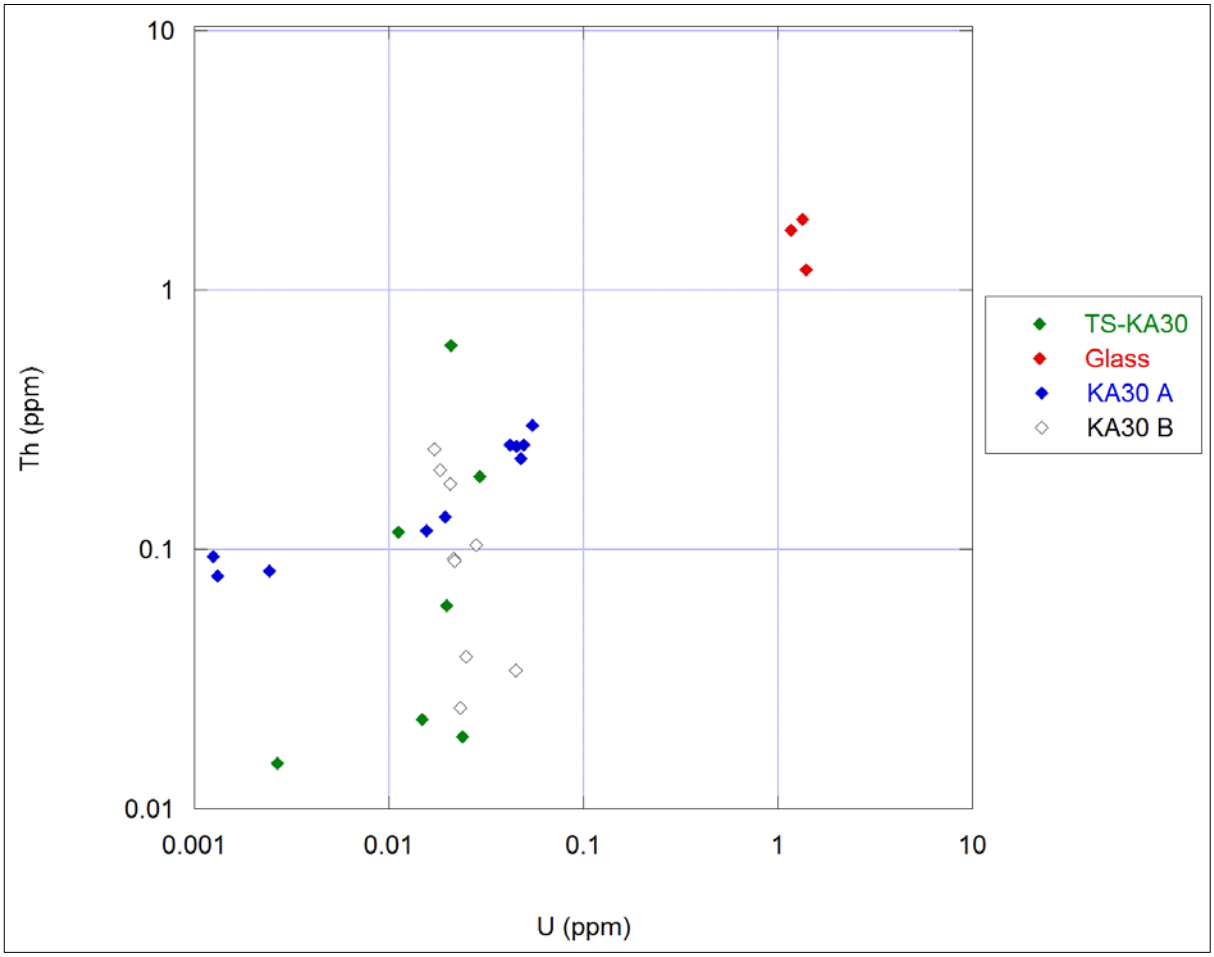

Figure 4.15 Graph of Th vs U levels for the 3 samples analysed.

The results for the thin section provide a wide distribution of values scattered along the Th axis and minimal spread along the U axis with the exception of track TS-KA30-9 which plots in the bottom left. This trend is also seen in the KA30 B results which has a narrower spread. Conversely the distribution of KA30 A is again narrow but spared along the U axis with minimal spread in the Th axis. KA30 A can also be divided into two groups which contain track 1 and track 2 and 3 respectively. The tracks that hit the glass slide are included and show an obvious signature plotting in a tight group in the top right corner. The spread seen in the Th-

U indicates that overall the TS-KA30 and core fragment results are equivalent, with possible glass and epoxy contamination able to be recognised and therefore accounted for.

4.3.4.3 Trends Seen in the Rare Earth Elements (REE) and Trace Element Distribution

During the initial analysis of the thin section the light grey or yellow orange (Mn enriched) regions appeared to have elevated levels of trace elements and Rare Earth Elements (REE) compared to the CL dark grey or red orange (Fe enriched) regions. TS-KA30-8 was of interest due to the fact that it showed a similar variation of trace elements and REE in the form of zones along its path towards the base of the crystal within the red orange core (Figure 4.11).

The chondrite normalised REE diagram (Figure 4.16, 4.17, and 4.18) displays the variation between spots in the different zones within all the carbonate crystals examined. All analyses exhibit a light REE enriched pattern (negative slope). The thin section results have the widest distribution in trends (Figure 4.16) when compared to the rock fragments (Figure 4.17 and 4.18) which both have a tighter distribution.

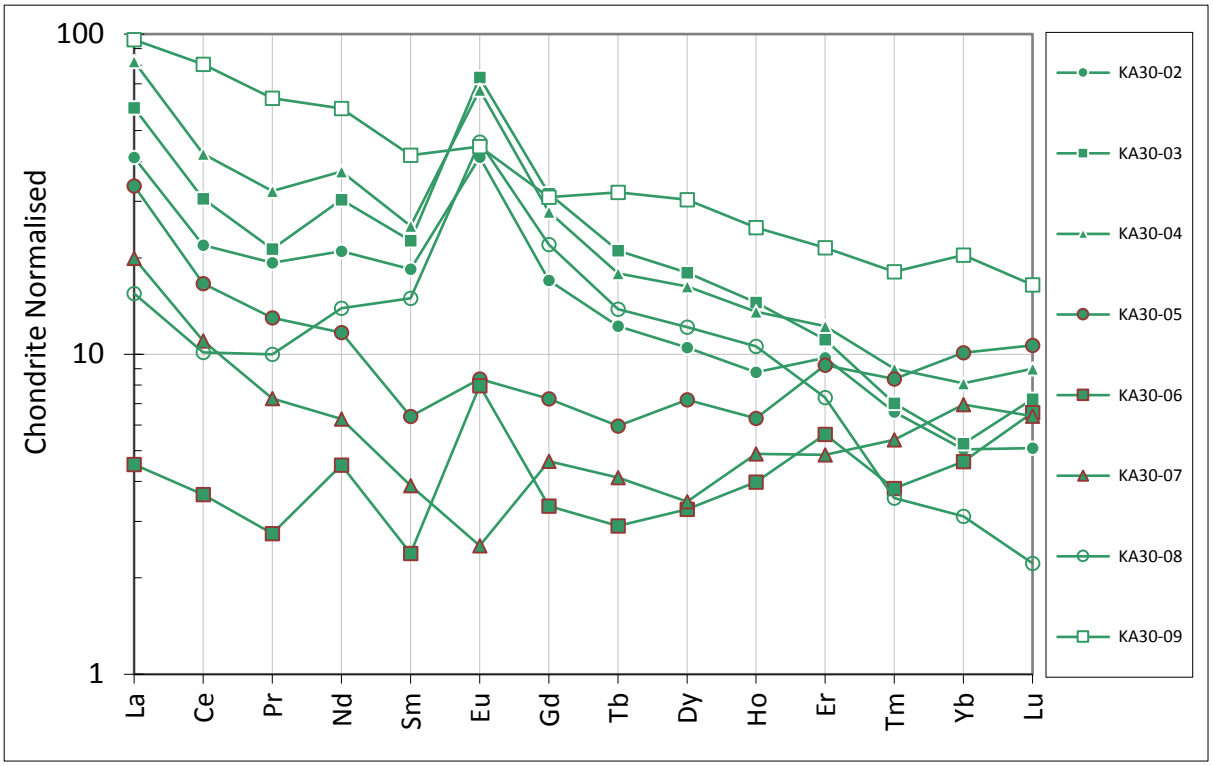

Figure 4.16 The chondrite normalised REE diagram of the thin section analysis displaying a slight negative trend. All analyses show a wide distribution in REE levels, with KA30-07 showing a negative depletion of Eu.

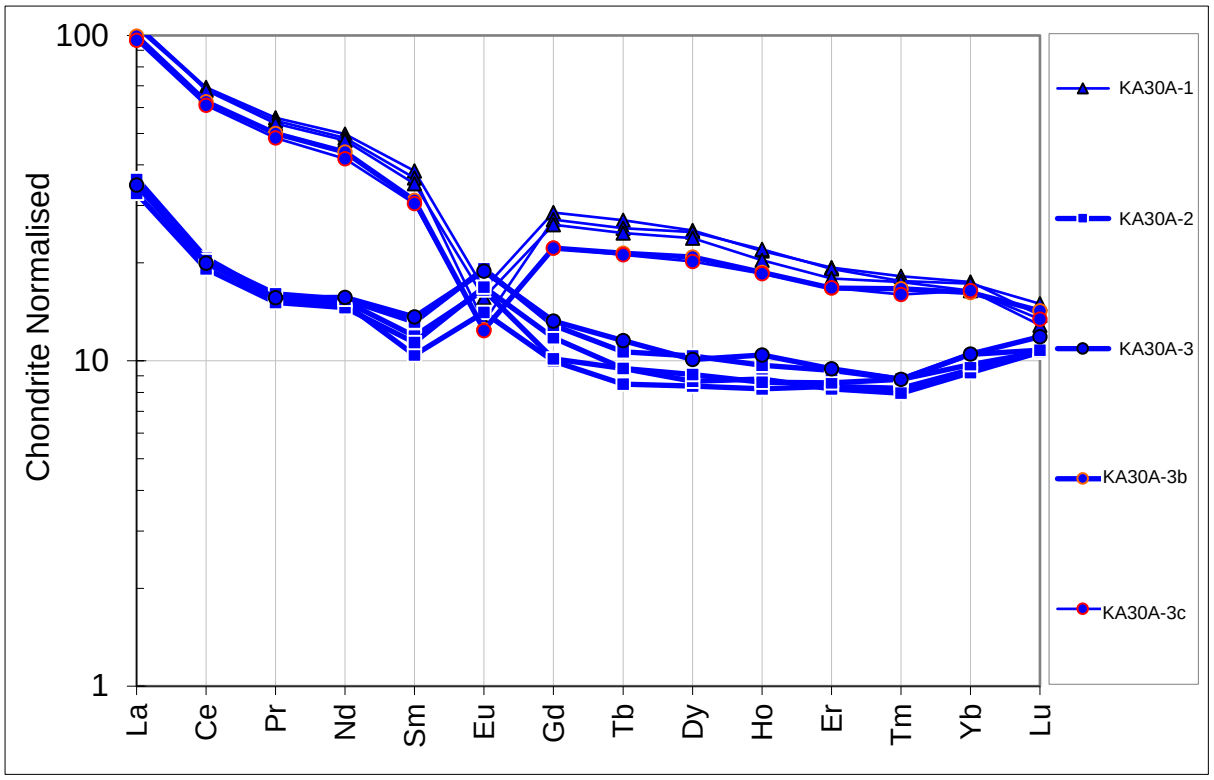

Figure 4.17 The chondrite normalised REE diagram of the KA30 A sample analysis, displaying a slight negative trend. There are two distinct groupings within the 9 laser tracks which either show a negative or positive anomaly in Eu enrichment.

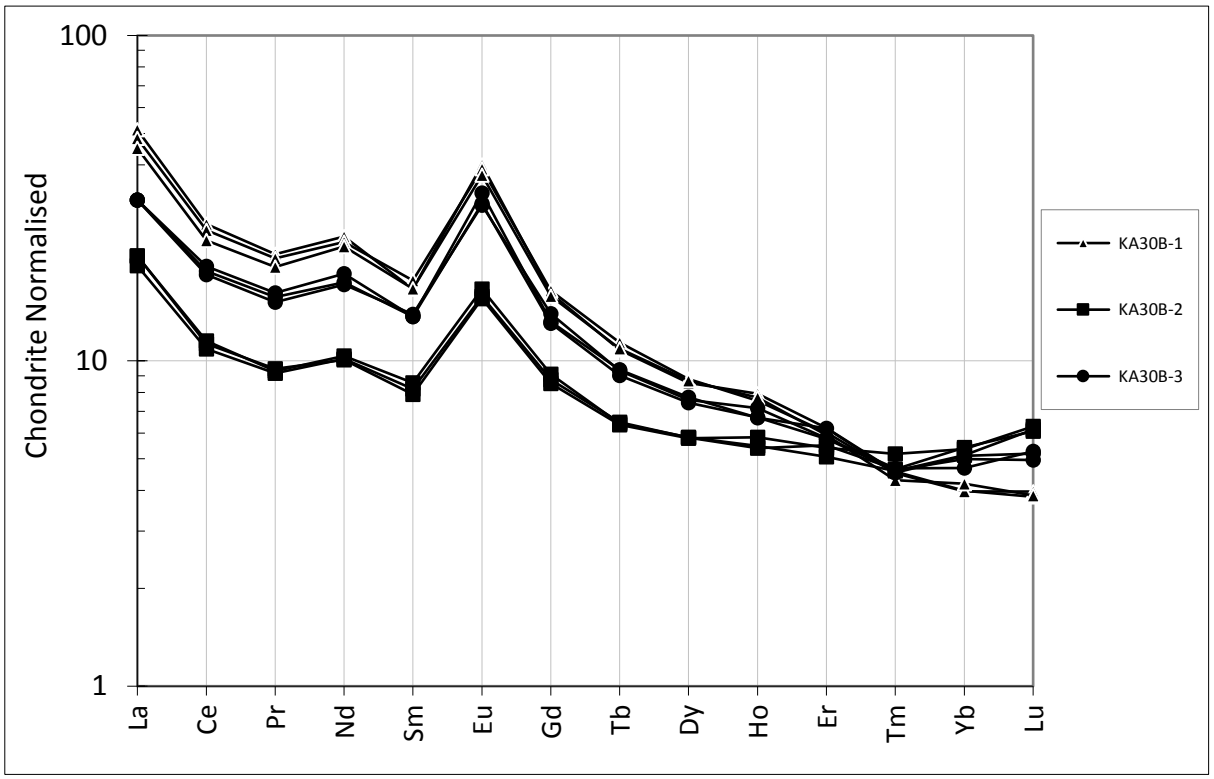

Figure 4.18 The chondrite normalised REE diagram of the sample KA30 B analysis displaying a slight negative trend. All the laser sites display a positive trend in Eu.

A positive europium (Eu) anomaly was seen in all but 6 laser locations for all 3 samples. A negative Eu anomaly was identified in TS-KA30-07, KA30 A-1a, KA30 A-1b, KA30 A-1c, KA30 A-3b, and KA30 A-3c. In addition, analyses with negative Eu appear to show an enrichment in all REEs. The spots in rock fragment A with the negative Eu anomaly also plot higher then then the rest for this fragment.

4.4 Discussion

4.4.1 Th-U Levels and Resulting Dating Possibilities

Laser ablation variables of the thin section show that it is possible to carry out in-situ analysis if caution is taken to avoid contamination from the mounting material. Overall the U and Th levels are equivalent which indicates there is no issue with glass or epoxy contamination. Where the glass and epoxy were ablated the obvious spike in U and Th concentrations could be identified. The measured Th-U ratios are a magnitude higher than required for U-Series dating. This is due to the elevated Th and low U concentrations observed across the bladed calcite vein from LA-ICP-MS analysis. For these results to be able to be used to evaluate the sealing mineralisation the source of the elevated Th needs to be identified and separated from the Th generated by the decay of U.

The assumption that the bladed calcite has remained a closed system is favoured if none of the $^{230}Th/^{234}U$ ratios are significantly higher than 1 (Sturchio and Binz, 1988). This assumption indicates a lack of evidence that chemical loss of U or Th gain has occurred since crystal precipitation. The measured Th/U ratios for this study are significantly higher than 1 for all analysis. However, the high ratios we observed may be entirely due to the ablation of minor silica components. Sturchio and Binz (1988) also suggests a more rigorous test to identify if the calcite associate it with the $^{230}Th/^{234}U$ system.

Another source of the elevated Th may be the ablation of minute silicate inclusions entrained between calcite blades or as surface inclusions. Th can preferentially substitute into the silicate crystal structure during formation. The process of laser ablation vaporises all material along the path of the track including any additional silicate material which may be present, producing a possible signature for silica.

A plot of Th against Si (Figure 4.19) can assess if the Th is sourced from these silicate constituents. The trend represented in this plot indicate that there is evidence of some silicate contamination.

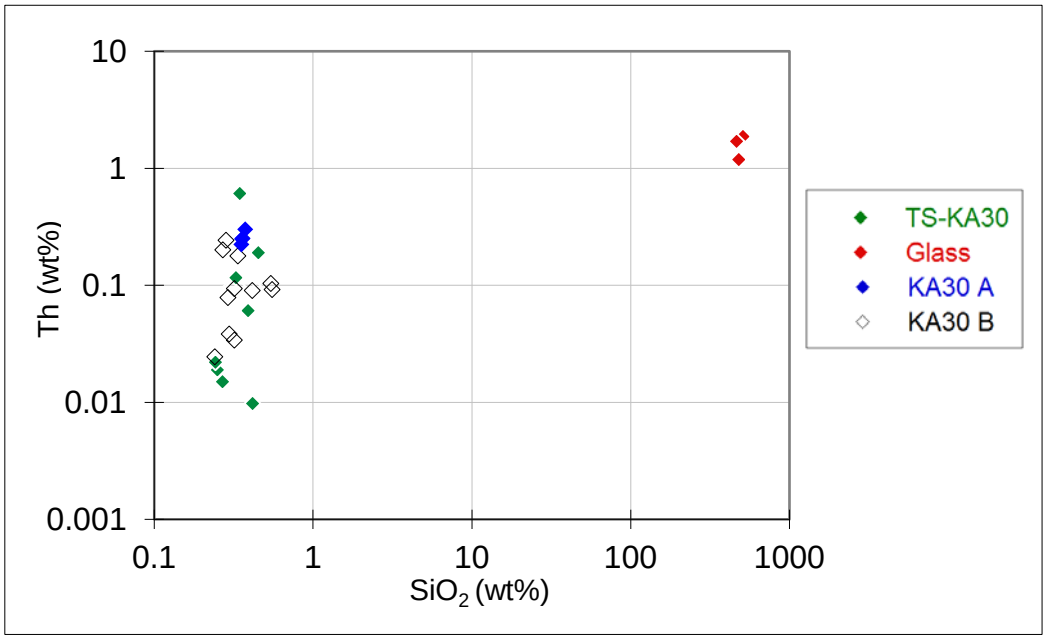

Figure 4.19 Levels of Th vs SiO_2 indicating the cluster for the glass signatures and possible silicate inclusions. The tight grouping of the rock analysis and glass indicates that the elevated Th levels are not from the glass and may be from inclusions in the carbonates.

These silicates add variability to both Th and U concentrations. Several analysis sites close to crystal boundaries including TS-KA30-3, TS-KA30-4, TS-KA30-5, and all tracks of KA30 A 2 (Figure 4.3, 4.4, and 4.6) appear to have elevated levels of Th. Laser ablation at these sites may have vaporised contaminates along the edge of the crystal. Contrasting to this, tracks TS-KA30-7, TS-KA30-8, and TS-KA30-9 which were located towards the crystal centres (Figure 4.3) have lower levels of Th. The inclusions of minor silicate contaminates may be due to speed at which the bladed form of calcite grew within the open fracture or from wall rock contamination during sample polishing and preparation. To remove the possibility of ablating silicic wall rock contamination each analysis included a pre-ablation spot or track, this removed the surface layer of material and any silicic contamination. The possibility of wall rock contamination explaining the high Th count is excluded as both rock fragments show that there is little variation between the initial track (pre-ablation track) and subsequent two tracks. As mentioned, earlier attempts to date geothermally precipitated calcite have also noted elevated levels of Th and silicate components. The in-situ LA-ICP-MS concentrations measured here are within the same range as measured by Grimes et al. (1998) for geothermal calcite. The silicate contamination can be corrected for by using the leachate-leachate isochron method

(Grimes et al., 1998). There are several isochron techniques that can be utilised to correct the silicate contamination signature of Th in geothermal calcite which are summarised by Grimes et al. (1998) to include, Ku and Liang (1984), Schwarcz and Latham (1989), Bischoff and Fitzpatrick (1991), Ludwig and Tittering (1994). These methods may be used in conjunction with in-situ LA-ICP-MS to characterise the source of Th for future use of this method to date bladed calcite veins and therefore geothermal activity.

As discussed by Huberty et al. (2010) there may be a correlation between elemental uptake and the orientation of the surface of the crystal face analysed by ablation. To assess if this was the controlling factor for the bladed calcite's U and Th concentration for TS-KA30 the values were overlaid on a folded IPF colour projection (Figure 4.10). The range of crystallographic orientation shows that this has no obvious control on the U or the Th levels. In addition, there was a range of concentration values seen within the single calcite crystal for analysis numbers 2, 3, 4, and 6. These observations indicate that crystal orientation has no observable control over U and Th, though, it must be noted the small number of crystal grains that this data set includes.

The initial aim of this stage of the study was to assess the possibility of using in-situ LA-ICP-MS to directly age fracture sealing mineralisation by U-Series dating. The process of in-situ laser ablation is possible to be used as a method of data collection for U and Th concentrations. But for these concentrations to be meaningful for U-Series dating a method needs to be developed which can separate the Th that is sourced form U decay from silicate sourced Th. This method does show that it can be used for spatial trace element analysis on sealing mineralisation from geothermal precipitate.

4.4.2 Europium Anomaly

The trends identified within the spider diagram provide information relating to sources of the fluids in the reservoir as well as interactions between these fluids and the reservoir rock. As the in-situ testing was carried out on whole crystals this information can also indicate spatial variations and changes in fluids over time as the crystal precipitated.

Carbonates with positive Eu anomalies may indicate that fluids acquired the REE signature during flow through, and hydrothermal alteration of, plagioclase-rich igneous rocks, possibly intermediate composition plutonics. Plagioclase is the only mineral that exhibits a positive Eu anomaly due to preferential incorporation of Eu (II) relative to REE during igneous

crystallisation. Since plagioclase is also enriched in Sr, a plot of ΔEu/Eu against Sr concentration in the carbonates should provide a test of this hypothesis. The observed negative correlation is opposite to that expected and indicates a more complex origin (Figure 4.20).

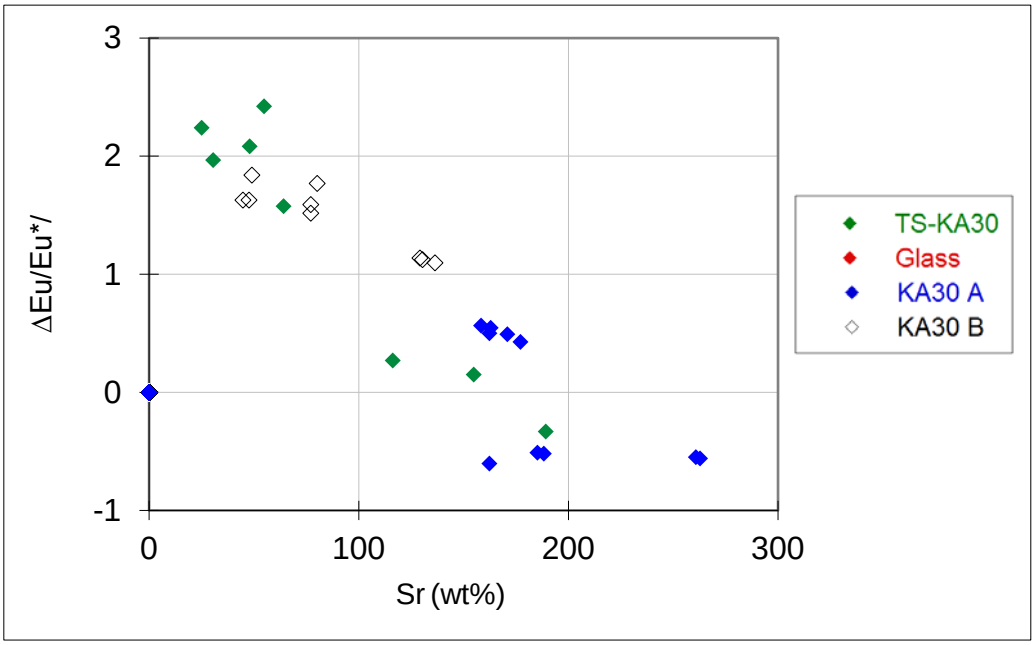

Figure 4.20 A plot of ΔEu/Eu against Sr (wt%) with a slight negative trend indicating the complex source of the fluids that the carbonates precipitated from and that the enrichment in plagioclase may not be the cause for the Eu irregularity seen in the REE analysis.

Carbonates with negative Eu anomalies may indicate that fluids acquired their REE signature during flow through, and hydrothermal alteration of, evolved igneous rocks, possibly obsidian, felsic volcanics. Evolved melts commonly exhibit negative Eu anomalies due to fractionation of plagioclase. Such evolved igneous rocks should also be enriched in a variety of incompatible elements (e.g. K, Rb, Nb, and Th). Unfortunately, such elements do not readily substitute into carbonates and the scatter seen in the data by plotting ΔEu/Eu against their concentrations cannot provide a test of this hypothesis.

Alternatively, carbonates with negative Eu anomalies may indicate that fluids were reduced in which case Eu (II) would be excluded from minerals during precipitation. Under reducing conditions, Fe (II) and Mn (II) would be expected to be preferentially incorporated into carbonates. The overall negative trends seen for the Eu anomaly against Fe (Figure 4.21) and Mn (Figure 4.22) concentrations provide support for this hypothesis. Furthermore, the elemental zones identified in the CL and EDX results from Chapter 2, 3, and above indicate preferential inclusions of these elements within the bladed calcite.

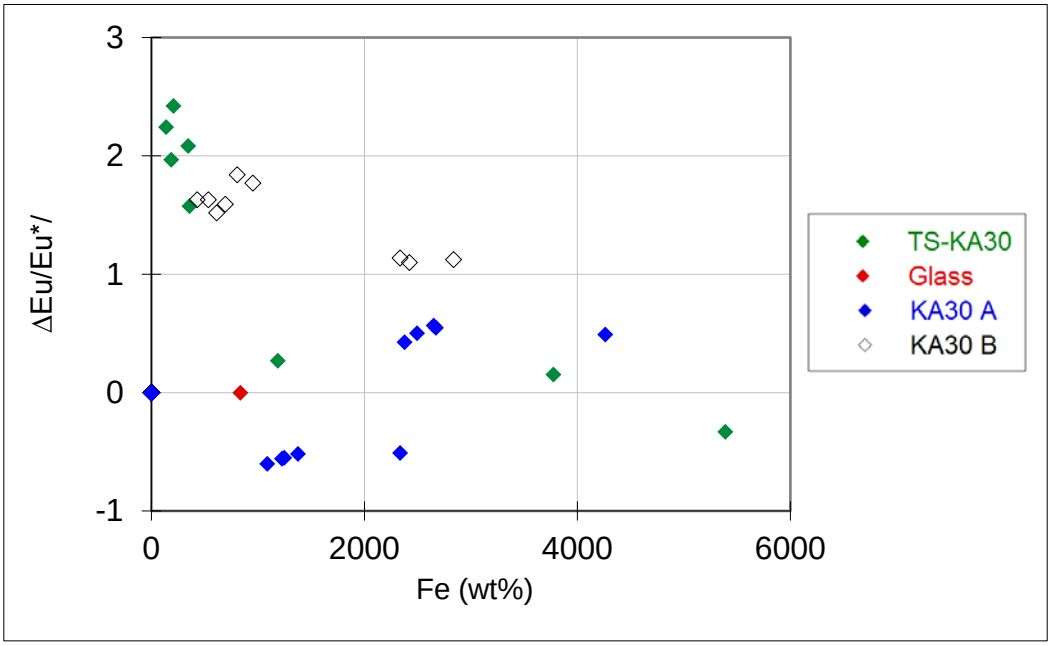

Figure 4.21 A plot of ΔEu/Eu against Fe (wt%) with a broad negative trend indicating the carbonates may have precipitated in reducing conditions as Fe is preferentially incorporated into the carbonates.

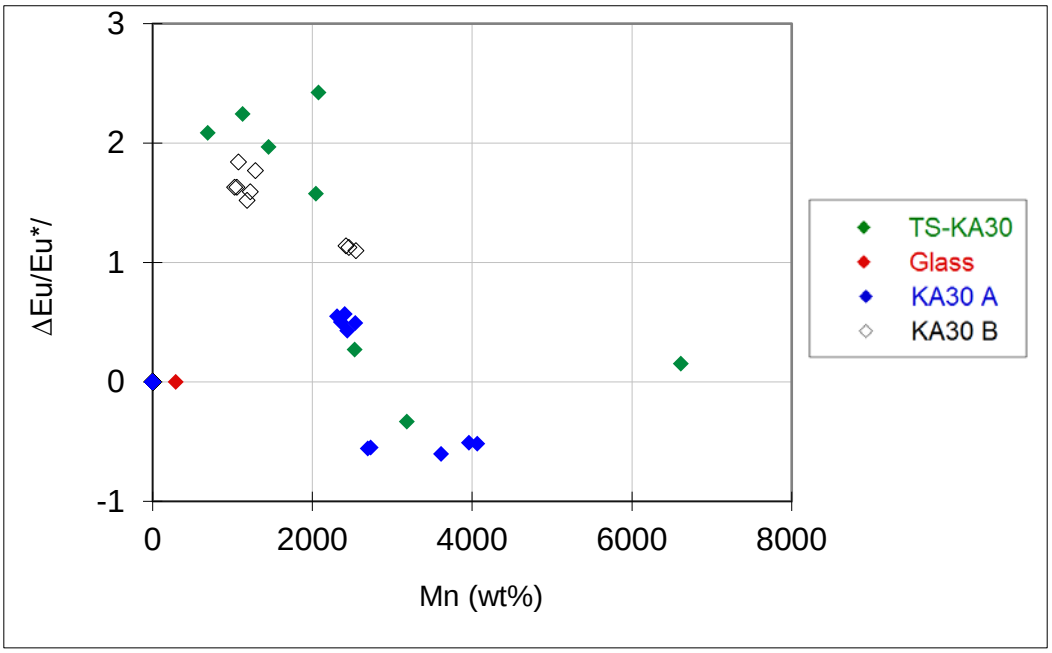

Figure 4.22 A plot of ΔEu/Eu against Mn (wt%) with a broad negative trend indicating the carbonates may have precipitated in reducing conditions as Fe is preferentially incorporated into the carbonates.

Having both trends for the Eu anomaly in the bladed calcite may indicate that it precipitated from a changing composition of boiling fluids from varied sources in the reservoir. Grains that displayed a negative Eu trend may have precipitated from a fluid that had previously deposited

calcite and vice versa with the positive Eu anomaly indicating fluid that had not yet deposited sufficient calcite to deplete the fluid composition.

The Eu anomaly and the related trends seen (Eu vs Sr, Eu vs Fe etc.) alone indicate that there is no simple solution to retracing the fluids past. This is expected for geothermal fields as they are complex systems made up of many interconnected processes. Past studies have identified that the heated fluids are a mixed source with a minor component of magmatic interaction, also that these fluids migrate from the heat source located in the South of the field (Absar and Blattner, 1985: Absar 1988; Christenson, 1987, 1997). The REE trend seen within the bladed calcite may be related to how these elements are entrained in the crystal structure during the growth process and how they respond to changes in fluids.

4.4.3 Interaction of the Evolution of Fracturing and Sealing Episodes Identified in the Reservoir

Faulting activity in the area has been inferred to be episodic and localised along major fault structures identified in the basement lithologies (Bignall and Milicich, 2012; Milicich et al., 2013). There is evidence of a change in localised normal fault orientated northwest-southeast (post 1.5 Ma) from northeast-southwest structures (pre 1.5 Ma) (Milicich et al., 2013). This record of faulting activity demonstrates that this region has undergone an extensive and complex history of fracturing events which may be much older than the geothermal field itself (Milicich et al., 2013). It is this faulting, localised in the basement greywacke that is responsible for providing principal pathways for high temperature fluids, flowing from depth into the overbearing stratigraphic layers (Adams et al., 2009; Leonard et al., 2010; Milicich and Bignall, 2012). As these fluids ascend through the layers of Quaternary sediments, and volcanic deposits (900-1000 m) changes in chemistry, pressure and temperature occur resulting in mineralisation within fractures. The geothermal history of fracture sealing mineralisation activity at Kawerau is recorded in 3-4 isotopically preserved events (Nairn and Wiradadja, 1980; Absar and Blattner, 1985: Absar 1988; Christenson, 1987, 1997, Milicich et al., 2014b). From observations of the extent and stratigraphic associations of an initial phase of sealing with faulting structures Christenson (1987) has concluded that geothermal activity may be as old as 400,000 years. Further work by Milicich et al. (2014b) proposes that that Kawerau geothermal field is a combination of two overprinted hydrothermal systems over this time period relating to the older Caxton Formation (0.36-0.43 Ma) and Mt. Putauaki magamtics (2400-8350 years (Carroll et al., 1997)). It is unclear if Kawerau has experienced periods of low or has been

absent of geothermal activity related to these changes during this time but it is suggested that the modern system at Kawerau was initiated approximately 16 Ka (Milicich et al., 2014b).

The first stage of geothermal sealing is the wairakite-prehnite mineralisation event which is not recognised within the drill core fragments at this depth but can be seen in thin sections from 1098 mRF. It is suggested in Absar and Blattner (1985) that this stage of mineralisation and the second stage of wairakite-calcite crystallisation can be split into several phases where each species of mineral was dominant depending on the flux of CO_2 in the geothermal fluid.

The following episodes are represented in the core fragments examined in this study with the dull blocky calcite-wairakite phase and the bladed calcite phase clearly distinguishable. The petrographic studies with additional geochemical analysis indicate that these 2 different stages of alteration are present within the thin section in Chapter 2 and the analysis of the rock fragments. The separation of these phases of sealing is most obvious when comparing fracture sealing events using fracture orientation, EDX, and CL images. Crystal structures of the calcite identified in the thin section and both drill core fragments are also distinctly different between the two episodes of fracture sealing. Rock fragment A is most representative of the relationship identified in the thin section, Chapter 2, with fragment B presenting a more complicated association between phases. The phase association in fragment B may be the result of replacement alteration or fracture re-activation as a fluid pathway enabled the precipitation of bladed calcite in open space to finally seal the fracture.

The second and third phases are indistinguishable isotopically from results in this study, however, from the location of these samples in KA30 it can be inferred that it is these stages of alteration that may have created the permeability barrier that lead to the migration of the geothermal fluids north to generate the present state of geothermal activity.

Geophysical investigations have delineated the migration of fluids from the south to the north, with this and petrographic evidence of past fluid movement in the south the migration of the producing zone of the field can be retraced (Christenson, 1987; Allis et al., 1993; Clark et al., 2015). The resulting evidence of fluid migration in turn with strontium and oxygen isotopic analysis have been used extensively to study the source and interactions of the geothermal fluids and reservoir rocks at Kawerau (Nairn and Wiradadja, 1980; Absar and Blattner, 1985: Absar 1986; Christenson, 1987, 1997; Milicich, 2013). The results from these studies have produced a primary model of fluid flow interactions between reservoir rocks and the degree of alteration that is observed. The fluid flow model of Kawerau is of a plume of hot fluid that rises

in the southern sector with a complex mixing and boiling regime with evidence of meteoric and magmatic fluids (Absar 1986; Bignal and Milicich, 2012). These fluids then travel along major basement structures, secondary fractures, and upon reaching the more permeable volcanic formations spread laterally (Nairn and Wiradadja, 1980; Absar and Blattner, 1985: Absar 1986; Christenson, 1987, 1997, Wood et al., 2001; Wallis et al., 2012). As the Eu anomaly and resulting geochemical trends seen in this study suggests the bladed calcite was formed in a reducing environment from fluids with a complex origin, also explored in both Absar (1986) and Christenson (1987). Previous studies suggest that a majority of the permeable channels in the southern areas of the field are now sealed due to large-scale deposition of secondary minerals (predominantly calcite and quartz with minor adularia) due to mass influxes of geothermal fluids and gasses from localised magmatic events (Browne, 1978a; Nairn and Wiradadja, 1980; Absar and Blattner, 1985: Absar 1986; Christenson, 1987, 1997). The later fracture sealing episodes can be seen to control secondary porosity in the drill core. It is this control that is the main factor governing fracture permeability in the basement greywacke as seen throughout this geothermal field (Christenson, 1987).

The sealing of secondary fractures can lead to the over pressurisation of the multi-phase fluid flow resulting in brittle deformation of the surrounding rocks which in turn provide additional fluid pathways at Kawerau (Absar, 1988; Christenson 1987). These events have been evident at Kawerau with multiple occurrences of hydrothermal eruption breccia in the stratigraphic record and reactivation of mineralised sealed fractures due to large additions of CO_2 to the system (Nairn and Wiradadja, 1980; Absar, 1988; Christenson 1987; Milicich and Bignall, 2012; Milicich et al., 2014a; Milicich et al., 2015).

4.5 Conclusion

Incorporating the additional dimension of time to fracture sealing processes that occur in geothermal reservoirs can lead to a better understanding of the evolution of a geothermal resource. Presented in this study is an isotopic and geochemical analysis carried out by in-situ LA-ICP-MS for several bladed calcite mineralised fractures located in the reservoir basement rock at Kawerau. Even though this study was unable to date the bladed calcite sealing event successfully it presents a brief geochemical analysis of this phase of mineralisation in comparison to previous studies as well as a breakdown of the in-situ LA-ICP-MS technique including lessons learnt for future studies.

- This study shows it is possible to carry out high resolution in-situ ICP-MS testing on bladed calcite for spatial isotopic and geochemical analysis. For crystals such as geothermally precipitated bladed calcite this can provide information on geothermal fluids variations during crystal growth. This includes geochemistry variations in morphological zones and along the axis of individual crystals (TS-KA30 track 8). Furthermore this study shows that it is possible to work in thin sections. This has several advantages in collecting microstructural information prior to laser ablation and comprehensive chemical data.
- The elevated Th levels observed within the bladed calcite indicate that U-Series dating of the carbonate mineralisation using in-situ LA-ICP-MS alone cannot be undertaken. Consequently this requires further analysis to identify the concentration of the measured Th that is the result of radiogenic decay and to exclude concentrations from silicate ablation.
- The Eu anomaly that we identified in the geochemical analysis highlights the complex origins of the geothermal fluids that the bladed calcite precipitated from. The positive Eu anomaly in addition to the ΔEu/Eu and Sr association can not specify the origin of fluids alone. Along with the ΔEu/Eu and both the Fe and Mn relationships, the negative anomaly may indicate that the fluids precipitated within a reducing environment incorporating these elements preferentially over Eu. Further investigation into the cause of both positive and negative Eu anomalies being present within the bladed calcite and there relationship to boiling fluids is required.
- This study has provided an insight into the bladed calcite precipitation with relation to geothermal fluids and other phases of mineralisation identified within the basement reservoir. These observations characterise the stages of various phases of sealing mineralisation identified throughout this study and how these changed overtime. Interpretations of identified sealing phases in this study match with earlier studies carried out at Kawerau. The timing of emplacement of fracture sealing mineralisation identified at Kawerau is still open to be refined.

In summary the precise dating of impure carbonates with elevated Th can be difficult with in-situ LA-ICP-MS due to the inability to separate the source of Th contamination. Finally it is important to fully understand phases of fracture sealing episodes for detailed hydrological and evolutionary modelling of geothermal systems. This is especially essential for geothermal fields like Kawerau where this process is an integral part in the evolution of reservoir dynamics and fluid permeability migration.

Chapter 5

Thesis Summary

5.1 General Summary

Presented here is a multi-stage analysis of the fracture sealing mineralisation identified within the reservoir basement greywacke of the Kawerau Geothermal Field. Incorporating the information gained from the 3 stages of a dimensional analysis can provide a deeper understanding of how fluids migrate within the basement reservoir and the role fracture sealing has played in the evolution of activity in this field. The main objective of this study was to compare and evaluate several alternative techniques to better understand the process of fracture sealing in active geothermal systems using field samples. The key findings from each chapter of this study are summarised below:

5.1.1 Chapter 2: Calcite Sealing in a Fractured Geothermal Reservoir

- The crystal morphology recognised in the 2-D analysis of the fracture shows two separate sealing mechanisms occurring between different phases of calcite deposition. The initial phase associated with wairakite appears to be asymmetrical syntaxial growth, whereas the bladed calcite precipitates in an interconnecting fashion along fracture walls and in free space.
- The internal structure and composition between the two phases of calcite were also noted to vary. The bladed calcite exhibited internal concentric patterns of alternating Fe and Mn bands and a lack of internal deformation, indicating that this fracture represents the most recent tectonic event large enough to cause new fractures. There is also minimal twinning observed in the calcite, implying that since the precipitation of the bladed calcite minimal strain has been accumulated within the rock. The older calcite is duller in cathodoluminescence (CL) and is absent of the Fe and Mn zoning seen in the younger phase. Additionally, this stage of calcite mineralisation is intensely twinned which may potentially indicate that the lattice distortion represents a change in differential stress magnitude that the basement lithology has experienced in the past.

- This variation in calcite lattice distortion and preferred orientation may indicate an insight into the horizontal stress field orientation and how this has varied within the reservoir over time.

5.1.2 Chapter 3: 3-D Electron Backscatter Diffraction (EBSD) Analysis by Serial Sectioning

- Outlined within this chapter is the process for serial sectioning a large fragment of rock that we developed to produce a 3-D reconstruction of the mineralised fracture. This includes suggestions for scanning optimisation, sample preparation, method improvements, and data segmentation analysis.
- The various phases of sealing mineralisation recognised in 2-D can be seen in the 3-D analysis. By exploring the crystal morphologies using an EBSD serial sectioning technique shows that there is additional information that can be included by exploring the z-axis.
- The process of producing a 3-D representation of a mineralised fracture is an appropriate means to visualise crystal growth interactions. This method was useful to fully expand our understanding of growth mechanisms seen in the 2-D analysis.

5.1.3 Chapter 4: Evolution of Fracture Sealing by U-Series Dating

- This initial study for using in-situ laser ablation inductively coupled plasma mass spectrometry (LA-ICP-MS) shows it is possible to carry out high-precision geochemical analysis on geothermal bladed calcite. It is emphasized that the laser parameters and analysis conditions are varied to optimise the returned geochemical signature and to avoid slide contamination.
- In order to use the U-Series method for dating geothermally precipitated calcite extra analysis is required to identify and separate the Th signatures from the silicate ablation and the radiogenic decay of U.
- The Eu anomaly identified in the rare earth elements (REE) and the subsequent trends seen in the elemental relationships (ΔEu/Eu* vs Sr, ΔEu/Eu* vs Fe, ΔEu/Eu* vs Mn etc.) highlights that the geothermal fluids have experienced a complex history in flow dynamics and fluid-rock interactions. The complex history of the fluids that the bladed calcite precipitated from is expected for complicated geothermal fields such as

Kawerau, where fracture sealing has played such an integral role in the evolution of the field.

- Kawerau has experienced multiple phases of carbonate sealing within the reservoir. At least two of these fracture sealing events are recoded in the field samples we used for this study, the wairakite-calcite and bladed calcite phases. These sealing events have been linked to the episodic localised faulting activity of the region and the bladed calcite is thought to represent the latest sealing event.

5.2 Future Work

This section provides suggestions for further work to constrain the mechanisms and relationships of various phases of geothermal mineralisation and fracture sealing episodes identified at Kawerau. This additional research can aid to better clarify the outcomes of this study and to successfully relate these findings to active processes occurring in other geothermal fields within the Taupo Volcanic Zone (TVZ) and around the world:

- Additional examination of a wider set of calcite veins is proposed to conclude if there is a favoured growth mechanism of sealing calcite mineralisation in geothermal fields especially at Kawerau. This will assess if this recognised mechanism is dependent on variables, such as boiling conditions, during precipitation and crystal growth.
- A more in-depth examination of the stress field induced twining recognised within the carbonate mineralisation to potentially unravel the evolution of differential stress magnitudes and orientations that the reservoir has experienced. This can be carried out by observing the fracture in orthogonal slices and by looking at structurally oriented samples.
- The use of an automated serial sectioning system to accurately slice surfaces at a precise separation distance to provide a fully interactive 3-D model. This can then be utilised to assess the crystal shape and preferred orientation of bladed calcite precipitation in geothermal fracture sealing events.
- Further analysis on the 3-D structure of bladed calcite on a smaller scale may assess the link between the growth mechanisms and the grain boundary interactions. This in turn will lead to a better understanding how this controls the sealing ability of mineralisation in fractures that inhibit reservoir fluid flow.

- An examination of a larger set of calcite fractures by LA-ICP-MS will be required to successfully analysis the U levels, to separate the source of the Th and date the fracture sealing mineralisation by U-Series disequilibrium.
- Additional investigations into the source and movement of fluids will help further explain the reason for the Eu anomaly, especially the presence of both the negative and positive trends seen in the elemental relationship.

Reference List

Absar, A. (1988). Oxygen isotope and hydrothermal alteration studies at Kawerau and Ohaaki-Broadlands geothermal fields, New Zealand, *PHD Thesis, Auckland University.*

Absar, A., Blattner, P. (1985). Successive hydrothermal events, as indicated by oxygen isotope composition and petrography of greywacke basement rocks, Kawerau geothermal field, New Zealand, *Proceedings of the 7th New Zealand Geothermal Workshop,* 115-122.

Adams, C., Mortimer, N., Campbell, H., Griffin, W. (2009). Age and isotropic characterisation of metasedimentary rocks from the Torlesse Supergroup and Waipapa Group in the central North Island, New Zealand, *New Zealand Journal of Geology and Geophysics, 52,* 149-170.

Alcaraz, S., Rattenburry, M., Rosenberg, M., Soengkon, S., Bignall, G., Moerkerk, H. (2011). 3-D visualisation model of the Taupo Volcanic Zone basement, *New Zealand Geothermal Workshop 2011 Proceedings.*

Allis, R., Christenson, B., Nairn, I., Risk, G., White, S. (1993). The natural state of Kawerau geothermal field, *Proceedings of the 15th New Zealand Geothermal Workshop*.

Alkemper, J., Voorhees, P. (2001). Quantitative serial sectioning analysis, *Journal of Microscopy, 201 (3),* 388-394.

André, L., Rabemanana, V., Vuataz, F. (2006). Influence of water-rock interactions on fracture permeability of the deep reservoir at Soultz-sous-Forêts, France, *Geothermics, 35,* 507-531.

Arehart, G., Christenson, B., Wood, C., Foland, K., Browne, P. (2002). Timing of volcanic, plutonic, and geothermal activity at Ngatamariki, New Zealand, *Journal of Volcanology and Geothermal Research, 116,* 201-214.

Arnorsson, S. (1978). Precipitation of calcite from flashed geothermal waters in Iceland, *Contributions to Mineralogy and Petrology, 66,* 21-28.

Asanuma, H., Soma, N., Kaieda, H., Kumano, Y., Izumi, T., Tezuka, K., Niitsuma, H., Wyborn, D. (2005). Microseismic monitoring of hydraulic stimulation at the Australian HDR Project in Cooper Basin, *Proceedings World Geothermal Congress 2005*.

Bailey, R., Carr, R. (1994). Physical geology and eruptive history of the Matahina Ignimbrite, Taupo Volcanic Zone, North Island, New Zealand, *New Zealand Journal of Geology and Geophysics, 37,* 319-344.

Barker, S., Cox, S., Eggins, S., Gagan, M. (2006). Microchemical evidence for episodic growth of antitaxial veins during fracture-controlled fluid flow, *Earth and Planetary Science Letters, 250,* 331-344.

Barker, S., Bennett, V., Cox S., Norman, M., Gagan, M. (2009). Sm-Nd, Sr, C and O isotope systematics in hydrothermal calcite-fluorite veins: Implications for fluid-rock reaction and geochronology, *Chemical Geology, 268,* 58-66.

Baris, A. (2014). 3-D characterization of polycrystalline microstructure using a dual beam SEM-FIB system, *Master's Thesis, Eotvos University.*

Batzle, M., Simmons, G. (1976). Microfractures in rocks from two geothermal areas, *Earth and Planetary Science Letters, 30,* 71-93.

Begg, J., Mouslopoulou, V. (2010). Analysis of late Holocene faulting within an active rift using LIDAR, Taupo Rift, New Zealand, *Journal of Volcanology and Geothermal Research, 190,* 152-167.

Bertani, R. (2012). Geothermal power generation in the world 2005–2010 update report, *Geothermics, 41,* 1–29.

Bestmann, M., Prior, D. (2003). Intragranular dynamic recrystallization in naturally deformed calcite marble: Diffusion accommodated grain boundary sliding as a result of subgrain rotation recrystallization, *Journal of Structural Geology, 25,* 1597-1613.

Bibby, H., Caldwell, T., Davey, F., Webb, T. (1995). Geophysical evidence on the structure of the Taupo Volcanic Zone and its hydrothermal circulation, *Journal of Volcanology and Geothermal Research, 68,* 29–58.

Bignall, G., Milicich, S. (2012). Kawerau geothermal field: Geological framework. *GNS Science Consultancy Report 2012/118*, Institute of Geological & Nuclear Sciences, Lower Hutt, New Zealand.

Bignall, G., Milicich, S., Ramirez, E., Rosenberg, M., Kilgour, G., Rae, A. (2010). Geology of the Wairakei-Tauhara geothermal system, New Zealand, *Proceedings World Geothermal Congress,* 1-8.

Bischoff, J., Fitzpatrick, J. (1991). U-Series dating of impure carbonites: An isochron technique using total-sample dissolution, *Geochimica et Cosmochimica Acta, 55,* 543-554.

Blackwell, D., Negraru, P., Richards, M. (2007). Assessment of the enhanced geothermal system resource base of the United States, *Natural Resources Research, 15,* 283–308.

Bons, P., Elburg, M., Gomez-Rivas, E. (2012). A review of the formation of tectonic veins and their microstructure, *Journal of Structural Geology*, *43,* 33-62.

Brace, W. (1980). Permeability of crystalline and argillaceous rocks, *International Journal of Rock Mechanics and Mining Sciences & Geomechanics Abstracts, 17,* 241–251.

Brathewaite, R., Wood, C., Roesneberg, M., Faure, K. (2002). Porosity and permeabilty in the basement rocks at the Kawerau and Ohaaki geothermal fields, New Zealand, *Proceedings of the 24th New Zealand Geothermal Workshop,* 49-54.

Broomley, C. (2002). Putauaki (Kawerau) MT resistivity survey, *Proceedings of the 24th Geothermal Workshop,* 135-139.

Browne, P. (1978a). Petrological logs of drill holes Kawerau geothermal field, *Report NZGS, 84,* New Zealand Geological Survey, Lower Hutt, New Zealand.

Browne, P. (1978b). Hydrothermal alteration in active geothermal fields, *Annual Review of Earth and Planetary Sciences, 6,* 229-250.

Browne, P. (1979). Minimum age of the Kawerau geothermal field, North Island, New Zealand, *Journal of Volcanology and Geothermal Research, 6,* 213-215.

Browne, P., Ellis, A. (1970). The Ohaki-Broadlands hydrothermal area, New Zealand: Mineralogy and associated geochemistry, *American Journal of Science, 268,* 97-131.

Burkhard, M. (1993). Calcite twins, their geometry, appearance and significance as stress-strain markers and indicators of tectonic regime: A review, *Journal of Structural Geology, 15,* 351-368.

Carrol, L., Gamble, J., Houghton, B., Thordarson, T., Higham, T. (1997). A radiocarbon age determination for Mount Edgecumbe (Putauaki) vaolcano, Bay of Plenty, New Zealand, *New Zealand Journal of Geology and Geophysics,* 40, 559-562.

Chambefort, I., Lewis, B., Wilson, C., Rae, A., Coutts, C., Bignall, G., Ireland, T. (2014). Stratigraphy and structure of the Ngatamariki geothermal system from new zircon U-Pb geochronology: Implications for Taupo Volcanic Zone evolution, *Journal of Volcanology and Geothermal Research, 274,* 51-70.

Chen, K., Kunz, M., Tamura, N., Wenk, H. (2011). Deformation twinning and residual stress in calcite studied with synchrotron polychromatic x-ray microdiffraction, *Physics and Chemistry of Minerals, 38,* 491-500.

Christenson, B. (1987). Fluid-mineral equilibria in the Kawerau hydrothermal system, Taupo Volcanic Zone, New Zealand, *PHD Thesis, Auckland University.*

Christenson, B. (1997). Kawerau geothermal field: Geochemical structure of the reservoir and its response to exploitation, *Transactions of the Geothermal Resources Council, 21,* 17-24.

Clark, J., Milicich, S., Sewell, S., Askari, M., Wong, C. (2015). Finding sufficient permeability for outfield injection and recent drilling at Kawerau, New Zealand, *Proceedings World Geothermal Congress, 2015.*

Cole, J. (1979). Structure, petrology and genesis of Cenozoic volcanism, Taupo Volcanic Centre, New Zealand; a review, *Bulletin of volcanology, 51,* 177-185.

Cole, J. (1990). Structural control and origin of the volcanism in the Taupo-Hikurangi subduction system, *New Zealand Bulletin of Volcanology, 52 (6),* 445-368.

Cole, J. Darby, D., Stern, T. (1995). Taupo Volcanic Zone and Central Volcanic Region backarc structures of North Island, New Zealand, *Backarc Basins: Tectonics and Magmatism, 190 (1-2),* 123-135.

Cole, J., Lewis, K. (1981). Evolution of the Taupo-Hikurangi subduction system, *Tectonophysics, 72,* 1-21.

Cole, J., Spinks, K. (2009). Caldera volcanism and rift structure in the Taupo Volcanic Zone, New Zealand, *Geological Society, London, Special Publications, 327,* 9–29.

Cope, D., Bogie, I., Harvey, C., Menzies, A., Garcia, S. (1985). Calculation of calcite and anhydrite scaling potential in geothermal wells, *Proceedings of the 7th New Zealand Geothermal Workshop*, 123-130.

Davatzes, N., Hickman, S. (2010). Stress, fracture, and fluid-flow analysis using acoustic and electrical image logs in hot fractured granites of the Coso geothermal field, California, U.S.A., *in Dipmeter and borehole image log technology*, edited by Pöppelreiter, M., García-Carballido, C., Kraaijveld, M., AAPG Memoir, 92, 259-293.

Davatzes, N., Hickman, S. (2009). Fractures, stress and fluid flow prior to stimulation of well 27-15, Desert Peak, Nevada, EGS Project, *Proceedings of the 34th Workshop on Geothermal Reservoir Engineering*, 1-11.

De Bresser, J., Spiers, C. (1997). Strength characteristics of the *r*, *f*, and *c* slip systems in calcite, *Tectonophysics, 272,* 1-23.

Dempsey, D., Rowland, J., Archer, R. (2012). Modelling geothermal fluid flow and silica deposition along an active fault, *Proceedings of the 37th Workshop on Geothermal Reservoir Engineering*.

Dezayes, C., Genter, A., Valley, B. (2010). Structure of the low permeable naturally fractured geothermal reservoir at Soultz, *Comptes Rendus Geoscience, 342,* 517–530.

Dingley, D., Randle, V. (1992). Review: Microtexture determination by electron back-scatter diffraction, *Journal of Materials Science, 27,* 4545-4566.

Dobson, P., Kneafsey, T., Hulen, J., Simmons, A. (2003). Porosity, permeability, and fluid flow in the Yellowstone geothermal system, Wyoming, *Journal of Volcanology and Geothermal Research, 123,* 313-324.

Dodge, T. (1962). The determination of optic angle with the universal stage, *Journal Mineralogical Society of America, 19,* 62-75.

Eastwood, A., Gravley, D., Wilson, C., Chambefort, I., Oze, C., Cole, J., Ireland, T. (2013). U-Pb dating of subsurface pyroclastic deposits (Tahorakuri Fomation) at Ngatamariki and Rotokawa geothermal fields, *Proceedings of the 35th New Zealand Geothermal Workshop.*

Eggins, S., Grun, R., McCulloch, M., Pike, A., Chappell, J., Kinsley, L., Mortimer, G., Shelley, M., Murry-Wallace, C., Spotl, C., Taylor, L. (2005). In-situ U-Series dating by laser ablation multi-collector ICPMS: New prospects for Quaternary geochronogy, *Quaternary Science Reviews, 24,* 2523-2538.

Ferrill, D. (1991). Calcite twin widths and intensities as metamorphic indicators in natural low-temperature deformation of limestone, *Journal of Structural Geology, 13,* 667-675.

Ferrill, D., Morris, A., Evans, M., Burkhard, M., Groshong, R., Onasch, C. (2004). Calcite twin morphology: A low-temperature deformation geothermometer, *Journal of Structural Geology, 26,* 1521-1529.

Fournier, R. (1985). Carbonate transport and deposition in the epithermal environment, *Reviews in Economic Geology, 2,* 63-71.

Genter, A., Traineau, H. (1996). Analysis of macroscopic fractures in granite in the HDR geothermal well EPS-1, Soultz-sous-Forêts, France, *Journal of Volcanology and Geothermal Research, 72,* 121-141.

Genter, A., Evans, K., Cuenot, N., Fritsch, D., Sanjuan, B. (2010). Contribution of the exploration of deep crystalline fractured reservoir of Soultz to the knowledge of enhanced geothermal systems (EGS), *Competes Rendus Geoscience, 342,* 502-516.

Geyth, M. (2001). Reflections on the ^{230}Th/U dating of dirty material, *Geochronometria, 20,* 9-14.

Grant, M., Bixley, P. (2011). *Geothermal reservoir engineering (2nd Edition)*, Academic Press, Burlington.

Grimes, S., Rickard, D., Hawksworth, C., Calsteren, P., Browne, P. (1998). A U-Th calcite isochron age from an active geothermal field in New Zealand, *Journal of Volcanology and Geothermal Research, 81,* 327-333.

Grindley, G., (1965). The geology, structure and exploration of the Wairakei geothermal field, Taupo, New Zealand, *New Zealand Geological Survey Bulletin, 7,* 131.

Grindley, G., (1986). Subsurface geology and structure of the Kawerau geothermal field, *DSIR Geothermal Report 10,* 49-65.

Groshong, R. (1972). Strain calculated from twinning in calcite, *Geological Society of America Bulletin, 83,* 2025-2038.

Groshong, R., Teufel, L., Gasteiger, C. (1984). Precision and accuracy of the calcite strain-gage technique, *Geological Society of America Bulletin, 95,* 357-363.

Gupta, H., Roy, S. (2007). *Geothermal energy; an alternative resource for the 21st Century,* Elsevier, Oxford.

Halfpenny, A. (2010). Some important practical issues for the collection and manipulation of electron backscatter diffraction (EBSD) data from geological samples, *Journal of the Virtual Explorer, 35.*

Hébert, R., Ledésert, B., Genter, A., Bartier, D., Dezayes, C. (2011). Mineral precipitation in geothermal reservoir: The study case of calcite in the Soultz-sous-Forêts enhanced geothermal system, *Proceedings, 36th Workshop on Geothermal Reservoir Engineering*.

Hedenquist, J. (1990). The thermal and geochemical structure of the Broadlands-Ohaaki geothermal system, New Zealand, *Geothermics, 19,* 151-185.

Hedenquist, J., Henley, W. (1985). Hydrothermal eruptions in the waiotapu geothermal system, New Zealand: Their origin, associated breccias, and relation to precious metal mineralization, *Economic Geology, 80,* 1640-1665

Henneberger, R., Browne, P. (1988). Hydrothermal alteration and evolution of the Ohauri hydrothermal system, Taupo Volcanic Zone, New Zealand, *Journal of Volcanology and Geothermal Research, 34,* 211-231.

Hilgers, C., Dilg-Gruschinski, K., Urai, J. (2004). Microstructural evolution of syntaxial veins formed by advective flow, *Geology, 32,* 261-264.

Holm, A., Blodgett, L., JenneJohn, D., Gawell, K. (2010). *Geothermal; international market update,* Geothermal Energy Association, accessed on the 15/05/2014 from

www.geo-energy.org/pdf/reports/gea_international_market_report_final_may_2010.pdf.

Houghton, B., Wilson, C., McWilliams, M., Lanphere, M., Weaver, S., Briggs, R., Pringle, M. (1995). Chronology and dynamics of a large silicic magmatic system: Central Taupo Volcanic Zone, New Zealand, *Geology, 23 (1),* 13-16.

Huberty, J., Kita, N., Kozdon, R., Heck, P., Fournelle, J., Spicuzza, J., Xu, H., Valley, J. (2010). Crystal orientation effects in $\delta^{18}O$ for magnetite and hematite by SIMS, *Chemical Geology, 276,* 269-283.

Hurst, A., Bibby, H., Robinson, R. (2002). Earthquake focal mechanisms in the central Taupo Volcanic Zone and their relation to faulting and deformation. *New Zealand Journal of Geology and Geophysics, 45,* 527–536.

Hurst, T., Bannister, S., Robinson, R., Scott, B. (2008). Characteristics of three recent earthquake sequences in the Taupo Volcanic Zone, New Zealand. *Tectonophysics 452,* 17– 28.

Jennejohn, D., Hines, B., Gawell, K., Blodgett, L. (2012). *Geothermal; international market overview report,* Geothermal Energy Association, accessed on the 15/05/2014 from http://geo-energy.org/pdf/reports/2012-GEA_International_Overview.pdf.

Jorgensen, P., Hansen, K., Larsen, R., Bowen J. (2009). A framework for automated segmentation in three dimensions of microstructural tomography data, *Ultrmicroscopy, 110(3),* 216-228.

Kakimoto, P. (1983). Hydrothermal alteration and fluid-rock interaction in the TH3 and THM1 drillholes, Tauhara geothermal field, New Zealand, *Master's Thesis, Auckland University.*

Kral, M., Mangan, M., Rosenber, R., Spanos, G. (2000). Three dimensional analysis of microstructures, *Materials Characterisation, 45(1),* 17-23.

Kral, M., Ice, G., Miller, M., Uchic, M., Rosenberg, R. (2004). Three dimensional microscopy, *in ASM Handbook, vol. 9, Metallography and Microstructure,* edited by Vander Voort, G. ASM International, accessed on the 15/05/2015 from http://www.asminternational.org/web/ims/store/-/journal_content/56/10192/ASMHBA0003760/PUBLICATION.

Krupp, R., Seward, T. (1987). The Rotokawa geothermal system, New Zealand; an active epithermal gold-depositing environment, Economic *Geology, 82,* 1109–1129.

Ku, T. (1976). The uranium-series method age determination, *Annual Review Earth Planet Sciences, 4,* 347-379.

Ku, T., Liang, Z. (1984). The dating of impure carbonates with decay series isotopes, *Nuclear Instruments and Methods in Physics Research, 233(1-3),* 563-571.

Lacombe, O., Laurent, P. (1992). Determination of principal stress magnitudes using calcite twins and rock mechanics data, *Tectonophysics, 202,* 83-93.

Lefaucheux, F., Robert, M., Authier, A. (1973). Étude des défauts créés lors de perturbations extérieures imposées au cours de la croissance hydrothermale de calcite, *Journal of Crystal Growth, 19,* 329-337.

Lefaucheux, F., Robert, M. (1977). Defects revealing two growth processes for a face case of hydrothermal synthetic calcite, *Journal of Crystal Growth, 38,* 29-37.

Leonard, G., Begg, J., Wilson, C. (2010). Geology of the Rotorua area: Scale 1:250,000, *Institute of Geological & Nuclear Sciences 1:250,000 geological map 5*, Institute of Geological & Nuclear Sciences Limited, Lower Hutt, New Zealand.

Litchfield, N., Van Dissen, R., Sutherland, R., Barnes, P., Cox, S., Norris, R., Beavan, R., Langridge, R., Villamor, P., Berryman, K., Stirling, M., Nicol, A., Nodder, S., Lamarche, G., Barrell, D., Pettinga, J., Little, T., Pondard, N., Mountjoy, J., Clark, K. (2014). A model of active faulting in New Zealand, *New Zealand Journal of Geology and Geophysics, 57,* 32-56.

Liu, T., Raabe, D., Zaefferer, S. (2008). A 3-D tomographic EBSD analysis of a CVD diamond thin film, *Science and Technology of Advanced materials, 9,* 1-6.

Ludwig, K., Tittering, D. (1994). Calculation of ^{230}Th/U isochrones, ages, and errors, *Geochimica et Cosmochica Acta, 58 (22),* 5031-5042.

Machel, H., Burton, E. (1991). Factors governing cathodoluminescence in calcite and dolomite, and their implications for studies of carbonite diagenesis, *in Luminescence Microscopy and Spectroscopy: Qualitative and Quantitative Application,* edited by Barker, C., Kopp, O., SEPM Short course 25, 37-57.

Machel, H., Mason, R., Mariano, A., Mucci, A. (1991). Causes and emissions of luminescence in calcite and dolomite, *in Luminescence Microscopy and Spectroscopy: Qualitative and Quantitative Application,* edited by Barker, C., Kopp, O., SEPM Short course 25, 9-25.

Mariani, E., Prior, D., McNamara, D., Pearce, M., Seaton, N., Seward, G., Tatham, D., Wheeler, J. (2008). Electron backscatter diffraction (EBSD) in the SEM: Applications to microstructures in minerals and rocks and recent technological advancements, *in Instrumental Techniques Applied to Mineralogy and Geochemistry,* edited by Subias, I., Bauluz, B., Seminarios de la Sociedad Espanola de mineralogia, 5, 7-19.

Marrett, R., Laubach, S. (1997). Diagenetic controls on fracture permeability and sealing, *International Journal of Rock Mechanics and Mining Sciences, 34*.

Massiot, C., McNamara, D., Nicol, A., Townend, J., (2015). Fracture width and spacing distributions from borehole televiewer logs and core in the Rotokawa geothermal field, New Zealand, *Proceedings World Geothermal Congress 2015*.

Meier, D., Gunnlaugsson, E., Gunnlaugsson, I., Jamtveit, B., Peacock, C., Benning, L. (2014). Microstructural and chemical variation in silica-rich precipitates at the Hellisheioi geothermal power plant, *Mineralogical Magazine, 78 (6),* 1381-1389.

Meunier, A. (2005). *Clays*, Springer, Berlin, 467.

McLean, K., McNamara, D. (2011). Fractures interpreted from acoustic formation imaging technology: Correlation to permeability, *Proceedings, 36th Workshop on Geothermal Reservoir Engineering*.

McNamara, D., Faulkner, D., McCarney, E. (2014). Rock properties of greywacke basement hosting geothermal reservoirs, New Zealand: Preliminary results, *Proceedings, 39th Workshop on Geothermal Reservoir Engineering*.

McNamara, D., Massiot, C., Lewis, B., Wallis, I. (2015). Heterogeneity of structure and stress in the Rotokawa geothermal field, New Zealand, *Journal of Geophysical Research, 120,* 1243-1262.

Melcher, A., Unser, A., Reichhardt, M., Nestler, B., Potschke, M., Selzer, M. (2010). Conversion of EBSD data by a quaternion based algorithm to be used for grain structure simulations, *Technische Mechanik, 30 (4),* 401-413.

Milicich, S. (2013). Petrology of selected samples from the Kawerau geothermal field, *GNS Science report 2013/05,* Institute of Geological & Nuclear Sciences, Lower Hutt, New Zealand.

Milicich, S., Bignall, G. (2012). Kawerau geothermal field geological framework, *GNS Science Report, 2012/33,* Institute of Geological & Nuclear Sciences, Lower Hutt, New Zealand.

Milicich, S., Wilson, C., Bignall, G., Pezaro, B., Bardsley, C. (2013). Reconstructing the geological and structural history of an active geothermal field: A case study from New Zealand, *Journal of Volcanology and Geothermal Research, 262,* 7-24.

Milicich, S., Bardsley, C., Bignal, G., Wilson, C. (2014a). 3-D interpretive modelling applied to the geology of the Kawerau geothermal system, Taupo Volcanic Zone, New Zealand, *Geothermics, 51,* 344-350.

Milicich, S., Chambefort, I., Bignall, G., Clark, J. (2014b). Overprinting hydrothermal systems in the Taupo Volcanic Zone, *Geothermal Resources Council Transactions, 38,* 511-516.

Milicich, S., Clark, J., Wong, C., Askari, M. (2016), A review of the Kawerau geothermal field, New Zealand, *Geothermics.*

Moyes, L., Parkman, R., Charnock, J., Vaughan, D., Livens, F., Hughs, C., Braithwaite, A. (2000). Uranium uptake from aqueous solution by interaction with goethite, lepidococite, muscovite, and mackinawite: An x-ray absorption spectroscopy study, *Environmental Science and Tecchnology, 34 (6),* 1062-1068.

Nairn, I. (2002). Geology of the Okataina Volcanic Centre: Scale 1:50,000, *Institute of Geological & Nuclear Sciences geological map 25,* Institute of Geological & Nuclear Sciences Limited, Lower Hutt, New Zealand.

Nairn, I., Beanland, S. (1989). Geological setting of the 1987 Edgecumbe earthquake, New Zealand, *New Zealand Journal of Geology and Geophysics, 32,* 1-13.

Nairn, I., Wiradiradja, S. (1980). Late Quaternary hydrothermal explosion breccias at Kawerau geothermal field, New Zealand, *Bulletin Volcanologique, 43(1),*1-13.

Nicol, A., Walsh, J., Berryman, K., Villamor, P. (2006). Interdependence of fault displacement rates and paleoearthquakes in an active rift, *Geology, 34,* 865.

Noiriel, C., Renard, R., Doan, M., Gratier, J., (2010). Intense fracturing and fracture sealing induced by mineral growth in porous rocks, *Chemical Geology, 269,* 197-209.

Nord, G. (1994). Transformation-induced twin boundaries in minerals, *Phase Transitions, 48,* 107-134.

Nüchter, J., Stöckhert, B. (2007). Vein quartz microfabrics indicating progressive evolution of fractures into cavities during postseismic creep in the middle crust, *Journal of Structural Geology, 29,* 1445-1462.

Okamoto, A., Sekine, K. (2011). Texture of syntaxial quartz veins synthesized by hydrothermal experiments, *Journal of Structural Geology, 33,* 1764-1775.

Piazolo, S., Prior, D., Holness, M. (2005). The use of combined cathodoluminescence and EBSD analysis: A case study investigating grain boundary migration mechanisms in quartz, *Journal of Microscopy, 217,* 152-161.

Prior, D., Trimby, P., Weber, U. (1996). Orientation contrast imaging of microstructures in rocks using forescatter detectors in the scanning electron microscope, *Mineralogical Magazine, 60,* 859-869.

Ratter, K. (2012). Surface preparation for electron backscatter diffraction investigation using low energy Ar and high energy focussed Ga ion beams, *Master's Thesis, Eotvos University*.

Reeder, R. (1991). An overview of zoning in carbonate minerals, *in Luminescence Microscopy and Spectroscopy: Qualitative and Quantitative Application,* edited by Barker, C., Kopp, O., SEPM Short course 25, 77-82.

Richards, L., Read, S. (2007). New Zealand greywacke characteristics and influences on rock mass behaviour, *11th Congress of the International Society for rock Mechanics*.

Rowe, K., Rutter, E. (1990). Palaeostress estimation using calcite twinning: Experimental calibration and application to nature, *Journal of Structural Geology, 12,* 1-17.

Rowland, J., Sibson, R. (2004). Structural controls on hydrothermal flow in a segmented rift system, Taupo Volcanic Zone, New Zealand, *Geofluids, 4,* 259-283.

Rowland, J., Simmons, S. (2012). Hydrologic, magmatic, and tectonic controls on hydrothermal flow, Taupo Volcanic Zone, New Zealand: Implications for the formation of epithermal vein deposits, *Economic Geology, 107,* 427–457.

Saishu, H., Okamoto, A., Tsuchiya, N. (2015). The role of silica precipitation in the permeable-impermeable boundary within the earth's crust, *Proceedings World Geothermal Congress 2015.*

Sausse, J., Fourar, M., Genter, A. (2006). Permeability and alteration within the Soultz granite inferred from geophysical and flow log analysis, *Geothermics, 35,* 544–560.

Schwarcz, H., Latham, A. (1989). Dirty calcites: 1. Uranium-series dating of contaminated calcite using leachates alone, *Chemical Geology (Isotope Geosciences Section), 80,* 35-43.

Seebeck, H., Nicol, A., Villamor, P., Ristau, J., Pettinga, J. (2014). Structure and kinematics of the Taupo Rift, New Zealand, *Tectonics, 33*.

Sheridan, J., Kovac, K., Rose, P., Barton, C., McCulloch, J., Berard, B., Moore, J., Petty, S., Spielman, P. (2003). In-situ stress, fracture and fluid flow analysis – East flank of the Coso geothermal field, *Proceedings 28th Workshop on Geothermal Reservoir Engineering*.

Simmons, S., Christenson, B. (1994). Origins of calcite in a boiling geothermal system, *American Journal of Science, 294,* 361-400.

Spanos, G., Rowenhorst, D., Lewis A., Geltmacher, A. (2008). Combining serial sectioning, EBSD analysis, and image-based finite element modelling, *MRS Bulletin, 33,* 597-602.

Spinks, K., Acocella, V., Cole, J., Bassett, K. (2005). Structural control of volcanism and caldera development in the transitional Taupo Volcanic Zone, New Zealand, *Journal of Volcanology and Geothermal Research, 144*, 7-22.

Steiner, A. (1955). Wairakite, the calcium analogue of analcime, a new zeolite mineral, *Mineralogical Magazine, 30,* 691-698.

Stimac, J., Nordquist, G., Sumnar, A., Sirad-Azwar, L. (2008). An overview of the Awibengkok geothermal system, Indonesia, *Geothermics, 37,* 300-331.

Studt, F. (1958). Geophysical reconnaissance at Kawerau, New Zealand, *New Zealand Journal of Geology and Geophysics, 1(2),* 219-246.

Sturchio, N., Binz, C. (1988). U-Series age determination of calcite veins, VC-1 drill core, Valles Caldera, New Mexico, *Journal of Geophysical Research, 93-B6,* 6097-6102.

Teng, H., Dove, P., De Yoreo, J. (2000). Kinetics of calcite growth: Surface processes and relationships to macroscopic rate laws, *Geochimica et Cosmochimica Acta, 64,* 2255-226.

Townend, J., Sherburn, S., Arnold, R., Boese, C., Woods, L. (2012). Three-dimensional variations in present-day tectonic stress along the Australia–Pacific plate boundary in New Zealand, *Earth and Planetary Science Letters, 353-354,* 47–59.

Tulloch, A. (1982). Mineralogical observations on carbonate scaling in geothermal wells at Kawerau and Broadlands, *Proceedings of the 4th New Zealand Geothermal Workshop*.

Turner, S., Van Calsteren, P., Vigier, N., Thomas, L. (2001). Determination of thorium and uranium isotope ratios in low-concentration geological materials using a fixed multi-collector-ICP-MS, *Journal of Analytical Atomic Spectrometry, 16,* 612-615.

Uchic, M. (2011). Serial sectioning methods for generating 3-D characterization data of grain and precipitate seal microstructures, *in Computational Methods for Microstrue-Property Relationships*, edited by Ghosh, S., Dimiduk, D., Springe, 31-52.

Unal-Imer, E., Uysal, T., Isik, V., Zhao, J., S, J. (2014). A high-resolution geochronological and geochemical study on Aegean carbonate deposits, SW Turkey, *EGU,* accessed on the 15/06/2015 from http://meetingorganizer.copernicus.org/EGU2014/EGU2014-16265-2.pdf.

Villamor, P., Berryman, K. (2001). A late Quaternary extension rate in the Taupo Volcanic Zone, New Zealand, derived from fault slip data, *New Zealand Journal of Geology and Geophysics, 44,* 243-269.

Villamor, P., Berryman, K., Nairn, I., Wilson, K., Litchfield, N., Ries, W. (2011). Associations between volcanic eruptions from Okataina volcanic centre and surface rupture of nearby active faults, Taupo Rift, New Zealand: Insights into the nature of volcano-tectonic interactions, *Geological Society of America Bulletin, 123,* 1383-1405.

Weir, G. (2001). Heat output from the spreading and rifting models of the Taupo Volcanic Zone, New Zealand, *Journal of Applied Mathematics and Decision Sciences, 5 (2),* 105-118.

Wallace, L., Beavan, J., McCaffrey, R., Darby, D. (2004). Subduction zone coupling and tectonic block rotations in the North Island, New Zealand, *Journal of Geophysical Research, 109,* 1978-2012.

Wallis, I., McNamara, D., Rowland, J., Massiot, C. (2012). The nature of fracture permeability in the basement greywacke at Kawerau geothermal field, New Zealand, *Proceedings, 37th Workshop on Geothermal Reservoir Engineering*.

Wilkinson, A., Meaden, G., Dingley, D. (2009). Mapping strains at the nanoscale using electron back scatter diffraction, *Supperlattices and Microstructure, 45,* 285-294.

Wilson, C., Rowland, J. (2016), The volcanic, magmatic and tectonic setting of the Taupo Volcanic Zone, New Zealand, reviewed from a geothermal perspective, *Geothermics.*

Wilson, C., Bignall, G., Chambefort, I., Cole, J., Charlier, B., Eastwood, A., Gravley, D., Ireland, T., Milicich, S., Pezaro, B., Rosenburg, M., Speulveda, F., Woodem, J. (2015). Insights into geothermal system from U-Pb dating of zircons in hydrothermally altered rocks: New Zealand experience, *Proceedings World Geothermal Congress 2015,* 19-25.

Wilson, C., Houghton, B., McWilliams, M., Lanphere, M., Weaver, S., Briggs, R. (1995). Volcanic and structural evolution of the Taupo Volcanic Zone, New Zealand: A review, *Journal of Volcanology and Geothermal Research, 68,* 1-28.

Wiltschko, D., Morse, J. (2001). Crystallisation pressure versus "crack seal" as the mechanism for banded veins, *Geology, 29,* 79-82.

Wohletz, K., Heiken, G. (1992). *Volcanology and geothermal energy,* University of California Press, Berkeley.

Wood, C., Brathwaite, R., Rosenberg, M. (2001). Basement structure, lithology and permeability at Kawerau and Ohaaki geothermal fields, *New Zealand, Geothermics, 30,* 461-481.

Xu, M., Kovarik, L., Arey, B., Felmy, A., Rosso, K., Kerisit, S. (2014). Kinetics and mechanisms of cadmium carbonate heteroepitaxial growth at the calcite (10-14) surface, *Geochimica et Cosmochimica Acta, 134,* 221-233.

Zaefferer, S., Wright, S., Raabe, D. (2008). Three-dimensional orientation microscopy in a focused ion beam-scanning electron microscope: A new dimension of microstrure characterization, *Metallurgical and Materials Transactions A, 39 (2),* 374-389.

Appendix 1: Sample Preparation Methodology

Samples of surface exposed basement greywacke were used in practicing preparation methods for serial sectioning of the drill core. These samples were collected from surface exposures for an earlier study to determine the mechanical properties of the basement terranes of the Kawerau Geothermal field (McNamara et al., 2014). Located in the major axial ranges along the edge of the Taupo Volcanic Zone (TVZ) these locations included the Blue Duck Quarry, Whakatane (Torlesse terrane) and Waotu Quarry, Tokoroa (Waipapa terrane) (Figure A.1.1) (McNamara et al., 2014). The exposed lithology of these ranges have been identified to comprise of Mesozoic to Cenozoic greywacke of the Torlesse (Composite) terrane to the South and East with the Waipapa terrane to the North and West, a physically and chemically similar greywacke as that which comprises the basement lithology of the Kawerau geothermal field and a majority of the TVZ (Cole and Spinks 2009; McNamara et al., 2014).

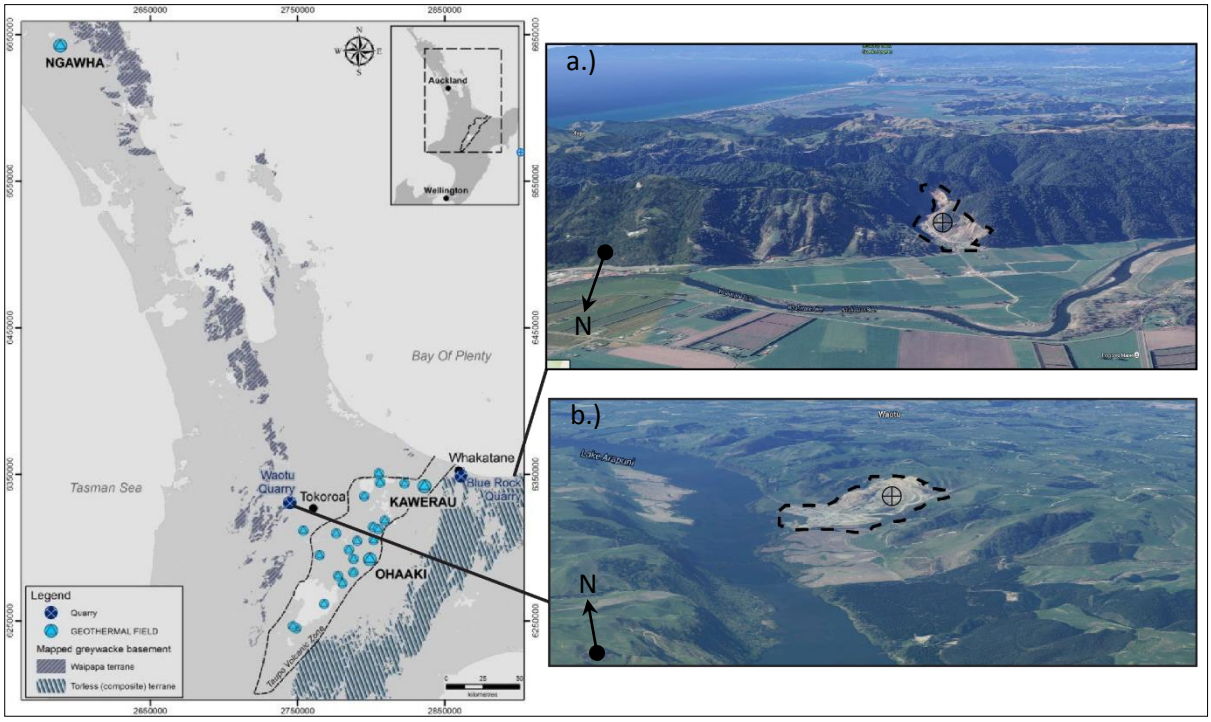

Figure A.1.1 Map locations for the samples taken for the initial preparation for serial section. Insert shows both locations a.) Blue Rock Quarry looking South and b.) Waotu Quarry looking North. (Adapted from McNamara et al., 2014).

All of the collected samples comprised of fresh greywacke which appeared similar to the core fragments which make up the bases of this study. A dark grey greywacke consisting of fine grained meta-sediments with black inclusions. There were also a series of wide (2-4 mm) white mineralised fractures present in some of the samples (Figure A.1.2).

Some of the mineralised fractures were initially confirmed to contain calcic minerals with weak hydrochloric acid with others being a mixture of possible quartz and zeolite.

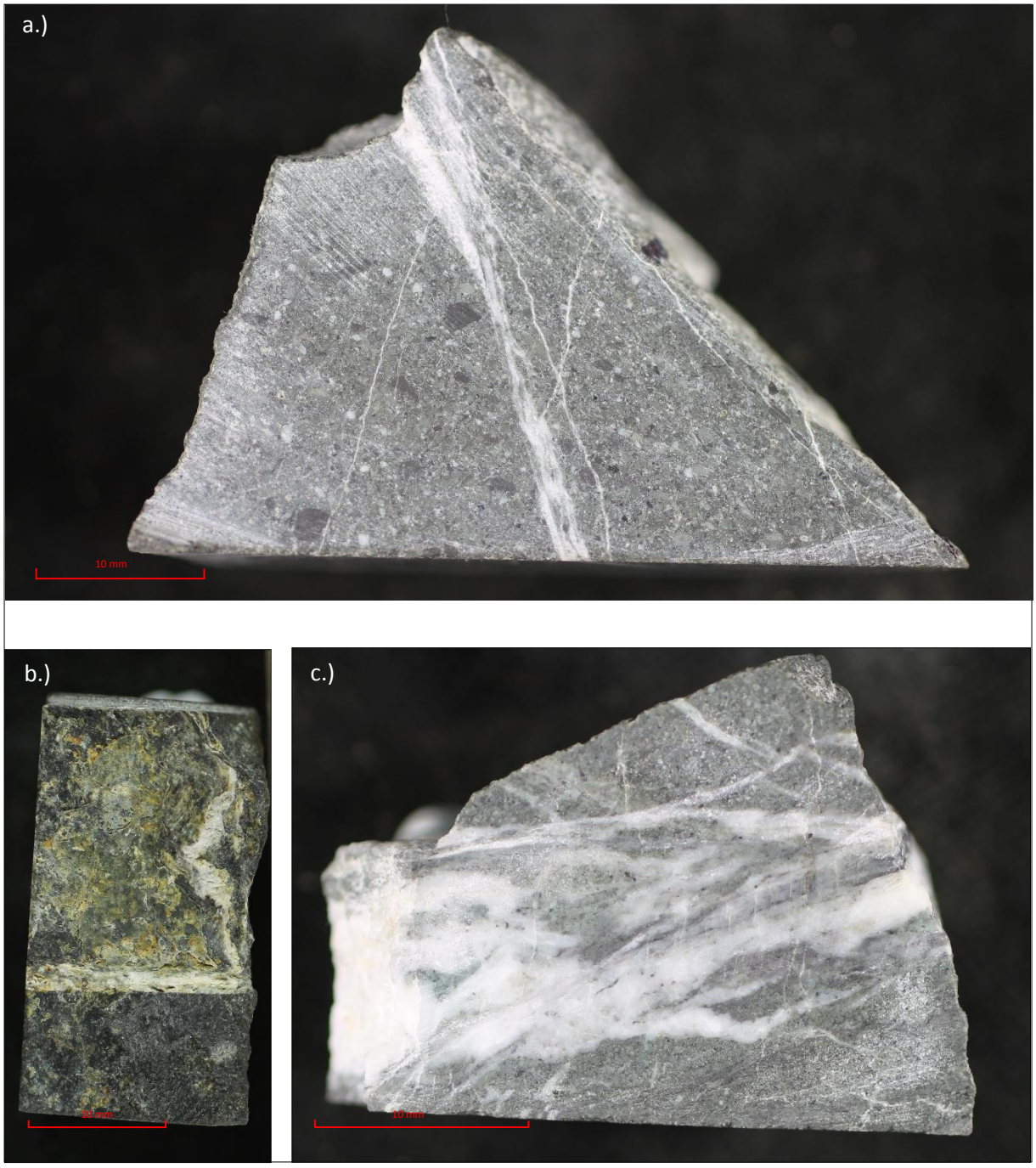

Figure A.1.2 Images of the 3 samples, a.) WAGW 0.0 vein has some calcite. b.) WAGW 11.3 unknown vein, possibly quartz, no reaction with HCL. c.) WAGW 11.11 vein has some calcite plus unknown minerals.

These samples of outcrop greywacke were used in this study to develop procedures related to preparation for serial sectioning due to the fact that they behaved similar mechanically to the drill-core. One noticeable difference between the core and outcrop samples is that the core has evidence of alteration related to geothermal processes. Practice preparation methods were

carried out and refined on these samples for their ease of availability and to preserve the core where possible for later analyses.

Four of these samples were prepared for initial electron backscatter diffraction (EBSD) and energy dispersive x-ray (EDX) analysis within the scanning electron microscope (SEM), two plugs (Figure A.1.3) were created using KonductoMet a powdered carbonite mounting compound and two plugs were prepared using resin epoxy (Figure A.1.4). During the process of creating the mounting plugs in the powdered carbonite Sample WAGW 11.11 was crushed along one side (Figure A.1.3a) within the mounting press. This was due to a lack of powdered carbonite material surrounding the sample leading to the platens applying excess pressure to the edges of the sample. Following this occurrence Sample plug WAGW 0.0 was packed with extra powder and mounted successfully without any visible defects in the greywacke or surrounding carbonite (Figure A.1.3b). For further information on the process of creating the carbonite plug see Chapter 3 and Appendix 2.

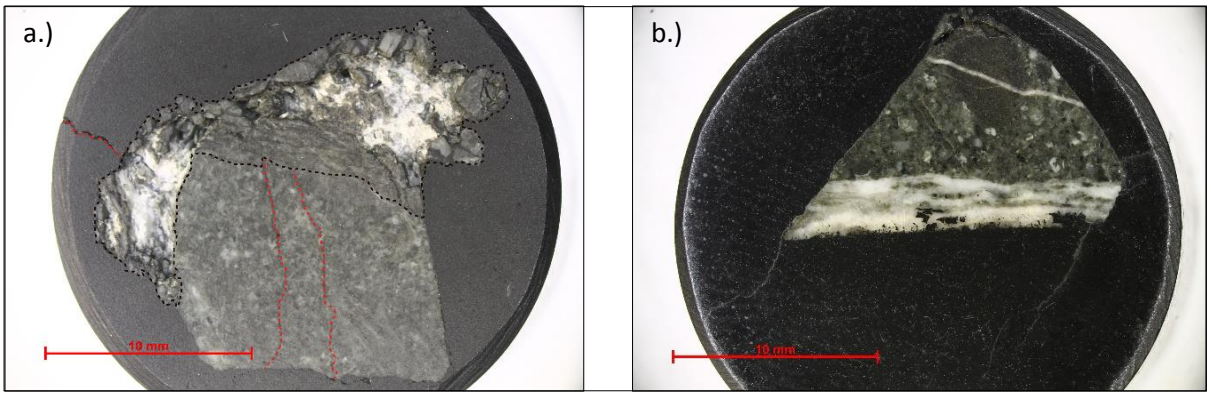

Figure A.1.3 Top down view of WAGW 0.0 (a.) and WAGW 11.11 (b.) carbonite plug, with the main mineralised fracture orientated horizontally as placed within the SEM. Note the crushed zones and both the cracks (red and black dotted lines) in the rock and carbonite material in b.).

Sample WAGW 0.0 and WAGW 11.11 were both encased in epoxy resin which resulted in no difficulties while preparing the mounting plugs (Figure A.1.4a and A.1.4b).

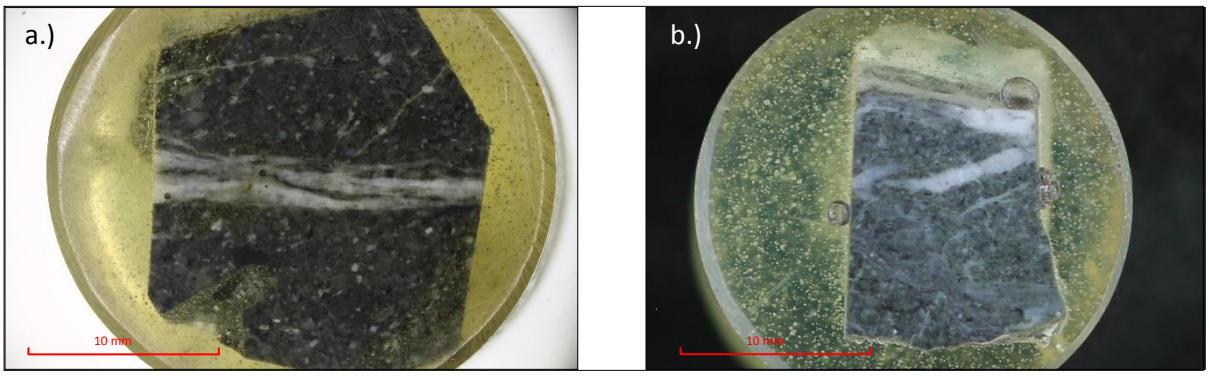

Figure A.1.4 Top down view of WAGW 0.0 (a.) and WAGW 11.11 (b.) epoxy plug, with the main mineralised fracture orientated horizontally as placed within the SEM.

Both types of plug were then polished and prepared for imaging in the SEM using the same method as outlined in Chapters 2 and 3. The powdered carbonite provided an evenly polished finish compared to the epoxy. To prevent further surface charging both plug's top surfaces were pre-coated in carbon by sputtering process prior to being placed in the SEM. Figure A.1.5a and A.1.5b displays the difference in the charging effect that can occur within the SEM with the powdered carbonite plug effectively preventing this from occurring.

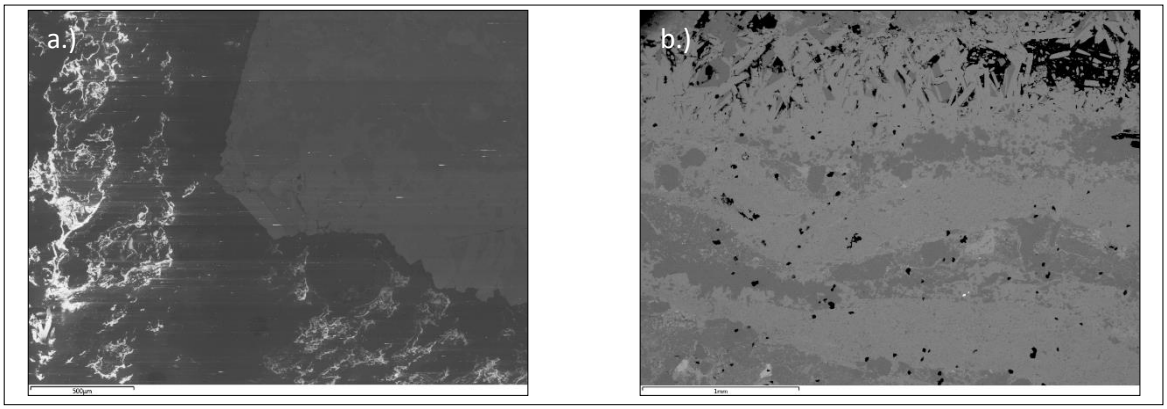

Figure A.1.5 Electron images showing the charging effect and lack of for both mounting materials within the SEM a.) An epoxy resin plug showing evidence of charging and b.) a powdered carbonite plug.

The EDX chemical signature of these veins indicated that the mineralisation present was predominantly zeolite minerals with silicic ribbons and rare disseminated calcite grains (Figure A.1.6 and A.1.7). Due to the crystallographic properties of zeolite which lead to poor EBSD indexing, EBSD grain orientation was not undertaken for this stage.

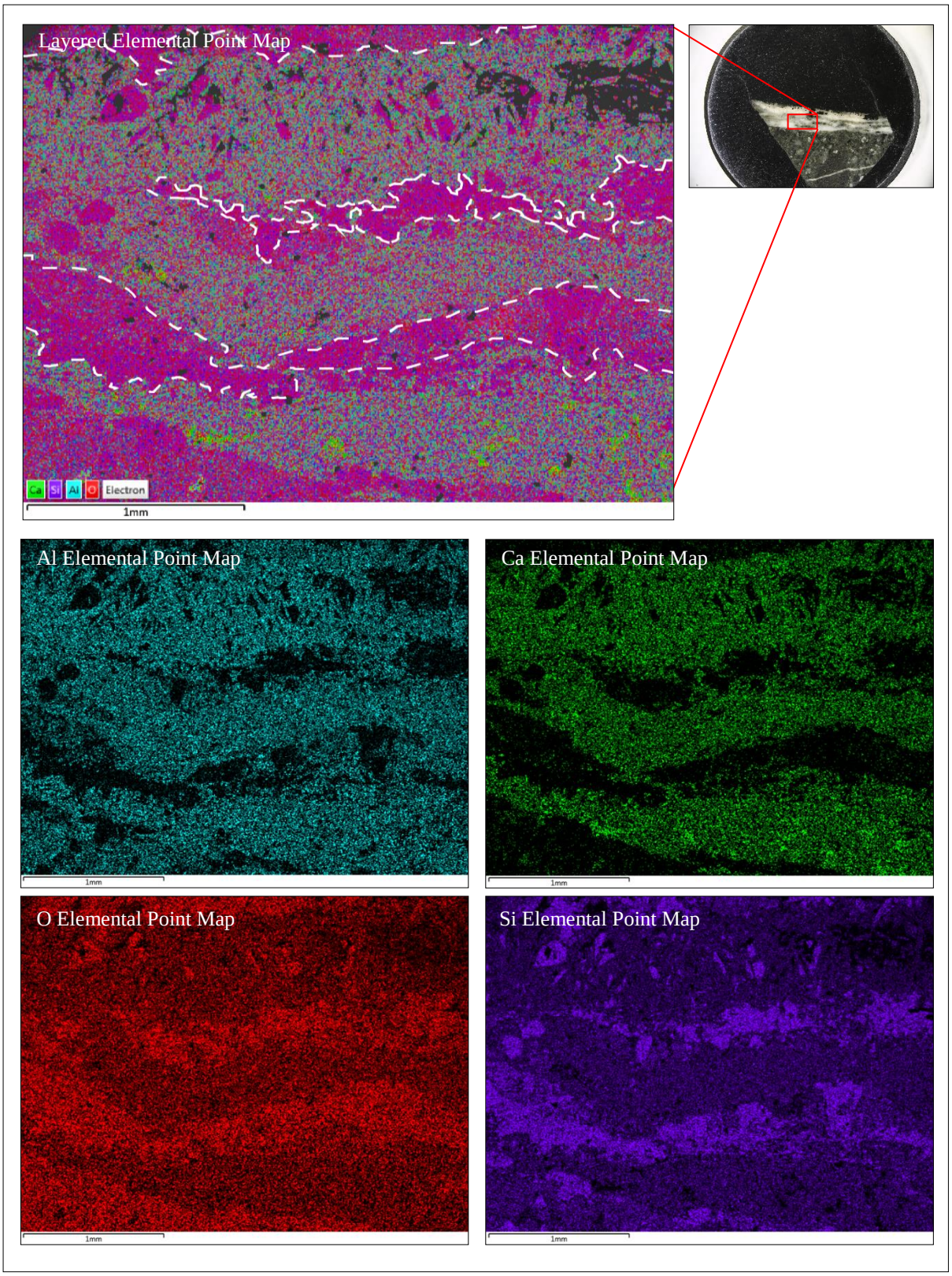

Figure A.1.6 EDX images of elemental point maps for the WAGW 0.0 in the carbonite plug. Dashed white areas include silicate regions within the vein.

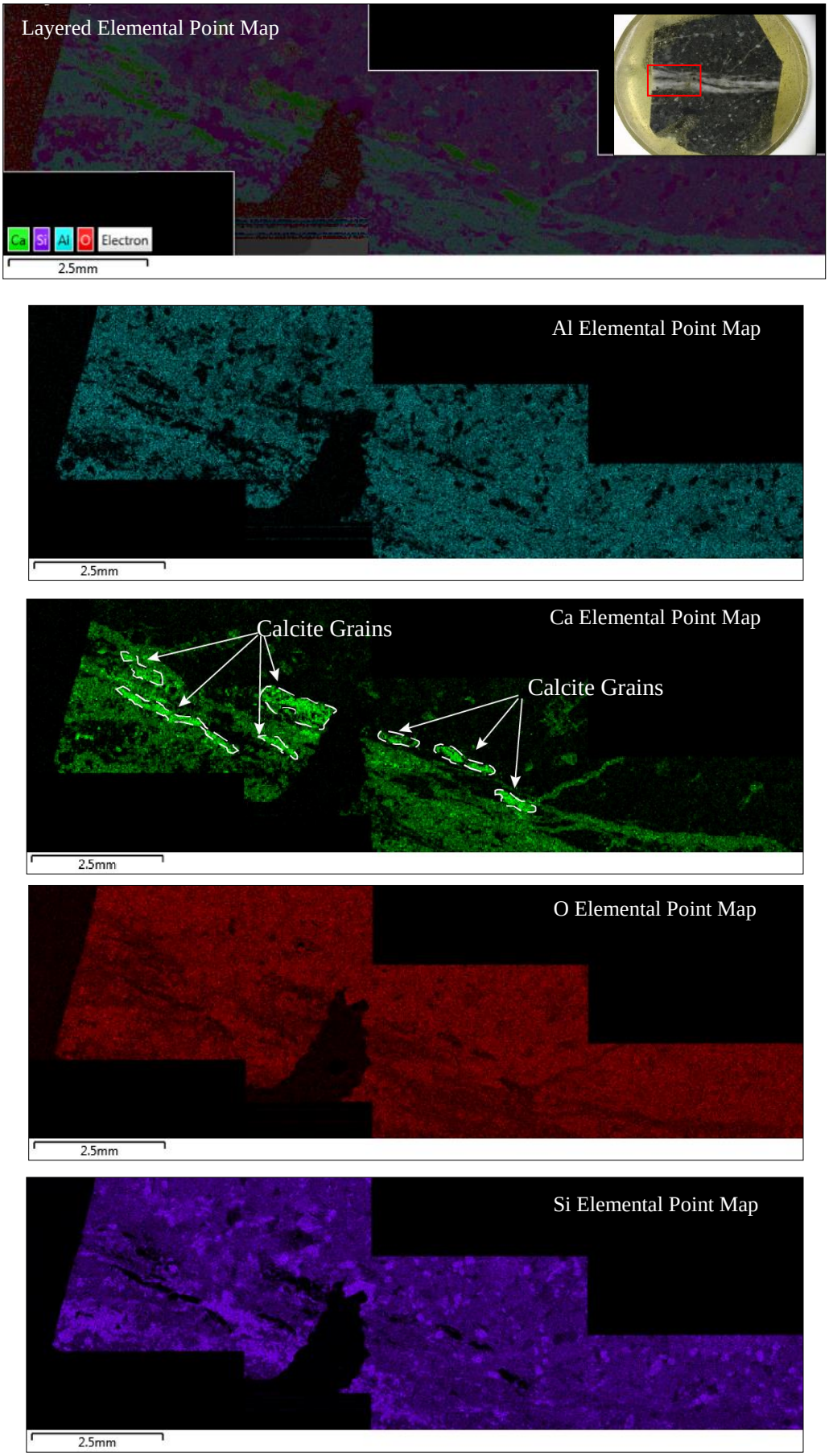

Figure A.1.7 EDX images of elemental point maps for the WAGW 0.0 in the epoxy plug with calcite grans highlighted.

The outcomes of this initial pilot study into the preparation methods for this style of serial sectioning indicate that;

1. The powdered carbonite was far superior then the epoxy for creating the sectioning plug. This is due to the fact that it provided a better finish to the scanned surface as well as reducing charging in the SEM even when the epoxy sample's was carbon coated.
2. We identified that the carbonite mounting process can induce significant damage to the sample. Therefore care is needed to be taken when preparing the carbonite plugs by packing adequate powder around the sample for mounting.
3. SEM operating parameters were refined to produce high quality scans in reasonable times, including sample orientation and placement within the SEM chamber. This included a pre-determined AZtec profile optimised for calcite detection.
4. Sufficient calcite mineralised veining was not present in the geothermally un-altered greywacke from both locations.

Appendix 2: Powdered Carbonite Briquette Mounting Process and Preparation for Scanning.

Outlined below is the process of producing the core fragment briquette (plug) in powdered carbonite for serial sectioning and scanning in the scanning electron microscope (SEM).

Once the ideal sample of core was selected it was mounted in a powdered material called KonductoMet, a conductive filled phenolic mounting compound produced by Buehler Ltd. and referred to in the text as powdered carbonite. This compound produced a conductive briquette or surrounding plug for the fragment. The briquette plug was produced using a Buehler SimpliMet 1000 automatic mounting press (Figure A.2.1) located in the thin sectioning lab, at the Department of Geology, University of Otago.

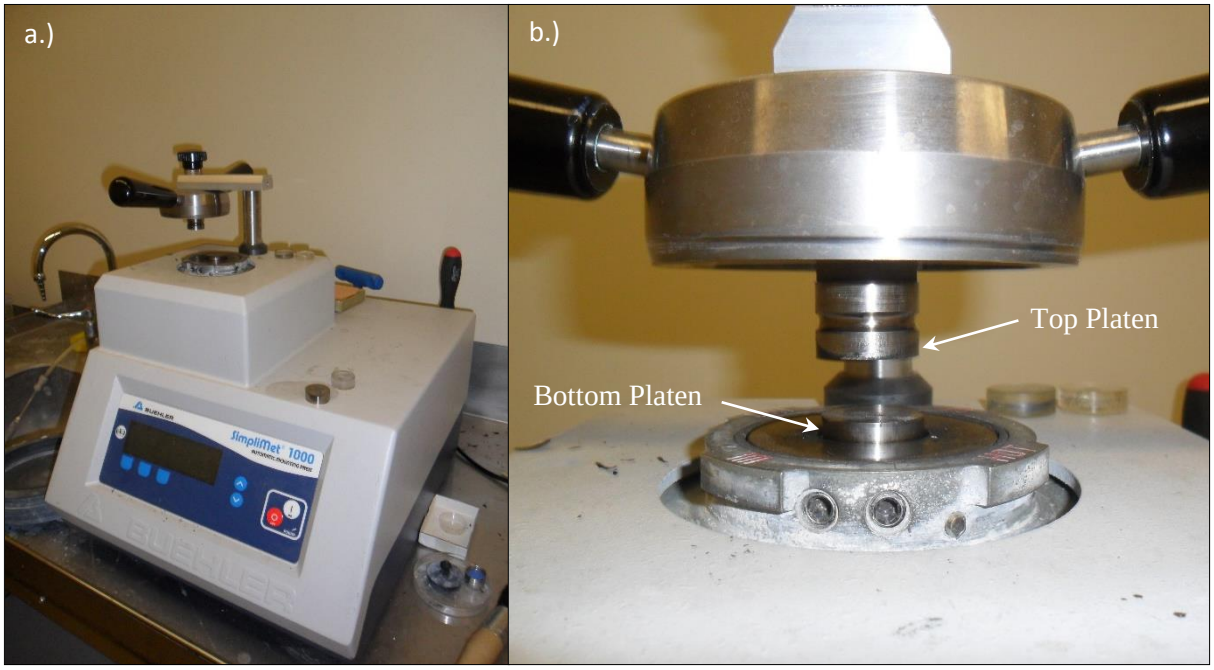

Figure A.2.1 a.) The Buehler Simplimet 1000 automatic mounting press located in the Polishing Lab, Department of Geology, The University of Otago. b.) The platens and chamber for the mounting process.

To create a briquette with the sample encased the fragment was placed within a mould filled with an adequate amount of the powdered compound and then mounted (Figure A.2.2). The mounting process for the powdered carbon compound required for the sample and powder to be heated to 150°C at 290 bar for a cycle at temperature of heat (1.5 minutes)/cool (3 minutes). The heat/cool times do not include ramp up and cool down time.

Figure A.2.2 Sample fragment surrounded in the powdered carbon.

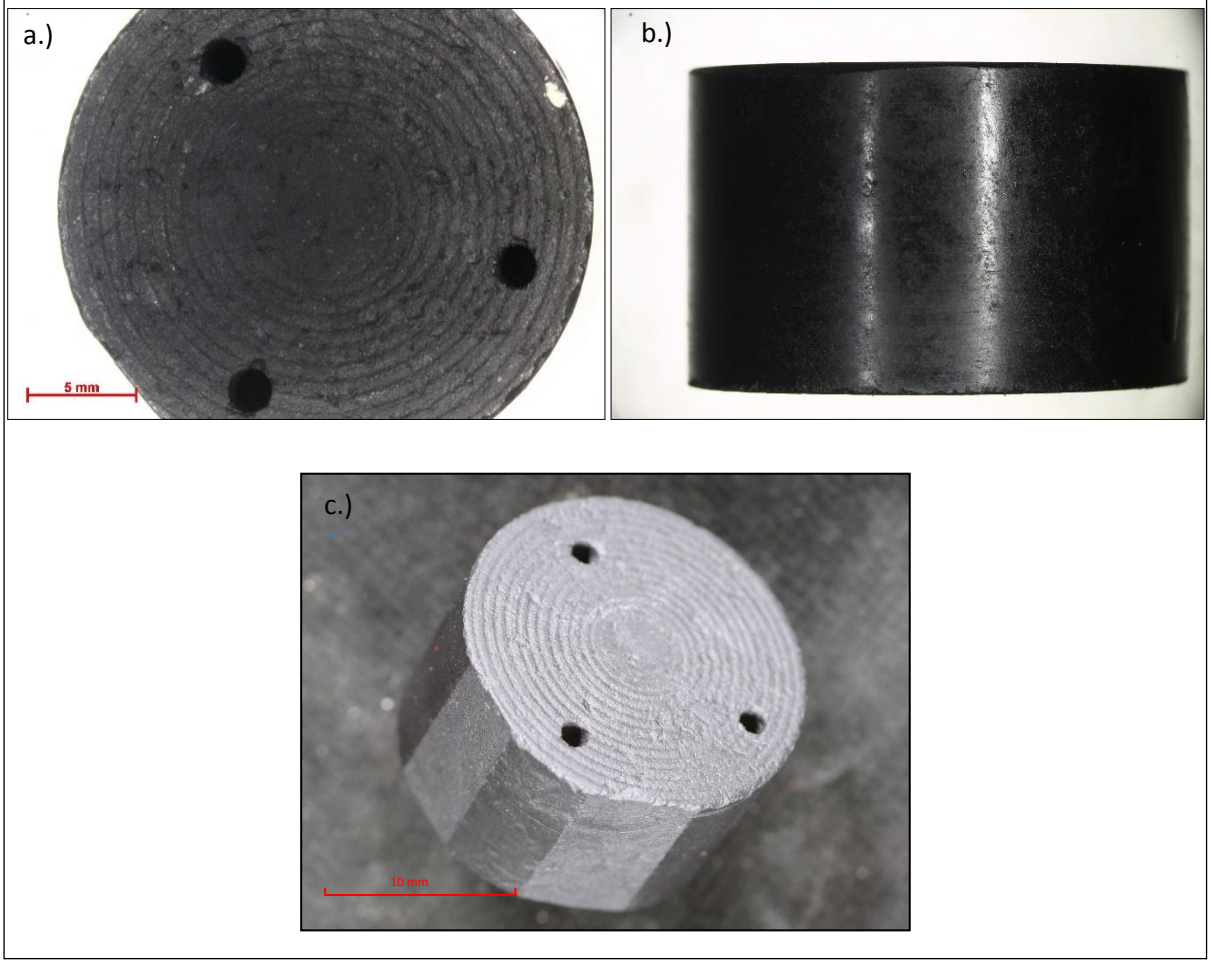

Figure A.2.3 The finished briquette, a.) looking down on the sample, b.) side on and c.) oblique angle.

Finally prior to scanning in the SEM the fresh surface was sputter coated with vaporised carbon using an Emitech K250 Carbon Coater located in the at the Otago Centre for Electron Microscopy (OCEM).

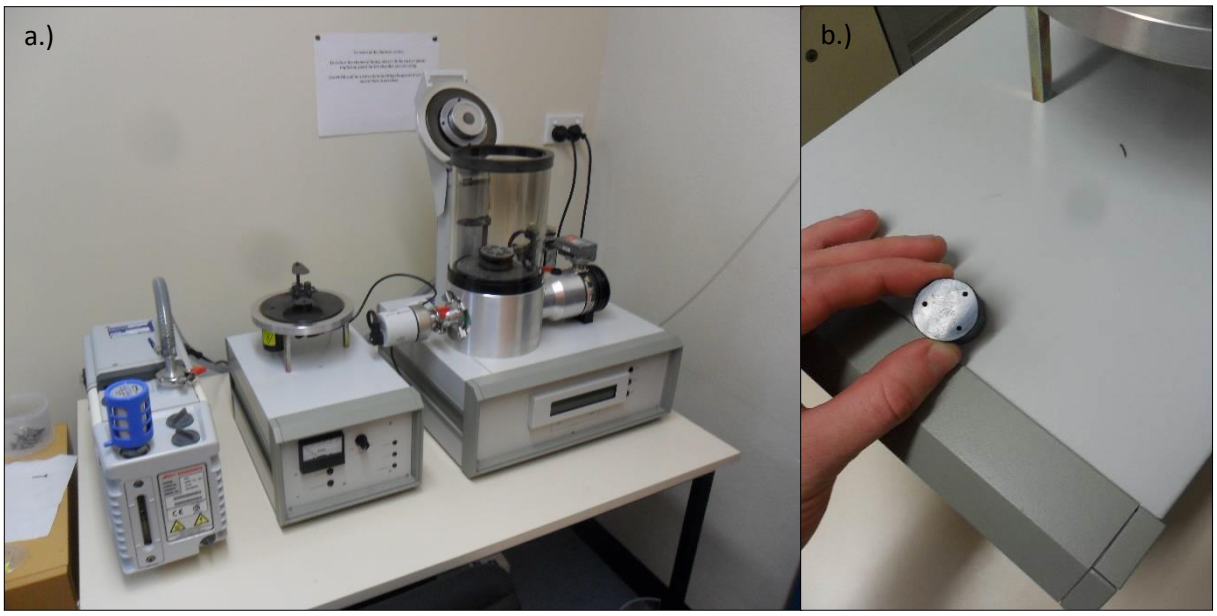

Figure A.2.4 a.) The carbon coater located at the OCEM and b.) the surface of the sample once it has been coated in vaporised carbon.

Appendix 3: Sectioned Slice Surfaces

Prior to each Scanning Electron Microscope (SEM) analysis an image of the freshly sectioned surface was taken, with these images presented below, included is the SEM electron image:

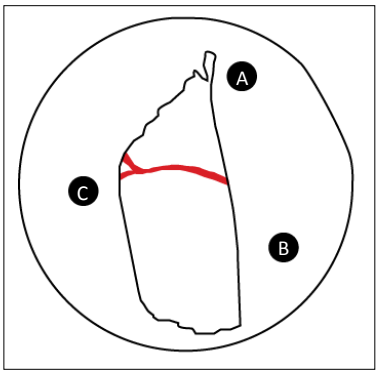

Figure A.3.1 Schematic of the vein (red) location within the briquette and labelled Fiducial markers.

Slice 1

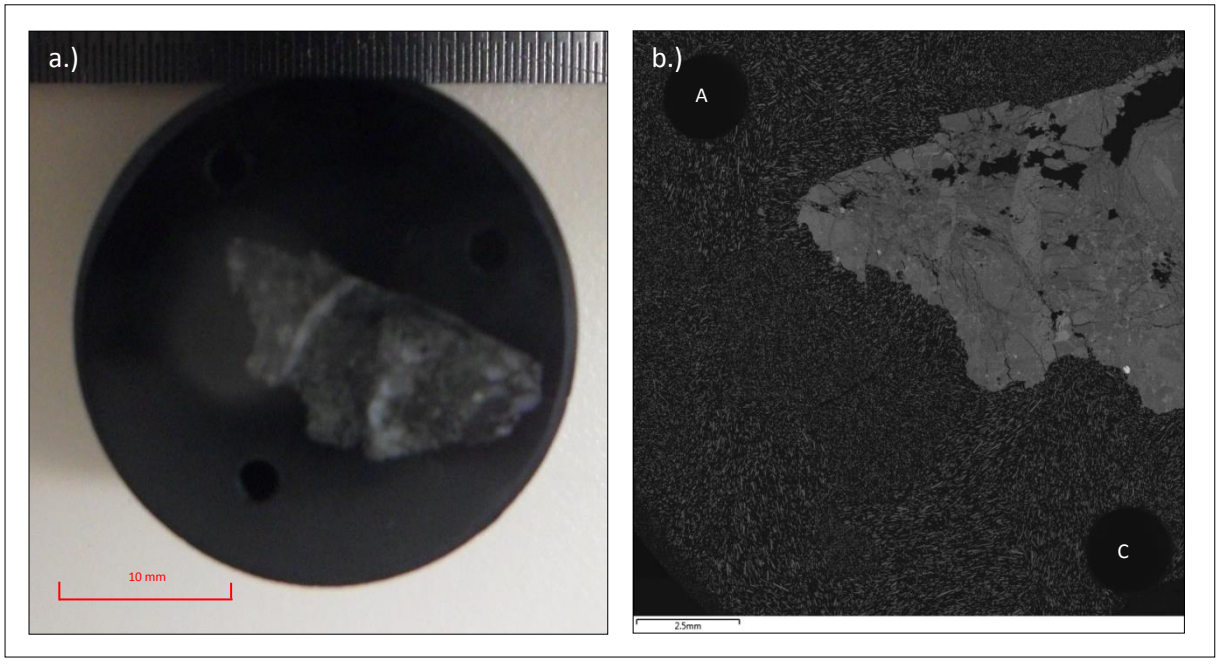

Figure A.3.2 a.) Scanned surface 1 with a partial view of the fracture and b.) SEM electron image.

Slice 2

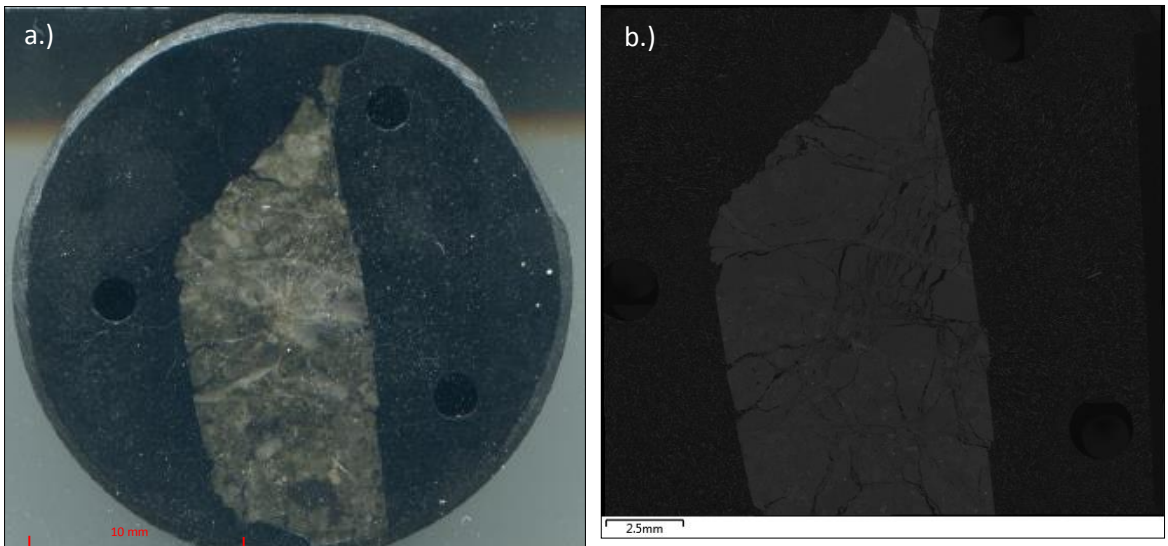

Figure A.3.3 a.) Scanned surface 2 and b.) SEM electron image.

Slice 3

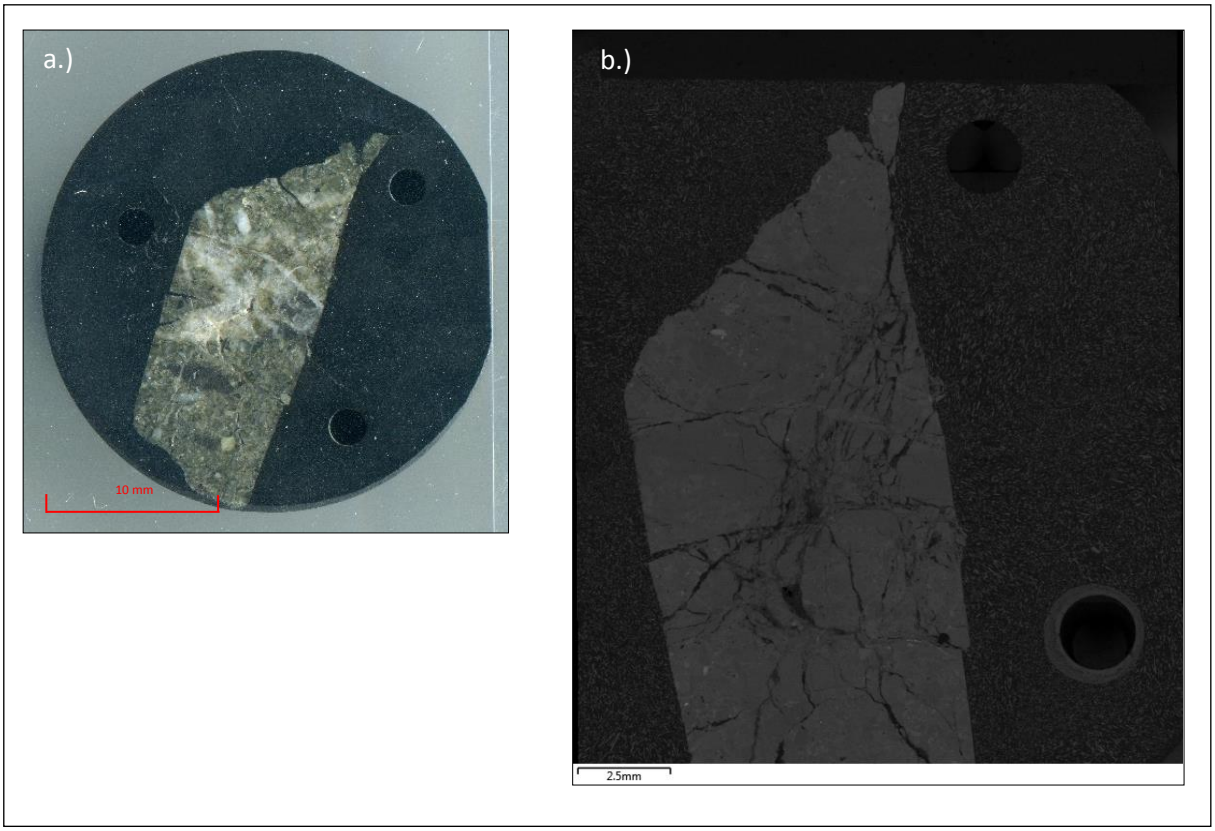

Figure A.3.4 a) Scanned surface 3 and b.) SEM electron image.

Slice 4

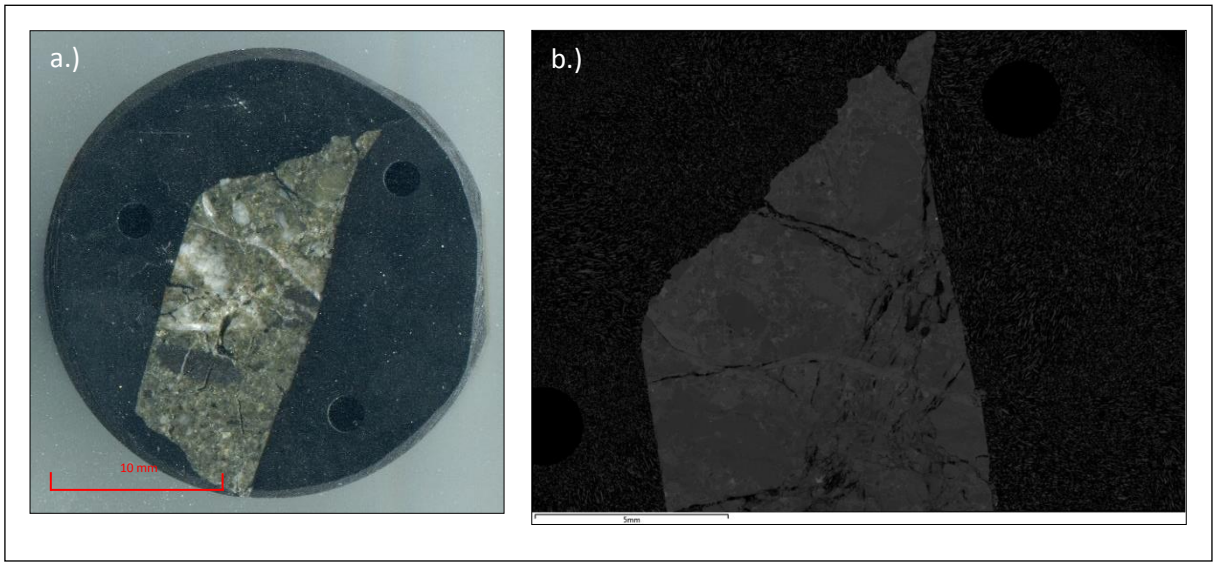

Figure A.3.5 a.) Scanned surface 4 with and b.) SEM electron image.

Slice 5

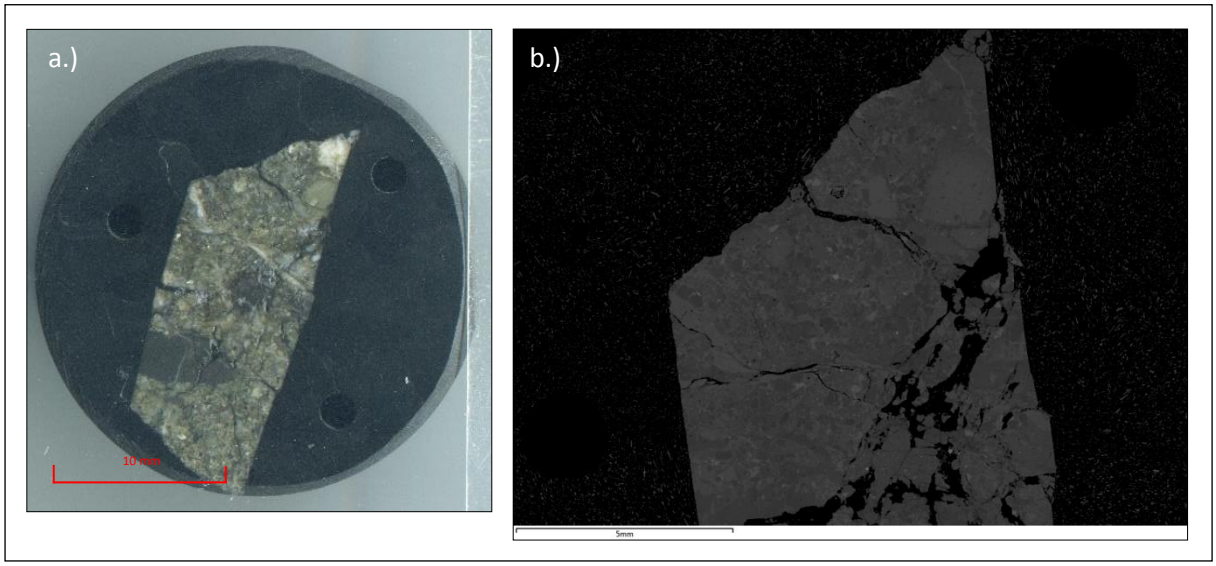

Figure A.3.6 a) Scanned surface 5 and b.) SEM electron image.

Slice 6

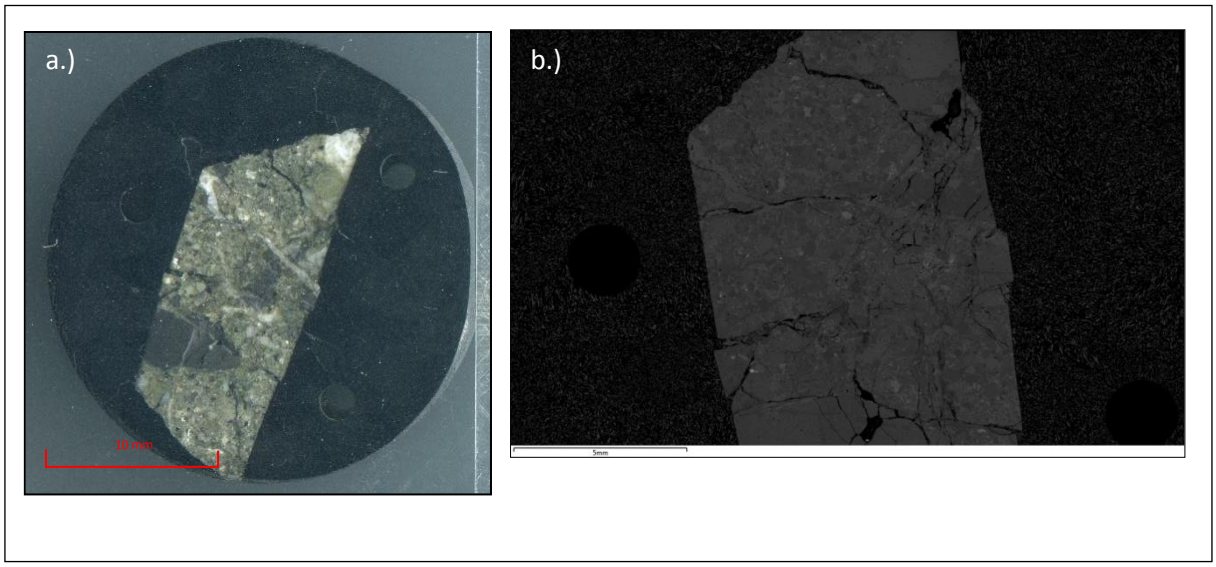

Figure A.3.7 a) Scanned surface 6 and b.) SEM electron image.

Slice 7

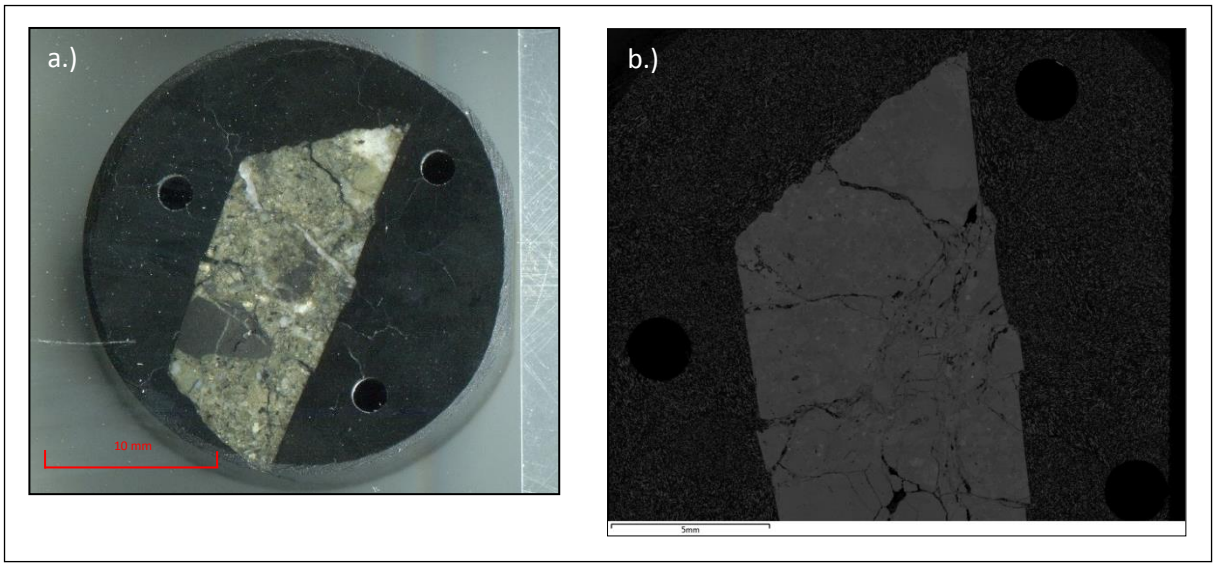

Figure A.3.8 a) Scanned surface 7 and b.) SEM electron image.

Slice 8

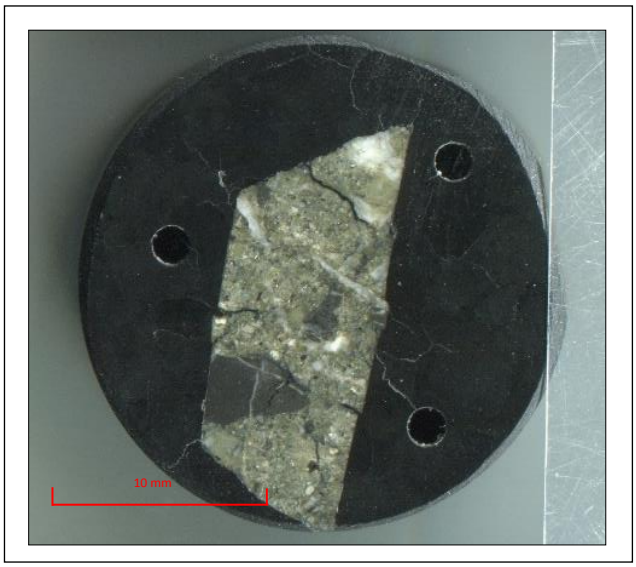

Figure A.3.9 Scanned image of surface 8, imaged but not scanned in the SEM.

Appendix 4: Table of Sectioning Slice Measurements

Due to the fact that each sectioned slice was not automated the briquette was measured between grinding sequences. Table A.4.1 presents the measurements for each slice and a brief comment on the polishing finish of the sectioned surface. The initial 3 surfaces were measured during the grinding process with the final 5 sections having additional calliper measurements. To assess if the surface was being ground level for the final 5 slices, an average of 3 measurements were taken at each point A, B, and C (Figure A.4.1) with an average of these final 3 measurements (A, B, and C) providing the final separation measurement.

Table A.4.1 Measurements between sectioned surfaces, including surface and sample comments.

Slice	Date Run	Δ D Measurement (μm)	Average Briquette Thickness Measurement at A (μm)	Average Briquette Thickness Measurement at B (μm)	Average Briquette Thickness Measurement at C (μm)	Average Briquette Thickness of A, B, and C (μm)	Comments
1	28/05/3014	0					Rough, only part of vein visible.
2	30/05/2014	≈170					Polish better, whole vein imaged.
3	5/06/2014	≈100					
4	6/08/2014	>100	16210	16240	16270	16310	
5	11/08/2014	750.0	15540.0	15546.7	15523.3	15560.0	Rough, needed epoxy set, major crack through right vein
6	26/08/2014	237.0	15286.7	15276.7	15303.3	15323.0	Smooth surface, nice polish less cracks then previous.
7	23/09/2014	10	15210.0	15223.3	15220.0	15200	
8	-	70.0	15123.3	15170.0	15133.3	15130	

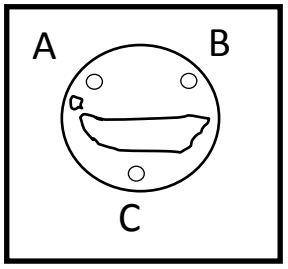

Figure A.4.1 Diagram depicting where each of the three measurements were taken in relation to the Fiducial markers.

Appendix 5: Serial Sectioning Energy Dispersive X-ray (EDX) Elemental Point Maps

Presented below are the energy dispersive x-ray (EDX) elemental count maps for each serial sectioned slice that included EDX analysis. These maps of elemental counts assist with qualitatively understanding both mineral and elemental distribution.

Slice 1:

No EDX data for this slice.

Slice 2:

No EDX data for this slice.

Slice 3:

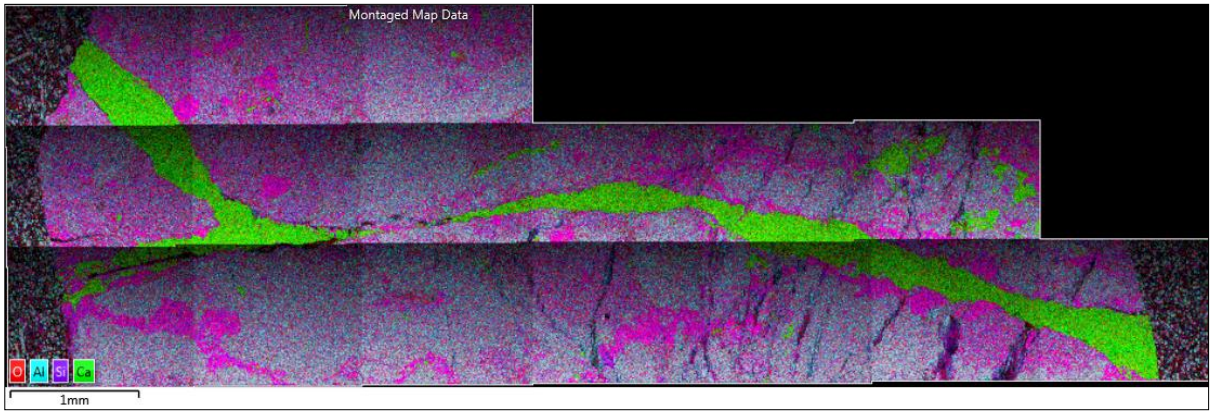

Figure A.5.1 Layered EDX elemental point map.

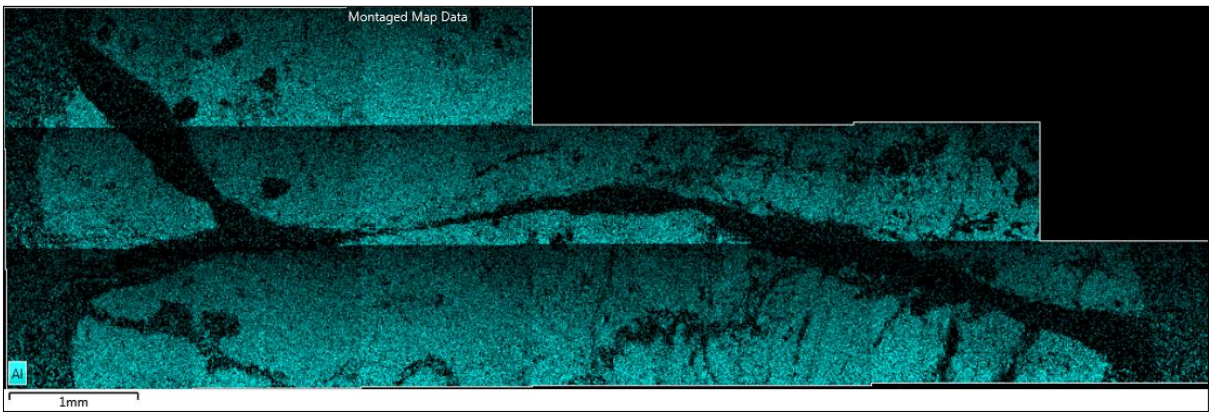

Figure A.5.2 EDX aluminium elemental point map.

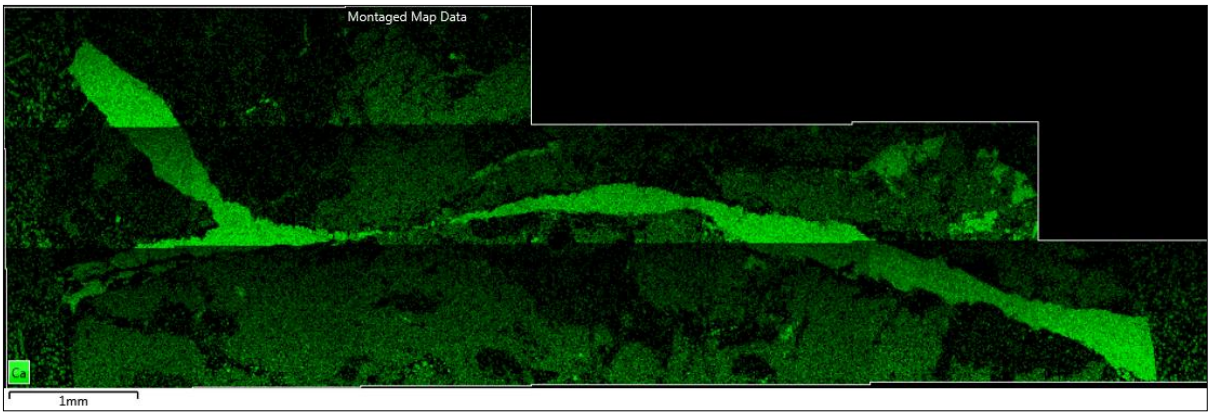

Figure A.5.3 EDX calcium elemental point map.

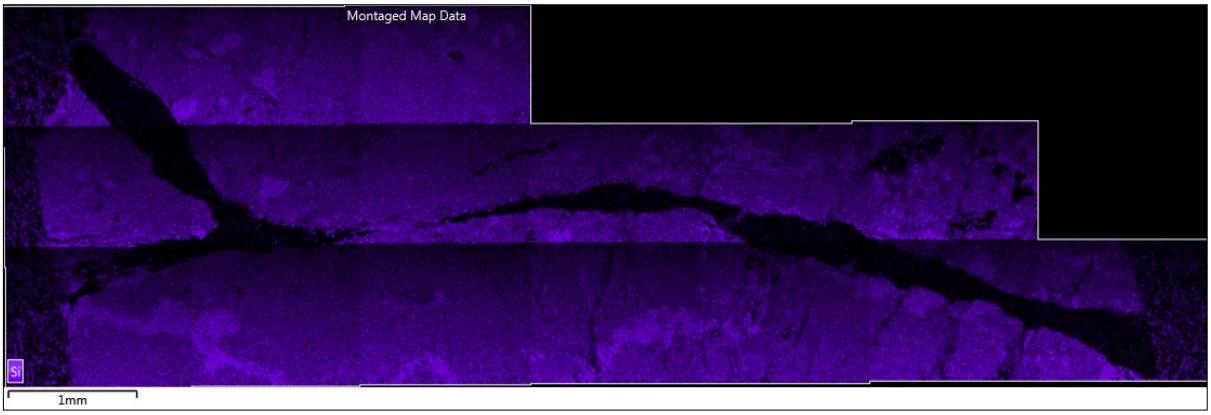

Figure A.5.4 EDX silica elemental point map.

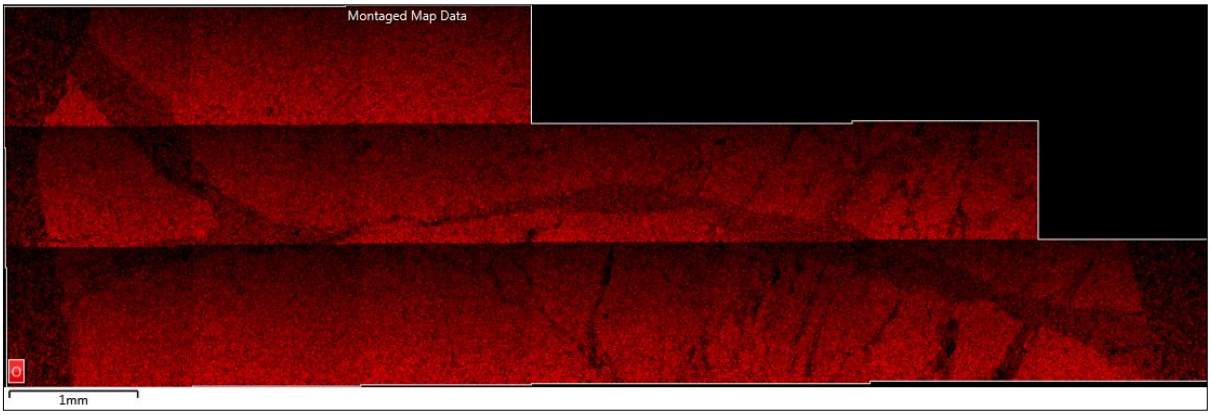

Figure A.5.5 EDX oxygen elemental point map.

Slice 4:

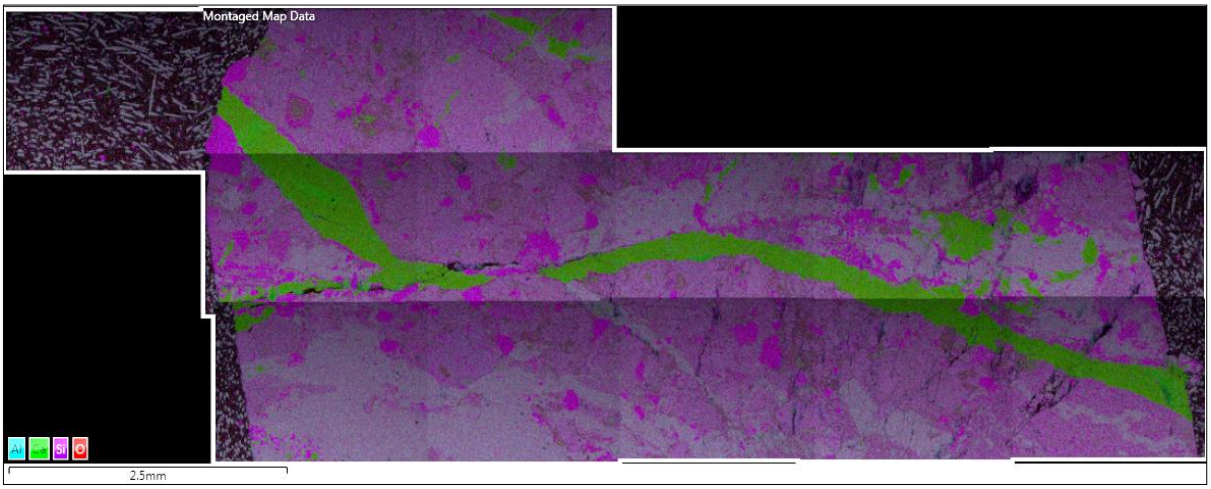

Figure A.5.6 Layered EDX elemental point map.

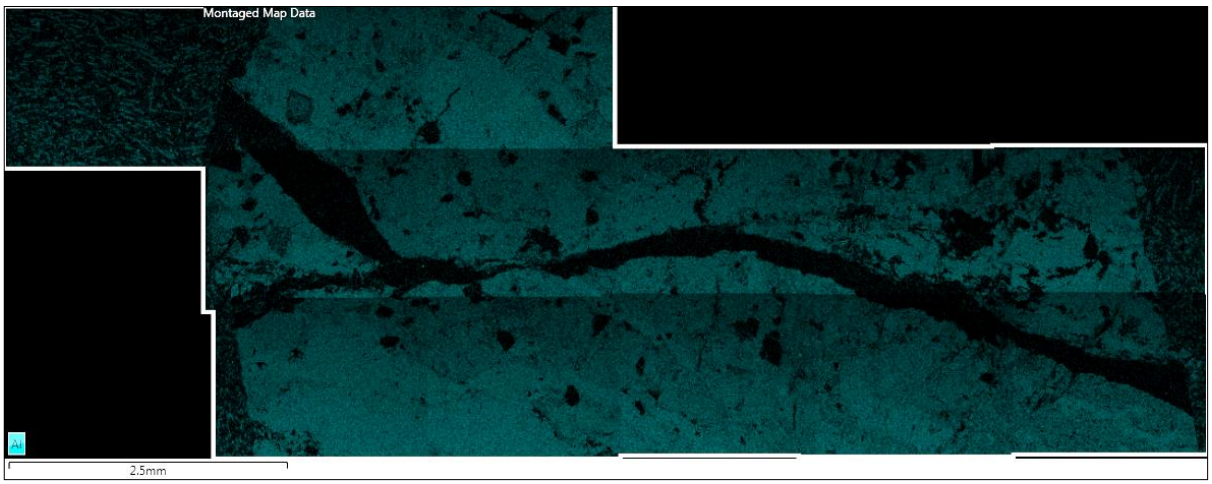

Figure A.5.7 EDX aluminium elemental point map.

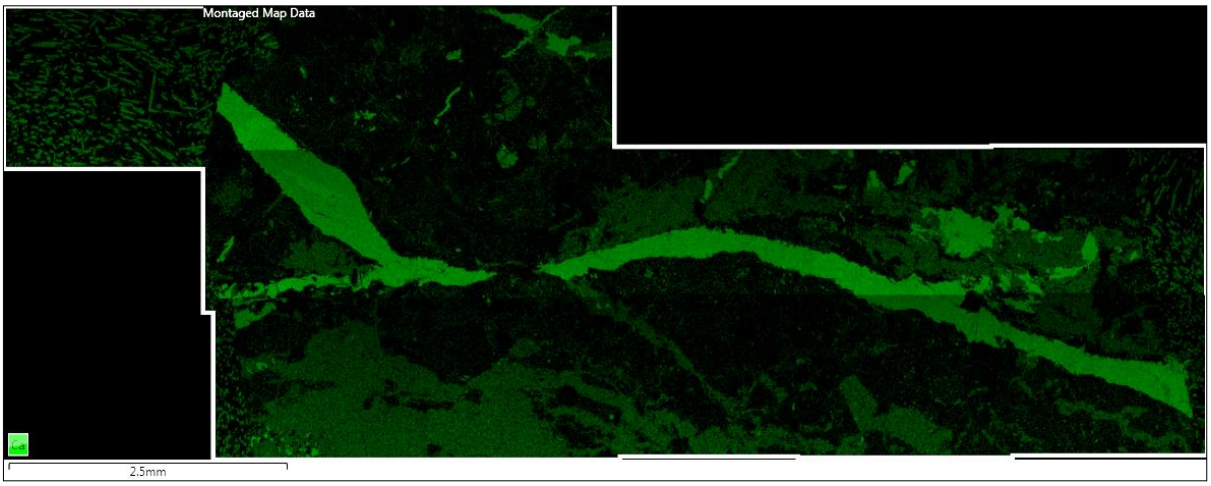

Figure A.5.8 EDX calcium elemental point map.

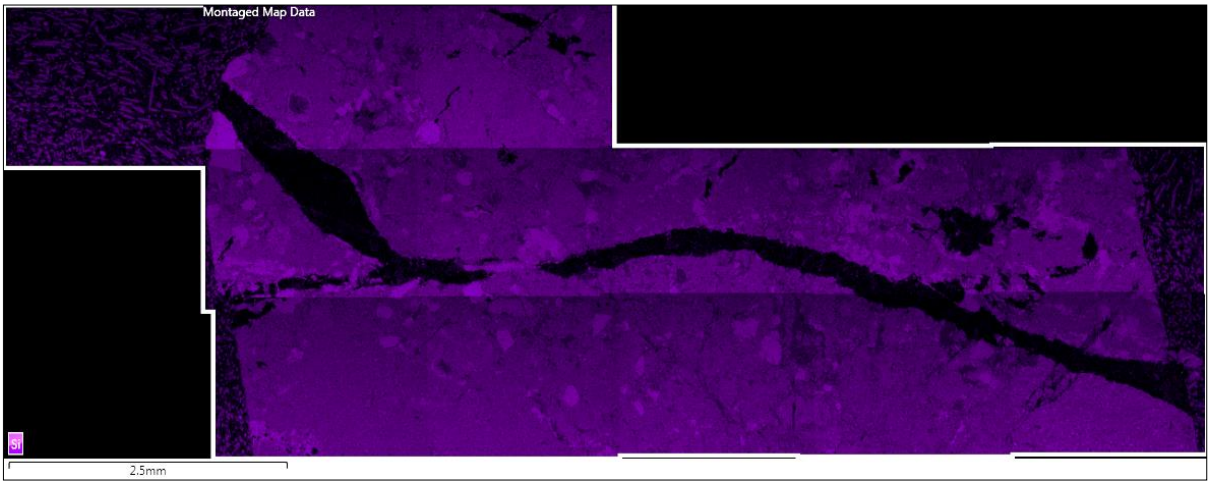

Figure A.5.9 EDX silica elemental point map.

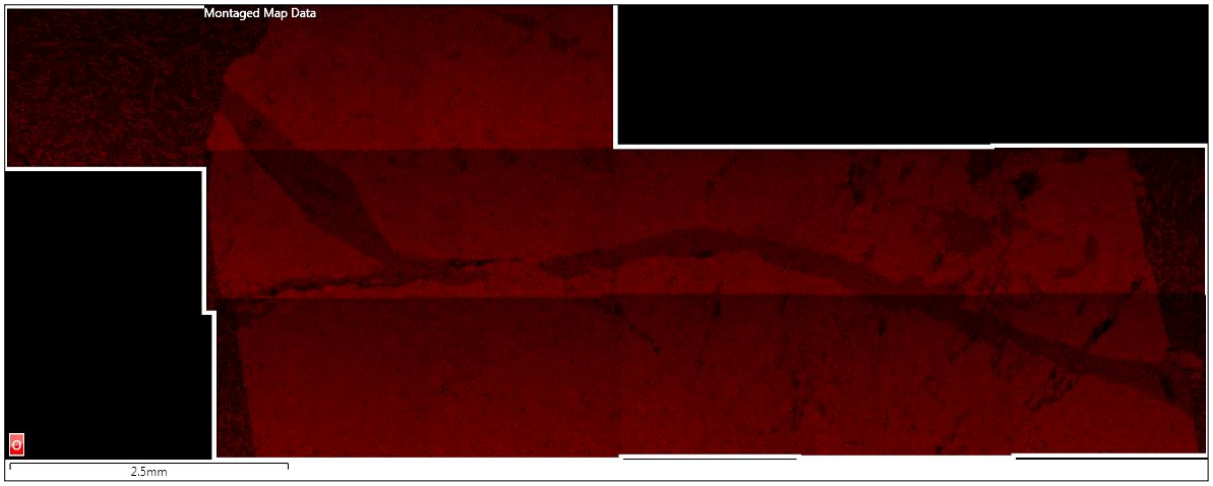

Figure A.5.10 EDX oxygen elemental point map.

Slice 5:

Poor quality EDX.

Slice 6:

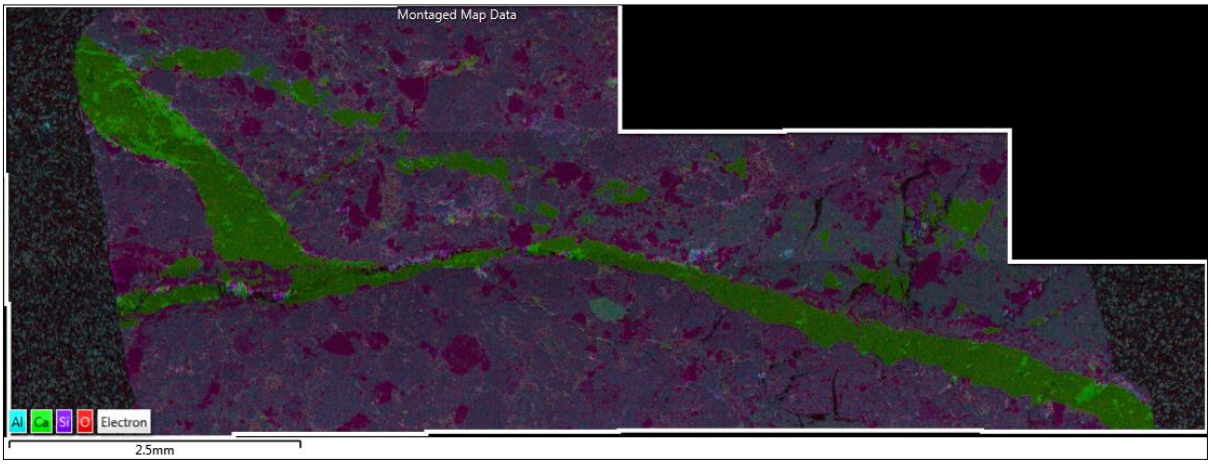

Figure A.5.11 Layered EDX elemental point map.

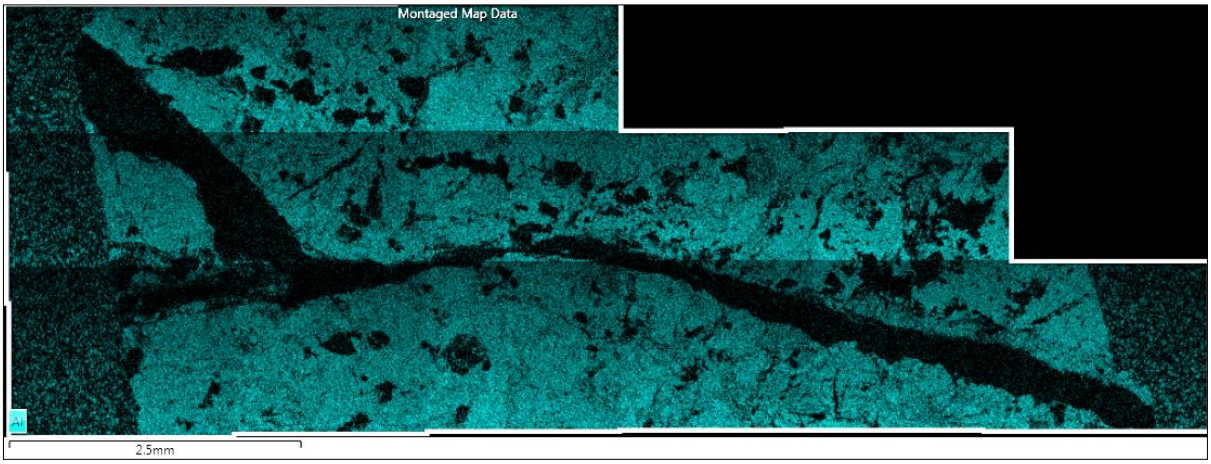

Figure A.5.12 EDX aluminium elemental point map.

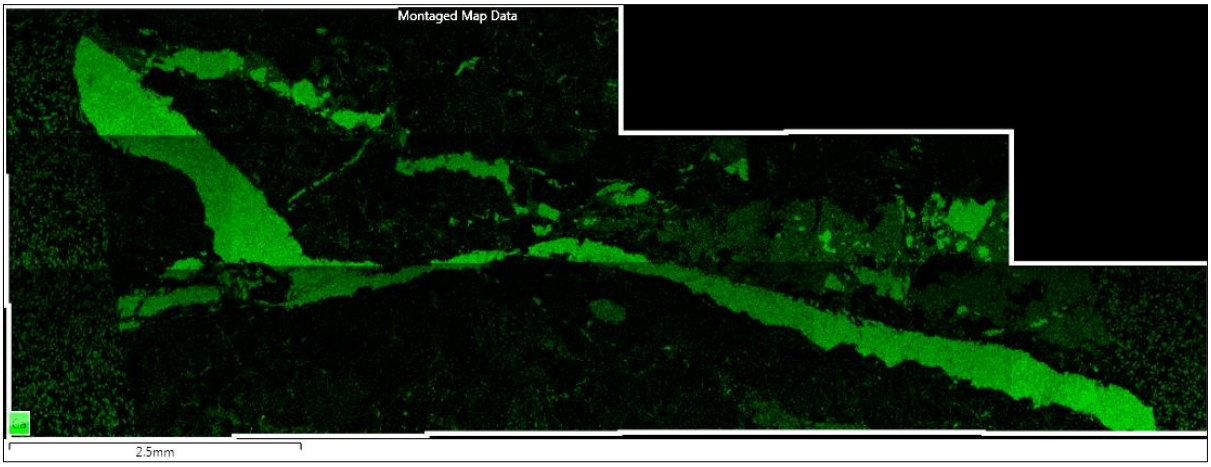

Figure A.5.13 EDX calcium elemental point map.

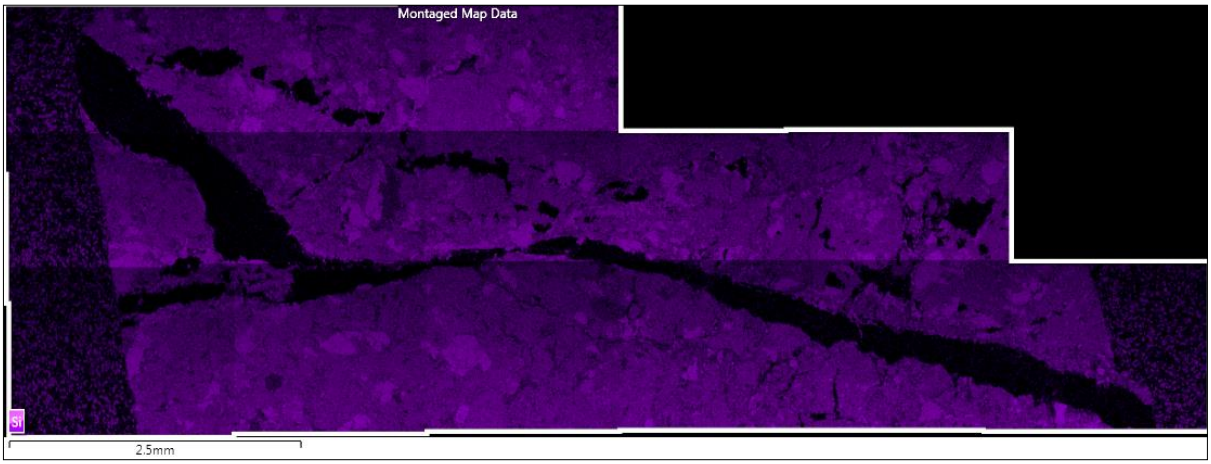

Figure A.5.14 EDX silica elemental point map.

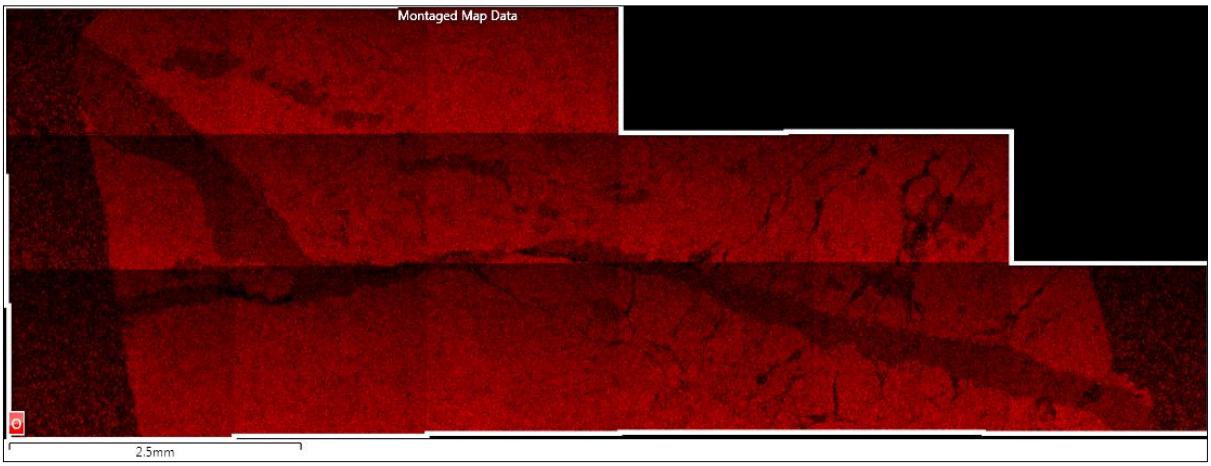

Figure A.5.15 EDX oxygen elemental point map.

Slice 7

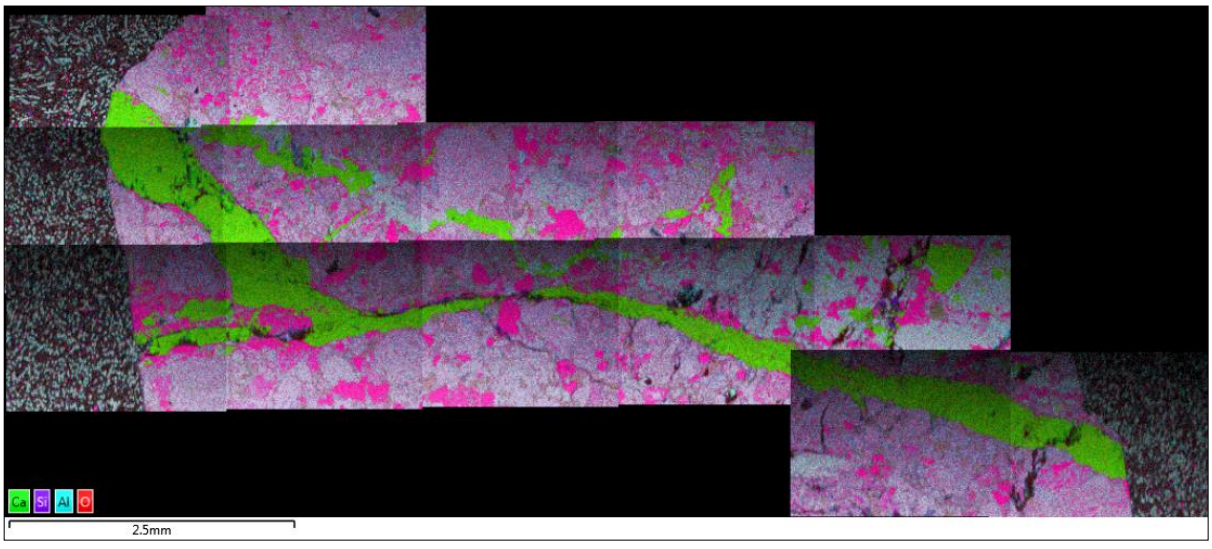

Figure A.5.16 Layered EDX elemental point map.

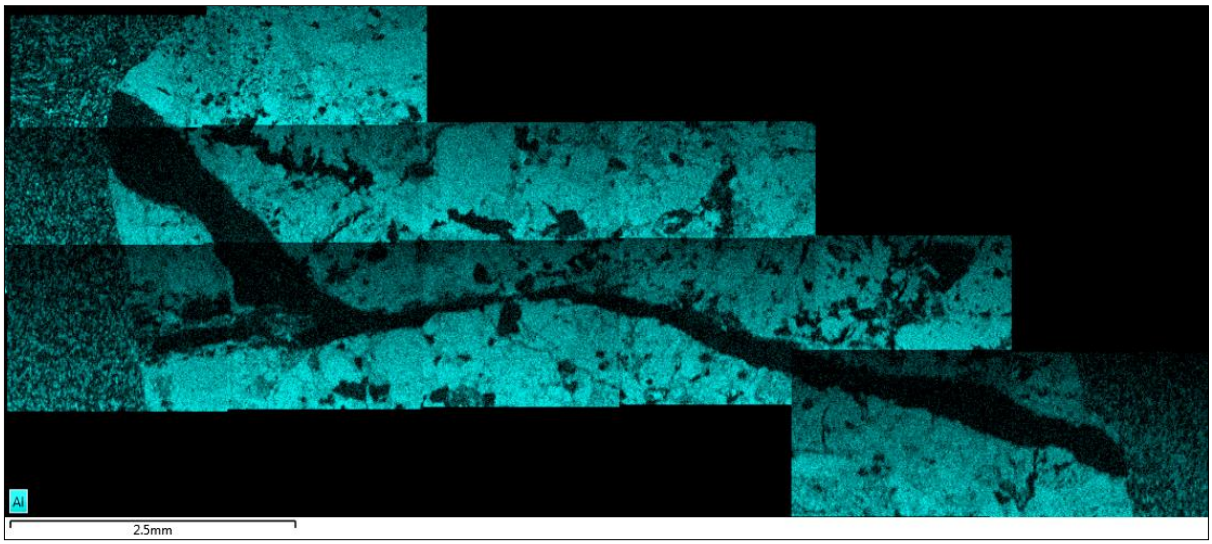

Figure A.5.17 EDX aluminium elemental point map.

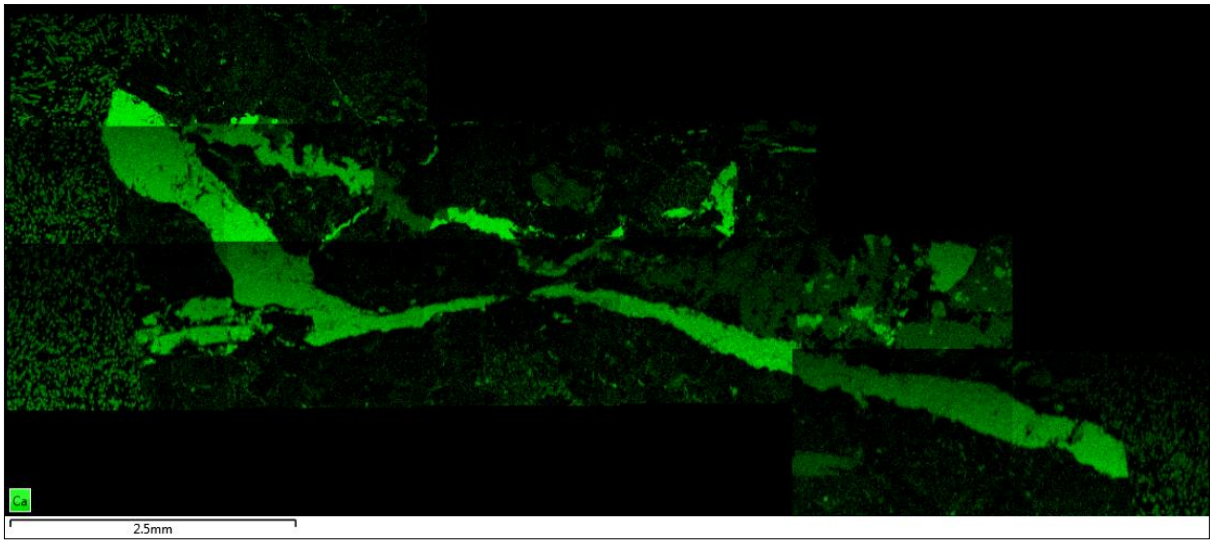

Figure A.5.18 EDX calcium elemental point map.

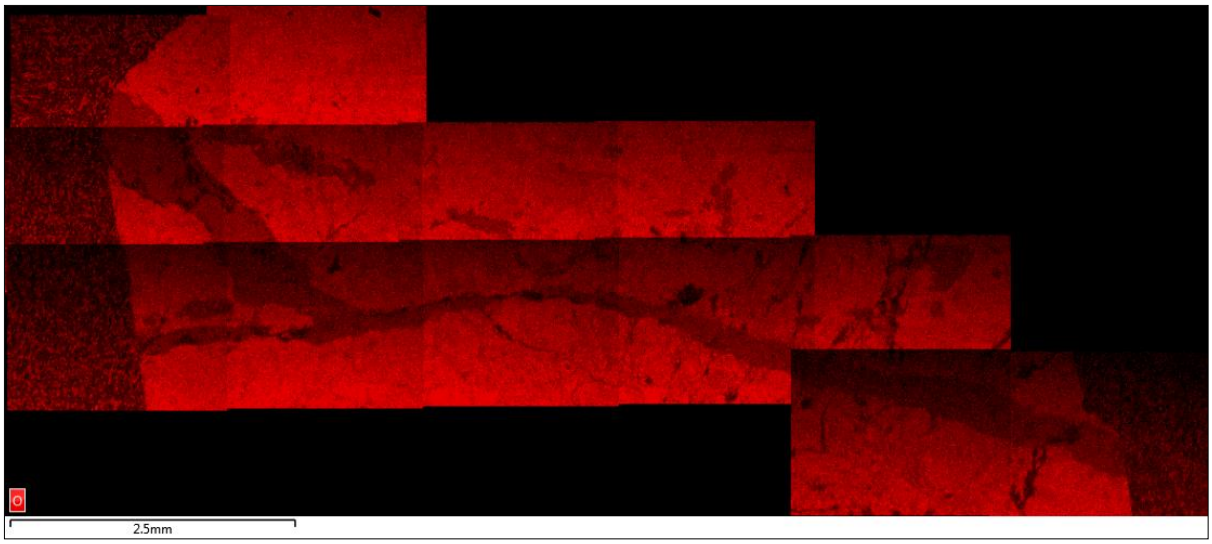

Figure A.5.19 EDX oxygen elemental point map.

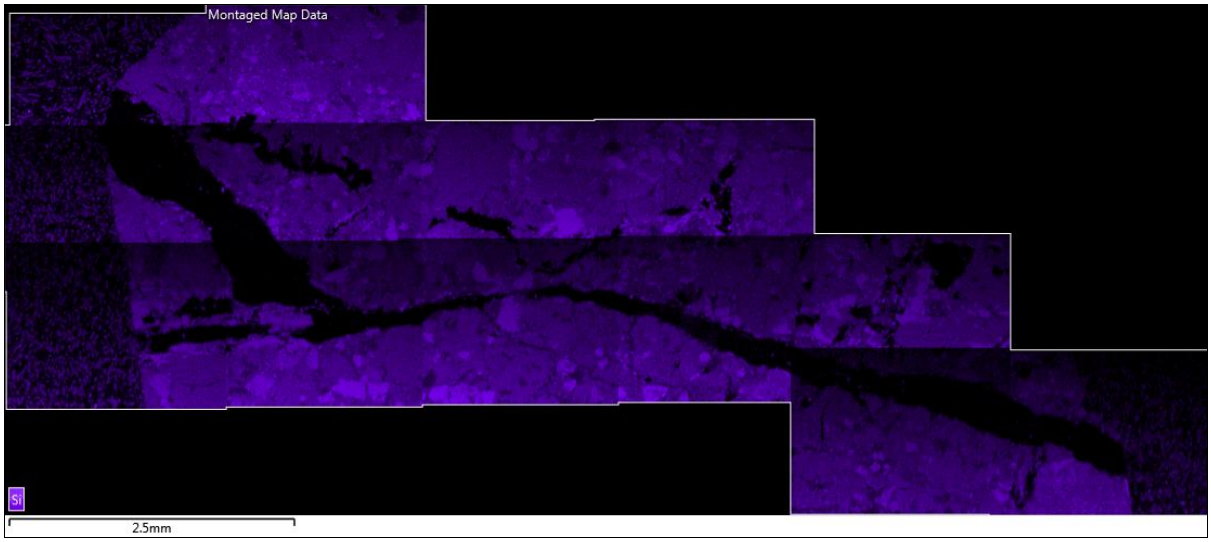

Figure A.5.20 EDX silica elemental point map.

Slice 8:

Prepared but not scanned.

Appendix 6: Cathodoluminescence (CL) Imaging of the Serial Sectioning Surfaces

Cathodoluminescence (CL) images were taken for both slice 5 and 6 of the sample during the serial sectioning process. Figure A.6.1 shows the CL set up and the briquette inside the CL chamber attached to the microscope located in the Department of Geology, Otago University. The CL system was operated under vacuum (0.05-0.08 Torr/17-20 V) at an accelerating voltage of 15-20 kV and a beam current of 550-600 μA. The same method of CL imaging is outlined in Chapter 2 with image analysis being carried out for both Chapter 3 and 4.

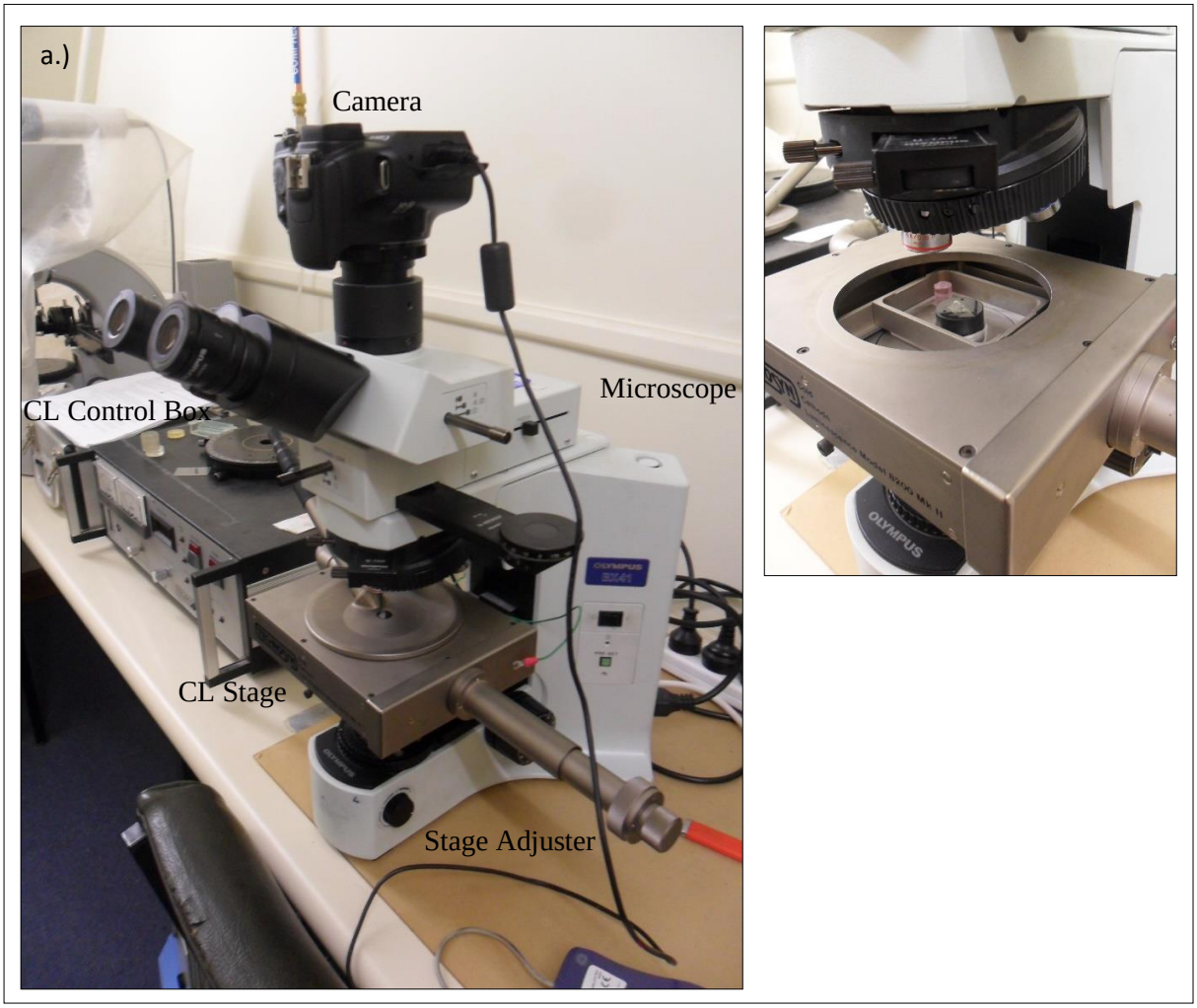

Figure A.6.1 The CL images were taken using a Technosyn cold cathode stage mounted on an Olympus BX41 microscrope with a trinoc head fitted with a digital camera. a.) CL set up and b.) the sample briquette sitting in the CL stage.

Slice 5:

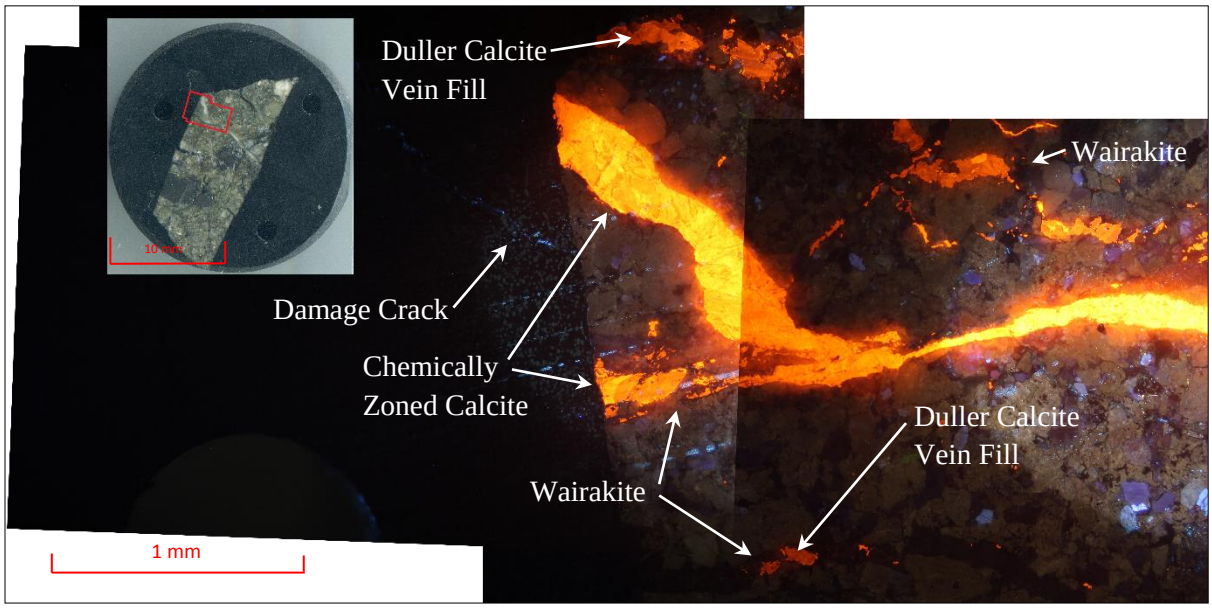

Figure A.6.2 CL image of the left side of the mineralised fracture showing the mineralisation identified. Insert red box defines area imaged. Note that charging can be seen along a crack in the briquette.

Figure A.6.2 shows the CL images of the left hand side of the fracture. This section of the fracture demonstrates the best elemental zoning identified within the bladed calcite for the sectioning process, as well as the variation in brightness between the two generations of mineralisation. Weak signatures of the wairakite mineralised vein (dull purple) can also be identified near the bottom left of the image and surrounding the older generation calcite. The surface damage can also be clearly seen on this surface, they appear as zones of bright blue charging and shadows on the edges of cracks and pits (Figure A.6.3a and Figure A.6.3b). The damage is particular bad along the right hand side of the fracture (Figure A.6.3b).

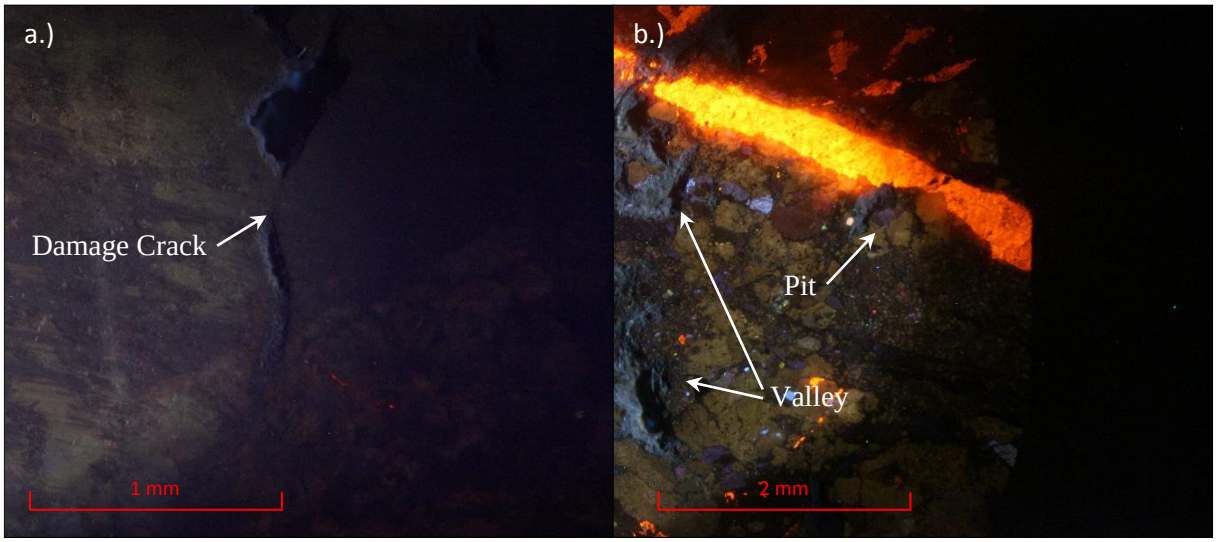

Figure A.6.3 Images of surface damage highlighted by electron charging and shadows in CL. a.) A crack and b.) valleys and pits located on the right hand side of the fracture.

Slice 6:

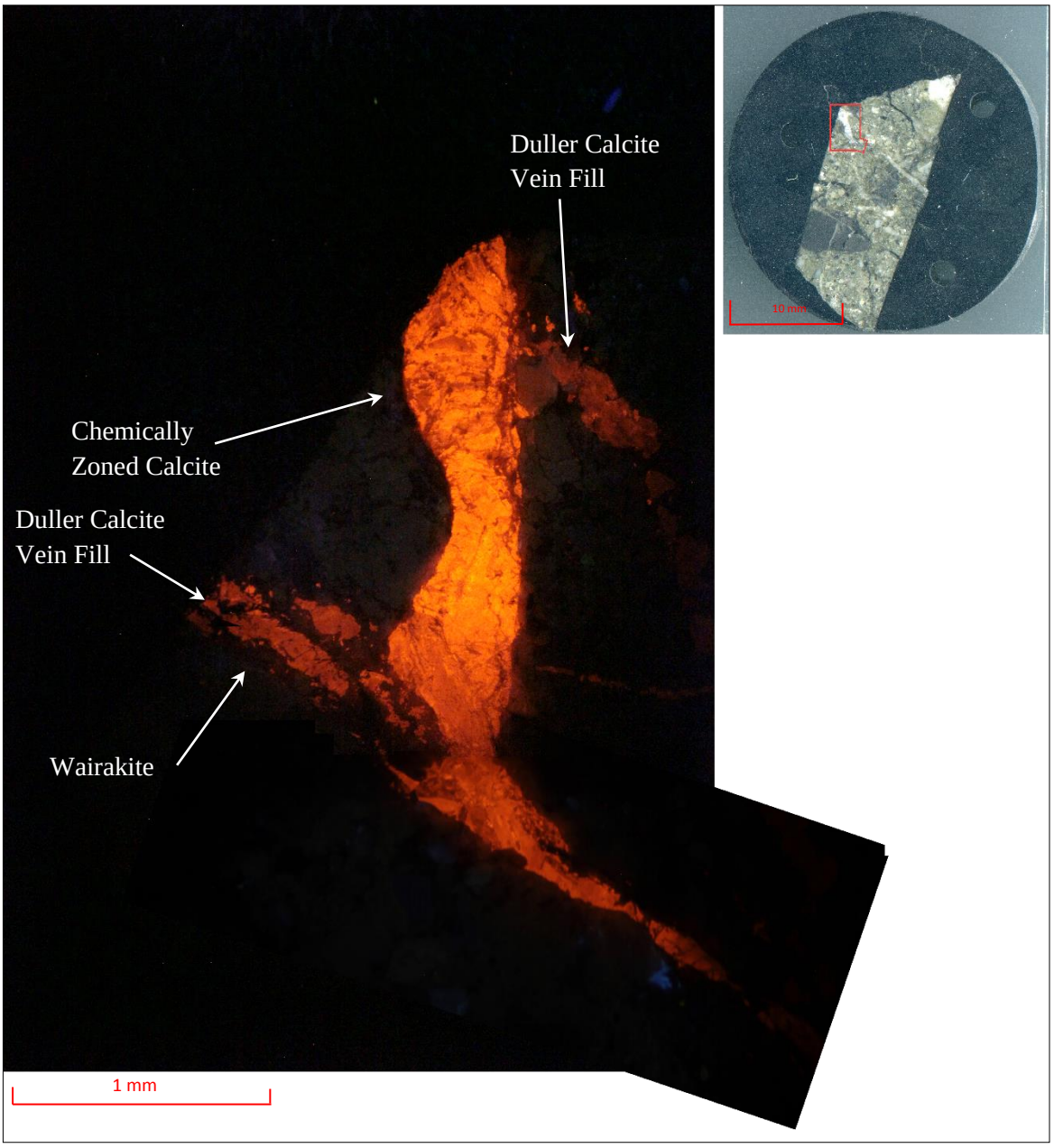

Figure A.6.4 CL image of the left side of the mineralised fracture showing the mineralisation identified. Insert red box defines area imaged.

Only the left hand side of the fracture was imaged for slice 6 due to the damage identified along the centre (Figure A.6.4). This section of the fracture does show the elemental zoning within the bladed calcite and the variation in brightness between the two generations of mineralisation. Weak signatures of the wairakite mineralised vein (dull purple) can also be identified near the bottom left of the image and surrounding the older generation calcite.

Appendix 7: Serial Sectioning Electron Backscatter Diffraction (EBSD) Orientation Maps.

Presented below are the electron backscatter diffraction (EBSD) orientation maps for each slice surface including; Band contrast images, grain boundary maps, Euler colour scheme, and inverse pole figure (IPF) colours (x, y, and z).

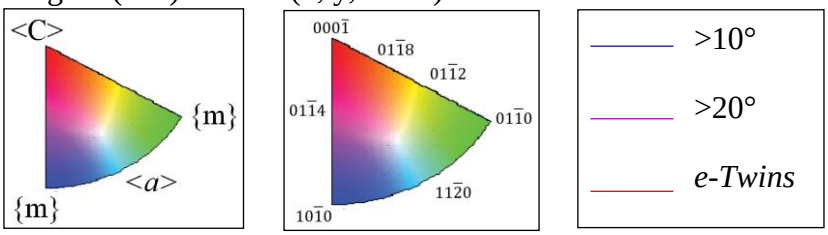

Figure A.7.1 IPF colour key and grain boundary values.

Slice 1:

Figure A.7.2 Band contrast image.

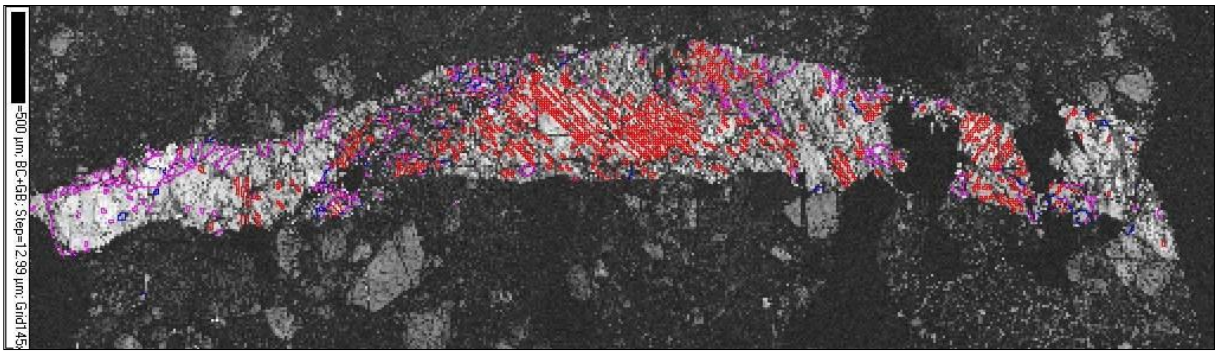

Figure A.7.3 Band contrast image with the grain boundary overlay.

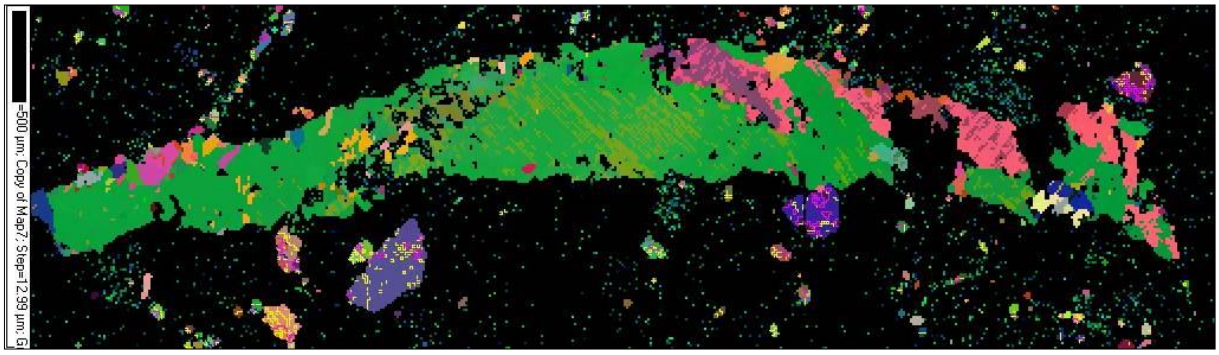

Figure A.7.4 Euler colour scheme. Note the crushed zone towards the left end of the crystal and the clear regions that have experienced grain plucking to right. Also included is the surrounding quarts phases.

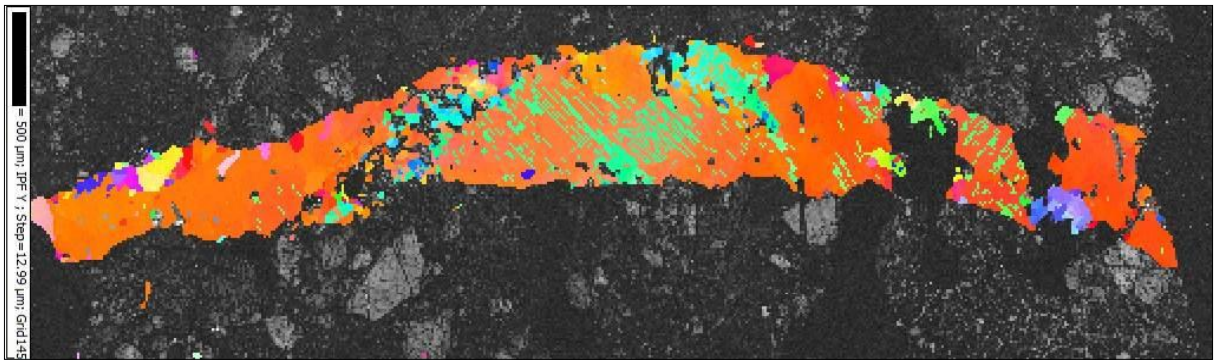

Figure A.7.5 IPF in the x-direction overlaid on the band contrast image.

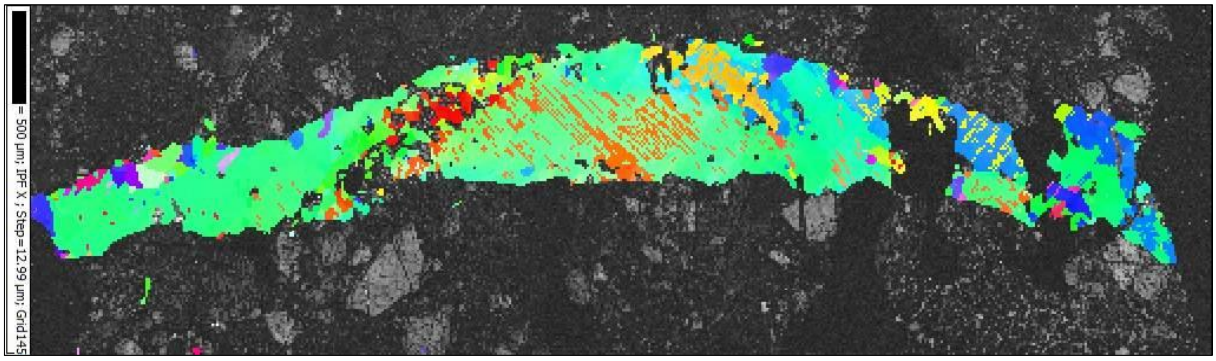

Figure A.7.6 IPF in the y-direction overlaid on the band contrast image.

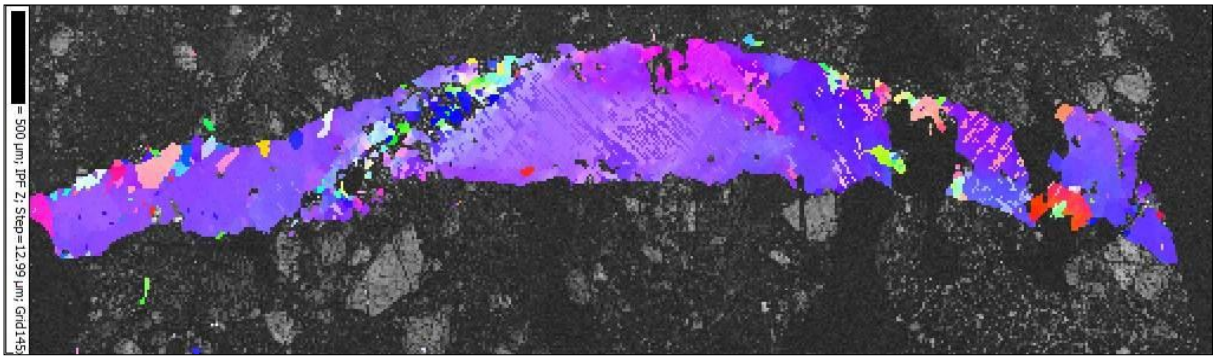

Figure A.7.7 IPF in the z-direction overlaid on the band contrast image.

Slice 2:

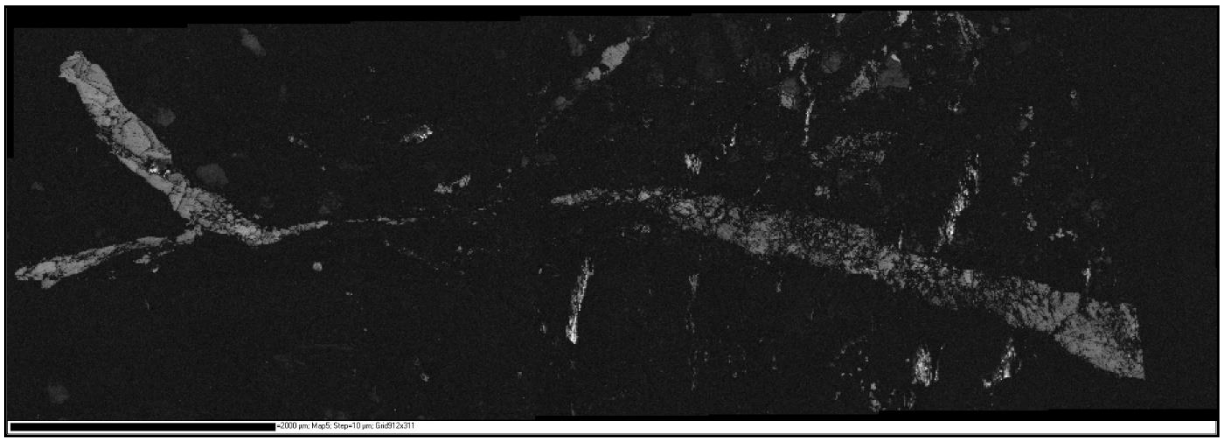

Figure A.7.8 Band contrast image.

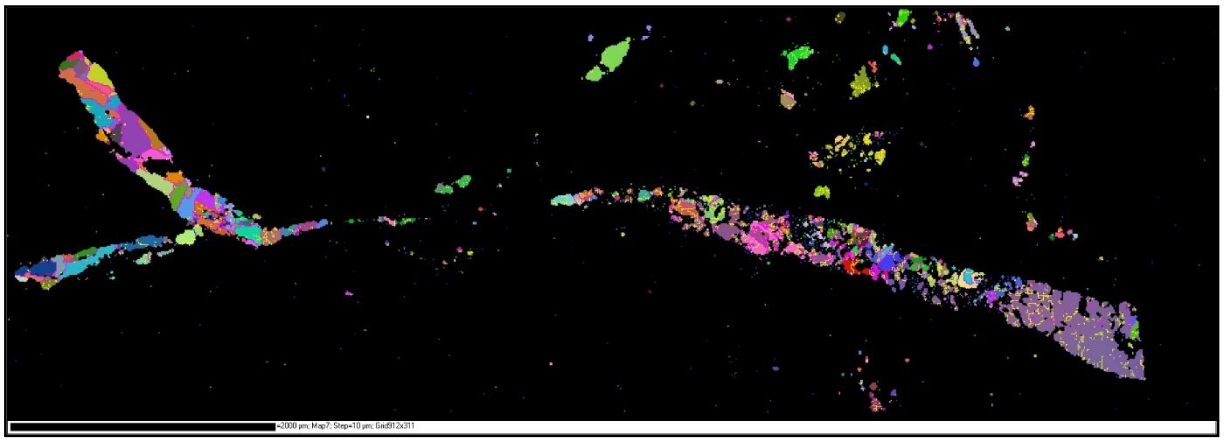

Figure A.7.9 Euler colour scheme with grain boundary.

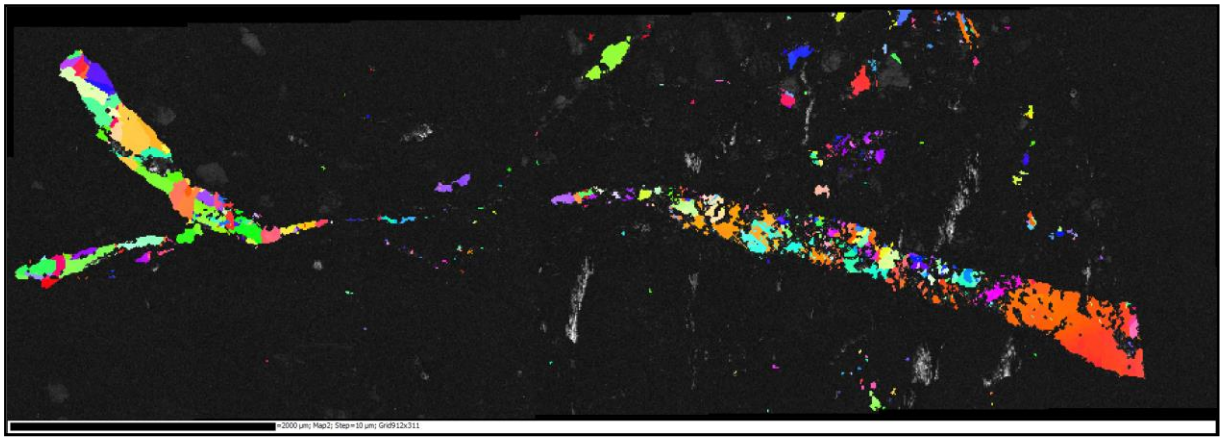

Figure A.7.10 IPF in the x-direction overlaid on the band contrast image.

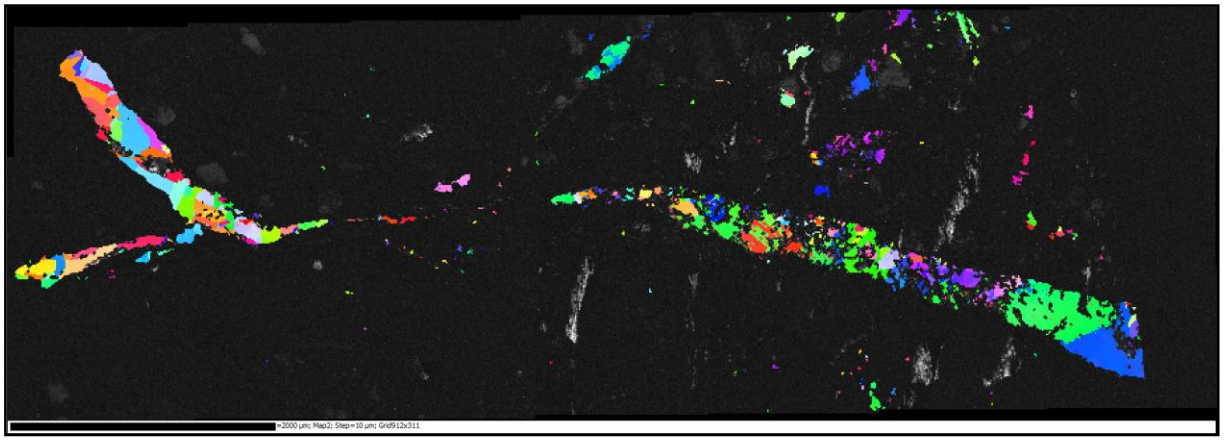

Figure A.7.11 IPF in the y-direction overlaid on the band contrast image.

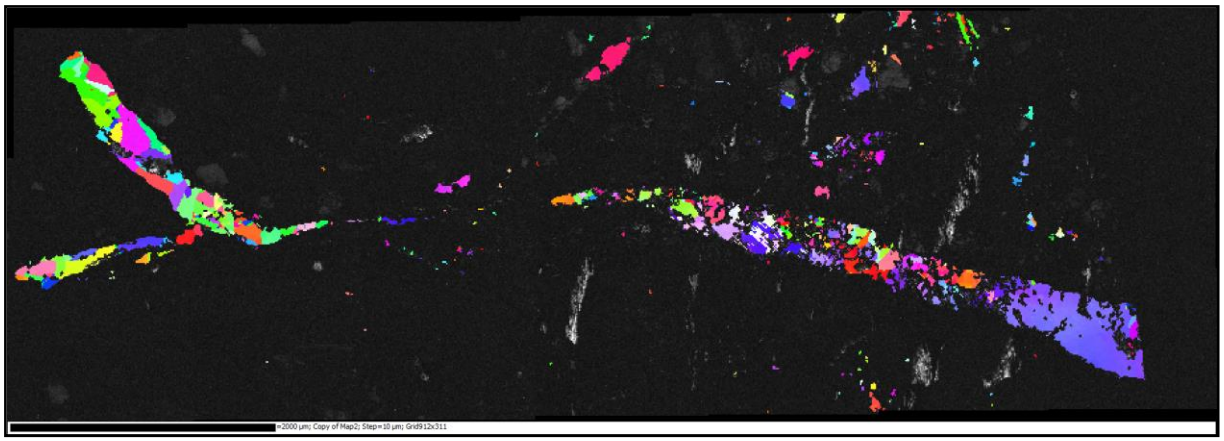

Figure A.7.12 IPF in the z-direction overlaid on the band contrast image.

Slice 3:

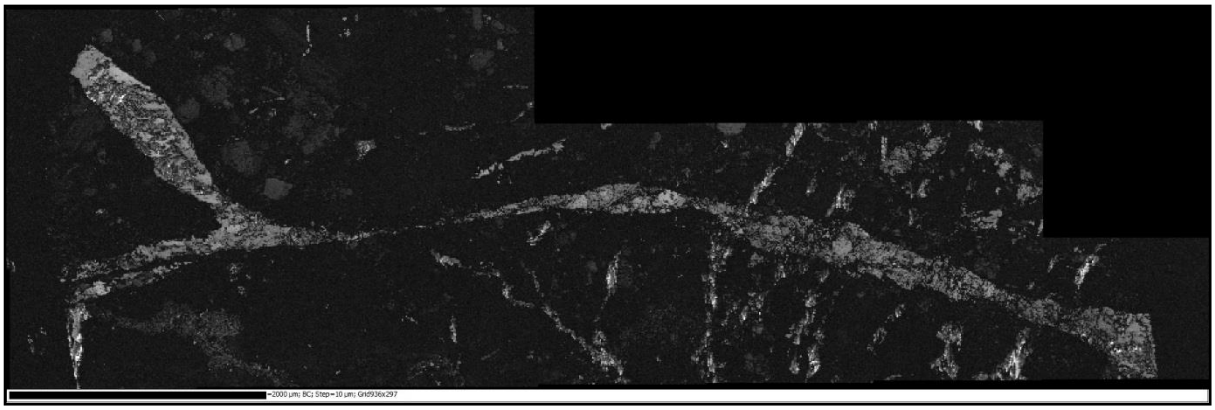

Figure A.7.13 Band contrast image.

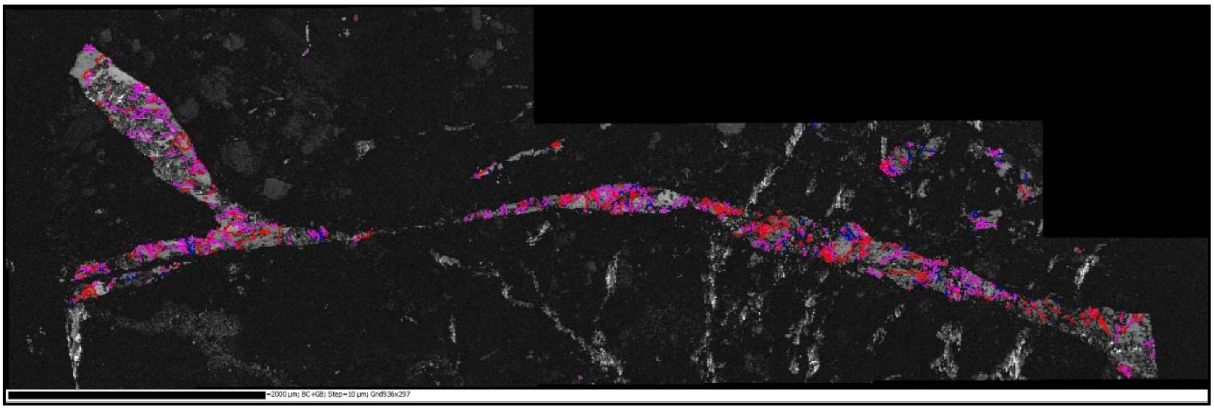

Figure A.7.14 Band contrast image with the grain boundary overlay.

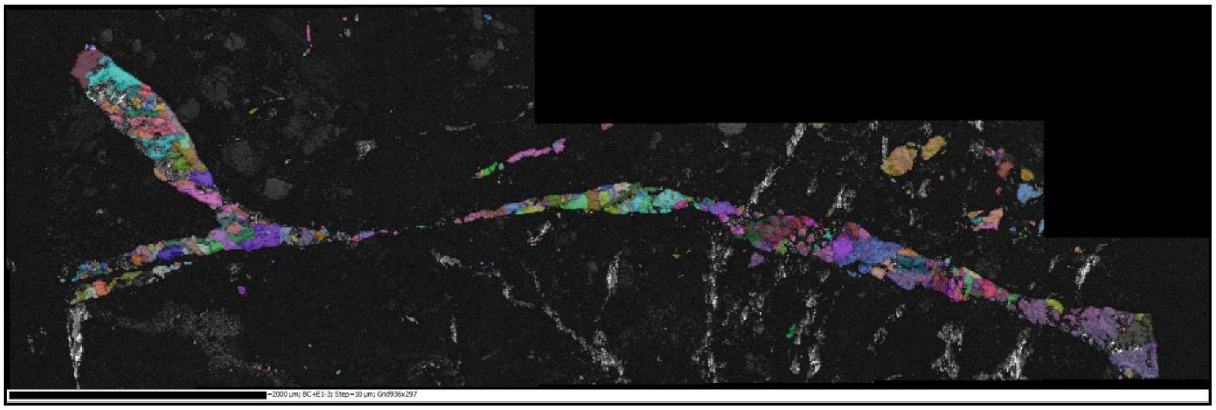

Figure A.7.15 Euler colour scheme.

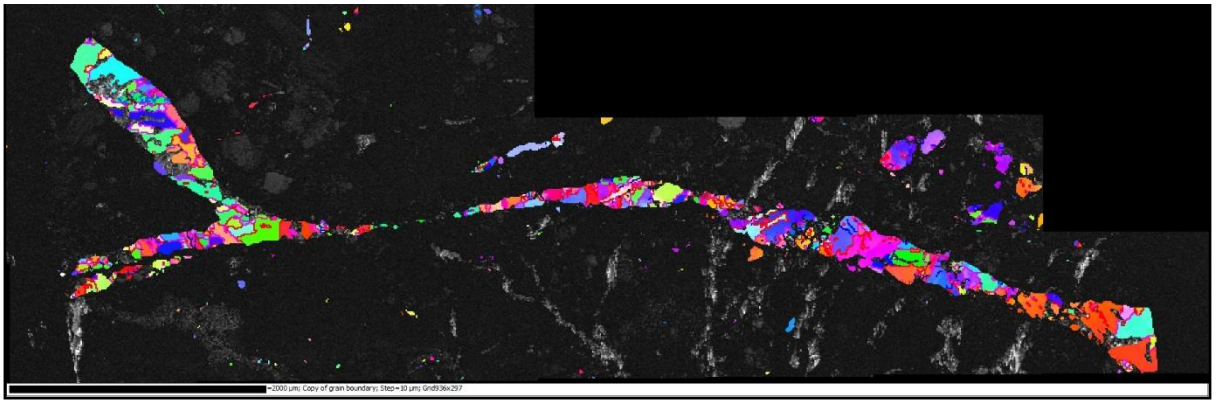

Figure A.7.16 IPF in the x-direction overlaid on the band contrast image with grain boundaries.

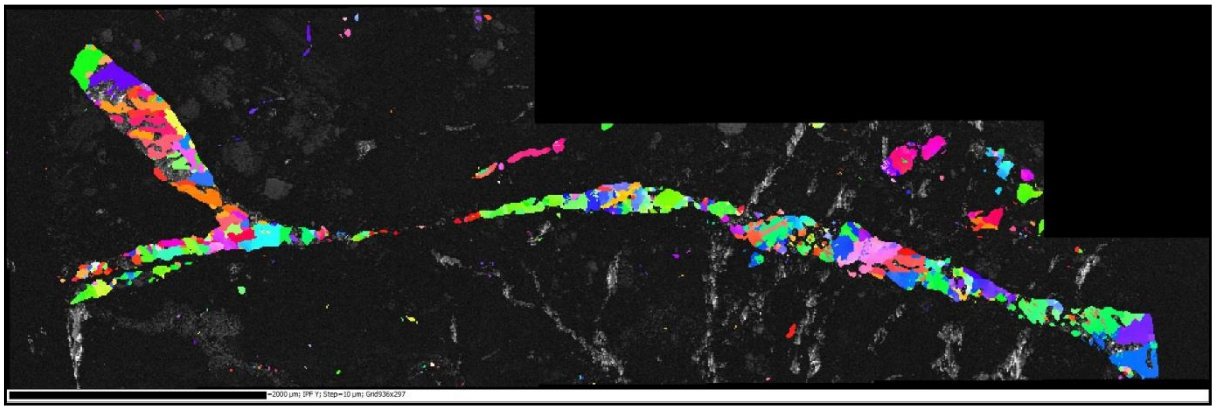

Figure A.7.17 IPF in the y-direction overlaid on the band contrast image.

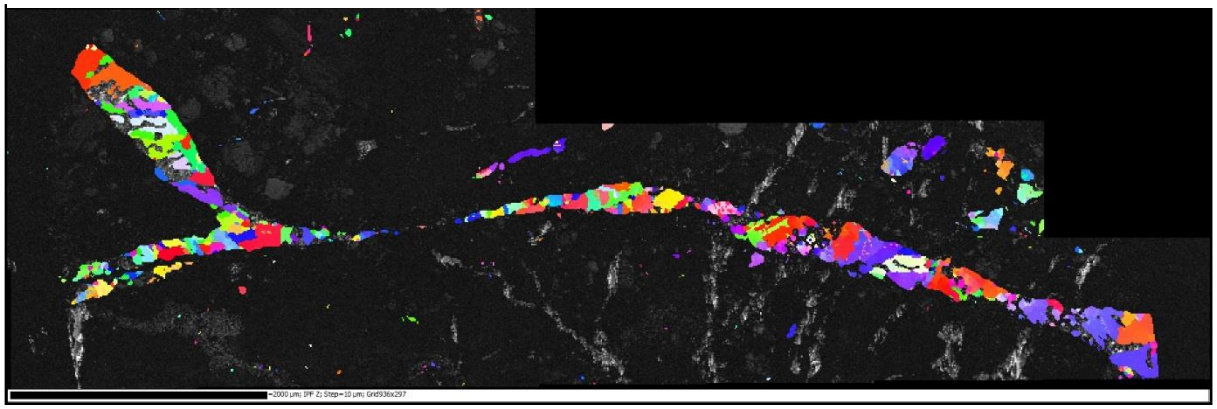

Figure A.7.18 IPF in the z-direction overlaid on the band contrast image.

Slice 4:

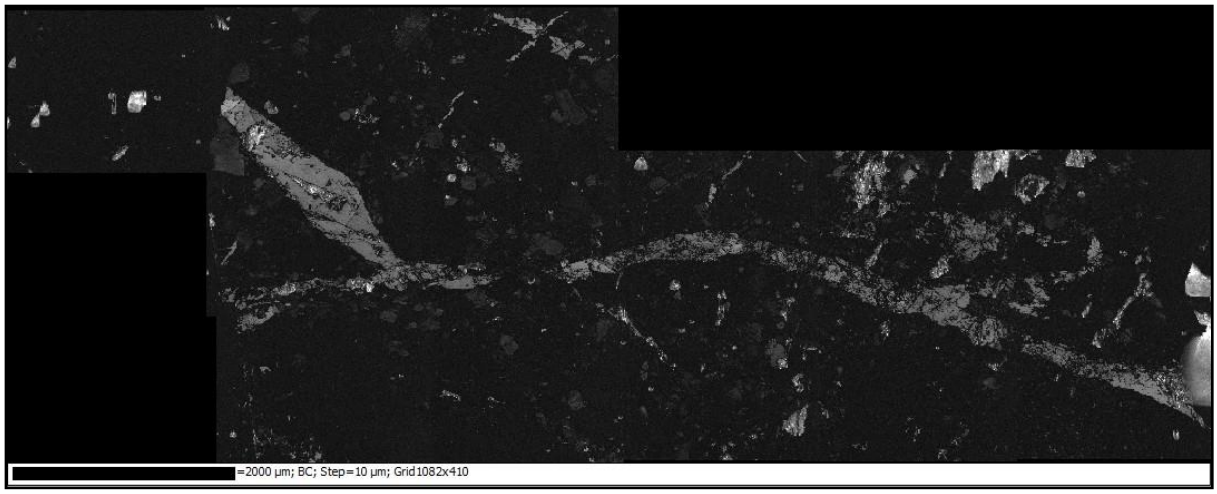

Figure A.7.19 Band contrast image.

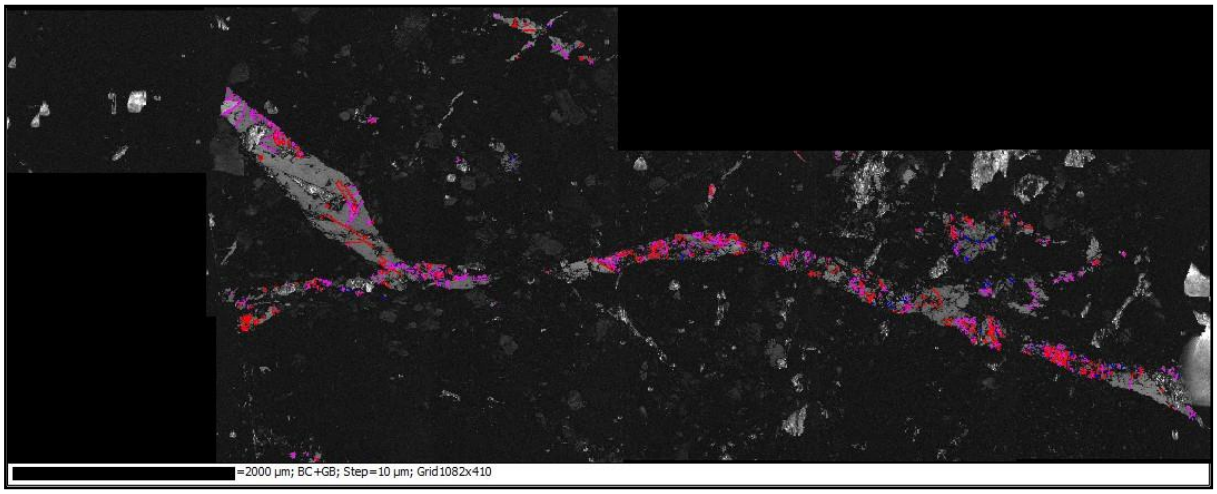

Figure A.7.20 Band contrast image with the grain boundary overlay.

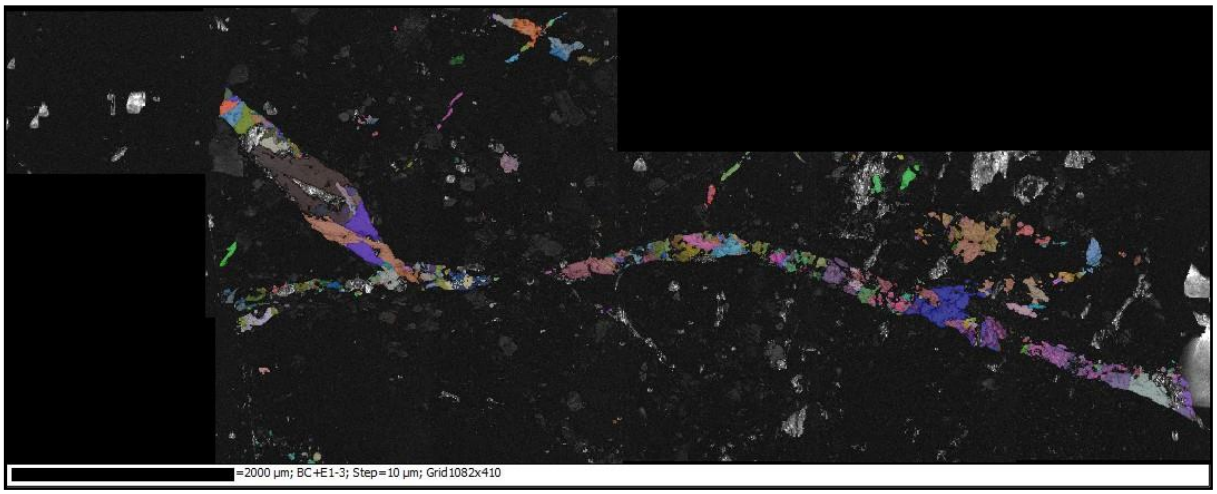

Figure A.7.21 Euler colour scheme with grain boundary.

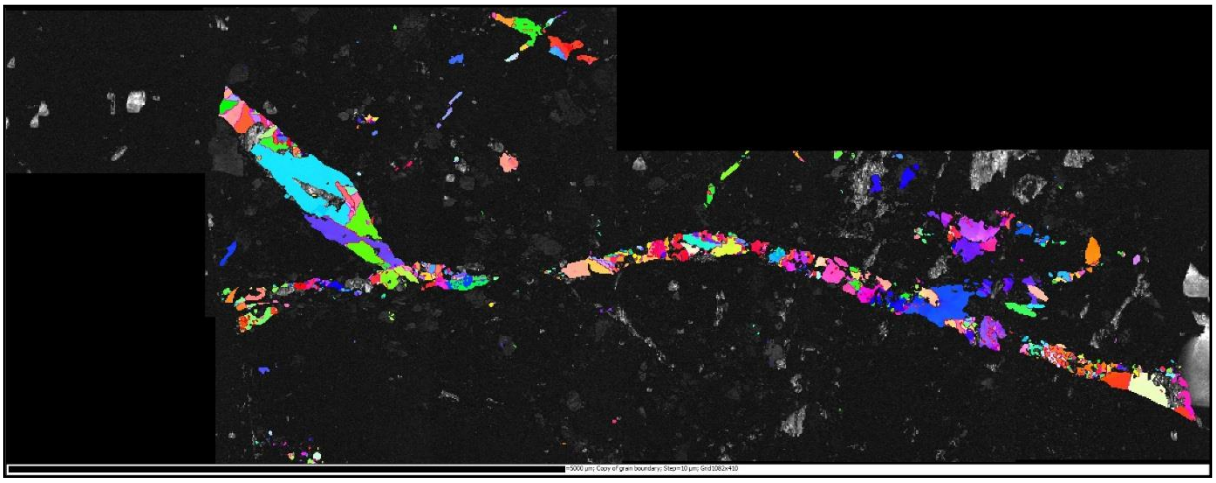

Figure A.7.22 IPF in the x-direction overlaid on the band contrast image with grain boundaries.

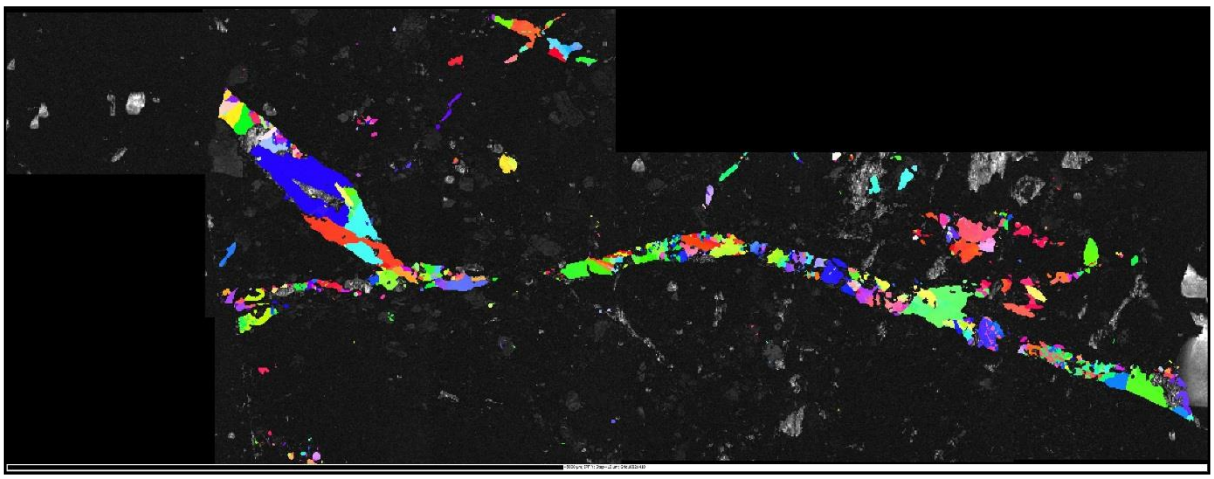

Figure A.7.23 IPF in the y-direction overlaid on the band contrast image.

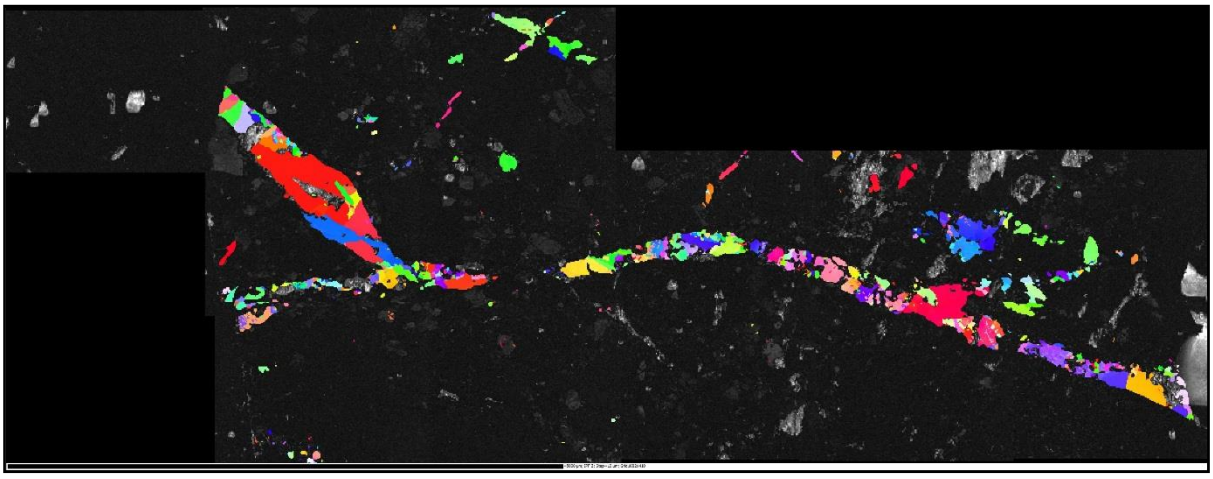

Figure A.7.24 IPF in the z-direction overlaid on the band contrast image.

Slice 5:

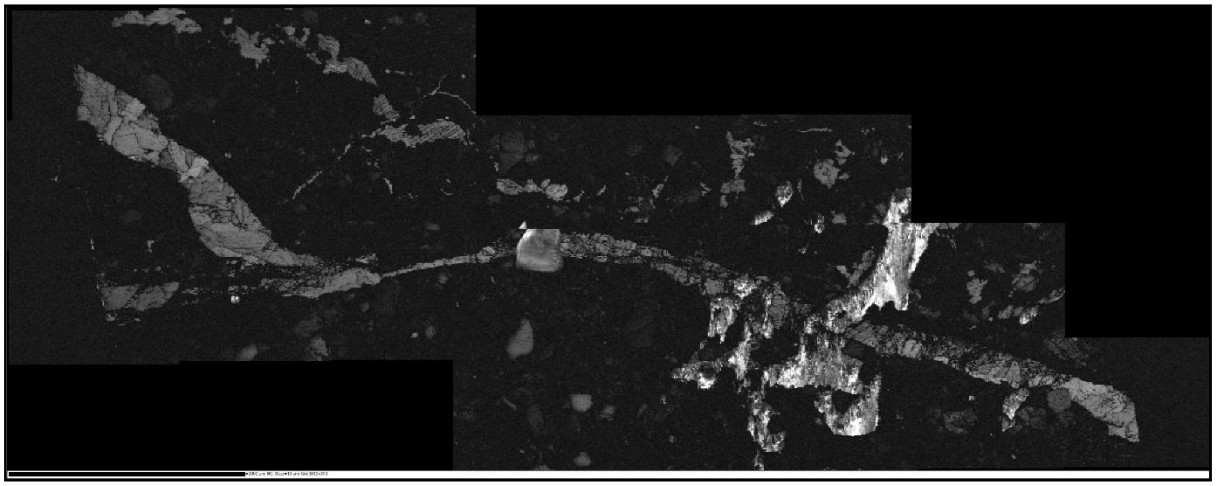

Figure A.7.25 Band contrast image.

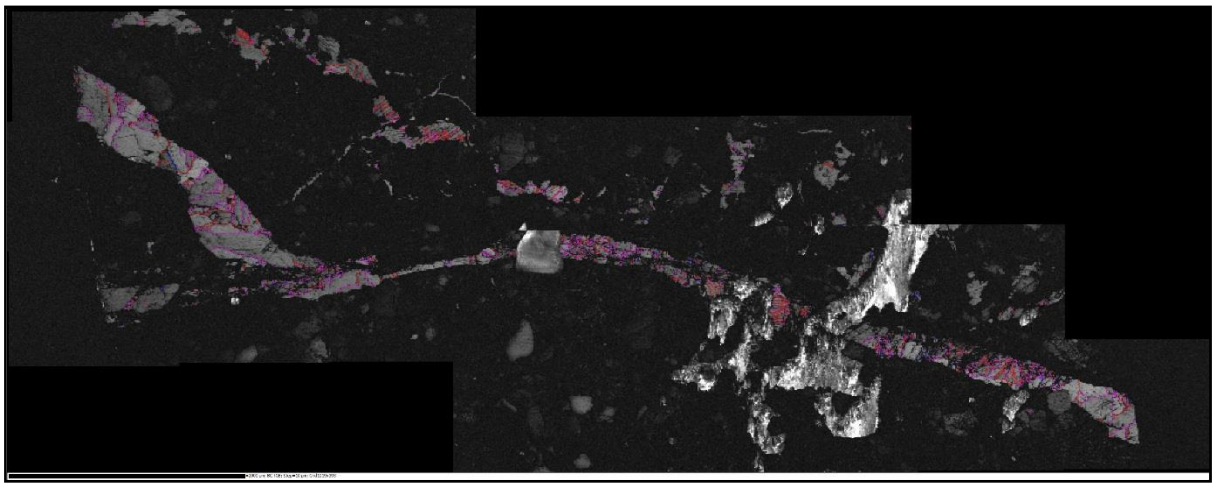

Figure A.7.26 Band contrast image with the grain boundary overlay.

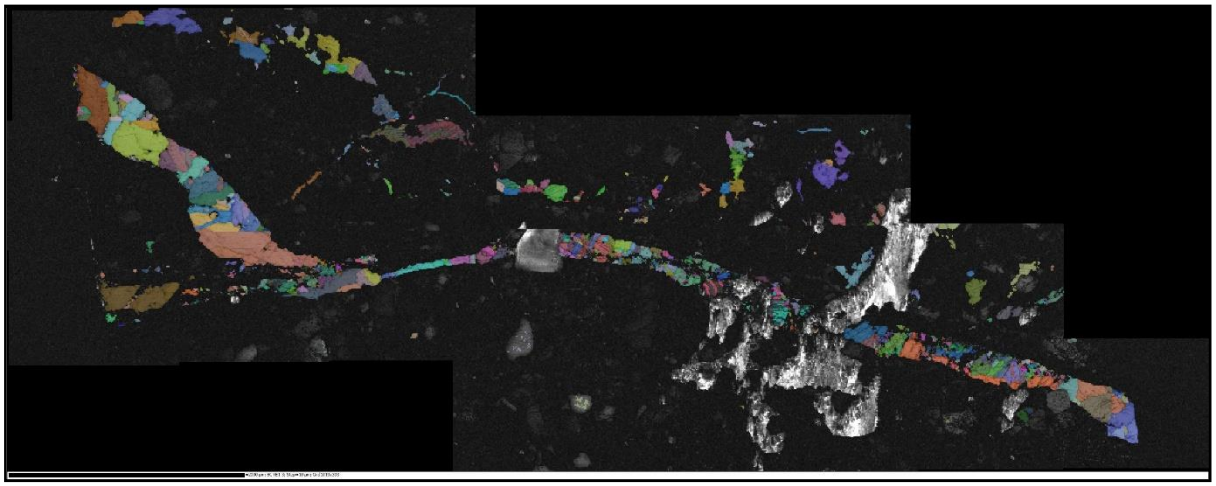

Figure A.7.27 Euler colour scheme.

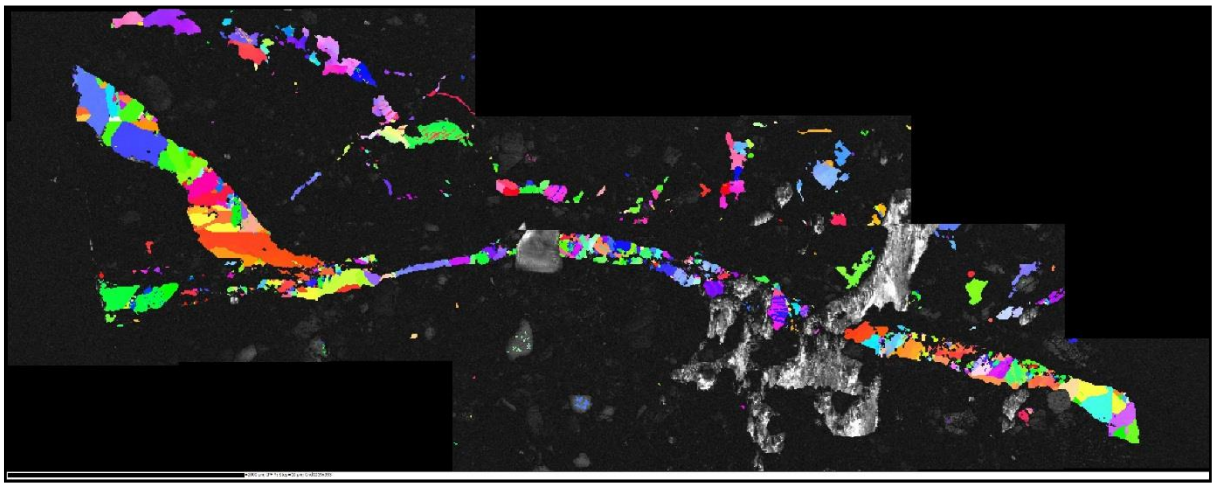

Figure A.7.28 IPF in the x-direction overlaid on the band contrast image.

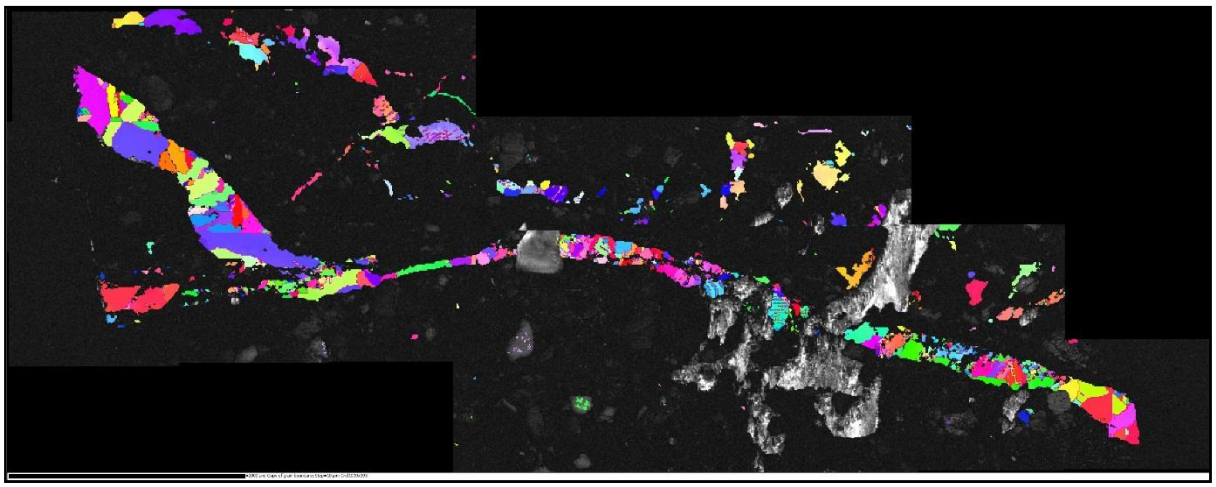

Figure A.7.29 IPF in the y-direction overlaid on the band contrast image.

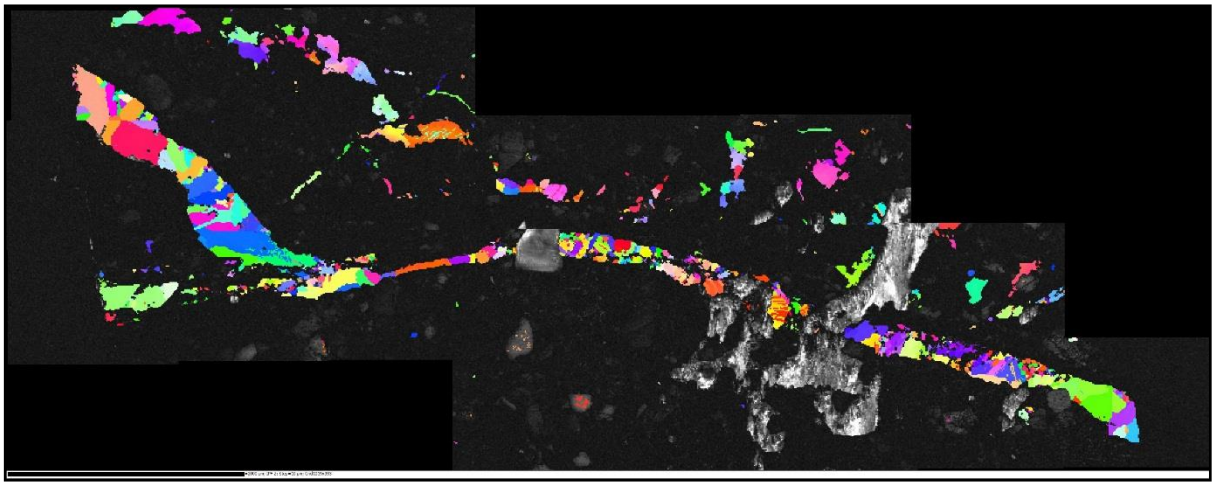

Figure A.7.30 IPF in the z-direction overlaid on the band contrast image.

Slice 6:

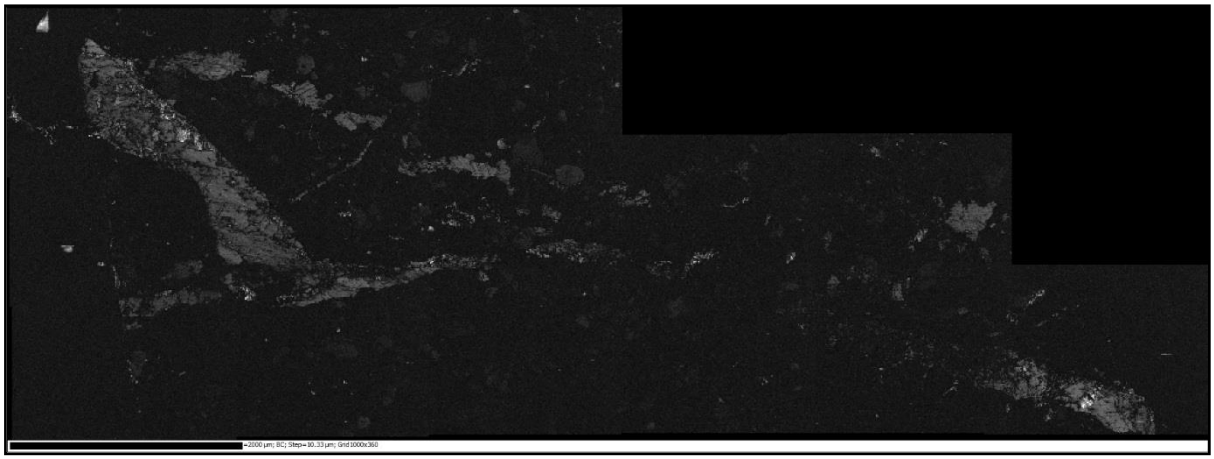

Figure A.7.31 Band contrast image.

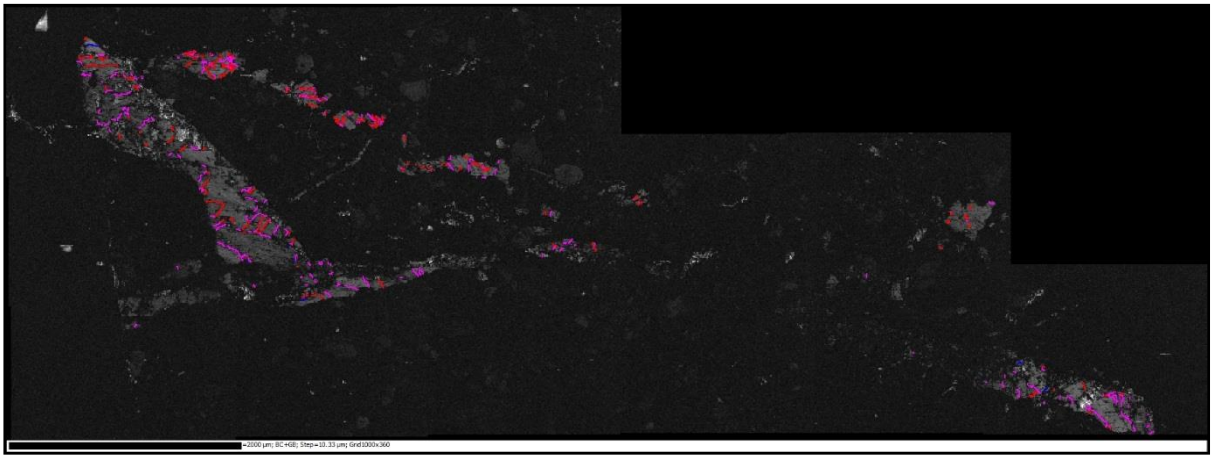

Figure A.7.32 Band contrast image with the grain boundary overlay.

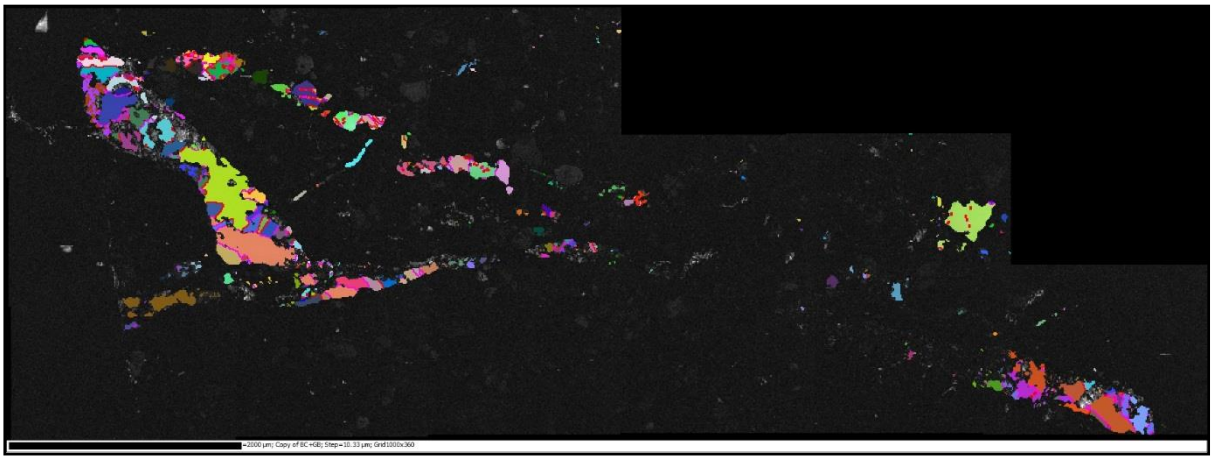

Figure A.7.33 Euler colour scheme with grain boundary on band contrast image.

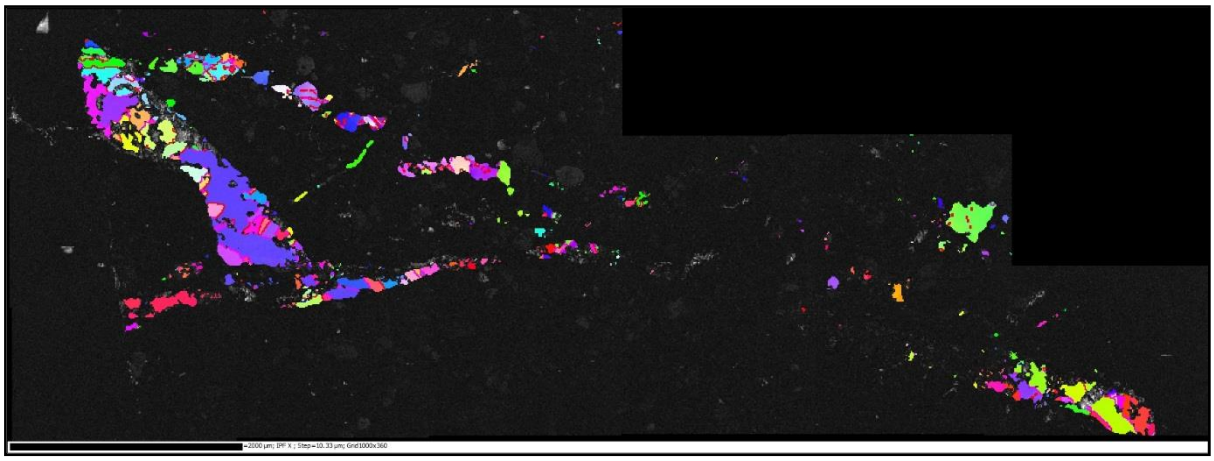

Figure A.7.34 IPF in the x-direction overlaid on the band contrast image with grain boundaries.

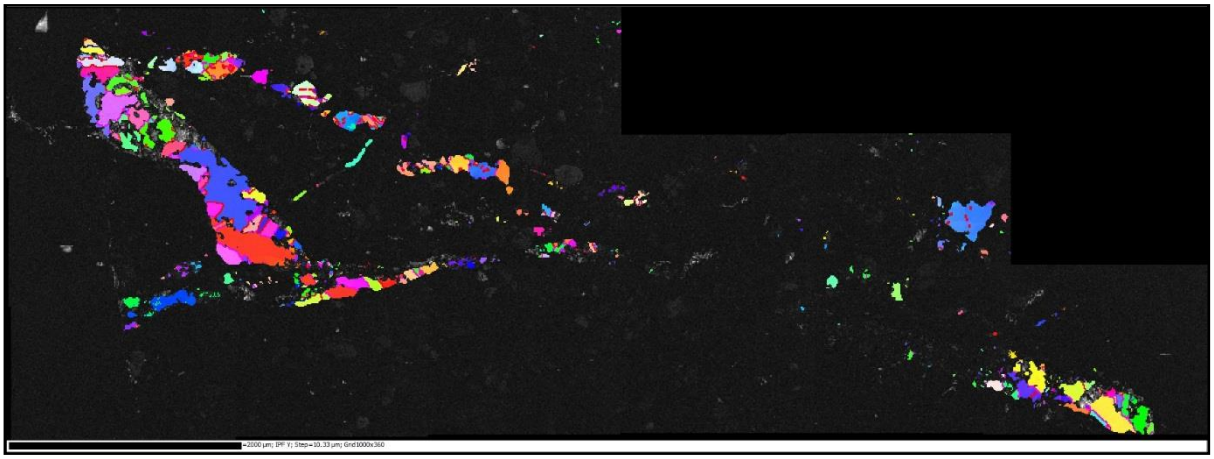

Figure A.7.35 IPF in the y-direction overlaid on the band contrast image with grain boundaries.

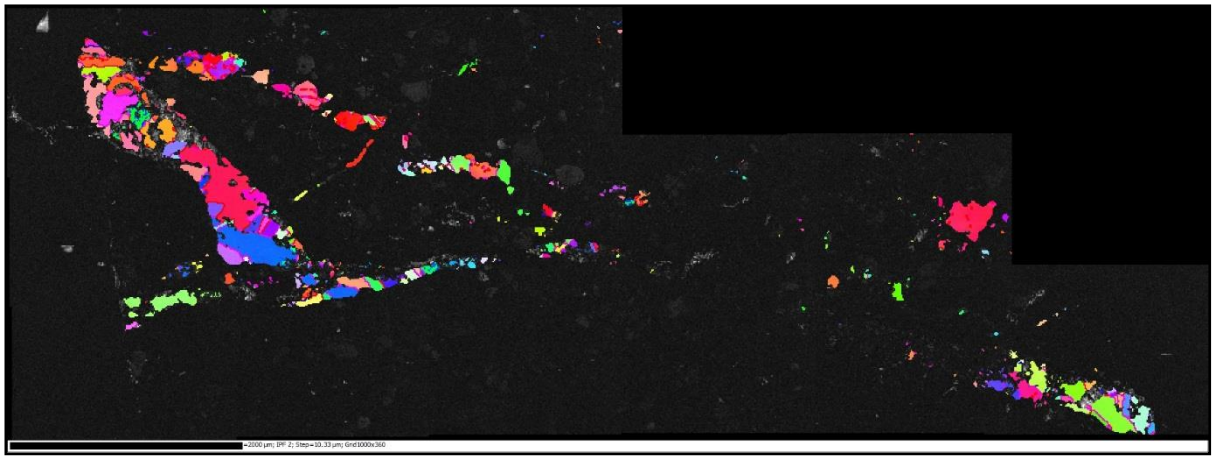

Figure A.7.36 IPF in the z-direction overlaid on the band contrast image with grain boundaries.

Slice 7:

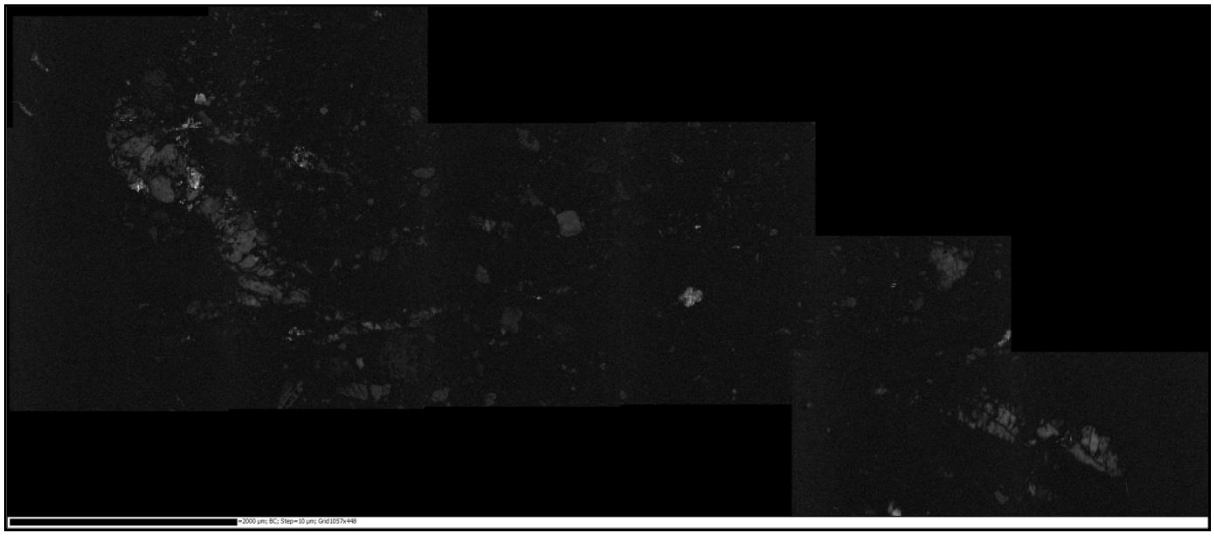

Figure A.7.37 Band contrast image.

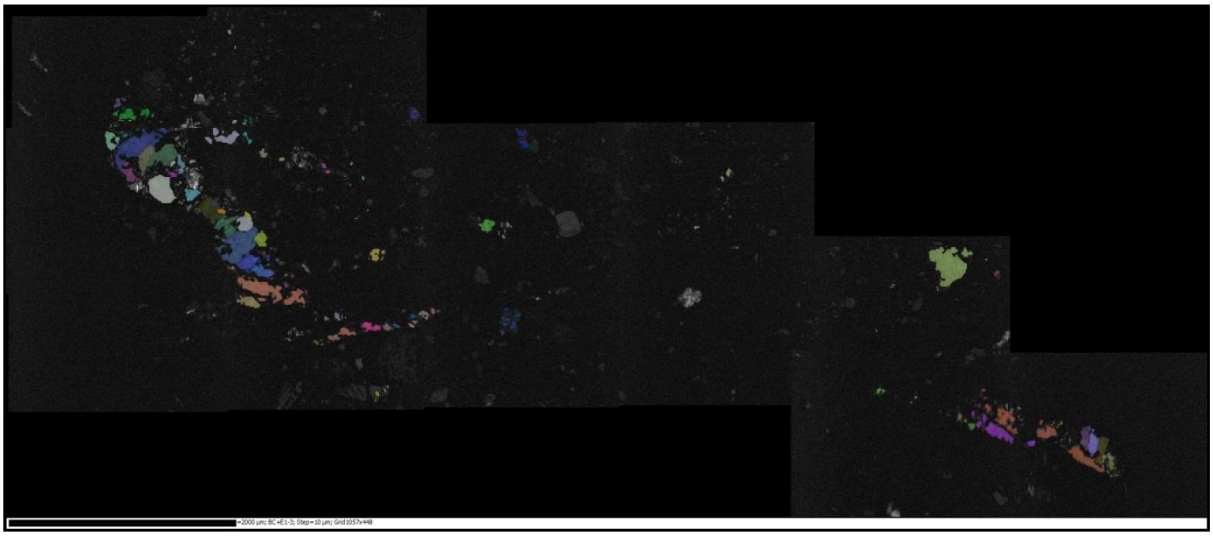

Figure A.7.38 Euler colour scheme.

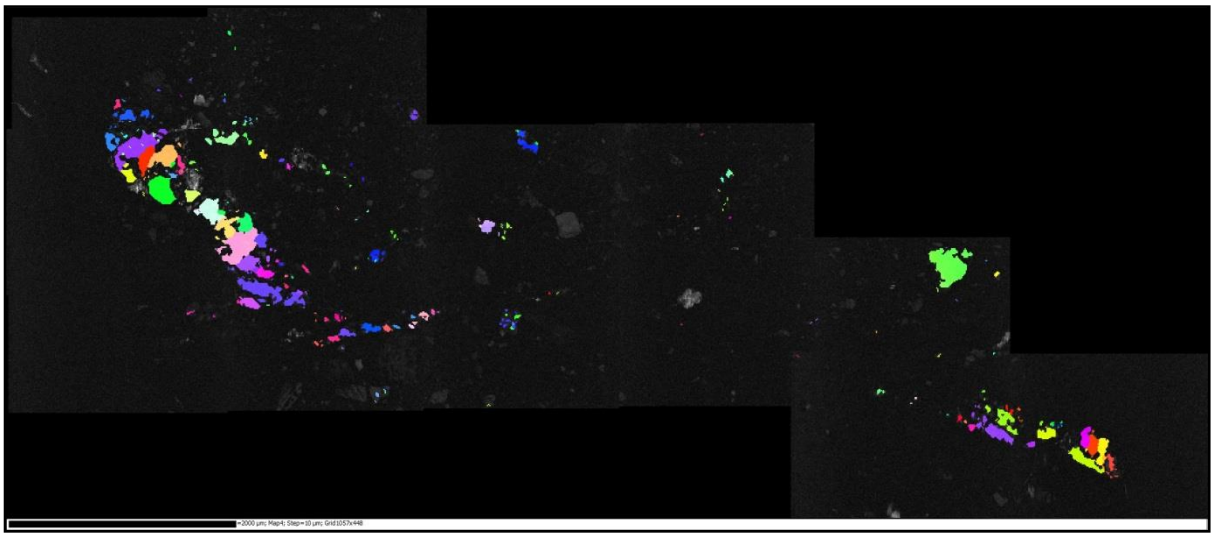

Figure A.7.39 IPF in the x-direction overlaid on the band contrast image.

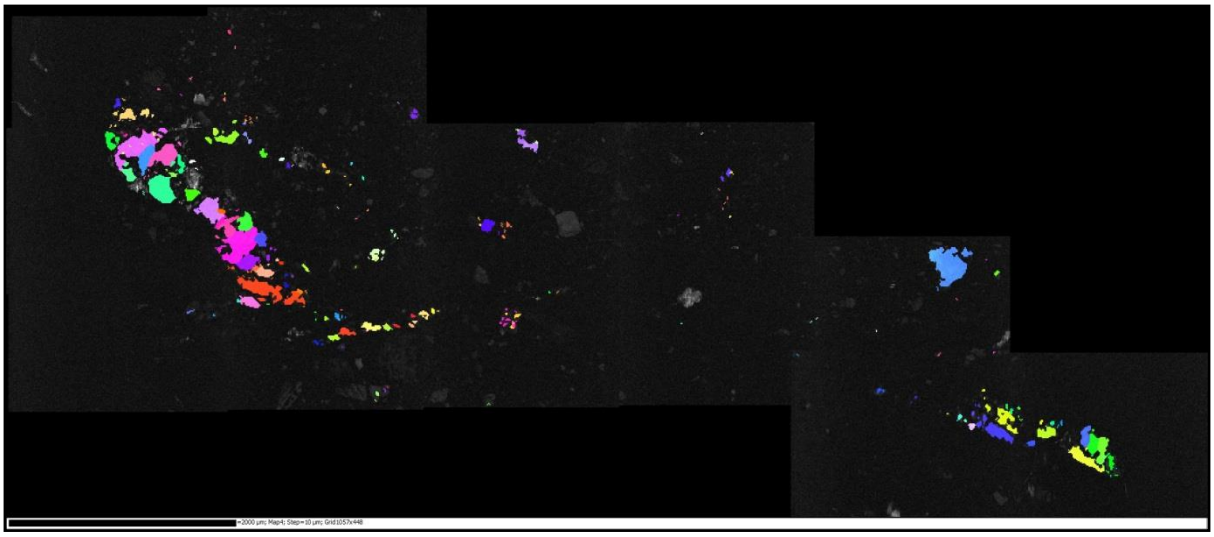

Figure A.7.40 IPF in the y-direction overlaid on the band contrast image.

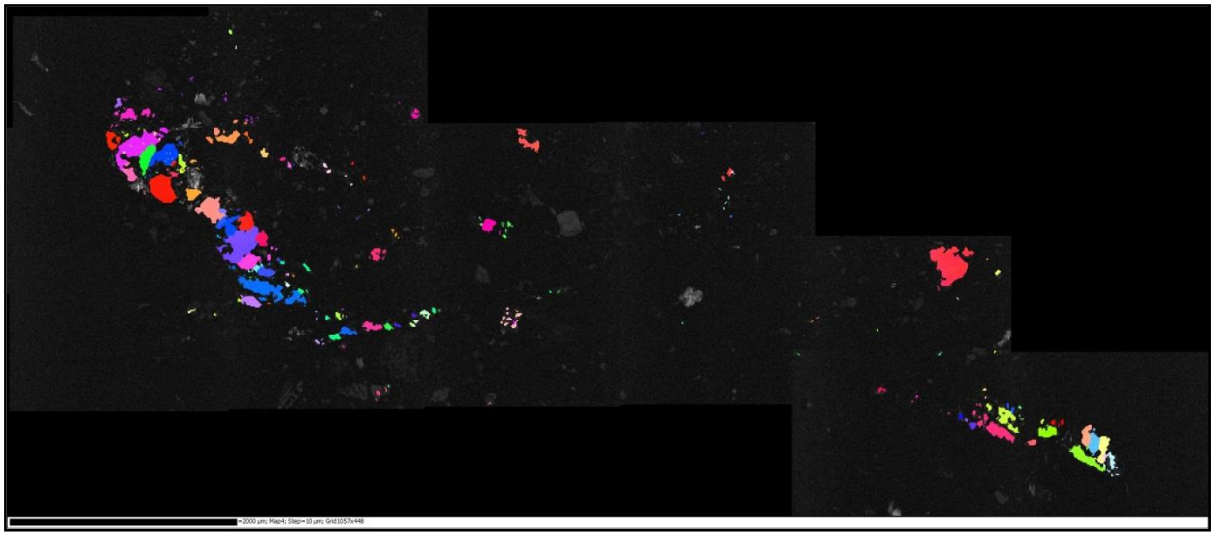

Figure A.7.41 IPF in the z-direction overlaid on the band contrast image.

Slice 8:

Prepared but not scanned in the SEM.

Appendix 8: Laser Ablation Parameters for Thin Section

Outlined below are the laser ablation parameters for the initial laser ablation inductively coupled plasma mass spectrometry (LA-ICP-MS) analysis run using the thin section from Chapter 2, included are brief comments noted during data acquisition. Possible glass signatures have been relocated to the bottom of the table. Figure 4.3, Chapter 4 shows the location of each spot and or track.

Table A.8.1 List of laser ablation parameters for the IC-PMS, including initial comments and observations.

Analysis Nº	Track or Spot	Parameters							Initial Comments and Observations
		Pre-Ablation	Laser (mV)	Length (µm)	Time (s)	Speed (μms^{-1})	Spot ⌀ (µm)	Frequency (Hz)	
0	Standard Run 610-01.D and 610-02.D								
KA30-2	Spot	No	Std.	-	Std.	-	50	Std.	Dark core with ~ glass signature separated.
KA30-3	Spot	No	80	-	Std.	-	50	Std.	Dark core
KA30-4	Spot	No	40	-	Std.	-	50	Std.	
KA30-5	Spot	Yes	50	-	Std.	-	50	Std.	Light grey zone Increase in REE
KA30-6	Spot	Yes	50	-	Std.	-	50	Std.	Same grain as 1-4
KA30-7	Track	Yes	80			10	50	Std.	Dark grey core
KA30-8	Track	Yes	80			15	75	Std.	Dark grey core
KA30-9	Track	Yes/No	50	300	20	15	75	Std.	Light grey zone Increase in REE
KA30-10	Track	-	-	-	-	-	-	-	Epoxy
KA30-11	Track	-	-	-	-	-	-	-	Glass or Epoxy
	Standard Run 610-01.D and 610-02.D								
KA30-12	Spot	-	-	-	-	-	-	-	Possible Glass
KA30-02 G	Spot	No	Std.	-	Std.	-	50	Std.	Possible Glass
KA30-0	Track	Yes	Std.	300	Std.	-	75	Std.	Possible Glass

(Std.)= Standard Operating Parameters

Appendix 9: Laser Ablation Parameters for Rock Fragments

Outlined below are the laser ablation parameters for the second laser ablation inductively coupled plasma mass spectrometry (ICP-MS) analysis run using the core fragments. For the analysis of the rock fragments all the laser parameters were keep constant (Table A.9.1).

Table A.9.1 List of parameters for laser ablation in the IC-PMS.

Parameters				
Track Length (μm)	**Run Time (s)**	**Speed (μms^{-1})**	**Laser Spot ⌀ (μm)**	**Laser Frequency (Hz)**
400	40	10	75	10

Included in the below table is the analysis information and brief comments noted during the acquisition of the IC-PMS data. Figure 4.5 and Figure 4.6, Chapter 4 both show the sample fragment and the location of each track within the bladed calcite vein respectively.

Table A.9.2 List of track information and initial comments and observations.

Analysis Nº	Rock Fragment	Spot or Track	Initial Comments and Observations
Standard analysis (6 12-01 and 6 10-01)			
1	Fragment B, Side ii	Track 1a	Pre-ablation track.
2	Fragment B, Side ii	Track 1b	Revised element table plus a high Al signature.
3	Fragment B, Side ii	Track 1c	Al signature variable.
4	Fragment B, Side ii	Track 2a	Pre-ablation track
5	Fragment B, Side ii	Track 2b	Initial section shows promising U/Th ratio.
6	Fragment B, Side ii	Track 2c	
7	Fragment B, Side ii	Track 3a	Pre-ablation track, high Th count.
8	Fragment B, Side ii	Track 3b	Th and Al levels approximately level.
9	Fragment B, Side ii	Track 3c	
Standard analysis (6 12-02 and 6 10-02)			
10	Fragment A	Track 1a	Pre-ablation track, Th near U levels.
11	Fragment A	Track 1b	Th near U levels.
12	Fragment A	Track 1c	Th near U levels.
13	Fragment A	Track 2a	Pre-ablation track.
14	Fragment A	Track 2b	Th near U levels.
15	Fragment A	Track 2c	Th near U levels.
16	Fragment A	Track 3a	Pre-ablation track.
17	Fragment A	Track 3b	Th near U levels.
18	Fragment A	Track 3c	Th near U levels.
Standard analysis (6 12-03 and 6 10-03)			